Self–Assembly of Helical Ribbons From Chiral Amphiphiles

by

Yevgeniya Vladimirovna Zastavker

B.S. Physics
Yale University, 1995

Submitted to the Department of Physics in Partial Fulfillment of the Requirements for the Degree of

Doctor of Philosophy in Biological Physics
at the
Massachusetts Institute of Technology

June 2001

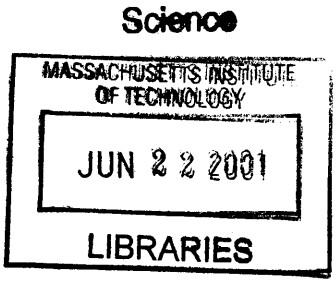

Signature of Author _____
Department of Physics
February 15, 2001

Certified by _____
George B. Benedek
Alfred H. Caspary Professor of Physics and Biological Physics
Thesis Supervisor

Accepted by _____
Thomas J. Greytak
Professor of Physics
Associate Department Head for Education

Self–Assembly of Helical Ribbons From Chiral Amphiphiles

by

Yevgeniya Vladimirovna Zastavker

Submitted to the Department of Physics on September, 2000
in Partial Fulfillment of the Requirements
for the Degree of Doctor of Philosophy in Biological Physics

ABSTRACT

The study of the self-assembly of helical structures has been motivated by their newly found biological and technological importance. In many systems, helical ribbons are precursors to the formation of tubules, which may be used in the controlled release of drugs or as templates for micron scale electronic components. Used as springs, helical ribbons open up an entirely new avenue for the measurement of forces on the biological scale. Given the importance of these structures, a series of experiments to probe the kinetics and energetics of helix formation has been performed. Theoretical interpretation and experimental measurements of helix elastic properties have also been performed. It was shown that the formation of helical ribbons of pitch angles of 11 and 54°, previously thought to be a property unique to model bile systems, is a general phenomenon of quaternary sterol systems composed of a bile salt or nonionic detergent, a phosphatidylcholine or a (mixture of) fatty acid(s), and a steroid analog of cholesterol in water. The majority of helical ribbons were right-handed; but some left-handed helices have been found. Additionally, a small number of helices with pitch angles between 30 and 47° were found in some systems. The elastic properties of the low pitch helical ribbons in Chemically Defined Lipid Concentrate were studied via relaxation experiments and measurements of force versus extension curves using silicon cantilevers as force probe. The helices exhibited linear behavior over a large range of extensions (up to 200% of helix original axial length). The forces involved in the deformation of low pitch helices have been found to be in the 0.25-1.0 nN range making them ideal for use as biological force probes. Additionally, a novel tension-induced reversible straightening transition of the helical ribbons has been observed: when a helix is extended beyond a critical value, part of it unwinds leaving separate straight and helical sections in equilibrium with each other. Probing these fascinating elastic properties is currently the best hope for more fully illuminating the microscopic nature of helical ribbons and the driving force behind their formation.

Thesis Supervisor: George B. Benedek

Title: Alfred H. Caspary Professor of Physics and Biological Physics

To

my Parents,

Elizaveta and Vladimir Zastavker,

whose vision I am about to fulfill

Acknowledgement

Here it is, the culmination of 22 years of education. These have been 22 drawn out but exciting years during which my world view has found its first seedlings, has started growing and developing and has expanded enough for me to be able to obtain my doctorate degree. This is the point in my life when for the first time I am ready to acknowledge the fact that I am about to fulfill the dream that both my parents and I have cherished for a very long time, through the pain of intimidation and persecution, through immigration and depression, and through the joys and sorrows of everyday life.

Unbeknownst to him, my path into the field of physics has been laid by my father, Vladimir Davidovich Zastavker. From an early age he satisfied my curiosity about why the wind was blowing and why the sky was blue. His enthusiasm for science, knowledge of physics and mechanical engineering, and patience had become a wonderful introduction into what would develop into my desire to become a scientist.

At Yale University, Professors Malcolm Boshier, Kurt Gibble, Dimitry Kusnezov and Jack Sandweiss have taught me to think as a scientist and encouraged me to continue my studies in physics despite the many obstacles that would be facing me in the future. Professors Moshe Gai of Yale University and University of Connecticut and Tom Rosenbaum of the University of Chicago taught me the basic research skills necessary in a physics laboratory. These scientists have also given me a sense of confidence and persuaded me to continue in the field of physics, cheering for all my successes throughout my undergraduate and graduate careers.

I am indebted to Professor George B. Benedek, my graduate research advisor, who has seen me through all the intellectual frustrations and victories that a research work brings to a scientist. His support, encouragement, and understanding of all the various intricacies of a graduate student life have paved the way for my vision of a woman scientist in today's world. I am forever grateful to Professor Benedek for bringing me into the field of Biological Physics, giving me the strength of mind and the ability to think critically.

I am also thankful to all the current and former members of Prof. Benedek's group. I would like to send special thanks to Mr. Brice Smith whose intellectual assistance at the end of my graduate career became a critical part of this thesis.

Brice's knowledge and experience as well as his desire to help have become invaluable components of the helical ribbon project. Dr. Aleksey Lomakin's adherence to the values of true science and his vision of the theoretical piece of the helical ribbon project have become crucial in the identification of the essential elements of the theory from the sea of irrelevant ideas. Dr. Neer Asherie's experience and sense of humor has seen me through all five years of my graduate research. Dr. Doo Soo Chung's original work with helical ribbons has served as the basis for my work; I am thankful to Doo Soo for his assistance and intellectual support during the first two years of my graduate career. I would like to extend my deep gratitude to Dr. Jayanti Pande for many stimulating discussions on the biochemical side of my research work and for overall scientific and moral support during my graduate career. Finally, Mr. Olutayo Ogun's (Ty's) belief in me helped me to always look on the bright side of things.

I am very grateful to Dr. Joanne Donovan for her assistance in deciphering the biochemistry of gallstone disease and brainstorming the research ideas. Dr. Anja Biere has given this project a new direction when she brought to our attention the existence of helical ribbons in CDLC. Dr. Joel Schnur's belief in the helical ribbon project and our many discussions were helpful in finding both the financial support and the new paths of the helical ribbon project. I would like to extend my thanks to Dr. Marybel Soto for her support of both the project and her personal support of me as a student. Prof. Mahadevan of M.I.T. has provided me with intuitive understanding of one of the theoretical concepts at the very end of my thesis writing, which has helped me to finalize this document. Ms. Lynn Roberson, Ms. Blanche Staton, Mrs. Peggy Berkowitz, and Mrs. Pat Solakoff have helped me to face the many difficulties and frustrations that I encountered in the past five and a half years. Their big hearts and their support was absolutely invaluable. Prof. Emeritus Gene Kangas and Mrs. Linda Kangas' kind encouragement and their vision of the artistic side of this thesis have given me the very much needed support and loving care.

There are no words that can truly describe the level of gratitude and debt that I am forever in to my parents, Vladimir and Elizaveta Zastavker. These unbelievable people have given up their future in order for me to have mine. They have always been there for me, crying with me and laughing with me, supporting me and caring for me. Their true deep love has helped me to survive through the hardest times of my life and has given me enough strength to move forward no matter what obstacles, no matter what fights, no matter which pain I was facing. My parents and my brother,

Vitaly Zastavker, are the real heros of this drama that is called graduate school.

Finally, I would like to express the deep gratitude to my husband, Dr. Erik Kangas, whom I met during the very first year of my graduate career. I am forever grateful to Erik for giving me clarity of mind and the sense of direction when I had none. I truly believe that the reason I have the awesome opportunity to write these words is because Erik did not let me give up my graduate career and held me through every "problem, triumph, and plateau". His constant moral and scientific support, his loving care, energy and desire to help have given me strength to persist and endure for the sake of the future I am about to enter.

Contents

Chapter 1

General Introduction

1.1 Historical Background

Many fields in molecular biology, physical sciences, and materials engineering consider a detailed understanding of the fundamental mechanisms by which synthetic and biological molecules self–assemble to be essential if scientific and technological progress is to be made. In polymer biosynthesis, for example, a primary goal is the exploration of biosynthetic routes for the preparation of biologically based polymers, such as natural fibers, modified natural proteins, and synthetic proteins that do not have close natural analogs.[1] In the synthesis of "decorated" membranes,[2] research focuses on the fabrication of synthetic membranes that mimic natural membrane function via inclusion of proteins, adsorbed colloidal particles, etc. In the field of self–assembled monolayers and multilayers, the approach is to determine the phase diagram of surfactant monolayers on both solid and fluid substrates.[3,4] This knowledge has already led to the understanding of how to attach cells to a substrate in a particular pattern[5,6] and to lithographic patterning of metals.[7] In organized structures in the mesoscopic range (this is the range intermediate between the atomic scale and macroscopic scale), one seeks to understand the kinetic and energetic processes involved in the spontaneous organization of biomolecular systems into crystalline structures whose lattice constants lie in the mesoscopic range.[8] The self–assemblies of interest in the field of organized structures on this scale have been vesicles used as long-term controlled–release systems,[9] smectic layers used as molecular sieves,[10] and tubules used as templates for electronic devices.[11] These are just a few examples of the variety of research areas founded upon the same conceptual framework — an application of the knowledge and understanding of the molecular, kinetic, and

thermodynamic factors controlling biomolecular self–assembly.

In the past decade, the self–assembly of the synthetic and biological amphiphiles into tubular and helical structures has received much interest. These structures are valuable in their technological applications and also play a central role in biological processes such as cholesterol crystallization. The cornerstone of research into understanding tubular and helical structures is the work performed by two independent groups. In early 1990's, J. M. Schnur and his co-workers at the Naval Research Laboratory (N.R.L.) in Washington D. C. laid the foundation for the study of tubules,[11] while D. S. Chung, G. B. Benedek, and their co-workers at M.I.T. and Harvard University laid the groundwork studying the formation and evolution of helical ribbons during the cholesterol crystallization process.[12] Since then, significant progress has been made studying the kinetics and thermodynamics of the formation and evolution of both tubular and helical structures.

The N.R.L. group has been concentrated on the tubules, which are hollow cylinders formed from the bilayer or multilayer membranes of diacetylenic lipids, such as $DC_{8,9}PC$, $DC_{8,11}PC$, and others. P. Yager and P. Schoen were the first to show that multilamellar vesicles of $DC_{8,9}PC$ produce tubules upon cooling below the L_α – L_c phase boundary.[13] Tubules formed in this way had typical diameters of 0.5 – 1.0 μm and lengths of 10 – 1000 μm.[11] They often exhibit helical markings that wind around the cylinder. To explain these helical windings, it was proposed[14] and later experimentally shown[15] that lipid bilayer ribbons wrap in a helical pattern; the merging of the ribbon edges results in a cylindrical geometry. Since the first discovery of the formation of diacetylenic tubules, a lot of thought has been placed into further studying their possible technological applications. Since tubules are essentially "microvials" in which a solid or liquid can be encapsulated, they have been used in controlled–release applications for marine antifouling (release over many years),[16] and for drug delivery purposes (release over several days to months).[11] Metal–clad tubules have interesting electromagnetic properties, and have been used in applications for their dielectric properties (as miniaturized microwave circuits), as absorptive filters,[11] and in electroactive composites.[17] However, in order to realize the potential of self–assembled tubules in the above applications, the geometrical dimensions of the tubules must be accurately controlled. To provide this control, an in-depth understanding of the factors contributing to the tubule formation must be achieved. Several investigators, including the N.R.L. group, have developed continuum elastic

theories based on molecular chirality in an attempt to explain the process of tubule self–assembly.[14,18,19]

In an independent study, Chung *et al.*[12] described a biologically important system, model bile, in which helical ribbons and tubules form. Model bile is a system of three species of chiral molecules in water: a bile salt, a phosphatidylcholine, and cholesterol.[20–28] Helical ribbons and tubules are metastable intermediates in the process of cholesterol crystallization in bile,[12,27,29] which precedes cholesterol gallstone formation.[20,25,27–30] In fact, helical structures in model bile systems transform into tubules via an increase in the helical ribbon width until merging and, frequently, subduction of one ribbon edge under another occurs. Unlike the helical ribbons and tubules found in other systems, structures formed in model bile systems have diameters in the range between 3 μm and 70 μm, and usually do not exceed 200 μm in length. Another feature that sets helical ribbons in model bile systems apart from the structures in other systems is the existence of helical ribbons of *two* pitch angles, high pitch (with a pitch angle of 54 $\pm 2°$) and low pitch (with a pitch angle of 11 $\pm 2°$).[12] Previous experimental and theoretical studies of helical ribbons in other systems have found pitch angles to be either $45°$[31–33] or $\sim 60°$.[13,34–36] Therefore the phenomenon of the formation of two helix pitch types with the above pitch angles was thought to be unique to model biles.

Since the groundbreaking work of Chung *et al.*,[12] significant progress has been made in the study of helical and tubular structures formed in the cholesterol crystallization process. Experimental and theoretical efforts in studying these structures have resulted in a deeper understanding of the molecular and thermodynamic factors governing their formation and evolution. A study of the elastic properties of helical structures may potentially result in their application as microsprings for the measurements of forces and energies associated with molecular interactions. It is the purpose of this thesis to briefly review the work of Chung *et al.*[12] and their colleagues at N.R.L.[18] and to present our new experimental and theoretical discoveries in studying the helical structures found in the process of cholesterol crystallization.

1.2 Thesis Organization

This thesis is divided into three conceptual parts, each presented in a separate Chapter. Each Chapter, in turn, is divided into sections, with introduction, materials and

methods, and results subsections.

The first part presented in Chapter II describes the experimental evidence for the formation and evolution of helical ribbons. There we present a detailed experimental study of the pathways of helix formation. We also present a study of helix composition in which we attempt to understand the role of cholesterol and phospholipids in helix formation. We further present evidence that the phenomenon of helical ribbons of two pitch types found in model bile systems is not unique to model biles. In fact, formation of such helices is a general phenomenon of a large number of multicomponent systems composed of three molecular species: a micelle–forming surfactant, a bilayer–forming surfactant, and a sterol in water. We further coin a term for these systems which from now on will be called quaternary sterol systems or simply QSS (model bile also being a QSS). This Chapter concludes by describing an application of forces to helical ribbons and their behavior under tension such as full elongation, relaxation, and a novel behavior of tension–induced straightening transition.

The second part of this thesis presented in Chapter III, contains a theoretical development of the continuum elastic theories describing the geometrical characteristics of helical structures. We present a new theoretical model of the formation of helical ribbons after first describing the relevant existing theories of Chung *et al.*[12] and Selinger *et al.*[18] This new model is based on the theory of the elastic properties of crystals as described by Landau and Lifshitz.[37] The existing models are compared to the new crystalline theory.

The third and final part of this thesis presented in Chapter IV, describes experimental and theoretical work related to the axial extension and compression of low pitch helices formed in one of the QSS. In this Chapter we illustrate the bulk behavior of a helix under an applied uniaxial force and find the expression for the helix spring constant, K. Relating this spring constant to the microscopic elastic moduli of helical ribbons provides a simple and direct measurement of what values these moduli can attain.

General conclusions to this thesis are presented in Chapter V.

Chapter 2

Experimental Evidence

2.1 Introduction

In this chapter, we describe our initial effort to study the process of cholesterol crystallization in quaternary sterol systems. In particular, we describe our endeavor in studying the formation and evolution of high, low, and intermediate pitch angle helical ribbons in quaternary sterol systems. In our numerous original experiments, the following achievements have been made:

1. we explored the biochemical nature of helical ribbons,
2. we learned how to produce high pure yields of helices of each pitch angle,
3. we followed the temporal sequence and the kinetics of helix formation and evolution.

These experiments have served as a basis for the entire body of work regarding the cholesterol crystallization in quaternary sterol systems and proved invaluable to our understanding of helical structures. In addition, our initial efforts inspired a large number of predictions describing helix formation and evolution. Some of these predictions will be addressed later in this thesis. The purpose of this chapter however is to describe the biochemical nature of helical ribbons in quaternary sterol systems and the predictions which pertain to the helix structure, helix formation and evolution.

In Section 2.2, we begin by describing the materials and methods used in the preparation of the quaternary sterol systems. In Section 2.2.1 we present the biochemical background necessary to understand the helix formation, as well as the current methods of helix production. Section 2.3 pertains to the temporal evolution of helical structures, their formation and decomposition (dissolution). Section 2.4

describes the experiments which focus on probing the helix chemical structure. We separately describe experiments concentrating on the function of cholesterol in helix formation (Section 2.4.1) and experiments directed at the study of the function of phospholipids in helix formation (Section 2.4.2). Section 2.5 demonstrates that helix formation is not unique to model bile systems but is rather a general phenomenon shared by a variety of quaternary sterol systems. Finally, we present a qualitative description of helical ribbon behavior under applied forces in Section 2.6. This section focuses on the initial set of experiments probing the helix elasticity. These experiments illustrate various patterns of helix behavior under the applied axial tension. This latter experimental work has inspired the new crystalline theory described in Section 3.3.

2.2 Materials and Methods

2.2.1 Biochemistry Involving Helix Formation in Quaternary Sterol Systems: The Background

It is a well known fact that hydrophobic cholesterol molecules are virtually insoluble in water: the maximum solubility has been found to be 2.6×10^{-9} M.[38] However, cholesterol can be solvated to concentrations of 5 - 50 mM within thermodynamically stable micelles and metastable unilamellar vesicles in human gallbladder bile.[30,39] Bile salt micelles incorporate small amounts of cholesterol. At constant temperature and total lipid concentration, the precise amount of cholesterol solvated in an aqueous solution of bile salts depends on the hydrophobic–hydrophilic balance that each bile salt species possesses due to its chemical structure.[30] At small cholesterol concentrations, both simple bile salt micelles and mixed bile salt–phospholipid micelles solvate cholesterol. When solubility of cholesterol in micelle is exceeded, unilamellar or multilamellar vesicles form. They are composed of both bile salt and phospholipid molecules.[40] Since bile salts easily form micelles, they are called a micelle–forming substance. On the other hand, since phospholipids molecules cannot form micelles by themselves, but rather form vesicles, this species of amphiphiles is called bilayer–forming substances. To summarize then, in human gallbladder bile cholesterol is solvated by the amphiphilic micelle– and the bilayer–forming substances.[30,40] In replicating human gallbladder bile by quaternary sterol systems (QSS),[41] the role of the micelle–forming bile salts is served by either bile salts or other non-ionic detergents;[20] the role of the

bilayer–forming phospholipids is served by either phospholipids or fatty acids,[20] as is further described in Section 2.5.

When an initially unsaturated quaternary sterol system (QSS), in which cholesterol is solvated in simple and mixed micelles,[20,25,26,28,29,42] is diluted with water, the resulting solution becomes supersaturated with cholesterol.[20,25,28,42] This process can be understood in terms of critical micelle concentration of amphiphilic molecules in water. When a micellar solution is diluted below a value of critical micellar concentration, micelles disperse and a monomeric solution of amphiphiles is formed.[30] In quaternary sterol systems, when a micellar solution is diluted below the critical micellar concentration, two processes occur: (1) large micelles and vesicles supersaturated with cholesterol form, and (2) free monomers of cholesterol form. Free cholesterol that is not solvated within the micellar "pockets" is believed to contribute to the growth of cholesterol monohydrate crystals by diffusing to crystals' surfaces.[30,40,43,44] Large micelles and vesicles are thermodynamically unstable, the stable form being cholesterol monohydrate plate-like crystals in supersaturated QSS. Therefore upon supersaturation (by dilution) the process of cholesterol crystallization commences. However, the slow rate of cholesterol crystallization (1 - 6 months) allows for the formation of intermediate metastable structures which can be resolved with light microscopy techniques. These metastable structures include filaments, arcs, helices of high, low and intermediate pitch angles (see Section 2.5), and tubules.

The types of intermediate structures seen in a particular QSS depend strongly on the initial concentrations of its components. This suggests that a useful description of the metastable structures' formation and evolution can be made in terms of a "phase diagram." In terms of the phase diagram, the dilution of an initially unsaturated QSS to form a supersaturated QSS is equivalent to crossing the phase boundary between a micellar region and a region of a diagram where cholesterol monohydrate crystals are stable.[45] A phase diagram then provides a useful framework for understanding conditions necessary for cholesterol crystallization. The phase diagram of a four-component system can be represented as a regular tetrahedron, whose corners represent a 100% concentration of each component. Holding one component at a constant concentration and varying the other three components, the system can be represented by a triangular phase diagram.

Figure 2.1 displays the triangular phase diagram of a typical QSS at 37°C, in which the concentration of water is held constant (at total lipid concentration of

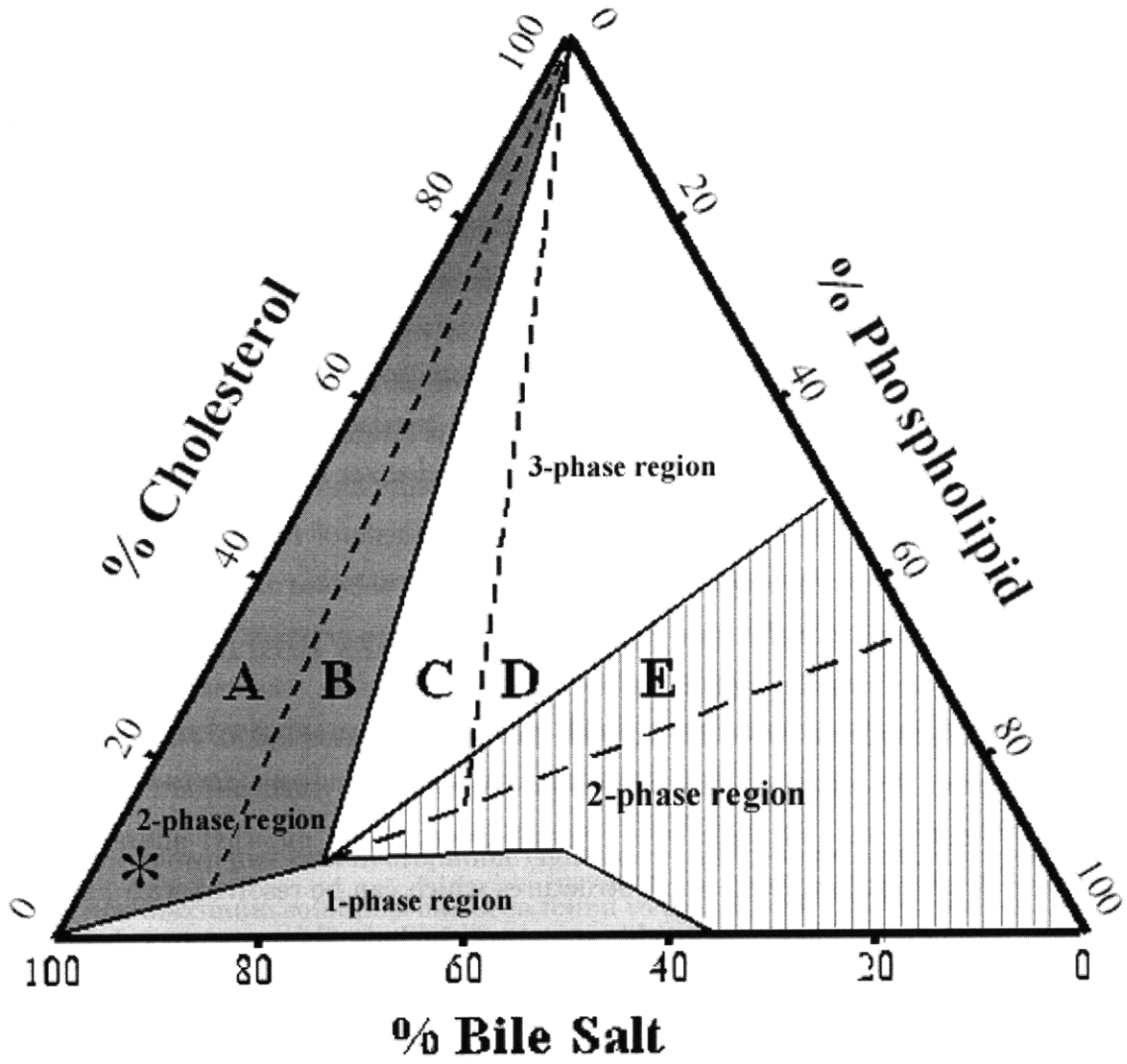

Figure 2.1: Phase diagram of a typical QSS with total lipid concentration $\approx$ 7.3 g/dL (in water). The components of QSS are expressed in moles percent. The micellar region ("1-phase region") at the bottom of the diagram is enclosed by a solid curved line. The number of phases given in each region represents the number of coexisting stable structures in each region. There are three different stable structures that can coexist with each other: saturated micelles, various liquid crystals, and cholesterol monohydrate crystals. In the "1–phase" region at the bottom of the phase diagram only micelles are stable (light grey region). In the "2–phase" region on the left cholesterol monohydrate crystals and micelles are stable (dark grey region), whereas in the "2–phase" region on the right micelles and liquid crystals are stable structures (hatched region). In the region, where three phases coexist all three types of structures are stable: saturated micelles, liquid crystal structures, and cholesterol monohydrate crystals (transparent region). Cholesterol monohydrate formation often occurs through the formation of metastable intermediate structures. They are filaments, helical ribbons of high, low and intermediate pitch angle, and tubules. In the regions of the phase diagram that are labeled "A" through "E", cholesterol monohydrate crystals are stable structures. Each of these regions however corresponds to different crystallization sequences,[26] i.e. sequences of formation of metastable intermediate structures. The QSS chosen for the work described in this thesis have concentrations that can be approximately identified by a star in the region "A", where the sequence of formation of metastable intermediates is filaments $\rightarrow$ helical ribbons $\rightarrow$ tubules $\rightarrow$ cholesterol monohydrate crystals.

7.4 grams per 1 dL of water).[26,29] The shape of the phase boundary depends on the total lipid concentration and the temperature of system. The axes of the diagram are the mole fractions of a QSS constituents: a bile salt, a phospholipid, and cholesterol. The phase diagram is divided into regions, which are identified by the number of stable structures. There exists three types of structures that could be stable: saturated micelles, various composition liquid crystals, and cholesterol monohydrate crystals.[26,29] In the "1–phase" region at the bottom of the phase diagram only micellar structures are stable (light grey region). In the "2–phase" region on the left cholesterol monohydrate crystals and micelles are stable (dark grey region), whereas in the "2–phase" region on the right micelles and liquid crystal structures are stable (hatched region). In the "3–phase" coexistence region all three types of stable structures coexist (transparent region). Cholesterol monohydrate crystals often form through intermediate metastable structures, such as filaments, arcs, helical ribbons of high, low and intermediate pitch angle, and tubules (very rarely "fused" crystals are also observed[25]). Depending on relative concentration of components in QSS, the sequence of metastable structures formed on the way to crystal formation varies. In fact, there exists five different sequences of formation of metastable structures. The regions of phase space in the phase diagram governed by each sequence of cholesterol crystallization are shown in Figure 2.1 as regions labeled "A" through "E."[26,29]

The experimental work described in this thesis concerns various QSS that prior to dilution have concentrations which place them in the "1–phase" region of the phase diagram, where only micelles are present. When diluted, these now supersaturated QSS have concentrations which place them in the region "A" of the phase diagram, where the temporal sequence of the formation of metastable structures is filaments $\rightarrow$ helical ribbons $\rightarrow$ tubules $\rightarrow$ cholesterol monohydrate crystals. This temporal evolution (including the order of appearance of high, low, and intermediate pitch helical ribbons) will be further discussed in Section 2.3. The star in the dark grey region corresponds to the approximate concentrations of components of QSS for the newly supersaturated system.

2.2.2 Chemicals and Chemical Procedure

The chemicals used in experiments described in this Chapter are detailed in the "Materials and Methods" subsections for each experiment; therefore, they will not be described here. This section will delineate the preparation methodology of various

quaternary sterol systems (QSS), which is the same for all experiments.

The procedure described below is based on the methodology of Konikoff *et al.*[20] In all experimental procedures, we used deionized Milli-Q (Millipore) water at ambient temperature (25°C). All of the quaternary sterol systems (QSS) were prepared from three components: bile salts or non-ionic detergents, phospholipids or fatty acids, and sterols. In our experimental work we used Pope washed bile salts;[46] however, this washing was not necessary for successful production of helical ribbons.[20] Prior to experiments, all components were stored in organic solvents (usually chloroform-methanol 2:1 mixture by volume) at −20°C. The dry weight of each component was determined by drying 50 μl of each stock solution for 20 minutes in a vacuum dessicator at room temperature (25°C) followed by a 1 hour incubation at 60°C. Based on the dry weight and the mole fraction of each component in QSS, we calculated the required volume of each component. These volumes were then aliquoted into a single test tube and evaporated under a stream of nitrogen leaving a lipid film. To further purify this lipid film from undesired organic substances, we rediluted the lipid film with a chloroform–methanol mixture (2:1 by volume) and then dried it again under nitrogen. The lipid films for each QSS were then lyophilized for at least 6 hours.

The lyophilized lipid films were stored at −4°C. To prepare a QSS from each lipid film, the latter was reconstituted in water to the appropriate concentrations of unsaturated quaternary sterol systems. Further six-fold dilution of unsaturated quaternary sterol systems with water, resulted in supersaturated systems.

2.2.3 Analytical Procedure: Instrumentation

The metastable structures and cholesterol monohydrate crystals were visualized using a phase contrast light microscopy technique (inverted microscope Diaphot-TMD, Nikon). The images were projected onto a CCD camera (Sony, DXC-970MD), recorded with a SVHS video recorder (Panasonic AG-1960), and further digitized with a built-in frame grabber on a Power Macintosh computer. For image enhancement and measurements, we used the public domain NIH-Image software package.[47] This process was used for visual monitoring, qualitative observations, and measurements. The microscope was placed on a vibration isolation tabletop (Newport Corporation, Irvine, CA). A piezoelectric micromanipulator (Burleigh, PCS-5000) was used to execute the delicate procedure of isolating a single helix and attaching it to rigid surfaces. With 60 nm resolution and a drift of less than one micron per hour (which was insignificant

on the time scale of the experimental measurement), we found this system to be well suited for our experimental work. Section 2.4.2 on fluorescence microscopy describes in further details the instrumentation necessary for those procedures. Quasielastic light scattering (QLS) measurements were performed at a constant scattering angle (90°) and ambient temperature (25°C) on a home–built apparatus equipped with digital autocorrelator.

2.3 Pathways of Formation of Helical Ribbons

In this section we discuss details of the pathways involved in cholesterol crystallization from a quaternary sterol system (QSS) composed of phospholipid (1-palmitoyl-2-oleoyl phosphatydilcholine, POPC), cholesterol, and sodium taurocholate bile salt. The temporal evolution of the metastable structures described here represents the typical behavior of metastable intermediates in cholesterol crystal formation. By design, all the quaternary sterol systems (QSS) studied had concentrations that place them in the "1–phase" region of the phase diagram (as shown in Figure 2.1) when they are unsaturated and in the region "A" when these QSS are supersaturated (see Section 2.2.1). For these QSS the temporal sequence of the formation of metastable structures is: micelles/vesicles → filaments → helical ribbons → tubules → cholesterol monohydrate crystals.

We observed the presence of micelles in a "1–phase" region of the phase diagram in the unsaturated QSS using quasielastic light scattering technique (QLS). Likewise we used QLS technique to observe the presence of saturated micelles and vesicles in the supersaturated QSS. To distinguish between various structures (micelles and vesicles), we measured the sizes of structures by acquiring their mean hydrodynamic radii in 200 μl aliquots of both the unsaturated QSS and the supersaturated QSS at 22°C. Prior to measurements, each sample was filtered through 0.22 μm unit Millipore at 25°C. According to the phase diagram, in unsaturated QSS only micelles should be present. However, our measurements showed populations of particles with two distinct values of hydrodynamic radii, $R_{H1} = 11 \pm 3$ Å and $R_{H2} = 40 \pm 5$ Å (figure not shown). Particles with the hydrodynamic radii of $R_{H1} = 11 \pm 3$ Å are presumably the micelles, which have been observed by other groups.[20,28] None of the previous QLS work, however, mentions the population of particles of the larger size, R_{H2}. This issue remains to be further investigated. Six–fold dilution of unsaturated QSS

to produce supersaturated systems generated larger size particles with hydrodynamic radii of $R_{H3} = 212 \pm 25$ Å,[20,24] as expected. Therefore, the QLS measurements indeed provided useful information on the existence of micelles in unsaturated QSS and on the existence of saturated micelles and vesicles in supersaturated QSS.

Filaments were the earliest microstructures observed with a light microscope during the process of cholesterol crystallization. They appeared within 2-4 hours of supersaturation of QSS. Filaments were replaced by helical wires that then grew laterally forming three types of helical ribbons: high pitch angle helical ribbons with a pitch angle of 54 ±2°, low pitch helical ribbons with a pitch angle of 11 ±2°, and intermediate pitch helical ribbons with a pitch angle in the range between 30 and 47°. This is the first time the existence and behavior of intermediate pitch helical ribbons has been established. Helical ribbons then proceeded growing laterally until their edges came into contact and fused thereby producing tubules. Therefore, tubules often presented clear helical patterns. However, we also observed tubules without helical patterns. The evolution of helices into tubules was observed only for high pitch and low pitch helical ribbons. In fact, the intermediate pitch helical ribbons were never found to transform into tubules and therefore into cholesterol monohydrate crystals. Unlike other authors,[12,26,34] we observed not only the fusion of helical ribbon edges to form tubules, but also the subduction of one ribbon edge under another. We found that in all QSS helical ribbons of high pitch form first, followed by low pitch helices, while intermediate pitch helical ribbons coexisted with either of the other two types of helices. We never observed a direct transition from helical ribbons of one pitch to another, in agreement with Chung *et al.*[12]

We also found that high and low pitch helical ribbons were very stable: at 37°C, high pitch helices were stable for up to 1 week and low pitch helical ribbons were stable for up to 3 weeks. At lower temperatures, these two types of helical ribbons were stable for up to 1 month for high pitch structures, and up to 6 months for low pitch helices. Intermediate pitch helical ribbons, on the other hand, were stable for only 1-2 days at 37°C and for less than 1 week at 4°C.

Figure 2.2 describes the pathways of cholesterol crystallization in QSS as this process pertains to formation and evolution of high pitch helical ribbons. In this Figure, solid and dashed lines represent observed and presumed transitions, respectively. For example, we have never observed direct transition from saturated micelles and vesicles ("M/V") to filaments ("F") and to small sizes of cholesterol monohydrate crystals

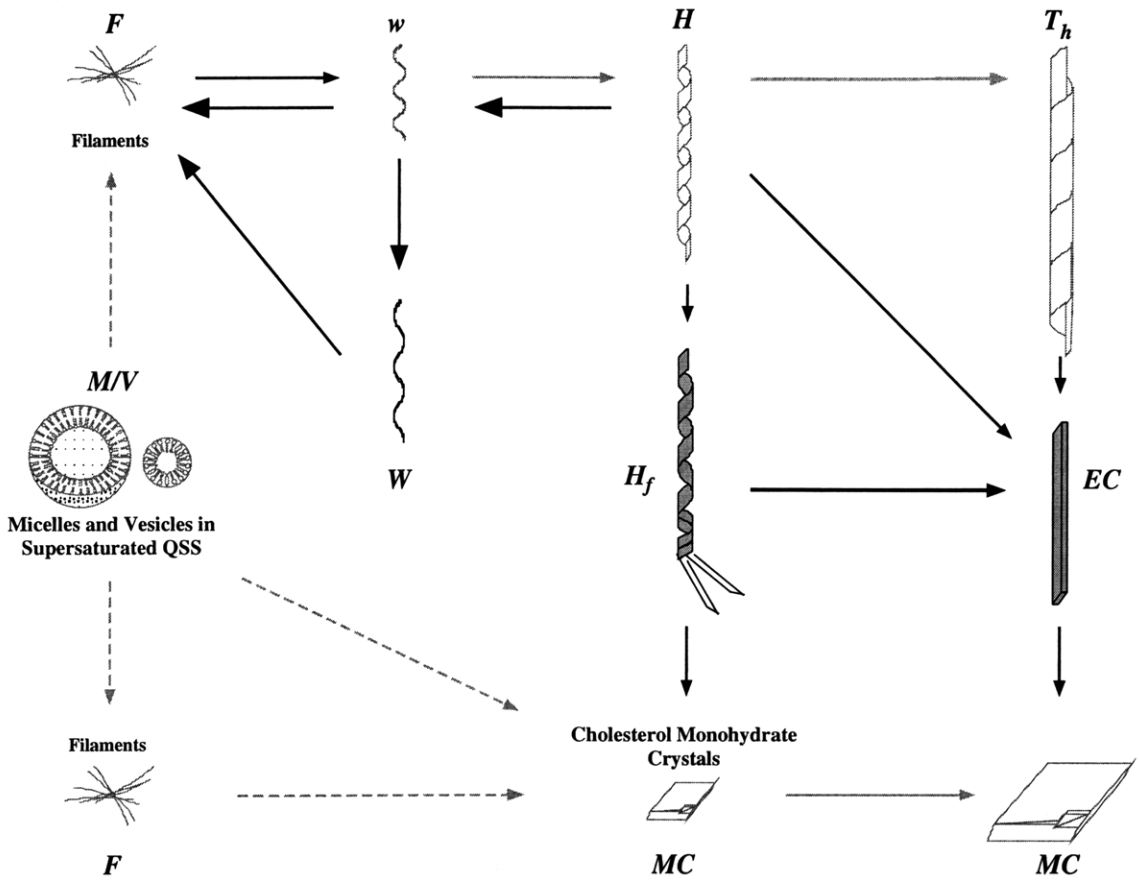

Figure 2.2: The pathways in the cholesterol crystallization process pertaining to the formation of high pitch helical ribbons and observed in supersaturated QSS. Each pathway is illustrated by an arrow. Solid and dashed arrows represent, respectively, observed and presumed transitions. Shown is the transformation from saturated micelles and vesicles ("M/V") to filaments ("F") to high pitch helical wires ("w"). The latter then grow laterally to form high pitch helical ribbons ("H") and tubules with helical patterns ("T_h"). The tubules either collapse on themselves or unravel to form elongated crystals ("EC"), which either fracture or grow laterally to form typical cholesterol monohydrate crystals ("MC"). We often observed high pitch helices to fray along their lengths to form flat ribbons ("H_f"). The latter fractured forming elongated crystals ("EC") or typical cholesterol monohydrate crystals ("MC") depending on the size of the fractured piece. Various metastable intermediates were found to dissolve. High pitch helical wires ("w") were found to unwind forming larger pitch helical wires ("W") which further unwound into filaments ("F"). These filaments then were found to dissolve. The grey arrows and transparent structures outlined in grey represent the pathways discovered prior to this study.[12,20,42] The black arrows and dark structures outlined in black represent the new–found pathways in cholesterol crystallization.

("MC"). The existence of these transition was inferred from multiple observations of formation of filamentous structures and of cholesterol monohydrate crystals on very short time scales (2-6 hours after supersaturation when incubated at 37°C). We have directly observed filamentous structures ("F") to coil thus forming helical wires ("w"). These wires then grew laterally to form helical ribbons ("H"). This lateral growth of helical wires was also accompanied by their axial growth into long (often up to 200 μm) helical ribbons. High pitch helical ribbons ("H") were often observed to continue their lateral growth until their edges came into contact and fused with each other or until one edge of a ribbon subducted underneath another. In this way, tubules with helical patterns were formed ("T_h"). These tubules were later found to either collapse on themselves or partially unravel and fracture. The result of either of these two processes was the formation of elongated crystals ("EC"), which are larger in one dimension than in the other, i.e. much longer than wider. These elongated crystals then grew laterally or fracture to form typical plate-like cholesterol monohydrate crystals ("MC"), whose length and width were approximately the same and whose angles were $\sim 101°$ and $\sim 79°$. We have also observed direct unraveling of high pitch helical ribbons ("H") to form elongated crystals ("EC"), which then followed the pathway described above. Another interesting phenomenon observed with high pitch helical ribbons ("H") was that they occasionally fray, i.e. split along their lengths to form flat ribbons of smaller widths ("H_f"). These flat ribbons either fractured to form small plate-like monohydrate crystals ("MC") or formed elongated crystals ("EC"). The latter then grew in size to form larger cholesterol monohydrate crystals. Finally, we have observed dissolution of elongated crystals (rare event, not shown in Figure) and dissolution of high pitch helical wires ("w"). The dissolution of high pitch helical wires of 54 $\pm 2°$ is shown in Figure. This process occurred in several steps: first, helical wires unwound to form helical wires of slightly larger pitch angle of $\sim 54 - -60°$ ("W"), which were stable for 1 to 2 days; second, these helical wires ("W") further unwound to form straight filaments ("F"); finally, these filaments dissolved. As can be observed in Figure 2.2, our results are consistent with evolution pathways described by Chung *et al.*[12] However, we made quite a few modifications and additions to Chung *et al.*'s results. To compare our new findings with those of Chung *et al.*, we used two different colors: arrows depicted in grey color stand for Chung *et al.*'s findings,[12] and the solid black arrows represent our new observations.

Figure 2.3 describes the pathways of cholesterol crystallization in QSS as this

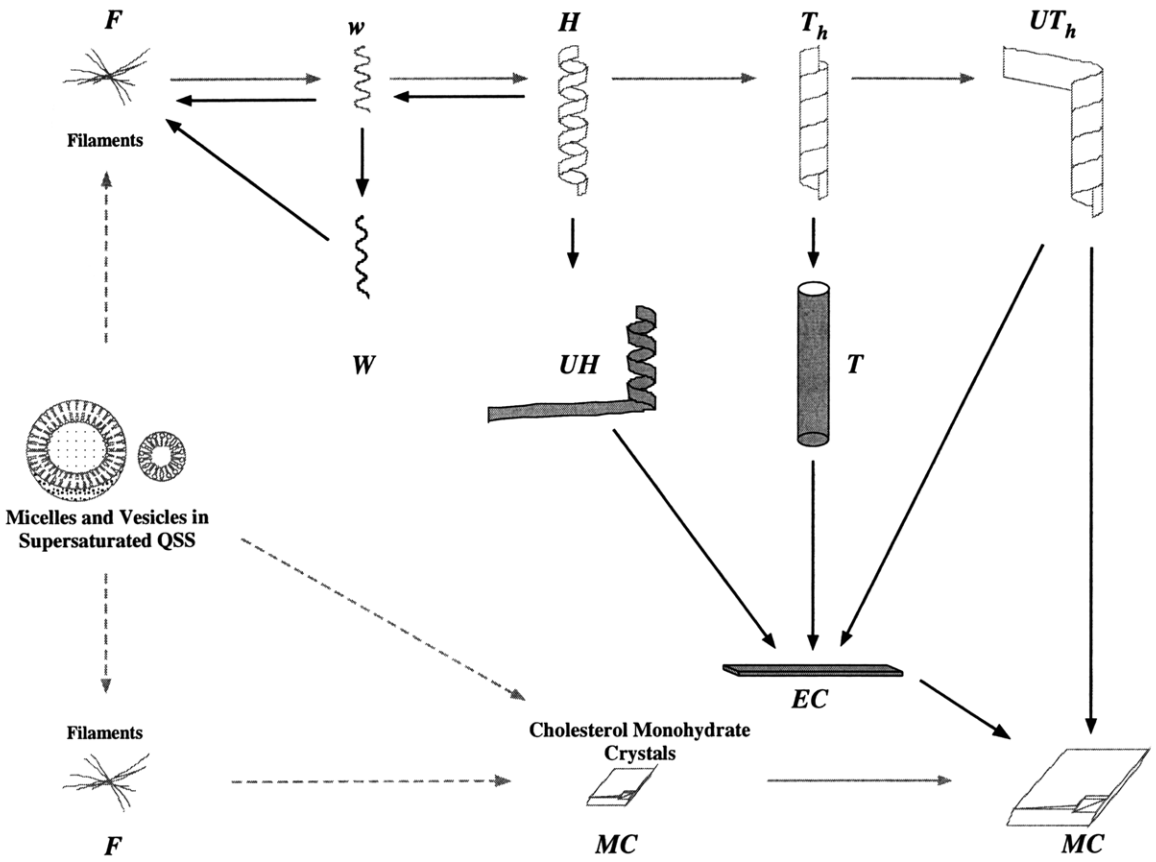

Figure 2.3: The pathways in the cholesterol crystallization process pertaining to the formation of low pitch helical ribbons and observed in supersaturated QSS. The transitions from saturated micelles and vesicles ("M/V") to filaments ("F") and plate-like cholesterol monohydrate crystals have not been observed directly, but rather were inferred from multiple experimental observations. However, we have directly observed filaments ("F") coiling to form low pitch helical wires ("w"), which then grew laterally to form low pitch helical ribbons ("H"). This lateral growth of helical wires was accompanied by their axial growth, such that on the average low pitch helical ribbons were reached axial lengths of approximately 100 μm. Further lateral growth of low pitch helical ribbons ("H") resulted in their edges either touching fusing with each other or subducting one under another to form tubules with helical patterns ("T_h"). Very often the lateral growth of ribbons resulted in formation of tubules without helical patterns ("T"). These latter tubules were often found to collapse on themselves forming elongated crystals ("EC"). The formation of plate-like cholesterol monohydrated crystals ("MC") from the elongated crystals ("EC") occurred either by their lateral growth or by elongated crystals fracturing perpendicular to their lengths. We often found that low pitch helical ribbons unwind completely ("UH") to form flat elongated crystals ("EC"). Another common pathway of cholesterol monohydrate formation was found to occur via tubules with low pitch helical pattern ("T_h") unwinding at their ends ("UT_h"); this unwound part then was found to fracture. Depending on the size of the fractured piece, either elongated crystals ("EC") or plate-like cholesterol monohydrate crystals ("MC") formed. As described above, elongated crystals rarely dissolved (not shown in the Figure). We also observed low pitch helical wires ("w") of pitch angles 11 $\pm 2°$ to dissolve by first forming larger pitch helical wires ("W"), whose pitch angles ranged between 13 and 17°, then unwinding completely to form filaments ("F"), which then dissolved. The grey arrows and transparent structures outlined in grey represent the pathways discovered prior to this study.[12,20,42] The black arrows and dark structures outlined in black represent the new–found pathways in cholesterol crystallization

process pertains to the formation and evolution of low pitch helical ribbons. The notation in this Figure is the same as in the Figure 2.2 above. The transitions from saturated micelles and vesicles ("M/V") to filaments ("F") and plate-like cholesterol monohydrate crystals have not been observed directly, but rather were inferred from multiple experimental observations. However, we have directly observed filaments ("F") coiling to form low pitch helical wires ("w'), which then grew laterally to form low pitch helical ribbons ("H"). This lateral growth of helical wires was accompanied by their axial growth, such that on the average low pitch helical ribbons were approximately 100 μm long. Further lateral growth of low pitch helical ribbons ("H") resulted in their edges either touching and fusing with one another or subducting one under another to form tubules with helical patterns ("T_h"). Very often the lateral growth of ribbons resulted in formation of tubules without helical patterns ("T"); this occurred when the ribbon width grew laterally and reached the length equivalent to tubule axial length. The tubules formed in this manner ("T") were often found to collapse on themselves forming elongated crystals ("EC"). The formation of plate-like cholesterol monohydrated crystals ("MC") from the elongated crystals ("EC") occurred either by their lateral growth or by fracturing of elongated crystals perpendicular to their lengths. We often found that low pitch helical ribbons unwind completely ("UH") to form flat elongated crystals ("EC"). Another common pathway of cholesterol monohydrate formation was found to occur via tubules with low pitch helical markings ("T_h") unwinding at their ends ("UT_h"); this unwound part then was found to fracture. Depending on the size of the fractured piece, either elongated crystals ("EC") or plate-like cholesterol monohydrate crystals ("MC") formed. As described above, elongated crystals rarely dissolved (not shown in the Figure). We also observed low pitch helical wires ("w") of pitch angles 11 $\pm 2°$ to dissolve by first forming larger pitch helical wires ("W"), whose pitch angles ranged between 13 and 17°, then unwinding completely to form filaments ("F"), which then dissolved.

Finally, we would like to describe Figure 2.4, where we illustrate formation and evolution of intermediate pitch helical ribbons of pitch angles ranging from 30 to 47°. These are the novel structures observed for the first time in this study. As high pitch and low pitch helical wires, intermediate pitch helical wires ("w") form from filaments ("F") by coiling or bending. The lateral growth of these structures results in formation of intermediate pitch helical ribbons ("H"). Unlike high and low pitch helical ribbons, intermediate pitch structures have not been observed to transform into

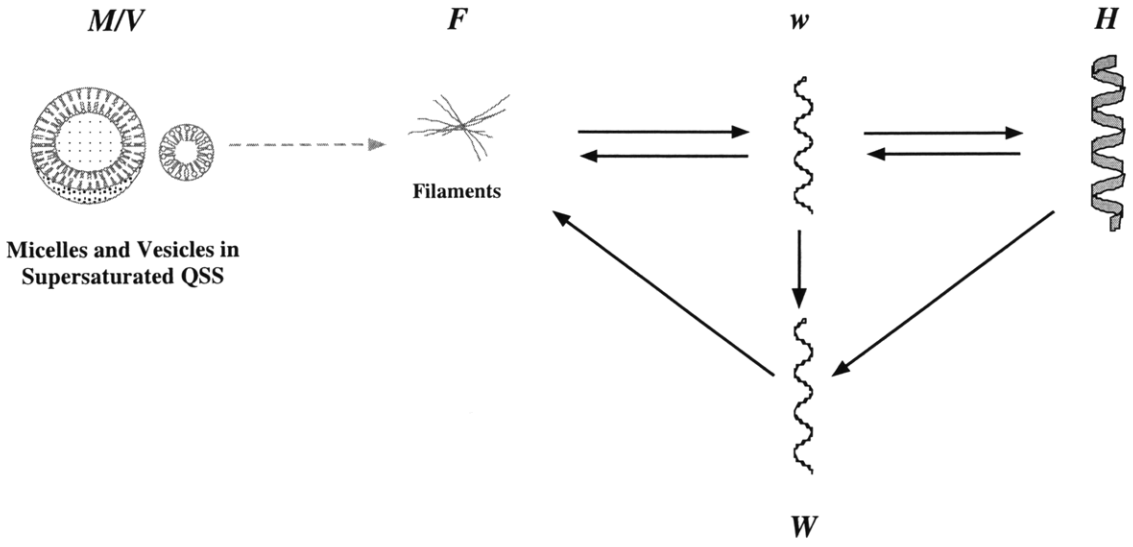

Figure 2.4: The pathways of the formation of intermediate pitch helical ribbons. These are the novel structures observed for the first time in this study. As high and low pitch helical wires, intermediate pitch helical wires ("w") form from filaments ("F") by coiling or bending. The lateral growth of these structures results in formation of intermediate pitch helical ribbons ("H"). Unlike high and low pitch helical ribbons, intermediate pitch structures have not been observed to transform into cholesterol monohydrate crystals. Rather, intermediate pitch helical ribbons ("H") were only observed to dissolve via loss of their width to transform back into helical wires of the same ("w") or slightly larger pitch helical wires ("W") followed by their unraveling to form straight filaments ("F"). The latter then dissolved. The function of the intermediate pitch helical ribbons in cholesterol crystallization process is not understood at this time and remains to be further investigated. As the formation of intermediate pitch structures is a newly found phenomenon, all structures in the Figure and the arrows representing the pathways of their evolution are depicted in solid grey color and are outlined in black color.

cholesterol monohydrate crystals. Rather, intermediate pitch helical ribbons ("H") were only observed to dissolve via loss of their width to transform back into helical wires of the same ("w") or slightly larger pitch helical wires ("W") followed by their unraveling to form straight filaments ("F"). The latter then dissolved. The function of the intermediate pitch helical ribbons in cholesterol crystallization process is not understood at this time and remains to be further investigated. As the formation of intermediate pitch structures is a newly found phenomenon, all structures in the Figure and the arrows representing the pathways of their evolution are depicted in solid grey color and are outlined in black color.

The qualitative observations of the cholesterol crystallization pathways described in Figures 2.2, 2.3, and 2.4 raise many interesting questions regarding the function and importance of various metastable intermediates as well as regarding their underlying structure. Besides the questions raised by formation of intermediate pitch helical ribbons in the process of cholesterol crystal formation, it is also interesting to study the function and the underlying structure of elongated crystals ("EC") and how it relates to monohydrate crystals. The findings of this study open new directions of further investigations of both cholesterol crystallization process, and of the geometrical shape of helical ribbons.

2.4 Study of Composition of Helical Ribbons

2.4.1 Presence of Cholesterol Within Helical Ribbons

Introduction to β-Cyclodextrin

In order to experimentally determine the presence of cholesterol molecules within the walls of a helical ribbon, we needed a mechanism that could extract cholesterol from these structures thereby possibly destabilizing them. Using this mechanism, we also expected to reverse the process of cholesterol crystallization, thus solvating tubules with helical patterns into helical ribbons and solvating helical ribbons into helical wires, which would further transform into straight filaments. For an experiment, in which the helical ribbons are placed in an aqueous solution of an "extracting" agent, the following conjectures were made. First, if we observe helix destabilization in the presence of "extracting" molecules, then this process occurred because the "extracting" molecules indeed removed cholesterol from the helix, and this cholesterol was intrinsic to the helix structure. This is in contrast to cholesterol being present within

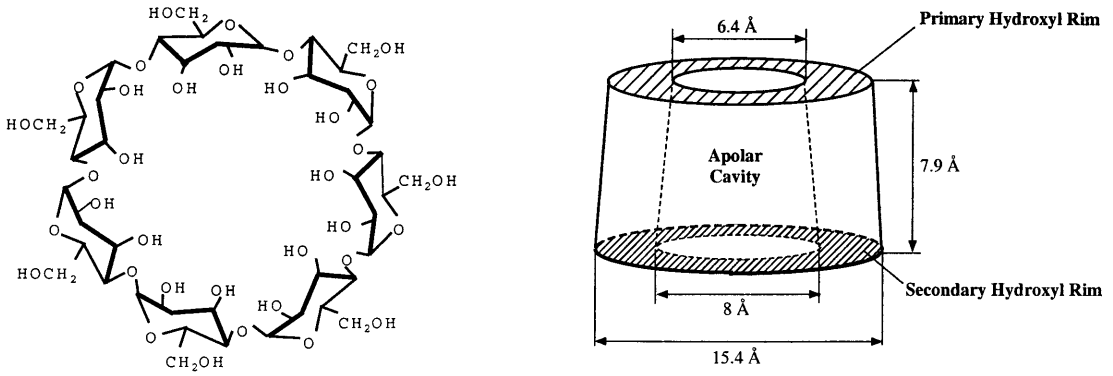

Figure 2.5: Schematic representation of the β-cyclodextrin molecule. (a) Structurally, it consists of 7 D-glucopyranosyl units connected by α-(1,4) glycosidic linkages (view from above). (b) The most stable three–dimensional molecular configuration of the β-cyclodextrin molecule — a truncated hollow cone. The upper (smaller) and lower (larger) openings of this cone contain the primary and secondary hydroxyl groups, respectively. Therefore, the exterior of β-cyclodextrin molecule is hydrophilic. The interior cavity of the β-cyclodextrin, on the other hand, is non–polar with relatively few opportunities for hydrogen bonding. The dimensions of the molecule are shown.

helical ribbons but not playing a central role in helix structure, for example being on helix surface. Second, the "extracting" molecules could be removing free cholesterol from the helix surroundings. In this case cholesterol intrinsic to helical ribbons abandons helical structures in favor of helix surroundings thereby reestablishing the quasi–equilibrium of helices with their surroundings. Third, though less likely, the mere presence of "extracting" molecules in solution could have a destabilizing effect on the helices. For example, the "extracting" molecules could be undermining helices through hydrogen bonding with helix surfaces, etc.

In our experiments, we have used the β-cyclodextrin molecule as a cholesterol "extracting" agent. In the past few decades β-cyclodextrin has been used as a natural cholesterol "pump" from cell membranes, and as a solubilizing agent of pure cholesterol. β-cyclodextrin is a cyclic oligomer of glucose; it consists of seven D-glucopyranosyl units connected by α-glycosidic links. The most stable three-dimensional structure of this molecule, in a time-averaged sense, takes the form of a truncated hollow cone, with a hydrophilic exterior and a hydrophobic interior cavity, as shown in Figure 2.5. This hydrophobic interior serves as a "host" to non-polar

molecules of appropriate sizes, "guests". Cholesterol molecule happens to be one of the most likely "guests" due to its size. When a "guest"–"host" inclusion complex between cholesterol and β-cyclodextrin is formed, the latter not only accommodates cholesterol but also serves as a vehicle transporting cholesterol.

Energetically, the formation of a "guest"–"host" inclusion complex between a hydrophobic molecule, the "guest", and a β-cyclodextrin molecule, the "host", is very favorable due to the following factors. In an aqueous solution, β-cyclodextrin is not well solvated since its interior cavity has to "host" water (geometrically, up to 11 water molecules can fit into a β-cyclodextrin interior cavity). This makes the water–β-cyclodextrin complex energetically unfavorable, because water molecules do not participate in the polar interactions with other water molecules if they were outside the β-cyclodextrin cavity. When an apolar molecule drives water out of the β-cyclodextrin interior cavity, the more energetically favorable inclusion complex is formed. While polarity of the "guest" molecule and the reaction medium play important roles in the formation of the "guest–host" inclusion complex, one of the most important conditions for complex formation is the three–dimensional complementarity of the shapes of the β-cyclodextrin cavity and the "guest" molecule. Additionally, atomic, thermodynamic, and solvent (hydrophobic) forces influence formation of a stable "guest"–"host" inclusion complex, where β-cyclodextrin serves a role of the "host". As can be seen in Figure 2.5, the β-cyclodextrin molecule has a truncated cone shape, with the diameter of the interior cavity ranging between 6.4 Å and 8.0 Å, and a height of approximately 7.9 Å.[48] Since the shape of the cholesterol molecule can be approximated by an elongated parallelogram of thickness 4 Å, height 7.7 Å, and length 19 Å for the unfolded side chain (less, if the side chain is in a folded conformation),[50] cholesterol can be hosted by β-cyclodextrin in several different ways. As can be seen if Figure 2.6, for 1:1 cholesterol:β-cyclodextrin inclusion complexes the B, C, and D rings of the cholesterol nucleus thread through the annulus of the cyclodextrin molecule;[48] however, for 1:2 inclusion complexes the rings A and D of the cholesterol molecule are included in two different β-cyclodextrins molecules;[49] 1:3 inclusion complexes have also been found.[51]

It has been found that the β-cyclodextrins have very high affinity for solubilization/extraction of sterols, specifically cholesterol, from cell membranes. This high affinity has made them invaluable in studies of cellular cholesterol content, cholesterol flux, and in manipulation of cellular cholesterol composition.[52] Since we expected he-

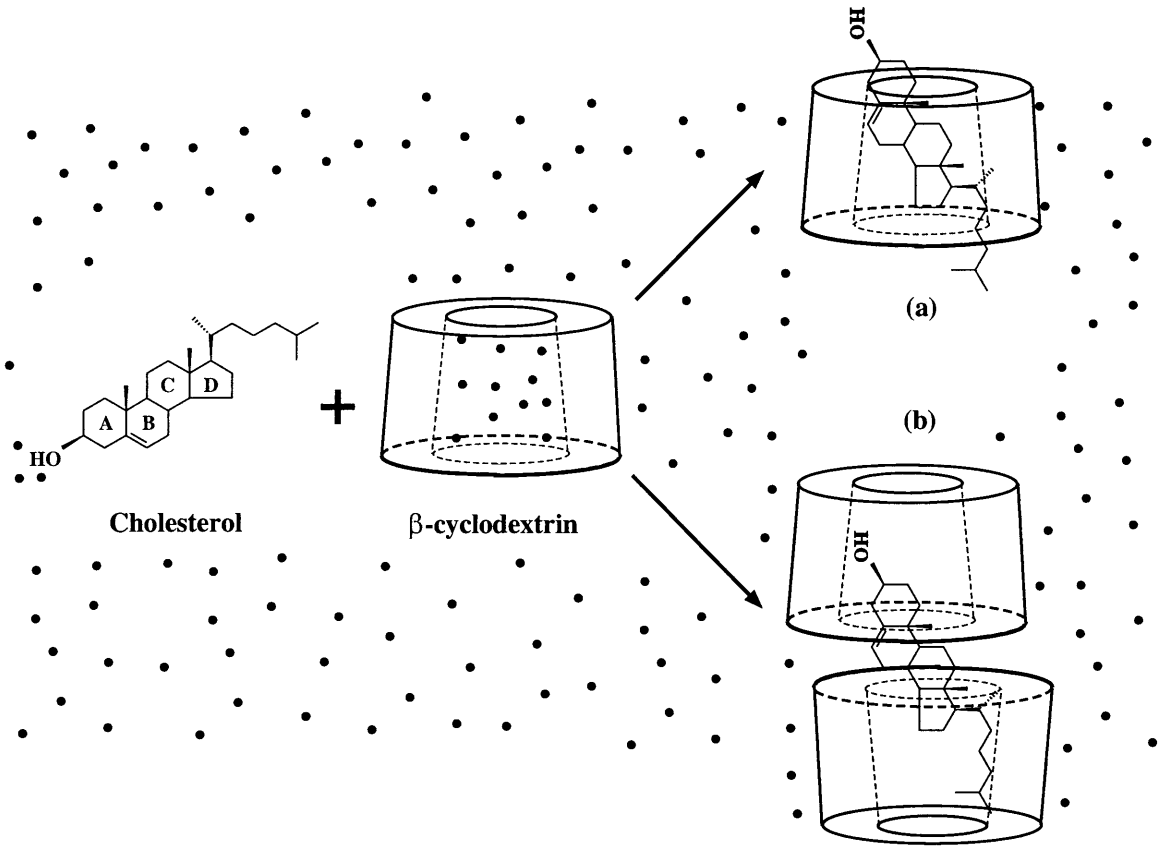

Figure 2.6: Schematic representation of the formation of a cholesterol–β-cyclodextrin inclusion complex. Hydrophobic cholesterol and β-cyclodextrin molecules, which have a hydrophobic interior cavity, are poorly solvated in water. It is energetically more favorable for these molecular species to form a "host"–"guest" inclusion complex. By driving the water molecules (shown as black dots) from the cavity of the β-cyclodextrin, such inclusion complex is formed. There are two conformations of these inclusion complexes: (a) for 1:1 cholesterol:β-cyclodextrin complexes, the B, C, and D rings of the cholesterol nucleus thread through the annulus of the cyclodextrin molecule;[48] (b) for 1:2 inclusion complexes, the rings A and D of the cholesterol molecule are included in two different β-cyclodextrins,[49] as shown.

lical ribbons to consist mostly of cholesterol molecules, and partially of surface phospholipid molecules,[20] we used the β-cyclodextrins for the extraction of cholesterol from helix walls. This process is analogous to the experiments in which cholesterol is extracted from cell membranes, where though shielded, cholesterol is extracted from membranes by the "pumping" action of β-cyclodextrin. By carefully tuning the concentration of β-cyclodextrin in supersaturated quaternary sterol systems (QSS), we expected to determine the following: first, whether, and to which extent crystals, helical ribbons, and tubules contain cholesterol; second, whether, and to which extent the process of cholesterol crystallization can be reversed; third, whether, and to which extent the process of cholesterol crystallization can be prevented. These experiments were performed in the following manner:

- placement of crystals, tubules, and helical ribbons into aqueous solutions of cyclodextrin of various molarity, and
- diluting (see Section 2.2.1) the unsaturated quaternary sterol systems with aqueous solution of cyclodextrin, instead of pure water, thus forming supersaturated QSS.

Materials and Methods

β-cyclodextrin was purchased from Sigma–Aldrich and was used without further purification. Aqueous solutions of β-cyclodextrin were prepared by mixing crystalline β-cyclodextrin with filtered (0.22-μm pore size filter) Milli-Q (Millipore) water at ambient temperature and stirring this mixture for 30 seconds. Three aqueous solutions of various molarities were prepared: 3 mM, 5 mM, 10 mM, and 15 mM.

Crystals, tubules, and helical ribbons in cyclodextrin–water solution

Each structure: crystal, tubule, or helical ribbon, was isolated from its native quaternary sterol system and placed into a cyclodextrin–water solution. In this way, both the effect of cyclodextrin concentration and the role of cholesterol in each structure were studied.

Supersaturation of unsaturated QSS with an aqueous cyclodextrin solution

The lipid film for each quaternary sterol system (QSS) was composed of sodium taurocholate (NaTC), 1-palmitoyl-2-oleoyl phosphatidylcholine (POPC) or egg yolk lecithin (EYPC), and cholesterol in the molar ratio 97.5:0.8:1.7, and was prepared as described in Section 2.2.1. To obtain an unsaturated QSS, each lipid film was diluted

in filtered (0.22-μm pore size filter) Milli-Q water (Millipore) at ambient temperature to a final lipid concentration of 70 mg/ml. This system was then incubated at 60°C for 1 to 3 hours to induce complete solubilization of cholesterol, which occurred when the system became transparent. To induce supersaturation, this system was further diluted six–fold with filtered (0.22-μm Millex-GV_4 filter, Millipore) 15 mM solution of cyclodextrin in water at ambient temperature. Supersaturated systems were kept at 37°C. 5-μl aliquots were taken periodically to observe the structures formed. We found that frequent probing of a bulk sample did not to affect the yield and variety of structures formed.

Structures in all of the above experiments were observed on glass slides using phase-contrast microscopy with a Diaphot-TMD microscope, Nikon. Images were taken with a Sony DXC-970MD CCD camera and digitized on a Macintosh computer with the help of the NIH-Image software package.[47]

Experimental Results

Crystals, tubules, and helical ribbons in cyclodextrin–water solution

Crystals grown from quaternary sterol systems (QSS) with POPC (1-palmitoyl-2-oleoyl phosphatidylcholine) and EYPC (egg yolk phosphatidylcholine) were placed in different concentration cyclodextrin–water solutions. We found that for some concentrations of cyclodextrin, crystals grown from either of the two QSS dissolved with different rates. In 15 mM solution, the crystals completely dissolved within 1 to 3 hours of their placement in the solution; however, in 5 mM solution the complete dissolution of crystals took up to 24 hours (Figure 2.7). Since the crystals placed in different concentration aqueous cyclodextrin solutions were of different sizes and thicknesses, it is difficult to make a precise comparison of their rates of dissolution. This experiment, however, does tell us that crystals found in quaternary sterol system contain mostly cholesterol, since cyclodextrin removes primarily cholesterol.

Next, we placed tubules grown from QSS with EYPC into a 15-mM aqueous cyclodextrin solution. Tubules started to dissolve immediately (Figure 2.8). We found that the tubules dissolved completely within 0.5 hours of their placement in 15-mM cyclodextrin solution. We did not observe a reversal in the process of tubule formation, i.e. we did not find a helical pattern in the dissolving tubule. However, the complete dissolution of a tubular skeleton in this experiment provides a confirmation to our conjecture that these structures are made mostly of cholesterol. This is not

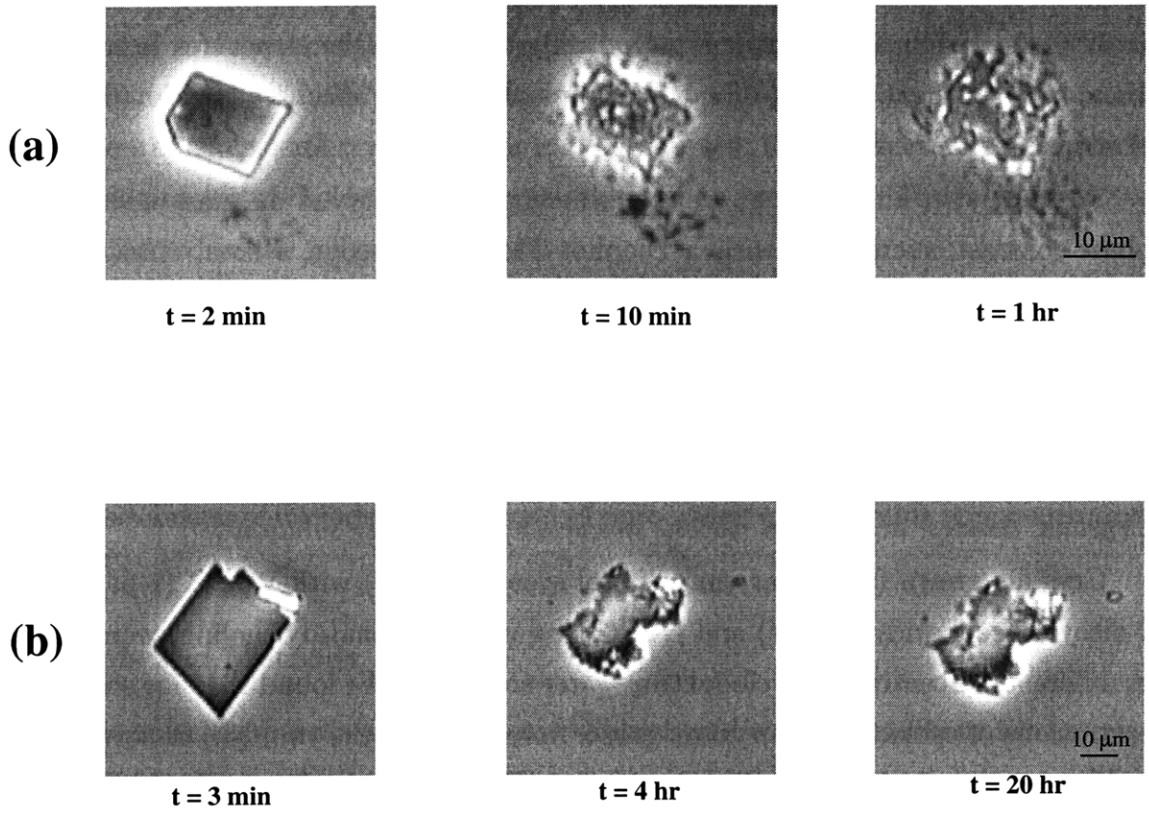

Figure 2.7: (a) Snapshots of cholesterol monohydrate dissolution in 15 mM aqueous solution of β-cyclodextrin at 2 minutes, 10 minutes and 1 hour after its placement in the "extracting agent" solution. The crystal was grown from QSS composed of the bile salt sodium taurocholate, POPC, and cholesterol. Complete dissolution of this crystal occurred in a little more than 1 hour. (b) Snapshots of cholesterol monohydrate dissolution in 5 mM aqueous solution of β-cyclodextrin at 3 minutes, 4 hours and 20 hours after its placement in the "extracting agent" solution. The crystal was grown from QSS composed of the bile salt sodium taurocholate, POPC, and cholesterol. Complete dissolution of this crystal occurred in $\sim$ 24 hours.

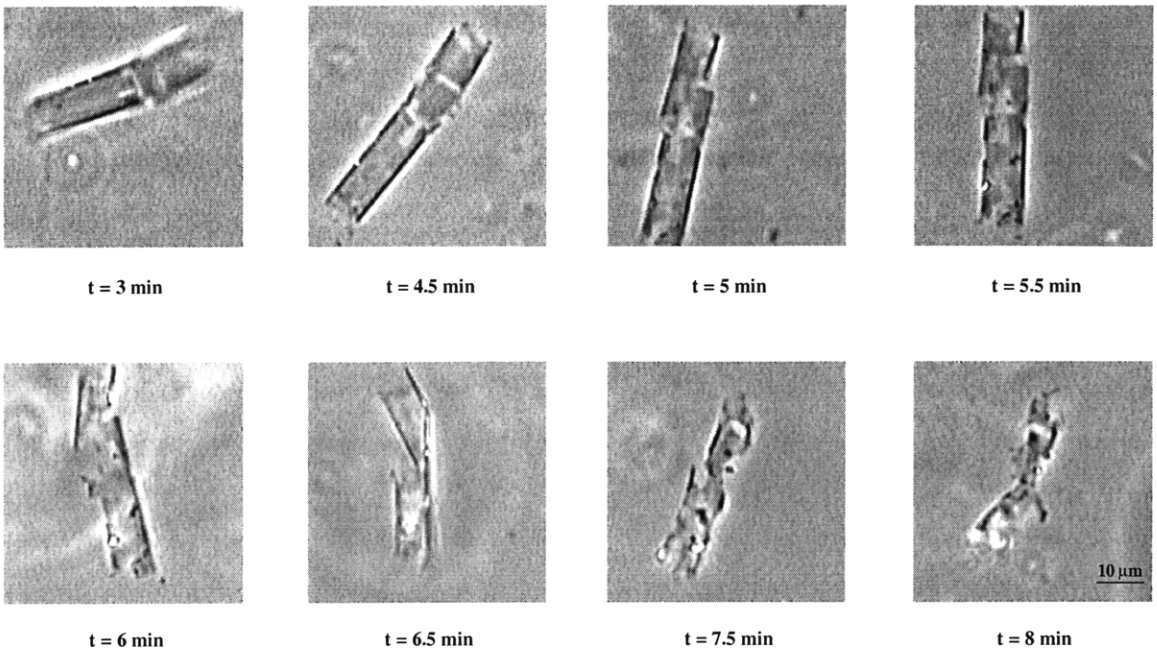

Figure 2.8: Snapshots of a tubule dissolving in a 15 mM aqueous solution of β-cyclodextrin at 3, 4.5, 5, 5.5, 6, 6.5, 7.5, and 8 minutes after its placement in the "extracting agent" solution. The tubule was grown from QSS composed of the bile salt sodium taurocholate, EYPC, and cholesterol. Complete dissolution of this tubule occurred in approximately 9 minutes after its placement in a β-cyclodextrin–water solution.

unreasonable since tubules are the precursors of the cholesterol monohydrate crystals.

Since dissolution of tubules in 15-mM aqueous cyclodextrin solution occurred very quickly, less concentrated aqueous cyclodextrin solutions were necessary to be considered. Therefore, we studied the behavior of both high and low pitch helical ribbons grown from QSS with POPC in solutions of 3-mM aqueous β-cyclodextrin in water for slower rates of decomposition. Figure 2.9 depicts the behavior of typical high pitch helices when placed in 5 mM cyclodextrin solution; low pitch helices behave in the same manner. As can be observed from this Figure, helices unravel or flatten to form filaments. This implies that as helices lose cholesterol, they follow one of the pathways illustrated in Figures 2.2, 2.3, and 2.4, transforming from helical ribbons to helical wires, which then unwind to form filaments that later dissolve. We observed that formation of filaments was a necessary step in the process of helix dissolution (not shown in Figure 2.9). Therefore, we can mimic the helix dissolution by placing it into an aqueous cyclodextrin solution. This process of helix dissolution supports the hypothesis that helix formation can be reversed. As before, our experiment confirmed the assumption that helices are mostly made of cholesterol. (This type of

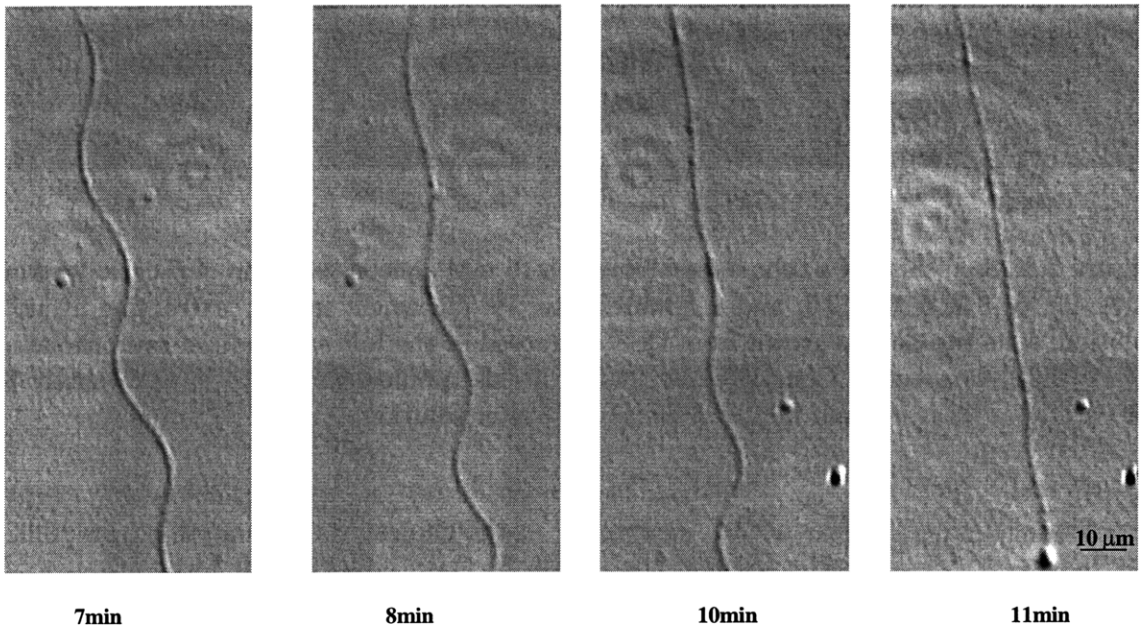

Figure 2.9: Snapshots of a high pitch helix straightening in 5 mM aqueous solution of β-cyclodextrin at 7, 8, 10, and 11 minutes after its placement in the "extracting agent" solution. The high pitch helix was grown from the QSS composed of bile salt sodium taurocholate, POPC, and cholesterol. Complete dissolution of this helix occurred in approximately 12 minutes after its placement in β-cyclodextrin–water solution, i.e. 1 minute after the last snapshot shown.

experiments was not performed with intermediate pitch helices due to the low yield of these structures in the QSS studied.)

Supersaturation of unsaturated QSS with an aqueous cyclodextrin solution

This set of experiments was performed to determine whether and to which extent the process of cholesterol crystallization can be prevented. The QSS for this set of experiments were prepared as discussed in Section 2.4.1. We were not able to prevent cholesterol crystallization in these QSS. We have observed the following interesting results. First, the same pathways of cholesterol crystal formation were observed as described in Section 2.3. Specifically, filaments formed first, followed by high and later low pitch helical ribbons, then tubules, and finally plate-like crystals. Second, the rate of this temporal evolution was found to be much higher in these new systems: within a 3 day interval, the only structures found were plate-like crystals, unlike the 4 week interval needed for this process to occur in a typical quaternary sterol system at ambient temperature. Third, the yield of the intermediate metastable structures was found to be lower in these new systems compared to the QSS studied before. (The latter observation was made qualitatively.)

The higher rate of cholesterol monohydrate crystal formation can be explained in the following way. Since the cholesterol crystallization in this set of experiments occurs in the presence of β-cyclodextrin molecules, they sequester free cholesterol from the supersaturated QSS with the rate limited only by diffusion. As a result, smaller numbers of cholesterol molecules are left in the supersaturated QSS from which metastable structures may form. However, these intermediate structures are even less stable in the presence of β-cyclodextrin, as this molecule extracts cholesterol from metastable structures at greater rates than from stable cholesterol crystals (see earlier result). Our experimental observation that the yield of intermediate metastable structures was very low in the presence of β-cyclodextrin is in agreement with the above statement. It is plausible then that in the presence of β-cyclodextrin, the major pathway of cholesterol crystallization is by direct formation of cholesterol monohydrate crystals from supersaturated micelles and vesicles rather than through metastable intermediates, as described in Section 2.3. The direct formation of cholesterol crystals from micelles and vesicles is also characterized by the higher rates of crystal formation, which is in agreement with our experimental observation of crystal formation in the presence of β-cyclodextrin.

Conclusions

The two experiments above are in agreement with the hypothesis that cholesterol is one of the major components of the metastable intermediate microstructures, helical ribbons and tubules, and of cholesterol monohydrate crystals formed in the cholesterol crystallization process in QSS. When any of the above structures is placed in a β-cyclodextrin–water solution, free cyclodextrin molecules sequester the cholesterol available to them, that which makes up the intermediate metastable structures, helical ribbons or tubules. The result of this process is the complete dissolution of a structure.

Another important conclusion comes from the observation that upon the loss of cholesterol in β-cyclodextrin–water solution, high and low pitch helices unravel to form filaments. This observation confirms the conjecture that cholesterol is one of the major components in helix structure and plays an important role in helix formation from straight filaments. This experiment also shows that cholesterol crystal formation can be reversed at least at the stage of helical ribbons. We did not observe helical patterns on tubules during their dissolution. This implies that the pathway of cholesterol crystallization in which helices transform into tubules via fusion of ribbon edges cannot be exactly reversed with the concentrations of β-cyclodextrin used.

Finally, we were unable to prevent formation of cholesterol crystals in supersaturated QSS. The following conclusions were drawn from our results. When β-cyclodextrin–water solution is used to form supersaturated QSS (see Section 2.2.1), two processes occur simultaneously:

1. cyclodextrin molecules form complexes with free cholesterol

2. filaments start nucleating.

The "free" cholesterol that does not get sequestered by cyclodextrin is incorporated into filaments that grow into helical ribbons, tubules, and finally crystals. Once all of the cyclodextrin molecules form inclusion complexes, no further extraction of cholesterol from the microstructures can occur, i. e. the cholesterol crystals will no longer dissolve.

2.4.2 Presence of Phospholipids within Helical Ribbons

Introduction

In early nineties, Konikoff *et al.* showed that the precursors of helical ribbons, filaments, are covered by a surface layer of phospholipid molecules.[20,25,28] It was found that filaments are composed of a core of greater than 95% cholesterol and a surface layer of less than 5% lecithin.[28] At that time, the influence of a large variety of phospholipids and related lipids on crystallization of cholesterol in QSS was studied. However, the only surface–adsorbed molecular species examined were the lecithin species of phospholipids, i.e. phosphatidylcholines, PC.[25,28] To determine the relative concentrations of lecithin molecules throughout filaments, Konikoff *et al.* modified the preparation of QSS described in Section 2.2.2 by substituting 0.5 - 5 mol% of lecithin with fluorescent probe R-PE, *N*-(lissamine rhodamine B sulfonyl)-phosphatidylethanolamine. Observing samples with a Zeiss Standard 16 fluorescence microscope equipped with phase contrast optics, Konikoff *et al.* found that filaments were highlighted by lecithin fluorescent probes. To confirm their hypothesis that lecithin forms a monolayer on filaments' surfaces, the researchers washed filaments with various bile salts attempting to absorb a layer of molecules from the filamentous surfaces. Their experiment was successful in that with the addition of a few microliters of a bile salt, the fluorescence was gradually lost without dissolution of filaments indicating that the lecithin monolayer was hydrophobically adsorbed on filaments' surfaces.[20]

Unfortunately, the same experiments have not been performed for helical ribbons, and their successors, cholesterol monohydrate crystals. It is therefore interesting to see whether and to which extent lecithin and other phospholipid molecules are adsorbed onto surfaces of filaments, helical ribbons, and cholesterol crystals. This information is of particular interest for comparison of various pitch types of helical ribbons: high, low, and intermediate with pitch angles of approximately $54°, 11°$, and $30 - 47°$, respectively. The particular interest in this issue due to the necessity of finding whether and how the differences and/or similarities of the surface layers of these three helix pitch types are reflected in the differences and/or similarities of their composition and molecular arrangement within these structures. The data from this experiment can also indicate whether and how various helix pitch types are related to their precursors, filaments, and their successors, cholesterol monohydrate crystals. In what follows we will describe the experiment which attempts to answer the above

raised questions.

Materials and Methods

QSS systems for this set of experiments were prepared by the method of Konikoff *et al.*[20] described in Section 2.2.2. The compositions of these QSS systems were as follows: common bile salt sodium taurocholate (NaTC), a phospholipid, and cholesterol in the molar ratio 97.5:0.8:1.7. Sodium taurocholate was purchased from Sigma–Aldrich (St. Louis, Missouri) and was further purified by the method of Pope.[46] Cholesterol was also purchased from Sigma–Aldrich (St. Louis, Missouri) and was used as received without further purification. Synthetic phospholipids used to prepare QSS systems were: 1,2-dioleoyl-glycero-3-phosphocholine (DOPC, *sn*-1-18:1-*sn*-2-18:1 PC), 1,2-dioleoyl-glycero-3-phosphoethanolamine (DOPE, *sn*-1-18:1-*sn*-2-18:1 PE), 1-palmitoyl-2-oleoyl-glycero-3-phosphocholine (POPC, *sn*-1-16:0-*sn*-2-18:1 PC), 1-palmitoyl-2-oleoyl-glycero-3-phosphoethanolamine (POPE, *sn*-1-16:0-*sn*-2-18:1 PE), 5-(Dimethyl-amino)-naphthalene-1-sulfon-amide-1,2-dioleoyl-glycero-3-phospho-ethanolamine (dansyl-DOPE, dansyl-*sn*-1-18:1-*sn*-2-18:1 PE), L-α-Phosphatidyl-ethanolamine-N-(4-nitrobenzo-2-oxa-1,3-diazole) (NBD-Egg PE). Systems prepared with the first four phospholipids were used as controls. Systems with the latter two phospholipids which have autofluorescing groups, were used for fluorescence study. All phospholipids were purchased from Avanti Polar Lipids (Alabaster, Alabama) and were used without further purification. Table 2.1 summarizes the systems studied and their constituents. This set of experiments followed the procedures described above in the Sections 2.2.2 and 4.2.2.

For the analytical part of this experiment, we used Zeiss Axiophot D-7082 fluorescence microscope equipped with phase contrast optics. The acquired images were digitized with Optronics Engineering DEI-750 CE digital camera and further enhanced with public domain NIH-Image program and Adobe Photoshop software package. To compare the fluorescence signature of various structures, we measured the grey scale values of both unenhanced and identically enhanced images of each structure studied. Though only qualitative, these measurements serve as good indicators of whether and

Table 2.1: Composition of the QSS for the fluorescence study

QSS Number	Surfactant	Sterol	Phospholipid	Phospholipid Chemical Formula
1	NaTC	Cholesterol	DOPC	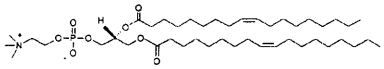
2	NaTC	Cholesterol	DOPE	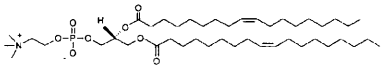
3	NaTC	Cholesterol	POPC	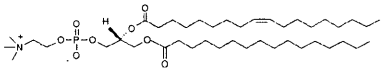
4	NaTC	Cholesterol	POPE	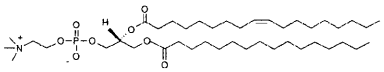
5	NaTC	Cholesterol	dansyl-DOPE	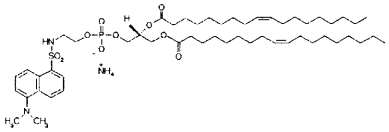
6	NaTC	Cholesterol	NBD-POPE	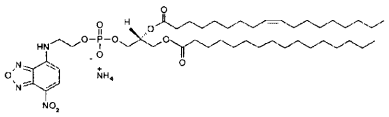

to which extent various structures in QSS exhibit fluorescence properties. The results described below represent the average fluorescence signature over the whole ensemble of each structure observed, filaments, cholesterol monohydrate crystals, and three pitch angle helical ribbons.

Experimental Results

The purpose of this set of experiments was to see whether and to which extent phospholipid molecules coat (or cover) the surfaces of various pitch types helical ribbons, and whether the helix coating pattern is related to precursors of helices, filaments, and successors of helices, cholesterol monohydrate crystals. To do so, we performed experiments similar to the work of Konikoff *et al.*[20] We used fluorescently labeled phospholipids to see whether and how the surfaces of the structures are coated with these molecules. Unlike the phospholipids in the experiments of Konikoff *et al.*, all of the phospholipids used in our work were fluorescently labeled. To diminish an effect of autofluorescing labels on phospholipid function, if any, in formation of helices we chose the smallest available fluorescent groups, dansyl, (5-(Dimethylamino)naphthalene-1-sulfonamide), and NBD, N-(4-nitrobenzo-2- oxa-1,3-diazole), as shown in figures of

Table 2.1.

As phospholipids are amphiphiles, if they coat the helical ribbon skeleton made of cholesterol, they do so by interactions of their hydrophobic tails with cholesterol and of their hydrophilic headgroups with aqueous medium in which helices grow. Therefore, it was necessary to obtain phospholipid molecules with appropriate headgroups and fatty acid tales. To prevent possible interactions of fluorescent groups with cholesterol within the bilayer, we chose to have the fluorescent labels be placed on the phospholipid headgroups rather than on one of the fatty acid tales. This decision, however, minimized our choices of available fluorescently labeled phospholipids: the only commercially available phospholipids with labeled headgroups were phosphatidylethanolamines (PE). As we have not performed experiments with phosphatidylethanolamines (PE) before, it was necessary to see whether substitution of the phosphatidylcholine (PC) headgroup by the phosphatidylethanolamine (PE) headgroup affects formation and pitch types of helical ribbons. On the other hand, to maximize the production of helical ribbons, the hydrophobic tales for the PE were chosen based on the previous work of Chung *et al.*[12] to be identical to those found in egg yolk lecithin (PC) (model bile "C" in Chung *et al.* and #3 in our work). In other words, we chose PE derived from egg yolk PC (transphosphadilated egg lecithin in the presence of ethanolamine), which is a mixture of PE's with various hydrophobic fatty acid tales that are predominantly palmitic and oleic fatty acids,[53] such that the majority of phospholipids, 38.2%, are 1-palmitoyl-2-oleoyl-glycero-3-phosphoethanolamine (POPE, *sn*-1-16:0-*sn*-2-18:1 PE)[54] (QSS #6 in our work). We also chose a pure synthetic PC, 1,2-dioleoyl-glycero-3-phosphocholine (DOPC, *sn*-1-18:1-*sn*-2-18:1 PC) for QSS #1, and a pure synthetic PE, 1,2-dioleoyl-glycero-3-phosphoethanolamine (DOPE, *sn*-1-18:1-*sn*-2-18:1 PE) for QSS #2, to imitate Chung *et al.*'s model bile "D" with 1,2-dipalmitoyl-glycero-3-phosphocholine (DPPC, *sn*-1-16:0-*sn*-2-16:0) phospholipid. As in the Chung *et al.*'s model bile "D", our QSS contained a 1,2-diacyl-*sn*-glycero-3-phosphocholine and a 1,2-diacyl-*sn*-glycero-3-phosphoethanolamine. However, we substituted a palmitoic hydrophobic chains (16:0) from Chung *et al.*'s work by oleic chains (18:1) in QSS #1, 2, and 5. This was done to lower the bilayer gel–to–fluid transition temperature of these phospholipids from values above the body temperature (37°) for palmitoic hydrophobic tales to those below the room temperature (approximately 24°), at which the experimental measurements were performed, for the oleic hydrophobic tales. It was hypothesized that the reason QSS "D" in

Chung *et al.*'s experiments did not produce any helical ribbons was a very high gel–to–fluid phase transition temperature of phospholipids with palmitoic hydrophobic tales (41.4°),[55] and the phospholipids were not "fluid enough" to assist in formation of helical ribbons. In this way, we chose QSS #1, 2, 3, and 4 to be controls for the formation and growth of helical ribbons, whereas QSS #5 and 6 were the ones in which we intended to observe fluorescence signature.

In all six systems we observed formation, growth, and dissolution of filaments, all three pitch angle helical ribbons, cholesterol monohydrate crystals, and very small numbers of tubular structures. The temporal crystallization sequences observed in all six systems were identical to those described in Section 2.3, i. e. filaments served as precursors to formation of helical ribbons and cholesterol monohydrate crystals are helix successors. However, varying the phospholipid species affected the number and the kinetics of helix formation and growth. The fluorescence signature was observed on the second, third, and fourth days after preparation of QSS systems. Prior to the second day and following the fourth day, helical ribbons were not found in QSS #5 and 6, and therefore we did not perform observation of these systems with fluorescence optics at those times.

In both fluorescently labeled QSS systems, thick filaments exhibited fluorescence signature, as we expected from the results of Konikoff *et al.*[20] However, cholesterol monohydrate crystals showed quite different behavior in the two systems. On the one hand, the thick crystals formed in the QSS system #5 (with dansylated PE) exhibited very strong fluorescence signature; on the other hand, very thin crystals in this system expressed a fluorescence signature only on their edges. The cholesterol monohydrate crystals in the model bile #6 (with NBD–labeled PE) did not exhibit any fluorescent signature. These results are in a good agreement with observations of Konikoff *et al.*,[25] who demonstrated that during cholesterol crystallization from QSS, the phospholipid molecular layer covering structures is more pronounced on filaments rather than on plate-like cholesterol monohydrate crystals.[25] Based upon these observations and the previous work, Konikoff *et al.* postulated that filaments are more hydrophobic than cholesterol monohydrate crystals, which possibly reflects the anhydrous nature of filamentous structures.[20,25,42,56] Konikoff *et al.*'s study also demonstrated that the more hydrophobic phospholipid species are preferentially adsorbed on the surface of both filamentous structures and cholesterol monohydrate crystals.[25] This result is also in direct agreement with our experimental observations, since the more hydrophobic

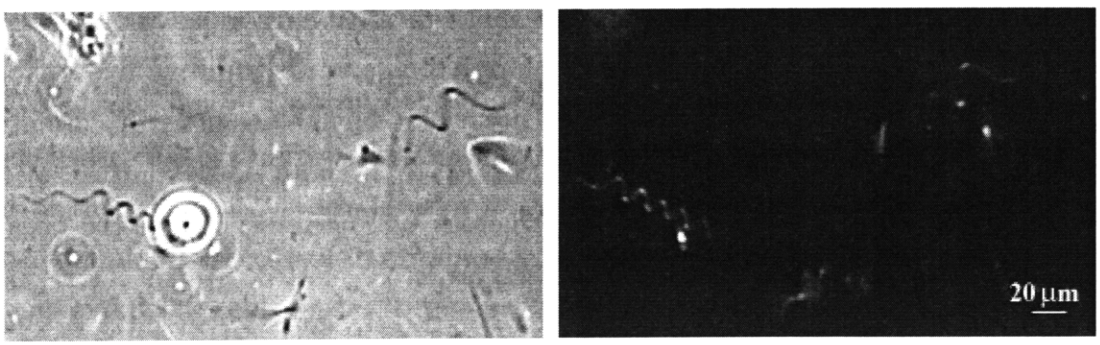

Figure 2.10: A typical image of low pitch helical ribbons in QSS #5 with dansylated POPE. (a) Image of two low pitch helical ribbons obtained with phase contrast optics. (b) The same two helices observed with fluorescence optics.

dansylated POPE, which is adsorbed onto surfaces of cholesterol monohydrate crystals, displays stronger fluorescence signature than the less hydrophobic NBD–labeled DOPE. We were not able to observe such differences in the level of fluorescence of filaments possibly due to their high hydrophobicity.[20,25,42,56]

We also observed the fluorescence signature of helical ribbons. A typical image of a low pitch helix fluorescence pattern is shown in Figure 2.10. The image of the same structures obtained by phase contrast microscopy is also shown in the same figure. The observed fluorescence signature of helical ribbons followed the same pattern as that of filaments and cholesterol monohydrate crystals. We found that helices formed in the QSS with dansylated POPE, expressed more fluorescence that those formed in the QSS with NBD–labeled DOPE. Following the postulate of Konikoff *et al.*,[25] we again justify this observation by the fact that POPE is more hydrophobic than DOPE[24] and thus POPE is adsorbed to the surfaces of helical structures to a larger extent than DOPE. Comparing the fluorescence signatures of various pitch angle helices within each QSS systems, we obtained the following results. For the QSS #5 with dansylated POPE,

- the thick high pitch helices and thick low pitch helices express approximately the same level of fluorescence; thin high and low pitch helices do not express any observable fluorescence signature even when the images are enhanced with Adobe Photoshop software package.

- thick intermediate pitch helices also express fluorescence signature, but to a lesser degree than either high or low pitch helices.

For the QSS #6 with NBD–labeled DOPE,

- the high pitch helices express slightly higher fluorescence signature than low pitch helices, since only thick low pitch helices display fluorescence signature, in comparison to larger variety of low pitch helix thicknesses
- intermediate pitch helical ribbons display no observable fluorescence signature.

It is clear that the differences in fluorescence for the structures in QSS #5 are harder to observe due to the stronger interactions between hydrophobic dansylated POPE and the helix skeleton. However, in the case of QSS #6, where less hydrophobic NBD–labeled DOPE is used, the differences between high and low pitch structures become clearer. It is feasible that the higher fluorescence signature of high pitch helices in the QSS #6 reveals the higher hydrophobicity of these structures in comparison to the low pitch helices. This suggestion is very plausible if one considers the pathways of cholesterol crystallization and the temporal evolution of metastable intermediates, filaments and helical ribbons (Section 2.3). High pitch helices are the first helix type to emerge in the process of cholesterol crystallization. Low pitch structures, on the other hand, are the last and the longest–lived helix type to emerge in this process. In fact, low pitch helices have been observed to unravel, directly forming cholesterol monohydrate crystals, while the same observation have not been made for the high pitch structures. This implies that the transformation in the intensity of the fluorescence signature upon evolution from filaments to monohydrate crystals is mimicked by the less apparent transformation in the fluorescence intensity between high pitch helices, which in their temporal sequence are closer to filaments, and low pitch structures, which are closer to cholesterol monohydrates. As to intermediate pitch structures, it appears that they do not follow the above pattern. Their fluorescence signature in both QSS systems was much smaller than that of any other structures.

Conclusions

This section demonstrates two novel experimental findings: (1) helical ribbons of high, low, and intermediate pitch angle were obtained in new systems containing PE rather than PC phospholipids, and (2) the fluorescence signature of helical ribbons in QSS systems was observed and described for the first time. The results of these experiments show that helical ribbons of exactly the same three pitch angles form in all systems studied notwithstanding the size and the hydrophobicity of the

phospholipid headgroup. When the autofluorescing groups were attached to the PE headgroups, two experimental observations were made. First, we were able to qualitatively compare the extent to which various PE molecules coat helical ribbons by using PE molecules with varying hydrophobic tails. We found that the PE molecules with more hydrophobic tails coat all helices to a larger degree. Second, we showed that PE molecules coat the surfaces of helical ribbons to varying degree depending on the helix pitch angle. Based upon the strength of the fluorescent signature, we were able to deduce that high pitch helical ribbons are more hydrophobic than the low pitch structures, and that the intermediate pitch helices are the most hydrophobic species of all.

These results, though qualitative, serve as the first step into the study of the chemical structure of helical ribbons of each high, low, and intermediate pitch angles. Our experimental results are promising in that they provide the first indication of the fact that the high, low, and intermediate pitch helices have different microscopic structures, at least on their surfaces. A lot more work needs to be done to further study the underlying microscopic organization of helical ribbons. Possibly, further quantitative investigation of helix fluorescence signatures may prove to be an important tool in this study.

2.5 Helical Ribbons in Quaternary Sterol Systems as a General Phenomenon[a]

2.5.1 Introduction

Prior to the work described below, it has been thought that formation of helical ribbons of *two* pitch types (high pitch, with a pitch angle of 54 $\pm$ 2°, and low pitch, with a pitch angle of 11 $\pm$ 2°) is a property unique to model biles. To recollect, model bile is a quaternary sterol system consisting of a mixture of three types of chiral molecules in water: a bile salt, a phosphatidylcholine, and cholesterol.[20–28] Helical ribbons are metastable intermediates that are found in the process of cholesterol crystallization in model bile,[12,26,27] a process which precedes cholesterol gallstone formation.[20,25–28,30,57] Previous work showed that all three components of model bile are

[a]Parts of this section appear in the *Proceedings of the National Academy of Sciences, U. S. A.*: Y. V. Zastavker, N. Asherie, A. Lomakin, J. Pande, J. M. Donovan, J. M. Schnur, and G. B. Benedek, Self-Assembly of Helical Ribbons, *Proc. Natl. Acad. Sci. U.S.A.*, **96**: 7883-7887 (1999).

required for helical ribbons to form. In the absence of the phosphatidylcholine, only needle-like crystals form,[20,28] while without the bile salt only stable plate-like crystals are produced.[58] Konikoff *et al.*[20,28] also argued that phosphatidylcholine is necessary only for the initial stages of helix formation, since its removal does not affect preformed helical structures. They also claimed that the helix formation is unaffected by the specific identity of phosphatidylcholine and bile salt, although the kinetics of helix formation is affected dramatically.[20,22,24,27,28,59] In our experiments with fluorescently labeled phospholipids (Section 2.4.2), we have shown that indeed the identity of phospholipids did not affect the production of helical ribbons. In fact, not only did "model biles" or QSS with various phosphatidylcholines produced helical ribbons, but QSS with phosphatidylethanolamines and fluorescently labeled phosphatidylethanolamines produced helices. Various experimental techniques including synchrotron x-ray diffraction, conventional x-ray diffraction, and density gradient centrifugation,[20] as well as our own experiments with β-cyclodextrin, described in Section 2.4.1, were consistent with the hypothesis that cholesterol is the major constituent of helical ribbons. Cholesterol was inferred to determine the bilayer structure; hence, the formation of helices of two pitch types was attributed exclusively to the structure of cholesterol.[12] However, direct substitution of cholesterol by its analogs to confirm this hypothesis has never been performed.

Below we show that the formation of helical ribbons of at least two pitch types is a general phenomenon observed in a wide variety of multicomponent systems containing a sterol.[41] The distinctive values of high and low pitch angles are not unique to model biles, but are a general property of a whole range of multicomponent systems, that contain a micelle–forming surfactant, a bilayer–forming amphiphile, and a sterol. We describe our experiments on a variety of quaternary sterol systems, on a fatty acid system, and on two lipid concentrate systems defined below. In addition to high and low pitch helical ribbons, almost all systems studied exhibited a third pitch type of helical ribbon with an intermediate pitch angle, whose value ranges between 30° and 47°. Although all the components, which make up the systems studied were enantiomerically pure, specifically L-enantiomers, some systems produced both right- and left-handed helical ribbons. Left-handed helical ribbons, however, were not observed in quaternary fatty acid system and in lipid concentrate systems.

Current explanations for the self-assembly of helices are based on theories of multilamellar liquid crystal bilayers or hexatic phases.[12,18,19] These theories assume that

high and low pitch helices correspond to two different molecular packings within the bilayer. This assumption implies that sterols other than cholesterol may pack differently within their bilayers, since their molecular structures differ from that of cholesterol. However, we found that helical ribbons of exactly the same three pitch angles formed in QSS with sterols other than cholesterol. Furthermore, current theories for liquid crystal bilayers assume that molecular chirality is the major factor behind helix formation.[12,18,19,60,61] However, the results of Thomas *et al.*[34,35] as well as the results of our experiments suggest that chirality is not the only factor in helix formation. In the following we qualitatively observe the effect of varying molecular chirality on helix formation and delve into the implications of these results on current theoretical models.

2.5.2 Substitution of Sterols

Materials and Methods

Quaternary sterol systems used in this set of experiments were composed of the common bile salt sodium taurocholate (NaTC), 1,2-dioleoyl-glycero-3-phosphocholine (DOPC, *sn*-1-18:1-*sn*-2-18:1), and a sterol in the molar ratio 97.5:0.8:1.7. Sodium taurocholate was purchased from Sigma–Aldrich (St. Louis, Missouri) and was further purified by the method of Pope.[46] The following natural sterols were used: cholest-5-en-3β-ol (cholesterol), 5β-cholestan-3β-ol (coprostanol), 5β-cholestan-3α-ol (epicoprostanol), 5α-cholestan- 3β-ol (cholestanol), cholesta-5,7-dien-3β-ol (7-dehydrocholesterol), ergosta-5,7,22-trien-3β-ol (ergosterol), 5α-lanosta-8,24-dien-3β-ol (lanosterol). Cholesterol (Nu-Chek Prep, Elysian, MN), and other sterols (Sigma–Aldrich, St. Louis, MO) were used as received without further purification. Phosphatidylcholine DOPC was purchased from Avanti Polar Lipids (Alabaster, Alabama) and was also used without further purification. Table 2.2 summarizes the systems studied and their constituents.

Lipid films for each system were prepared as described by Konikoff *et al.*[20] Each lipid film was diluted in filtered (0.22 μm pore size filter) Milli-Q water at ambient temperature to a total lipid concentration of 70 mg/ml to obtain a system unsaturated with cholesterol. In previous work, Chung *et al.*[12] prepared QSS with 0.15M NaCl to screen molecular charges and 3mM NaN_3 as an antibacterial agent. We did not add these salts to our systems as we demonstrated helical ribbon production in their absence. To induce complete solubilization of cholesterol microcrystals, we

Table 2.2: The Compositions of Quaternary Sterol Systems with Varying Sterols, QSS1

Surfactant	Phospholipid	Sterol	Sterol Chemical Formula
NaTC	DOPC	Cholesterol	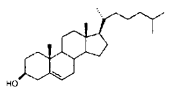
NaTC	DOPC	Coprostanol	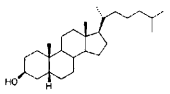
NaTC	DOPC	Epicoprostanol	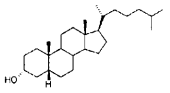
NaTC	DOPC	Cholestanol	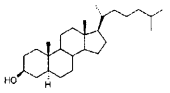
NaTC	DOPC	7-Dehydrocholesterol	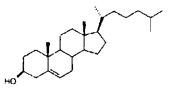
NaTC	DOPC	Ergosterol	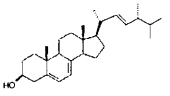
NaTC	DOPC	Lanosterol	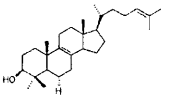

incubated the unsaturated systems for 2 hours at 61°C. These systems were then filtered through a 0.22 μm Millex-GV$_4$ filter (Millipore, Cambridge, MA) and diluted six–fold with Milli-Q water at ambient temperature to induce supersaturation. Supersaturated systems were incubated at 37°C, and 5 μl aliquots were removed daily to study structures formed. Frequent sampling did not affect the yield and variety of the structures formed.

The 5 μl aliquots were observed on glass slides using a phase-contrast microscope (Diaphot-TMD, Nikon). Images were taken with a camera (Sony, DXC-970MD) and digitized with a built-in frame-grabber on a Power Macintosh computer. For image enhancement and measurements, we have used the public domain NIH-Image software package. Measurements of pitch angles were performed according to the method of Chung *et al.*[12] Since the apparent handedness of helices changed during a through-focus scan, the handedness of helical ribbons was unambiguously determined by positioning the microscope objective focal plane on the upper surface of the structures.

Experimental Results

To study the formation of helical ribbons in various multicomponent systems, the basic approach used was a method of systematic substitution. Different sterols were substituted into multicomponent sterol systems, leaving phospholipid species and bile salt unchanged. The sterols in the quaternary sterol systems were chiral analogs of cholesterol and were chosen in such a way as to investigate the effects of their structure on helix formation. To study the influence of a planar sterol nucleus, sterols with a double bond at the 5-position (cholesterol, 7-dehydrocholesterol, ergosterol), and sterols with either 5α (cholestanol, lanosterol) or 5β (coprostanol, epicoprostanol) hydrogens were chosen. We also investigated the influence of the 3β-hydroxy group (cholesterol, coprostanol, cholestanol, 7-dehydrocholesterol, ergosterol, lanosterol) as compared to the 3α-hydroxy group (epicoprostanol). The effects of the sterol side chains on formation of helical ribbons were also studied by comparing sterols with saturated side chains (cholesterol, coprostanol, epicoprostanol, cholestanol, and 7-dehydrosterol), and sterols with unsaturated side chains (ergosterol and lanosterol). For these quaternary sterol systems, DOPC was used, since this phospholipid species produced the largest long-lived yields of both high and low pitch helical ribbons in quaternary sterol systems with cholesterol (Table 2.2).

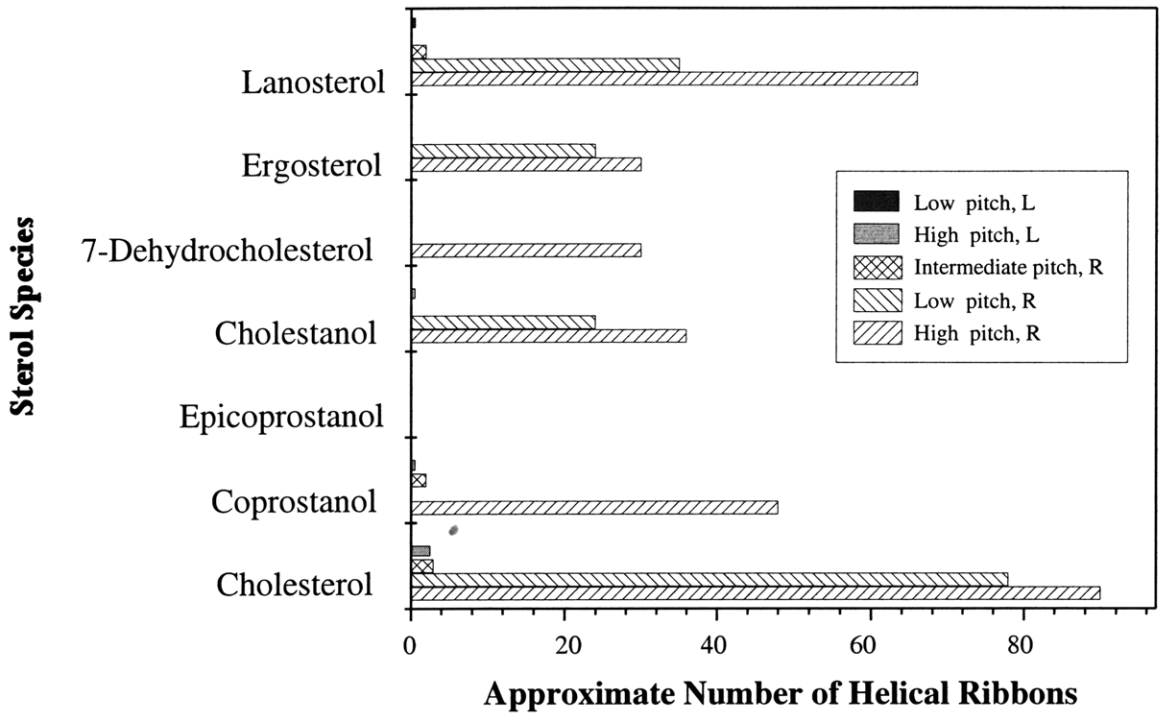

Figure 2.11: Approximate number of helical ribbons per typical field of view (0.071 mm^2) at the time in the helix temporal evolution when the yield of helical ribbons in QSS is at its maximum value. All QSS are composed of bile salt sodium taurocholate, DOPC, and various sterols (Table 2.2). Striped bars represent the number of right-handed helical ribbons; the solid bars represent the number of left-handed helices.

The systems studied were chosen in such a way as to place them in the "2–phase" region of a phase diagram, where plate-like sterol crystals and saturated micelles coexist in an equilibrium state.[26] Additionally, the concentrations of the components were such that the temporal crystallization sequences in the systems studied was the same as that described above in Pathways Section: filaments followed by helical wires that grew laterally to form helical ribbons, then tubules, and finally plate-like crystals.

The majority of systems studied in our experiments produced high pitch helices, with a pitch angle of 54 ± 2°, and low pitch helices with a pitch angle of 11 ± 2°. Additionally, in almost all systems studied, we found small amount of intermediate pitch helices. The value of the pitch angle of these helices depended on the sterol species used and was in the range between 30 and 47°.

Figure 2.11 displays the approximate number of helical ribbons as a function of sterol species in a typical field of view (magnification x60) at the time of maximum yield of helical structures. This time of maximum yield varied from system to system but usually was within 2 to 5 days after supersaturation of an unsaturated system. With exception of epicoprostanol, all sterol systems formed right-handed helical ribbons of at least one pitch type, either of high or low pitch angle. Right-handed intermediate pitch helical ribbons were observed in QSS with cholesterol, coprostanol, and lanosterol. Left-handed helical ribbons were observed only in QSS with cholesterol, coprostanol, cholestanol, and lanosterol. The only metastable structures formed in the sterol system with epicoprostanol, however, were short straight non-flexible filaments, 3 to 5 μm long (this is in contrast to long flexible filaments formed in all other systems, 80 μm).

In addition, in quaternary sterol systems with cholesterol, coprostanol, and lanosterol intermediate pitch helices also formed. The specific values of the pitch angle of these structures depended on the particular sterol species used. Figure 2.11 indicates that, in addition to right-handed helical structures, we also found small quantities (1-2 structures per typical field of view) of left-handed helices in quaternary sterol systems with cholesterol, coprostanol, cholestanol, and lanosterol.

2.5.3 Substitution of Phospholipids and Fatty Acid

Materials and Methods

Quaternary sterol systems, QSS2, for this set of experiments were composed of the common bile salt sodium taurocholate (NaTC), one type of phosphatidylcholine, and cholesterol in the molar ratio 97.5:0.8:1.7. The quaternary fatty acid system, QFAS, was composed of the common bile NaTC, oleic acid, and cholesterol in the molar ratio 97.5:0.8:1.7. As before, sodium taurocholate was purchased from Sigma-Aldrich (St. Louis, Missouri) and was further purified by the method of Pope.[46] Cholesterol (Nu-Chek Prep, Elysian, MN) was used as received without further purification. Synthetic L-enantiomers of lecithin used to prepare quaternary sterol systems were: 1,2-dioleoyl-glycero-3-phosphocholine (DOPC, *sn*-1-18:1-*sn*-2-18:1), 1,2-dielaidoyl-glycero-3-phosphocholine (DEPC, *sn*-1-*trans*18:1-*sn*-2-*trans*18:1), 1,2-dipalmitoyl-glycero-3-phosphocholine (DPPC, *sn*-1-16:0-*sn*-2-16:0), 1,2-dimyristoyl-glycero-3-phosphocholine (DMPC, *sn*-1-14:0-*sn*-2-14:0), 1,2-dilauroyl-glycero-3-phosphocholine (DLPC, *sn*-1-12:0-*sn*-2-12:0), dipalmitoleoyl phosphatidylcholine (DZPC, *sn*-1-16:1-*sn*-2-16:1), 1-palmitoyl-2-oleoyl-glycero-3-phosphocholine (POPC, *sn*-1-16:0 -*sn*-2-18:1), 1-oleoyl-2-palmitoyl-glycero-3-phosphocholine (OPPC, *sn*-1-18:1-*sn*-2 -16:0), 1-stearoyl-2-oleoyl-glycero-3-phosphocholine (SOPC, *sn*-1-18:0-*sn*-2-18:1), 1-oleoyl-2-stearoyl-glycero-3-phospho-choline (OSPC, *sn*-1-18:1-*sn*-2-18:0). All phospholipids and oleic acid were purchased from Avanti Polar Lipids (Alabaster, Alabama). Phosphatidylcholines and oleic acid were used without further purification. Table 2.3 summarizes the systems studied and their constituents. This set of experiments followed the procedure above for the production and observation of helical ribbons formed.

Experimental Results

This set of experiments is a follow-up of the study on the presence of phospholipids within the walls of helical ribbons, as described above in Section 2.4.2. Below we present a quantitative analysis of the helix formation in QSS with various phospholipids.

The formation of helical ribbons in these multicomponent systems was also studied by systematic substitution. Different phosphatidylcholines and a fatty acid (Oleic acid) were substituted into multicomponent sterol systems, leaving sterol species, cholesterol, and bile salt unchanged. The chiral phosphatidylcholines were substituted

Table 2.3: The Compositions of Quaternary Sterol Systems with Varying Phospholipids, QSS2, and Oleic Acid, QFAS

Micelle–Forming Surfactant	Sterol	Bilayer–Forming Amphiphile	Amphiphile Chemical Formula
NaTC	Cholesterol	DOPC	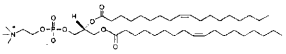
NaTC	Cholesterol	SOPC	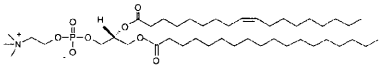
NaTC	Cholesterol	DEPC	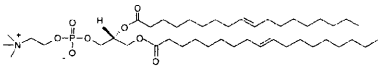
NaTC	Cholesterol	POPC	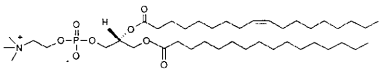
NaTC	Cholesterol	OSPC	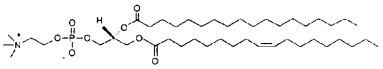
NaTC	Cholesterol	OPPC	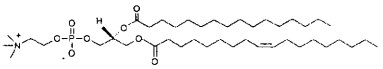
NaTC	Cholesterol	DZPC	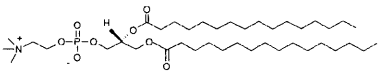
NaTC	Cholesterol	DMPC	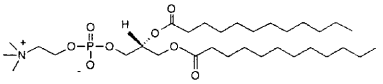
NaTC	Cholesterol	DPPC	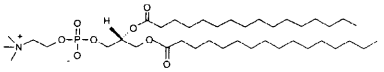
NaTC	Cholesterol	DLPC	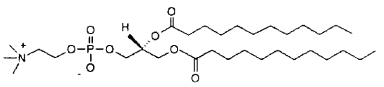
NaTC	Cholesterol	Oleic Acid	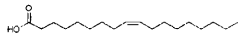

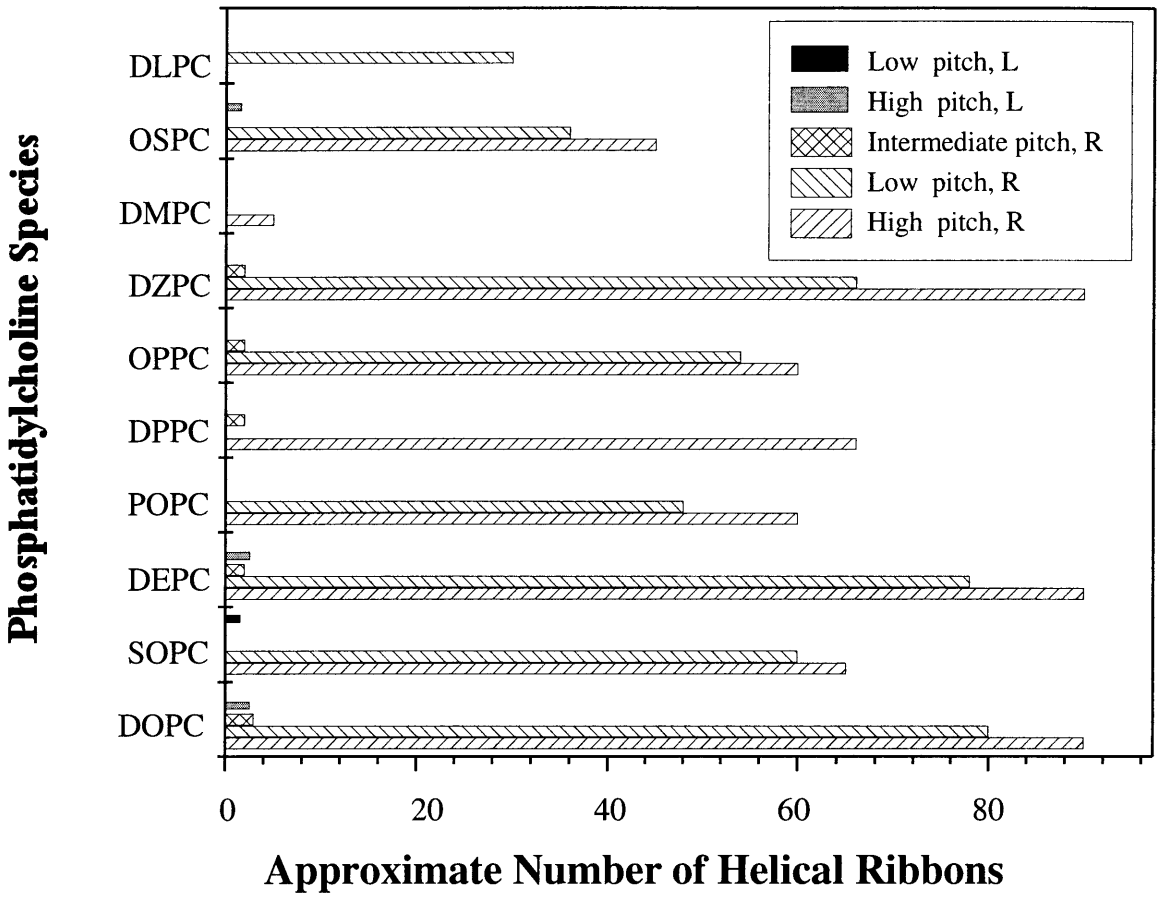

Figure 2.12: Approximate number of helical ribbons per typical field of view (0.071 mm^2) in QSS made with cholesterol and various phosphatidylcholines (Table 2.3). Striped bars represent right-handed helices; solid bars represent left-handed helices at the time of maximum yield of structures, typically between second and fifth days after the supersaturation (quenching) of unsaturated QSS.

by non-chiral fatty acid to see whether and how chirality of phospholipid affects formation and growth of helical ribbons. As previously, we chose systems in such a way as to place them in the "2–phase" region of a phase diagram, where plate-like sterol crystals and saturated micelles coexist in an equilibrium state.[26] On the other hand, the temporal crystallization sequences in the systems were the same as described above in Pathways Section due to the chosen concentrations of the components of these quaternary sterol systems.

Varying the phospholipid species in QSS (Table 2.3) affected the number of helical structures formed, the kinetics of their formation, and their handedness. Figure 2.12 displays the approximate number of each helix pitch type observed in a typical microscopic field of view (magnification x60). The Figure represents maximum yield of structures during their temporal evolution, which occurs between the second and fifth day after unsaturated QSS are quenched. As can be seen in this figure, almost all quaternary sterol systems formed both right-handed high and low pitch helices. The two exceptions were QSS with DMPC and DLPC, in which helical ribbons of only high or low pitch, respectively, were found. Additionally, QSS with DOPC, DEPC, OPPC, DZPC, and DPPC formed right-handed intermediate pitch structures. We also observed left-handed helical ribbons in quaternary sterol systems with DOPC, SOPC, DEPC, OSPC. Consistent with the observations of Chung *et al.*,[12] all helical ribbons, without exception, were right-handed in quaternary sterol systems with POPC. Contrary to the results of Konikoff *et al.*,[25] our experimental technique did yield helical ribbons in quaternary sterol system with DLPC. We also found that quaternary sterol systems with DPPC produced low quantities of helical ribbons in the first 5 days of formation.

These results indicate that the precise nature of phospholipids does not affect the formation of high and low pitch helices. However, the nature of the phospholipids present does affect the kinetics and yield of helical ribbons formed. By choosing a species of phospholipid for a quaternary sterol system, one may selectively produce large yields of predominantly high or low pitch helical ribbons. This experimental advancement may facilitate the experimental determination of the internal structure of helical ribbons of either pitch angle.

Additionally, we prepared a simpler system, the quaternary fatty acid system, QFAS. This system is a mixture of bile salt sodium taurocholate, oleic acid, and cholesterol in water. The molar ratio of the components in the quaternary fatty

acid system is identical to that of the components in the quaternary sterol system (Table 2.3). In this case, both cholesterol and bile salt are chiral species in the fatty acid system, whereas oleic acid is achiral. As displayed in Figure 2.12, we observed the formation and evolution of helical ribbons with the same values of pitch angles, high, low, and intermediate. All of the helical ribbons found in this system were right-handed.

2.5.4 Lipid Concentrate Systems

Introduction

A new class of systems, lipid concentrates, that also form helical ribbons of high, low and intermediate pitch angles, was discovered.[b] We studied two concentrated lipid emulsions, chemically defined lipid concentrate (CDLC) and lipid concentrate (LC). Chemically Defined Lipid Concentrate (CDLC) is a concentrated lipid emulsion consisting of a mixture of anionic surfactants, fatty acids, and cholesterol, in 10% ethanol. CDLC is used as a cell culture medium for insect cell culture (Sf9), Chinese hamster ovaries cell culture (CHO), and various hybridoma cell cultures. Since it provides ample quantities of lipids, important structural components and energy source in living cells, CDLC's function is to promote cell growth in serum-free media.[62–65] The commonly used lipid concentrates as cell culture media utilize marine oils as a source of lipids. However, undefined nature of these lipids in marine oils might present a problem in defining the cellular interactions and therefore cannot be used for therapeutic studies.[66,67] To alleviate this problem, Chemically Defined Lipid Concentrate has been used, since CDLC is a well defined combination of saturated and unsaturated fatty acids. Table 2.4 describes the composition of CDLC in greater details. LC, on the other hand, is a concentrated lipid emulsion that consists of anionic surfactants, cod liver oil, and cholesterol, in 10% ethanol. Though used for the same purposes as CDLC, LC's lipid content is not completely defined since cod liver oil varies in its composition. However, the majority of fatty acids in cod liver oil are the same as in CDLC: Myristic, Palmitic, Palmitoleic, Oleic, Stearic, α-Linoleic, Stearidonic, Gadoleic, Gondoic, 5,8,11,14,17-Eicosapentaenoic, Euricic, 7,10,13,16,19-Docosapentaenoic, 4,7,10,13,16,19-Docosahexanenoic[54,68] (Table 2.4).

[b]We thank Dr. A. L. Biere for drawing our attention to the presence of helices in the CDLC system.

Table 2.4: The Composition of Chemically Defined Lipid Concentrate, CDLC

Component	Common Name	Concentration, mg/ml
Fatty Acids	Myristic Acid	10.00
	Palmitic Acid	10.00
	Stearic Acid	10.00
	Palmitoleic Acid	10.00
	Oleic Acid	10.00
	α-Linoleic Acid	10.00
	Linolenic Acid	10.00
	Arachidonic Acid	2.00
Sterol	Cholesterol	220.00
Surfactants	Tween^{TM} 80	2,200.00
	Pluronic® F-68	100,000.00
Antioxidant	Vitamin E	70.00

Materials and Methods

Chemically defined lipid concentrate (CDLC) and lipid concentrate (LC) were purchased from Gibco BRL Products (Gaithersburg, MD) and observed without further manipulation. Multicomponent systems, CDLC and LC are analogous to the quaternary sterol systems in that they are mixtures of three groups of components, surfactants (that serve a role of the bile salt), fatty acids (that serve a role of a phosphatidylcholine), and cholesterol (Table 2.4).

We studied the effects of evaporation, oxidation, light, pH, and temperature on formation and growth of helical ribbons in CDLC and LC. Lipid concentrates were exposed to the above conditions for up to 7 days and the results were compared with the control. We found that neither evaporation of ethanol with hydrated Argon, nor oxidation of fatty acids by air displacing the Argon layer, nor exposure of CDLC and LC to light had any effects on formation and growth of helical ribbons. Variation of pH in the range between 1.8 and 9.7 led to no changes in lipid concentrates at high pH, however at low pH (pH < 4.5) we observed formation of amorphous aggregates.

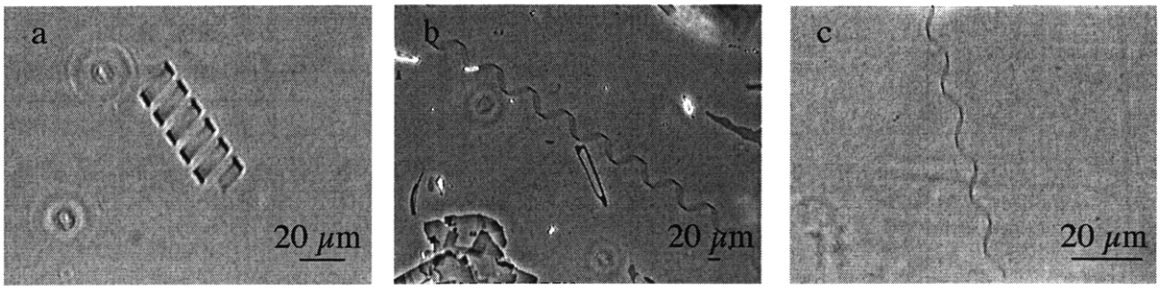

Figure 2.13: Typical helical ribbons in CDLC system. (a) Low pitch helical ribbon with a pitch angle $\psi = 11 \pm 0.5°$; (b) intermediate pitch helical ribbons with a pitch angle $\psi = 40.8 \pm 0.5°$; (c) high pitch helical ribbon with a pitch angle $\psi = 54 \pm 0.5°$.

Finally, temperature seemed to have the largest effect on formation of helices on the scale of our experiment: at 4° no formation of helices was observed, but at 37° increased number of structures was observed. It is possible, however, that on a larger time scale all of the above conditions play a cumulative role in the process of formation and growth of helical ribbons.

Experimental Results

Even though there is only a single chiral component in CDLC and LC, as opposed to all other quaternary sterol systems studied, where either two or three components were chiral, we nonetheless observed the formation and evolution of all the same structures: helical ribbons of high, low, and intermediate pitch angles. Figure 2.13 illustrates these three pitch types of helical ribbons formed in the CDLC system. By virtue of their composition, CDLC and LC fall into the region of a phase diagram where plate-like cholesterol crystals and saturated micelles and vesicles coexist in an equilibrium state,[26] as we described in Section 2.2.1. This is the same region in which QSS and QFAS are and is designated by "star" in Figure 2.1. This composition of CDLC and LC, in fact, leads both of the systems to follow the same evolution pathways as in quaternary sterol systems (QSS) and the quaternary fatty acid system (QFAS) described above: filaments followed by helical wires that grow laterally to form helical ribbons, then tubules, and finally plate-like crystals. The approximate numbers of helices of high and low pitch angles are displayed in Figure 2.14. All helical ribbons in CDLC and LC were right-handed, without exception.

The kinetics of formation of all structures in both lipid concentrate systems was analogous to the quaternary sterol systems. The evolution of the structures from

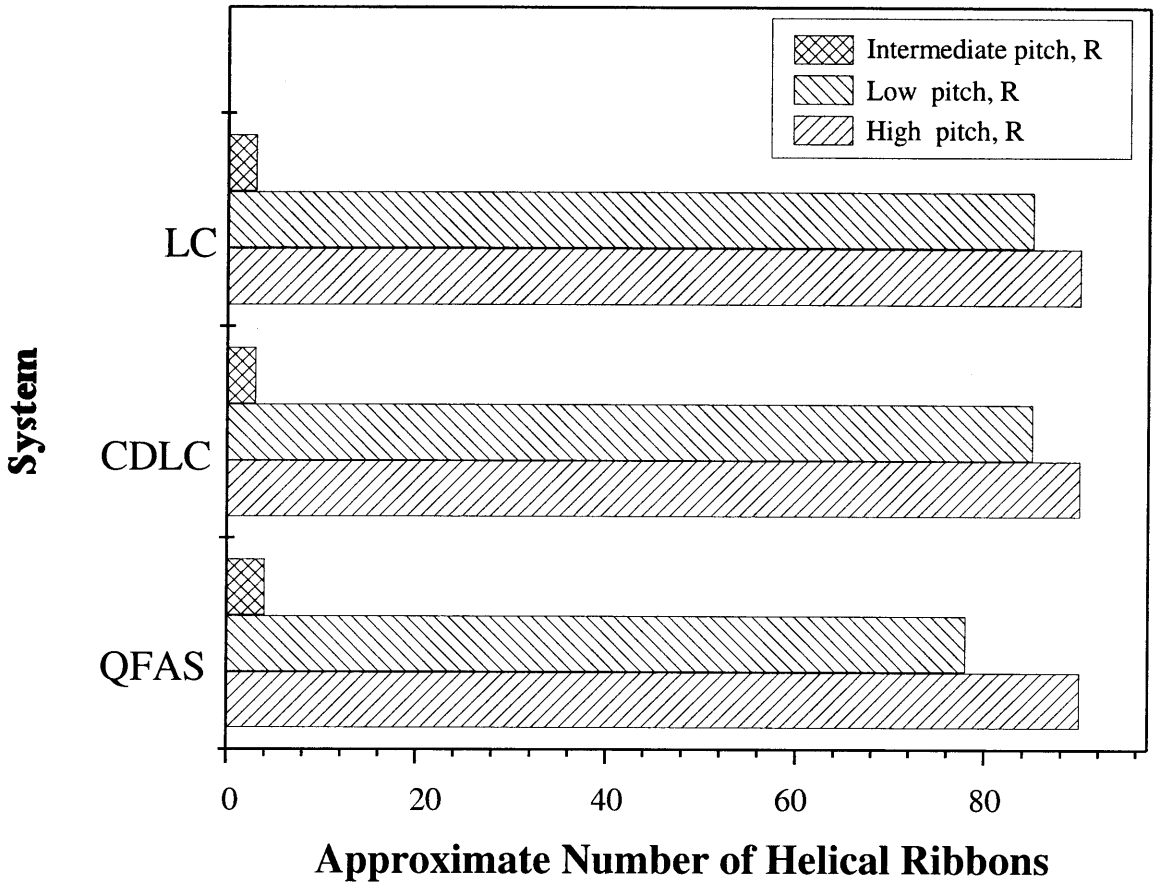

Figure 2.14: Approximate number of high, low, and intermediate pitch right-handed helical ribbons per typical field of view (0.071 mm^2) in the lipid concentrate systems, CDLC and LC at the time in their temporal evolution when the yield of structures is maximum. The number of helices produced in the QFAS at the time of maximum yield is shown for comparison.

helical ribbons to tubules to crystals is identical to that in QSS and QFAS. In fact, the evolution from high pitch helical ribbons to tubules was clearly observed for the first time in CDLC. In comparison, such a transition in QSS and QFAS is a very rare event. The yields of the structures were very high, as in the quaternary sterol system with DOPC and cholesterol (Fig. 2.14).

Moreover, it is very important to stress that the production of the intermediate metastable structures in QSS and QFAS is a result of the dilution of the unsaturated model bile, i.e. the crossing of the phase boundary. We have discussed the role of evaporation, oxidation, light, changing pH, and temperature on formation and growth of helical ribbons. It seems that an amalgamation of all these conditions is responsible for helix formation in CDLC and LC. It is also interesting to note that once formed, structures in CDLC can be dehydrated for a short period of time while preserving

their geometrical structure. This, combined with the very high yield of structures, can be used to our advantage for the Environmental Electron Microscopy experiments and Atomic Force Microscopy.

2.5.5 Conclusions

The formation of helical structures exhibiting two distinct pitch angles has previously been regarded as a phenomenon unique to model bile systems. The present work, on the other hand, reveals that helical ribbons of two distinct pitch angles can be formed in a wide variety of multicomponent systems containing alternative sterols, including quaternary sterol systems (QSS), quaternary fatty acid systems (QFAS), and a set of lipid concentrate systems (CDLC, LC). It is important to recognize that with the current improved experimental techniques, we have achieved very high yields of self-assembled helical ribbons. The concentration of helices in the majority of systems studied, some of which are readily available, is typically a factor of ten greater than that found previously in the model bile system. This high concentration greatly facilitates the detection, observation and isolation of individual helical ribbons.

The distinctive values of 54±2° for the high pitch and 11±2° for the low pitch helical ribbons were similarly regarded as a special property of model biles. However, we find that helical ribbons of precisely these pitch angles form in almost all the systems studied regardless of surfactant, phosphotidylcholine (fatty acid), or sterol component. We also observe intermediate pitch helices with pitch angle in the range between 30° and 47° in almost all of the above systems. However, these helices represent less than ten percent of the total helical ribbon concentration.

To explain the observed values of the pitch angles, current theories model the helices as multilamellar liquid crystal bilayers in which the constituent molecules have orientational but not positional order.[12,18,19] The existence of two (or more) helical pitch types with different pitch angles was thought to result from different molecular packings within a bilayer of each helical pitch type. We have found that all the diverse helix-forming systems produce exactly the same high and low pitch angles. It is very unlikely that the same two (or more) packings occur for for each of the diverse molecular species in the various systems investigated.

Our work also raises questions about the role of molecular chirality in the formation of helices. Current theories[18,60,61] hold that the handedness of the macroscopic ribbon or tubule is a reflection of the chirality of the underlying constituent molecules.

However, we find that in seven out of the sixteen quaternary sterol systems studied, in which all the components are enantiomerically pure, both right- and left-handed helices are formed. This is consistent with the work of Thomas *et al.*,[34,35] who find both right- and left-handed helices in an enantiomerically pure system of phosphonate analogue of 1,2-bis(10,12-tricosadiynoyl)-*sn*-glycero-3-phosphocholine. It is to be noted that the left-handed helices in our systems typically represent less than five percent of the total helical ribbons observed (Fig. 2.12 and 2.11). In QFAS, CDLC, and LC the only chiral component is cholesterol. Interestingly, we find only right-handed helices in these systems.

The experiments of Konikoff *et al.*[20,28] in model bile show that filaments, the precursors of helical ribbons, are a polymorph of cholesterol monohydrate and anhydrous cholesterol covered by a monolayer of phospholipid. Furthermore, the helical ribbons themselves are precursors to stable cholesterol monohydrate crystals. This suggests that helical ribbons may actually have a crystalline, positionally ordered, molecular structure. If we model the helices as thin anisotropic crystalline ribbons, then it can be shown that in general there are two preferred directions for bending.[37] If such thin anisotropic crystalline ribbons have a propensity to bend, helices of two pitches are predicted to form. In this picture, both the high and low pitch helices could emerge from a single underlying molecular structure.

Finally, we found that neither the specific structure of phosphatidylcholines and fatty acids, nor the presence of charged groups on surfactant molecules affects the kinetics and yield of helix formation. However, the structural differences in sterols in addition to the kinetics and the yield of helices, also play an important role in whether helices can be formed. Our results suggest that if both a nonplanar sterol nucleus and a 3α-hydroxy group are present, then helices will not form (epicoprostanol). Further experiments need to be performed to investigate whether a 3β-hydroxy group is critical for the formation of helical ribbons (i. e. a sterol possessing a planar sterol nucleus and a 3α-hydroxy group, as in epicholestanol). On the other hand, the sterol side chain does not seem to affect the formation of helices. If indeed helical ribbons are crystalline in nature, the crystal structures of the sterols for which helices are formed should be similar. Furthermore, any change in the sterol structure which affects crystal formation should affect helix formation. The only crystallographic data available, to our knowledge, is that for anhydrous cholesterol, cholesterol monohydrate, and cholestanol dihydrate.[69] All of these crystals are triclinic in nature (space

group P1). It is also known that cholesterol crystals (both anhydrous and monohydrate) are of characateristic bilayer nature, with a molecular arrangement similar to that of cholesterol in biological membranes.[70] Such data is, however, not available for comparison for any of the other sterols used in our experiments. It would be interesting to have the crystallographic data for all sterols in our experiments to see whether and how their crystallographic space groups and the molecular arrangement within crystals affect helix formation. This information could be further used to estimate intermolecular forces between these molecules and give insight into relative sizes of spring constants and helix stabilities.

2.6 Application of Forces to Helical Ribbons

2.6.1 Introduction

To further investigate helical ribbons and their microscopic structure, it was necessary to perform experiments to study the structure of the free energy of the helical ribbons (see detailed explanation in Chapter IV). One such experimental procedure is the physical deformationof a helical ribbon. The easiest way to deform a helix is to apply an axial force which either stretches or compresses a helical structure along its axis. As a prerequisite to performing these experiments, the following questions needed to be addressed. Firstly, a means of tethering a helix had to be discovered. Secondly, a method of delivering the axial force had to be found. And thirdly, the effective force applied needed to be calibrated. Here we will describe the force application experiments from the qualitative point of view. Chapter IV will address the quantitative side of all these issues in conjunction with theoretical interpretations of the qualitative results (including the detailed quantitative analysis of helix behavior under tension). Therefore, in what follows we will describe qualitatively the experimental observations of helices' response to applied forces: helix recovery from tension in an aqueous solution, full elongation of a helix under tension, and finally tension induced phase separation (described only in this Chapter from the qualitative point of view).

Our experiments were performed with helical ribbons formed in Chemically Defined Lipid Concentrate system, CDLC. Initially, we chose to work with CDLC due to the ease of preparation and abundance of helical ribbons formed. As will be shown in this section, the low pitch helical ribbons formed in CDLC are also relatively easy

to tether compared to the other helix pitch types formed in CDLC and helices formed in other systems. Therefore, the majority of our experiments were performed with low pitch structures formed in CDLC.

We also discovered that the low pitch helical ribbons formed from CDLC system bind very strongly to Devcon 5-Minute Epoxy^{TM}. This epoxy does not dissipate in water neither when cured nor prior to curing. This allows us to manipulate and bond helical ribbons in aqueous solution without dehydrating them. Using this adhesive we developed a methodology of attaching one end of a helical ribbon to a stationary structure (reference glass beam), while attaching the other end to a mobile glass rod connected to a micromanipulator. Thus we can extend and compress helices with about 1 μm control. (For a very detailed discussion of tethering methodology and application of forces to helical ribbons, see Chapter IV.)

2.6.2 Experimental Observation of Helix Recovery From Tension Induced Elongation

Figure 2.15 illustrates typical images of helix micromanipulation. When a helical ribbon is placed under tension and the force is removed suddenly, one can observe helix recovery and measure helix spring constant from relaxation time. Experimentally, this is accomplished by extending a helix (pulling it) until one of the glue joints fails. This procedure is usually performed epoxy joints which have not had enough time to cure. A characteristic point on a helix is then followed as helix returns to its equilibrium. This process is slowed down due to the viscosity of aqueous solution. The quantitative investigation of this procedure is detailed in ChapterIV.

2.6.3 Experimental Observation of Tension Induced Phase Separation of Low Pitch Helical Ribbons

Long low pitch helices, i.e. low pitch helices with more than five full turns, undergo an unexpected phenomenon when subjected to axial tension. When stretched from their equilibrium pitch angle of approximately 11° to a pitch angle of about 30°, low pitch helices separate into helical and straight portions. The resulting helical segment posseses a pitch angle of approximately 17°, which is larger than the equilibrium pitch angle of low pitch helics by about 6°. As tension is increased further,the axial length of the structure increases via elongation of the straight segment, which does so at the expense of the shortened helical segment. Interestingly, the helical segment preserves

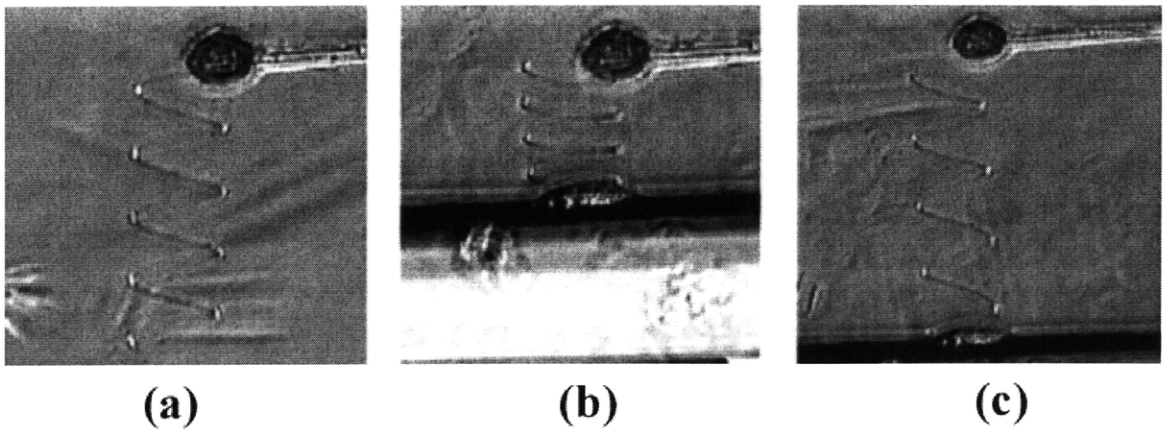

Figure 2.15: Micromanipulation of a typical low pitch helical ribbon in CDLC: (a) free from external force; (b) under compression; (c) under extension. Mobile glass rod with a spherical epoxy joint is shown at the top of each figure. Panel (b) also displays a reference beam at the bottom of the picture.

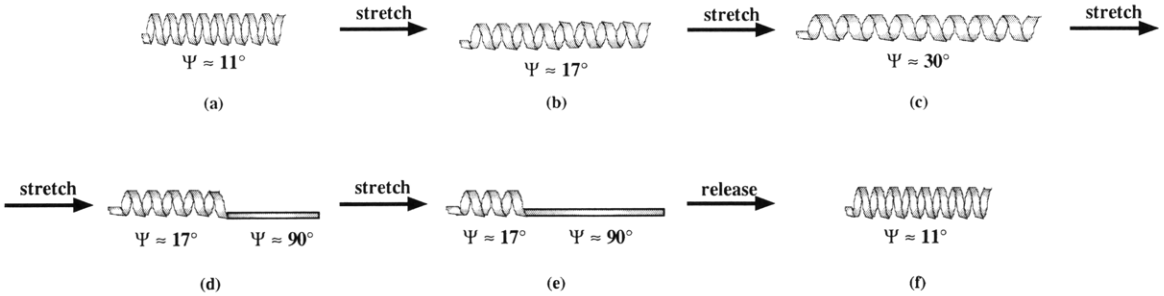

Figure 2.16: Schematic representation of a "long" low pitch helical ribbon undergoing a phase separation into straight and helical portions while under axial tension: (a) a helix free from external force; (b) the helix under small tension; (c) the helix at critical tension just before phase separation; (d) the helix under tension beyond phase separation value; (e) the helix at a larger tension with a straight segment being elongated at the expense of the axial length of a helical segment; (f) the helix after tension has been released.

its pitch angle of approximately 17° for the duration of the experiment decreasing in its axial length until no more coils are left. A schematic representation of this process is shown in Figure 2.16. An analogous representation of this process is shown in the set of photographs in Figure 2.17. It is worthwhile noticing here that helical ribbons display perfectly elastic behavior; when the tension is removed, the helices return to their original state. Moreover, helices behave elastically independently of the number and extent of stretching experiments including experiments resulting in a fully extending deformation. In other words, helices can be extended to more than 450% of their original axial length, and yet they come back to their original axial length and pitch angle without any sign of permanent deformation or fracutre.

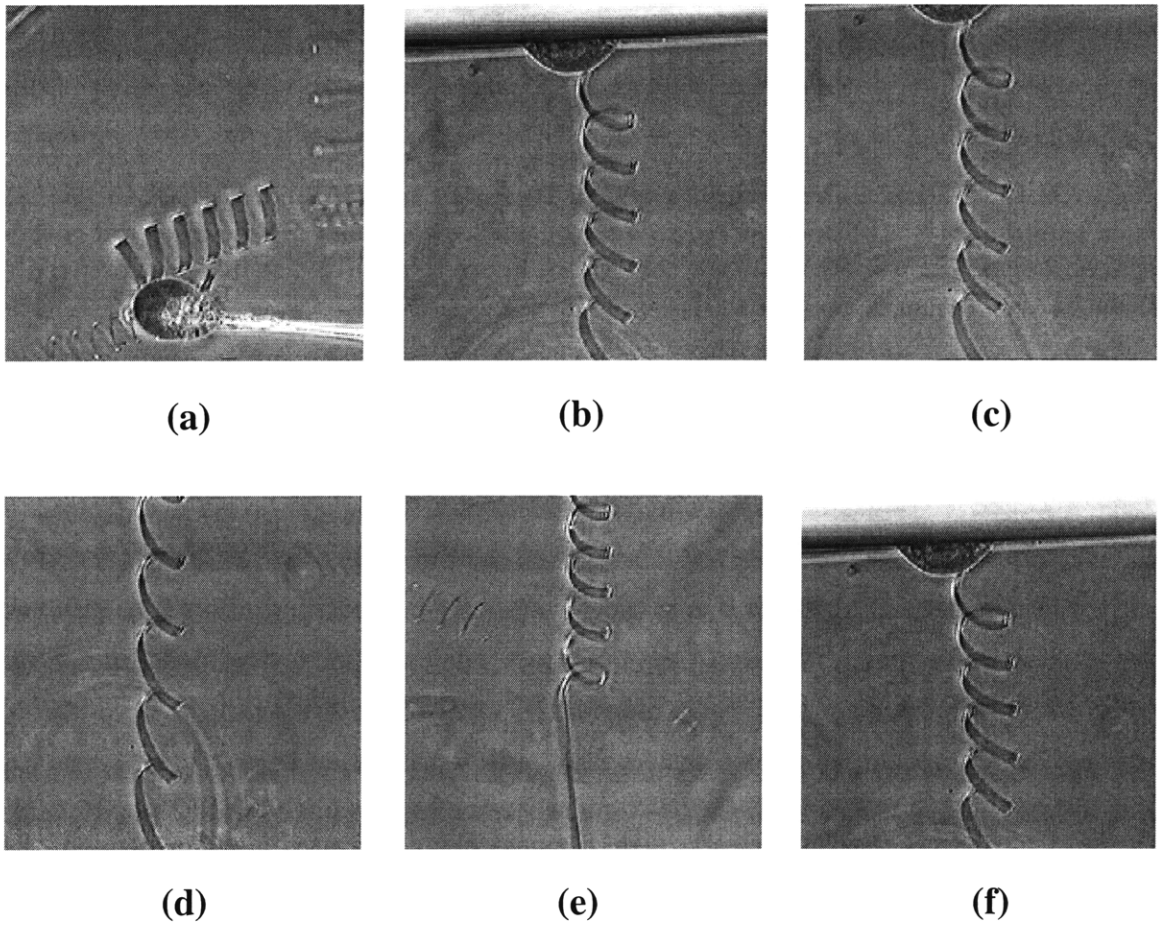

Figure 2.17: Photographs illustrating tension induced phase transition of a low pitch helical ribbon that separates into a flat and a helical portions: (a) a helix free from external force; (b) the helix at a small tension; (c) the helix at a larger tension; (d) the helix under a critical tension; (e) the helix under tension beyond critical value; (f) the helix at a larger tension with a straight segment being elongated at the expense of the helical segment.

In Chapter 4 we will discuss quantitatively whether and to which extent Hooke's law is obeyed when axial forces are applied to helices. At this point, however, it is worthwhile to make few more qualitative observations regarding helix response to applied axial forces. First, experimental observation of the tension induced phase separation of all suitably long helices, i.e. helices with five or more full turns, indicates that this process is not a consequence of the experimental conditions: the local environment of a helix under tension, the level of cure of a glue joint, the chemical concentration of helix surroundings, the exact positioning of a helical ribbon in a glue joint, the particular method of applying force, etc. Rather, the fact that *all* long helices undergo this process for deformations beyond critical tension implies that phase separation is a universal phenomenon. Second, the phase separation process is perfectly reversible. Third, the exact helix deformation at phase separation, i. e. pitch angle of approximately 30°, is an underlying property of helix structure since phase separation occurs at this angle in all experiments. Finally, it is worthwhile noting one more experimental observation. As mentioned earlier, upon helix extension phase separation occurs when the pitch angle reaches approximately 30°. However, upon release of the external force, a merging of the helical and straight segments into a single helical structure occurs as the helical segment increases in length at the expense of the straight segment. As the straight segment merges into the helical segment, the pitch angle of the helical segment remains approximately 17°.[c] Figure 2.18 is a schematic sketch of this process.

Here we draw a qualitative analogy of helix phase separation to a classical case of a first order phase transition. First order phase transitions involve a sudden discontinuous change in a physical property of a system as temperature, pressure or other thermodynamic variable changes. In the case of helical ribbons, the helix pitch angle undergoes a sudden discontinous change when placed under axial tension. The reversible nature of helix phase separation is further evidence that helices undergo a first order phase transition when subjected to axially applied forces. It is interesting to consider qualitatively the reversible phase separation of helices within the realm of this analogy of a first order phase transition; Chapter 4 will discuss this issue from a quantitative point of view. In this analogy, phase separation into helical and straight segments at the pitch angle of 30° is reminiscent of superheating. The real critical

[c]In what follows, we will use the terminology of "phase separation and merging" when explaining the process of helix separation into helical and straight segments and the merging of helical and straight segments back into a single helix, respectively.

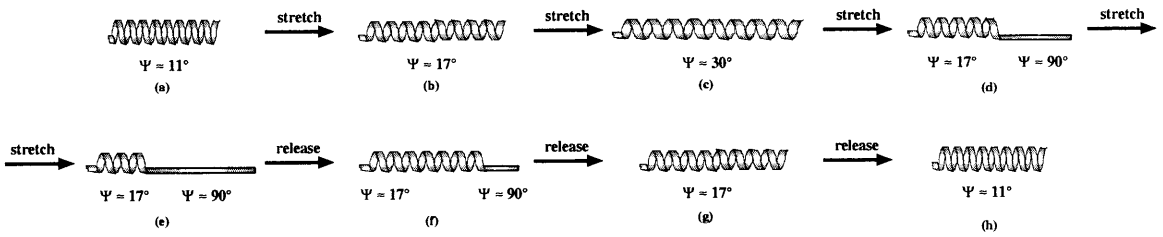

Figure 2.18: Schematic representation of a low pitch helical ribbon undergoing a phase separation into straight and helical portions while under axial tension: (a) a helix free from external force; (b) the helix under small tension; (c) the helix at critical tension; (d) the helix under tension beyond its critical value; (e) the helix at a larger tension with a straight segment being elongated at the expense of the axial length of a helical segment; (f) the helix upon release: straight portions decreases in length while helical portion becomes longer; (h) integrated helix upon tension release (g); the helix after tension has been released.

value of discontinuous parameter, pitch angle, is 17°, since this is the helix pitch angle which coexists with a straight segment. In principle, a new straight phase should nucleate at this critical value of helix pitch angle, but, in the analogy of gas–liquid phase transitions, helix is "superheated" and cannot nucleate this phase. This implies that a helix stretched to any pitch angle between 17° and 30°, where it finally formsa new phase, should immediately phase separate with any small disturbance such as physical agitation. As a helix is stretched beyond the pitch angle of 30°, no disturbance is necessary as the new phase nucleates by itself. Upon release of tension, as mentioned earlier, the merging of helical and straight segments into one helical phase at the critical value of pitch angle of 17°.

It interesting to study the phase separation both from the point of view of determining which theoretical model gives the best interpretation for the existence of helical ribbons, and from the point of view of learning what values various helix elastic moduli possess. As deep quantitative study phase transition theory of helical ribbons will not be presented in this thesis, we will deal only with experimental and theoretical results pertinent to a basic study and understanding of crystalline theory.

2.6.4 Experimental Observation of Tension Induced Full Elongation of Low Pitch Helical Ribbons

We have just described tension induced phase separation of long low pitch helical ribbons. By "long" we meant helical ribbons with more than five full turns. "Short" helical ribbons do not exhibit the phenomenon of phase separation. The reason for this is clear when one considers the geometry of phase separation process: if there is

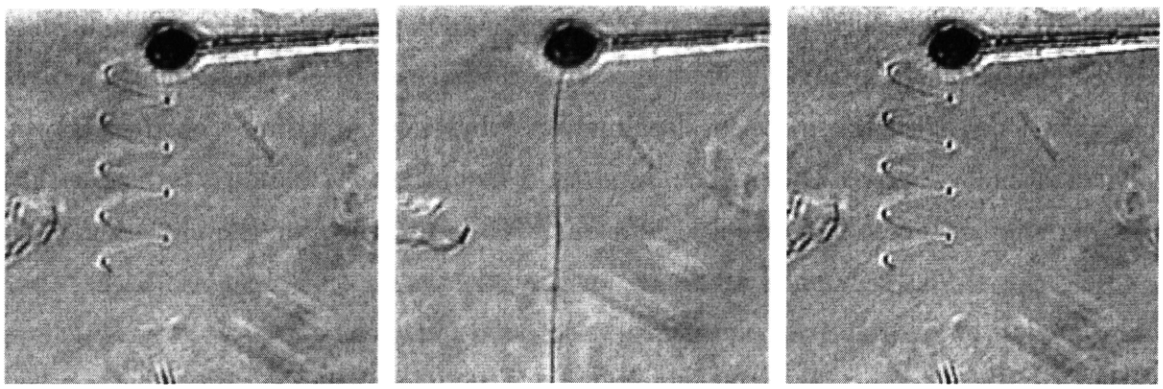

Figure 2.19: Elongation of a typical "short" low pitch helical ribbon in CDLC: (a) free from external force; (b) under full extension; (c) under extension. Mobile glass rod with a spherical epoxy joint is shown at the top of each figure. Panel (b) also displays a reference beam at the bottom of the picture. (As explained in text, "short" low pitch helical ribbons do not undergo tension induced phase separation.)

not enough ribbon length to hold both ends of a helix in glue joints AND insufficient number of turns between the glue joints for the exchange of ribbon length between helical and straight segments, the phase separation does not occur. Instead, when placed under tension, a helical ribbon fully elongates by gradually increasing its pitch angle and therefore its axial length until it is fully extended into a straight ribbon. Upon removing tension, a helix returns to its original conformation without any visible fractures or deformations; the axial length and pitch angle of a "short" low pitch helix released from tension are unaffected by the number of experiments and the extent of tension applied. An example of a helical ribbon with four and a half turns under tension is given in Figure 2.19. As one can see from this figure, "short" low pitch helices, are completely elastic, just as are "long" low pitch helices.

It is also important to point out that, under tension, helices take new shape without visible exchange of material with the chemical milieu in which they form and grow. This experimental observation is based on a study of the geometrical parameters of helices before and after tension is applied: helix axial length, pitch angle, pitch length, and ribbon width. We have also performed a qualitative analysis of helical ribbon thicknesses via measurement of the digitized image grey scale values before and after tension is applied. The grey scale values indicating darkness of a ribbon wall, are implicitly related to ribbon thickness: the darker the image of a ribbon wall, the thicker this ribbon is. Although such a comparison of ribbon

thicknesses is inadequate when different helices are compared, it is possible to do this study for one and the same helix before and after tension is applied. This analysis suggests that helix thickness is also unaltered by tension induced changes in the helical ribbon shape. This result is important, as on the one hand, it indicates that no inflow or outflow of material is necessary to compensate for the changing pitch angle of a helix as tension is applied. On the other hand, this result indicates that local variations in relative concentrations of solution constituents in which helices form and grow, do not affect the completely elastic behavior of helices under tension.

So far, we have

2.7 General Conclusions

In this chapter we described our initial effort in studying the formation and evolution of high, low, and intermediate pitch helical ribbons in quaternary sterol systems. We gave a full description of the formation pathways of helical ribbons, which are the precursors to cholesterol monohydrate crystal formation. The evolution of each helix pitch type was described separately and its relevance to the cholesterol crystallization was inferred.

We also determined that helices contain mostly cholesterol. Phospholipids are also an integral part of helix structure. We inferred that phospholipids coat helix surfaces and different pitch helices are coated by phospholipids to a different degree: high pitch helices are covered with more phospholipids than the low pitch structures. It is possible that the "amount" of phospholipids on helix surface reflects the differences in internal helix structure, i. e. high pitch helices are more hydrophobic than low pitch structures. However, more experiments need to be performed to confirm this hypothesis.

We have also shown that formation of helices of at least two pitch types (high and low) is not a property unique to "model bile" systems. Rather, it is a general phenomenon of a large variety of systems, quaternary sterol systems. These contain a micelle–forming surfactant(s), a bilayer–forming amphiphile(s), and a sterol. By changing any of the above components, we can now control the yield and the kinetics of the formation of each individual helix pitch type. This in turn makes the experimental study of the internal structure of each pitch type helices much easier, since we can now selectively produce large yields of helices of predominantly one pitch type.

Finally, we have shown qualitatively that axial forces can be applied to helices. By doing so we have observed that helices are completely elastic. Independent of the forces applied, they recover to their equilibrium. We have observed full elongation of helices and their full recovery. We have made one more important observation. Under tension, low pitch helical ribbons phase separate into a straight and helical parts when elongated beyond certain helix pitch angle. Though we discuss this novel phenomenon only from the qualitative point of view, it plays a very important role in helix behavior. The theoretical study of this phenomenon is now under way in the laboratory of Prof. Benedek at the Massachussetts Institute of Technology.

Chapter 3

Theoretical Models

3.1 Introduction

This chapter presents a new model describing the elastic free energy of helical ribbons after first describing the relevant existing theories. In Section 3.2.1, we present the historical background which demonstrates the necessity for the development of new theories of elasticity for helical ribbons and tubules. Section 3.2 describes two contemporary elastic theories of tubule and helix formation: Chung *et al.*'s[12] model is presented in Section 3.2.2 and Selinger *et al.*'s[18] model is introduced in Section 3.2.3). Though it is not the intent of this thesis to present the complete derivations of these models, we will nevertheless discuss the general features of each that are necessary for conceptual understanding and comparison to the new crystalline theory. In Section 3.3 we formulate the crystalline model of the existence of helical ribbons. This model is based on the theory of the elastic properties of crystals developed by Landau and Lifshitz.[37] Section 3.3.3 presents the areas in which this theory is consistent with the theories of Chung *et al.*'s[12] and Selinger *et al.*'s theories[18], and the areas and degree to which it is an improvement.

3.2 Previous Theories of Elasticity for Helical Ribbons

3.2.1 Historical Background for the Development of the Theories of Elasticity for Helical Ribbons

Prior to the formulation of the theories of elasticity of helical ribbons by Chung *et al.*[12] and Selinger *et al.*[18], three general approaches to the theory of tubule formation

had been made. Two of these theories are based on the formation of helical ribbons. First, de Gennes formulated a theory for the elastic properties of chiral and non-chiral smectic-C (SmC* and SmC, respectively) phases. Due to the lack of mirror reflection symmetry in the SmC* phase, this phase develops local ferroelectric features. De Gennes argued that the combination of the elastic and ferroelectric properties of the SmC* phase determines its macroscopic behavior, the most striking feature of which is the tendency for the local optical axis to form a helix, i. e., to precess in a helical fashion from layer to layer. The ferroelectric polarization of this phase also twists helically. In his book,[71] de Gennes analyzes the elastic free energy of a liquid crystal layer in the SmC phase. Then, he introduces chirality through the addition of a small amount of chiral solute. This approach results in a theory of elasticity for the SmC* phase. The chiral contribution to the elastic free energy is given by three terms, one of which "tends to transform a flat layer into a twisted ribbon"[71].

Later, de Gennes argued that if a bilayer of chiral molecules has in-plane order, then the edges of the bilayer become polarized.[72] This polarization develops in the direction perpendicular to the tilt direction. As a result, the electrostatic attraction between charges on the opposite edges of the bilayer induce buckling causing the narrow strip of bilayer membrane to form a cylinder.

Several authors have modified this original theory to describe helical windings resulting from electrostatic interactions.[73–75] These modifications predict a correlation of $\rho \propto l^{1/3}$ between the tubule radius ρ and its length l. In other words, the electrostatic interactions of the polarization charges on the edges of a ferroelectric bilayer ribbon contribute to the curvature in the tubules. Such interactions are strongly attenuated by dilute to moderate concentrations of dissolved electrolytes as well as water, suppressing the bilayer curvature. As a result, the tubule radius may vary as a function of the solvent electrolyte concentration, which screens electrostatic attractions. However, the experimental work of Chappell and Yager[73] shows little correlation between tubule radius and electrolyte concentration. It is only in the particular case of tubules composed of amphiphiles with charged head groups that this prediction holds.[75] These experimental findings suggest that electrostatic interactions do not play a dominant role in tubule formation.

Second, Lubensky and Prost developed a general phase diagram for bilayer membranes whose molecules have in-plane orientational order. These authors showed that the forces generating this molecular ordering "can favor a morphology change from a

sphere to a cylinder or to a torus" on a larger scale.[76] Their calculations are approximate in that they do not consider all possible shapes. They also neglect chirality in their calculations, which is an important characteristic of molecules in bilayer membranes. Nevertheless, their calculations are sufficient to show that orientational order is sufficient to cause the cylindrical shape to be an equilibrium topology for a bilayer membrane.

Lubensky–Prost's theory predicts that the cylinder dimensions are determined by a competition between the curvature and edge free energies. They predicted that the radius of a tubule scales with tubule length as $\rho \propto l^{1/2}$. These predictions do not compare well with experimental observations,[12,32] probably due to the neglect of properties such as chirality. It seems, therefore, that the competition between the curvature free energy and edge free energy is not enough to well describe tubule formation. This is the only theory of the three described in this section which does not relate the formation of tubules to the formation or existence of helical ribbons.

Third, in 1986 Helfrich proposed a simple elastic model to explain the formation of helical ribbons from a chiral bilayer membrane in a tilted phase.[77,78] This model employs the spontaneous torsion of the bilayer edges and the bending stiffness of the bilayer, leading to a universal pitch angle of 45° for a helical ribbon formed from an elastically isotropic ribbon. Two years later, Helfrich and Prost generalized this approach to describe bilayer membranes with anisotropic spontaneous curvature.[78] To make this generalization, the molecules in the bilayer membranes were allowed to be both tilted and chiral. Long chiral molecules do not pack parallel to each other in a bilayer membrane, but rather with a small twist angle with respect to their neighbors. This molecular twist from neighbor to neighbor causes the twist of the whole membrane into a helical ribbon or a cylinder. To refine their theory even further, Helfrich and Prost added a term linear in the surface curvature to their expression for the elastic free energy, thus explicitly allowing molecular chirality to enter their expression of the helix elastic free energy. However, the analysis of the pitch angle of helical ribbons was not made for anisotropic bilayers.

Several investigators have generalized the original Helfrich-Prost model in various ways. In 1990, Ou-Yang and Liu developed a version based on an analogy with cholesteric liquid crystals.[79] They modeled a helical ribbon as a layer of cholesteric liquid crystal and, as Helfrich and Prost, predicted the pitch angle of 45°. In 1991, Chappell and Yager considered a model in which the vector order parameter, de-

scribing the projection of the molecular tilt onto the plane of the bilayer, is defined by the direction of one–dimensional chains of molecules, rather than by the tilt of a single molecule.[80] One year later, Nelson and Powers further developed this theory by including the effects of thermal fluctuations on tubules via renormalization group theory.[81] Finally, in 1993, Selinger and Schnur presented a continuum theory, also based on the Helfrich-Prost model, for the self-assembly of cylindrical tubules from chiral lipid bilayers in any tilted fluid phase.[14] Selinger *et al.* further improved their theory in 1996 "to provide a more unified and systematic model of tubules and helical ribbons."[18]

The theory of Helfrich and Prost proved to be consistent with the experimental results from work with such materials as glutamic acid based amphiphiles with two hydrocarbon chains,[31,82–84] the monomer of a polymerizable lecithin containing a diacetylenic group half-way down each of its 23-carbon chains,[13] and others. However, in the case of the formation of helical ribbons in bile,[12] for example, this theory does not hold true: the experimentally observed helical ribbon structures have one of two distinctive pitch angles, 53.7° or 11.1°. One possible explanation for the discrepancy between the Helfrich–Prost prediction of a 45° helix pitch angle and the experimental findings described above is that Helfrich and Prost analyzed helical ribbons made of isotropic bilayers.[78] To correct this discrepancy and explain the phenomenon of formation of helices with pitch angles of 53.7° or 11.1°, Chung *et al.*[12] used the theory derived by de Gennes,[71] instead of generalizing the Helfrich-Prost model. They considered the elastic free energy associated with a small deformation of the SmC* layers, where they included the full elastic anisotropy of the chiral bilayer membrane. Using this model, Chung *et al.* related the pitch angle of helical ribbons and the optimal molecular phase angle of tubules to a ratio of membrane elastic constants.[12] It is important that the results of Selinger *et al.*[18], though derived in a different manner, are in exact agreement with the theory by Chung *et al.*[12]

In the following we will trace the footsteps of both Chung *et al.*[12] and Selinger *et al.*[18] in deriving expressions for the elastic free energy of anisotropic bilayer membranes of tilted chiral amphiphiles. Although we do not intend to present the full derivations, we will describe each theory separately showing the steps in the theoretical development and the assumptions made. We will then compare these two models and show how Selinger *et al.*[18] improved the apparent anomaly in the theory of Chung *et al.*,[12] which comprises of a prediction that for the low pitch helices the

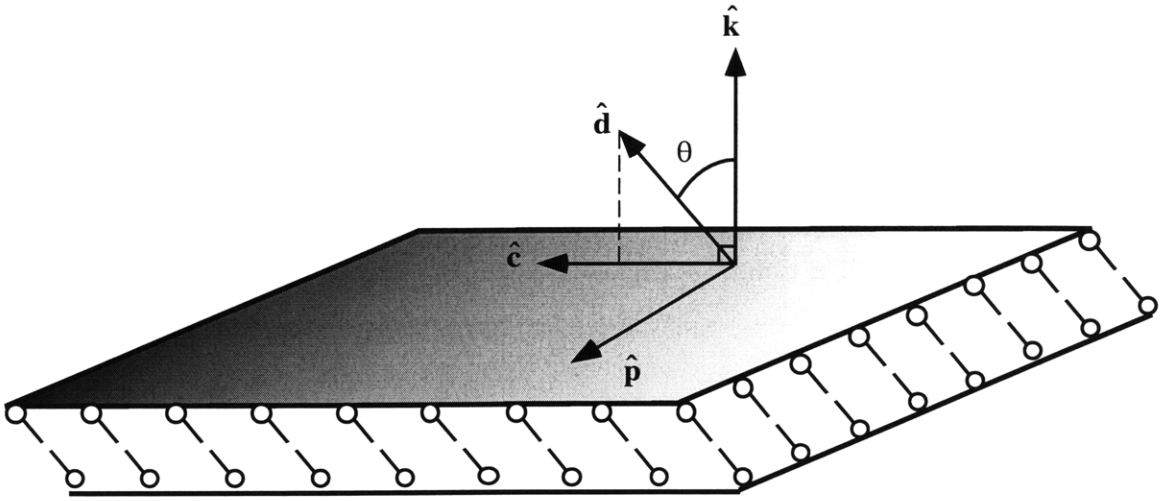

Figure 3.1: The local coordinate system of a symmetric tilted bilayer determined by the two unit vectors $\hat{\mathbf{k}}$ and $\hat{\mathbf{c}}$. Unit vector $\hat{\mathbf{k}}$ lies along the direction perpendicular to the bilayer plane; unit vector $\hat{\mathbf{c}}$ lies along the projection of the molecular tilt, $\hat{\mathbf{d}}$, onto the ribbon plane. The direction of molecular tilt $\hat{\mathbf{d}}$ forms an angle θ with the normal to the bilayer plane $\hat{\mathbf{k}}$.

energy cost of bending the bilayer membrane in the direction perpendicular to the molecular tilt is 700 times greater than that of bending the bilayer membrane parallel to the molecular tilt. Finally, we will explain why, if developed further, Chung *et al.*'s theory[12] could not only improve on its own predictions but be a better approximation to reality than Selinger *et al.*'s model.[18]

3.2.2 Theory for the Elastic Free Energy and the Shape of Tubules and Helical Ribbons Developed by Chung *et al.*[a]

I would like to thank Dr. Chung for helpful discussions regarding theoretical work and for his support in the first stages of development of the experimental work presented.

In their model, Chung *et al.* consider n symmetric bilayers of tilted chiral amphiphiles with a uniform tilt direction in each layer. These bilayers are assumed to have the same local structure as chiral tilted layers of liquid crystals in the SmC* phase (Fig. 3.1). Therefore, the theory of SmC* layers derived by de Gennes becomes the basis of the model by Chung *et al.*

[a]In what follows, we will use the superscript C to denote Chung *et al.*'s theory.[12]

In his book, de Gennes formulated an expression for the elastic free energy associated with small deformations of SmC* layers.[71] The analysis is performed in an ingenious way: the deformations are described in terms of small rotations, Ω_i's, of the local reference frame around the spatial axes, where the magnitude of rotation is Ω_i and the rotation axis is the i-axis. Then, the expression for the elastic free energy associated with a deformation of the SmC* layer can be given in terms of spatial derivatives of the Ω_i's. Expressions derived in this way, however, are not very intuitive. This difficulty arises because to analyze a deformed configuration, one must find a local frame of reference to describe each point and its surroundings. Though physically satisfying, these expressions are rather troublesome to handle.

In 1984, Dahl and Lagerwall proposed a reformulation of de Gennes' theory for "soft" deformations[b] in terms of three unit vectors $\hat{\mathbf{k}}, \hat{\mathbf{c}}$, and $\hat{\mathbf{p}} = \hat{\mathbf{k}} \times \hat{\mathbf{c}}$.[85] In this notation, $\hat{\mathbf{k}}$ is in a direction normal to the ribbon plane; $\hat{\mathbf{c}}$ is the "c-director", i.e. the unit vector parallel to the projection of the molecular tilt, $\hat{\mathbf{d}}$, onto the ribbon plane (Fig. 3.1). Using the Dahl-Lagerwall reformulation, de Gennes' expression for the elastic free energy per unit area of a SmC* layer can be expressed as

$$\mathbf{a^C} = \mathbf{a^C}_{\mathrm{k}} + \mathbf{a^C}_{\mathrm{c}} + \mathbf{a^C}_{\mathrm{kc}} + \mathbf{a^C}_{\mathrm{chiral}}, \tag{3.1}$$

and

$$\begin{aligned}
\mathbf{a^C}_{\mathrm{k}} &= \frac{A_{12}}{2}\left[\hat{c}\cdot\left(\vec{\nabla}\hat{k}\right)\cdot\hat{c}\right]^2 + \frac{A_{21}}{2}\left[\hat{p}\cdot\left(\vec{\nabla}\hat{k}\right)\cdot\hat{p}\right]^2 + \frac{A_{11}}{2}\left[\hat{c}\cdot\left(\vec{\nabla}\hat{k}\right)\cdot\hat{p}\right]^2, \\
\mathbf{a^C}_{\mathrm{c}} &= \frac{B_1}{2}\left[\hat{k}\cdot\left(\vec{\nabla}\times\hat{c}\right)\right]^2 + \frac{B_2}{2}\left[\vec{\nabla}\cdot\hat{c}\right]^2 + \frac{B_3}{2}\left\{\hat{c}\cdot\left[\vec{\nabla}\times\hat{c}\left(\vec{\nabla}\hat{k}\right)\cdot\hat{p}\right]\right\}^2 \\
&\quad -B_{13}\left[\hat{k}\cdot\left(\vec{\nabla}\times\hat{c}\right)\right]\left\{\hat{c}\cdot\left[\vec{\nabla}\times\hat{c}+\left(\vec{\nabla}\hat{k}\right)\cdot\hat{p}\right]\right\}^2, \\
\mathbf{a^C}_{\mathrm{kc}} &= -C_1\left[\hat{c}\cdot\left(\vec{\nabla}\hat{k}\right)\cdot\hat{p}\right]\left[\hat{k}\cdot\left(\vec{\nabla}\times\hat{c}\right)\right] - C_2\left[\hat{p}\cdot\left(\vec{\nabla}\hat{k}\right)\cdot\hat{p}\right]\left(\vec{\nabla}\hat{c}\right), \\
\mathbf{a^C}_{\mathrm{chiral}} &= -D\hat{c}\cdot\left[\vec{\nabla}\times\hat{c}+\left(\vec{\nabla}\hat{k}\right)\cdot\hat{p}\right] + D_1\hat{k}\cdot\left(\vec{\nabla}\times\hat{c}\right) - D_2\hat{c}\cdot\left(\vec{\nabla}\hat{k}\right)\cdot\hat{p}.
\end{aligned} \tag{3.2}$$

In these equations, A, B, C, and D are phenomenological elastic moduli integrated over the ribbon thickness. Now, consider each expression in Eq. (3.2), i.e. each term in Eq. (3.1), starting with non-chiral contribution.

$\mathbf{a^C}_{\mathrm{k}}$ describes the free energy per unit area associated with splay deformations in the shape of a smectic layer.[71] In this notation, zero energy is attributed to the flat state of a bilayer membrane.[78] The A_{12}, A_{21}, A_{11} terms must be positive to

[b] "Soft" deformations are purely elastic, locally small deformations, which involve no stretching of a material.

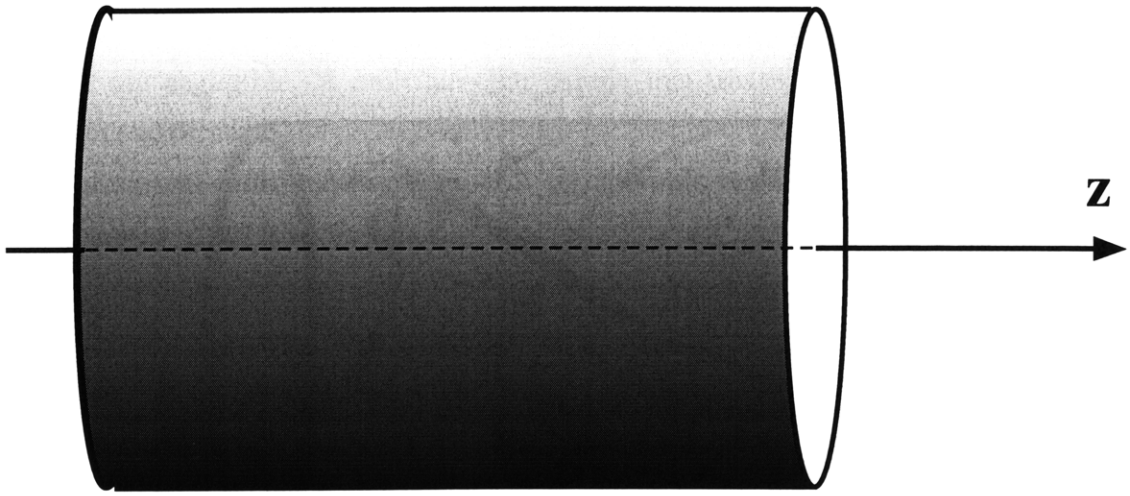

Figure 3.2: "Jelly-roll" model of chiral membranes.

satisfy the condition that the undistorted (flat) membrane conformation corresponds to the minimum of free energy.[71] The quadratic terms in $\left(\vec{\nabla}\hat{\mathbf{k}}\right)$, that are associated with A_{12}, A_{21}, and A_{11}, measure non-planarity of the bilayer membrane, since they correspond to the quadratic values of the spontaneous curvatures in $\hat{\mathbf{c}}$ and $\hat{\mathbf{p}}$ directions and to the Gaussian curvature[c], respectively. These coefficients also affect the C–director if the layers are bent.

$\mathbf{a}^{\mathbf{C}}{}_{\mathrm{c}}$ corresponds to deformations of the C–director within layer. The first two terms can be interpreted as the bend and the splay of the C–director, respectively. B_3 corresponds to the twist of C–director between adjacent layers. The B_{13} term couples the bend of $\hat{\mathbf{c}}$ within the layer to the twist of $\hat{\mathbf{c}}$ between the layers.

$\mathbf{a}^{\mathbf{C}}{}_{\mathrm{kc}}$ is the last non-chiral term in Eq. (3.1), which describes the coupling between the deformations of $\hat{\mathbf{c}}$ and the allowed deformations of the layer shapes, i. e. deformations of $\hat{\mathbf{k}}$.

The chiral term in the expression for the elastic free energy (Eq. (3.1)) contains three terms linear in $\left(\vec{\nabla}\hat{\mathbf{k}}\right)$ and $\left(\vec{\nabla}\times\hat{\mathbf{c}}\right)$. The D term is a typical twist term, causing the helicoidal arrangement of SmC* layer. The D_1 term forces the bend of the C–

[c]Gaussian curvature is the product of the two spontaneous curvatures. In this case, if we denote the spontaneous curvature in the $\hat{\mathbf{c}}$ direction as c and that in the $\hat{\mathbf{p}}$ direction as p, then the Gaussian curvature is equal to $c\ p$. As it is the product of two spontaneous curvatures, Gaussian curvature has units of ordinary curvature squared.

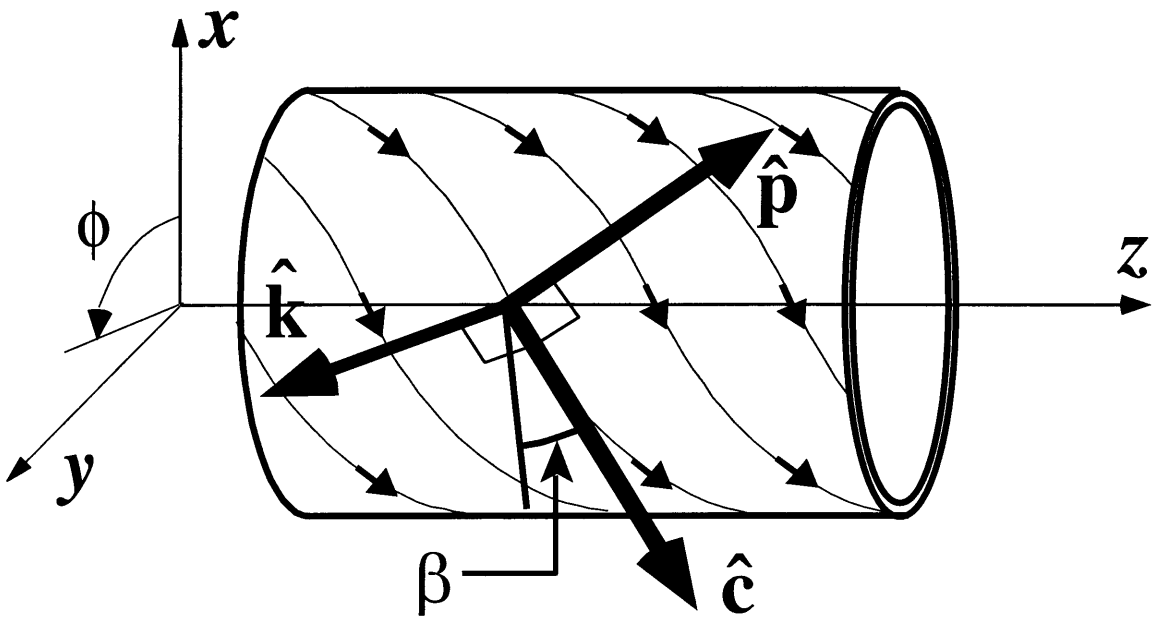

Figure 3.3: The local coordinate system of a tubule that is composed of a layer of tilted chiral molecules. The direction of $\hat{\mathbf{c}}$ is shown by the helical lines and arrows.

director to be constant. The effect of the D_2 term is to couple the C–director to the layer bend. More precisely, the D_2 term is equivalent to the square root of the Gaussian curvature A_{11} term in $\mathbf{a}^{\mathbf{C}}{}_{\mathrm{k}}$. Therefore, the two terms D_2 and A_{11} compete in their contribution to the total free energy density $\mathbf{a}$ in Eq. (3.1). The consequence of this competition can be recognized in the limit that the membrane curvatures are large. In particular, if the SmC* layers are arranged in a "jelly-roll" fashion, as shown in Fig. 3.2, then far from the central axis, $\hat{\mathbf{z}}$, the linear D_2 term will dominate over the $A_{11}, A_{12}, \text{and} A_{21}$ terms in $\mathbf{a}$, which are of the second order in the layer curvature. Additionally, if the molecules are arranged within a layer at a constant tilt angle θ to the $\hat{\mathbf{k}}$ direction (Fig. 3.1), then C–director $\hat{\mathbf{c}}$ aligns at an angle $\pm\beta^C$ in the local tangent plane between the tilt direction and the equator of the cylinder, the sign of this angle being dependent on the sign of D_2. As a result, the C–director is arranged in a pattern of helical windings aligned at a pitch angle of $\pm\beta^C$ (Fig. 3.3).

Based on this information, Chung *et al.*[12] constructed expressions for the elastic free energy of the bilayer membranes composed of tilted chiral molecules, with membranes arranged in geometrical shapes such as a cylinder (tubule) and a helix. They started by developing an expression for the elastic free energy of a tubule, which has the same structure as a helical ribbon but lacks the edges of a helical ribbon. The

assumption made here was that variations of molecular arrangement from bilayer to bilayer are negligible. A multilamellar tubule was treated as a single–bilayer tubule with an elastic constant dependent on the number of constituent bilayers, n. Then, in the cylindrical coordinate system (ρ, ϕ, z), the unit vectors $\hat{\mathbf{k}}, \hat{\mathbf{c}}$, and $\hat{\mathbf{p}}$ of the tubule are given by (Fig. 3.3)

$$\begin{aligned} \hat{\mathbf{k}} &= \hat{\rho} \\ \hat{\mathbf{c}} &= \hat{\phi}\cos\beta^C + \hat{\mathbf{z}}\sin\beta^C \\ \hat{\mathbf{p}} &= \hat{\mathbf{k}} \times \hat{\mathbf{c}} = -\hat{\phi}\sin\beta^C + \hat{\mathbf{z}}\cos\beta^C, \end{aligned} \tag{3.3}$$

where $\beta^C = \text{const}$ is the molecular tilt angle, as described above.

Using expression Eq. (3.1) to describe the elastic free energy per unit area of a ribbon with a uniform tilt of the C–director $\pm\beta^C$, Chung *et al.* established that

$$\mathbf{a^C} = \mathbf{a^C}_{\text{bilayer}}. \tag{3.4}$$

With β^C constant in the expression for $\mathbf{a^C}_{\text{c}}$ and $\mathbf{a^C}_{\text{chiral}}$, one obtains

$$\left[\vec{\nabla} \times \hat{\mathbf{c}} + \left(\vec{\nabla}\hat{\mathbf{k}}\right) \cdot \hat{\mathbf{p}}\right] = 0. \tag{3.5}$$

This implies that for β^C unchanged from layer to layer, the term $\left(\vec{\nabla} \times \hat{\mathbf{c}}\right)$ compensates for $\left(\vec{\nabla}\hat{\mathbf{k}}\right) \cdot \left(\hat{\mathbf{k}} \times \hat{\mathbf{c}}\right) = \left(\vec{\nabla}\hat{\mathbf{k}}\right) \cdot \hat{\mathbf{p}}$ for any deformation, i.e. $\partial\beta^C/\partial z = 0$. To obtain an expression for the free energy in Eq. (3.1), we use

$$\vec{\nabla} \times \hat{\mathbf{c}} = \frac{1}{\rho}\frac{\partial}{\partial\theta}\sin\beta^C - \frac{\partial}{\partial z}\cos\beta^C \tag{3.6}$$

and

$$\vec{\nabla} \cdot \hat{\mathbf{c}} = \frac{1}{\rho}\frac{\partial}{\partial\theta}\cos\beta^C + \frac{\partial}{z}\sin\beta^C. \tag{3.7}$$

Chung *et al.* further made the following substitutions:

$$K_n^{cc} = A_{12},\ K_n^{pp} = A_{21},\ K_n^{cp} = \frac{A_{11}}{2},\ \text{and}\ K_n^{*} = D_2, \tag{3.8}$$

where n denotes the dependence of the elastic constants on the number of bilayers. Further substitution of Eqs. 3.3 – 3.8 into Eq. (3.1) and Eq. (3.2) results in the following expression for the elastic free energy per unit area of a tubule:

$$\mathbf{a^C}_{\text{tubule}} = \frac{K_n^{cc}\cos^4\beta^C + K_n^{pp}\sin^4\beta^C + (K_n^{cp}/2)\sin^2 2\beta^C}{2R^2} - \frac{K_n^{*}\sin 2\beta^C}{2R}. \tag{3.9}$$

From Eq. (3.8) it is clear that the K_n^{cc} and K_n^{pp} terms correspond to the bending of the layer along the $\hat{\mathbf{c}}$ and $\hat{\mathbf{p}}$ directions, respectively. The K_n^{cp} term represents the twist of the coordinate system in the $\hat{\mathbf{c}} - \hat{\mathbf{p}}$ plane. The last term, K_n^*, corresponds to the anisotropic bending due to the molecular chirality. For non-chiral layers this term vanishes due to mirror symmetries which make the $\hat{\mathbf{p}}$ and $-\hat{\mathbf{p}}$ directions equivalent.

It is interesting to note that Eq. (3.9) is equivalent to the expression for the bending free energy per unit area of a bilayer obtained by Helfrich and Prost.[78] Their expression for the bending free energy per unit area of a chiral tilted monolayer is given by

$$\begin{aligned} \mathbf{a^{HP}} &= \frac{1}{2}\kappa_{cc}\left(\hat{\mathbf{c}}\cdot\vec{\nabla}\hat{\mathbf{k}}\cdot\hat{\mathbf{c}}\right)^2 + \frac{1}{2}\kappa_{pp}\left(\hat{\mathbf{p}}\cdot\vec{\nabla}\hat{\mathbf{k}}\cdot\hat{\mathbf{p}}\right)^2 \\ &\quad +\kappa_{cp}\left(\hat{\mathbf{c}}\cdot\vec{\nabla}\hat{\mathbf{k}}\cdot\hat{\mathbf{p}}\right)^2 + \bar{\kappa}\left[\left(\mathrm{Tr}\ \vec{\nabla}\hat{\mathbf{k}}\right)^2 - \mathrm{Tr}\ \left(\vec{\nabla}\hat{\mathbf{k}}\right)^2\right] \\ &\quad -\kappa_c\left(\hat{\mathbf{c}}\cdot\vec{\nabla}\hat{\mathbf{k}}\cdot\hat{\mathbf{c}}\right) - \kappa_p\left(\hat{\mathbf{p}}\cdot\vec{\nabla}\hat{\mathbf{k}}\cdot\hat{\mathbf{p}}\right) - \kappa^*\left(\hat{\mathbf{c}}\cdot\vec{\nabla}\hat{\mathbf{k}}\cdot\hat{\mathbf{p}}\right), \end{aligned} \tag{3.10}$$

where the superscript HP stands for Helfrich–Prost model. The expression in Eq. (3.10) becomes equal to Eq. (3.9) when the following notation of Chung *et al.* is used:

$$\kappa_{cc} = A_{12} = K_n^{cc},\ \kappa_{pp} = A_{21} = K_n^{pp},\ \kappa_{cp} = \frac{A_{11}}{2} = K_n^{cp},\ \text{and}\ \kappa^* = D_2 = K_n^*. \tag{3.11}$$

For tubules made of chiral tilted bilayers, Chung *et al.* also have

$$\left[\left(\mathrm{Tr}\vec{\nabla}\hat{\mathbf{k}}\right)^2 - \mathrm{Tr}\left(\vec{\nabla}\hat{\mathbf{k}}\right)^2\right] = 0, \tag{3.12}$$

and

$$\left(\hat{\mathbf{c}}\cdot\vec{\nabla}\hat{\mathbf{k}}\cdot\hat{\mathbf{c}}\right) = \left(\hat{\mathbf{p}}\cdot\hat{\mathbf{k}}\cdot\hat{\mathbf{p}}\right) = 0. \tag{3.13}$$

That is the $\bar{\kappa}$, κ_c, and κ_p terms vanish in Chung *et al.*' theory. This can be understood as follows. The Gaussian curvature term in Eq. (3.10) proportional to $\bar{\kappa}$ vanishes, as shown in Eq. (3.12), because it is a product of two principal curvatures, one of which is zero for a tubule. The first two linear terms in Eq. (3.10) also vanish, as shown in Eq. (3.13), because for two equal amphiphilic monolayers, which are combined to form a bilayer, both $\hat{\mathbf{c}}$ and $\hat{\mathbf{p}}$ change sign as one reverses $\hat{\mathbf{k}}$. Here, analogous to the theory of Chung *et al.*, the assumption is made that the tilted molecules are equally aligned in both monolayers.

Chung *et al.* found the optimal geometry of a tubule by simultaneously minimizing the elastic free energy in Eq. (3.9) with respect to the radius and the tilt angle of the molecules in the bilayers

$$\partial\mathbf{a}^{\mathbf{C}}{}_{\mathrm{tubule}}/\partial R = \partial\mathbf{a}^{\mathbf{C}}{}_{\mathrm{tubule}}/\partial\beta^C = 0, \tag{3.14}$$

and

$$\begin{aligned} \partial^2 \mathbf{a}^{\mathbf{C}}{}_{\text{tubule}}/\partial R^2 &> 0, \\ \partial^2 \mathbf{a}^{\mathbf{C}}{}_{\text{tubule}}/\partial (\beta^C)^2 &> 0. \end{aligned} \tag{3.15}$$

To obtain the minima conditions from Eq. (3.14), the assumption is made that the four elastic moduli in Eq. (3.9), K_n^{cc}, K_n^{pp}, and K_n^{cp}, are independent of tubule radius R and angle β^C in the local tangent plane between the tilt direction and the equator of the tubule. Eq. (3.14) then reduces to the following stability conditions:

$$RK_n^* = K_n^{cc} \cos^3 \beta^C \csc \beta^C + K_n^{pp} \sin^3 \beta^C \sec \beta^C + K_n^{cp} \sin 2\beta^C \tag{3.16}$$

and

$$RK_n^* = -K_n^{cc} \cos^2 \beta^C \tan 2\beta^C + K_n^{pp} \sin^2 \beta^C \tan 2\beta^C + K_n^{cp} \sin 2\beta^C. \tag{3.17}$$

It can be seen that the combination of Eq. (3.16) and Eq. (3.17) produces the remarkable relation:

$$\tan^4 \beta^C = K_n^{cc}/K_n^{pp}. \tag{3.18}$$

Eq. (3.18) implies that the molecular tilt direction β^C is independent of the elastic moduli K_n^{cp} and K_n^*, but is entirely dependent on the ratio of the remaining two elastic moduli. This is the ratio of the stiffness, K_n^{cc}, of the bilayer to bends parallel to the molecular tilt direction to the stiffness, K_n^{pp}, of the bilayer to bends perpendicular to the molecular tilt direction. For an isotropic membrane where $K_n^{cc} = K_n^{pp}$, the molecular tilt direction corresponds to the angle $\beta^C = 45°$, which is precisely the result obtained by Helfrich and Prost.[77,78] In an anisotropic membrane, K_n^{cc} maybe greater than K_n^{pp} (bending along the C–director is more difficult than along the $\hat{\mathbf{p}}$ direction) or less than (bending along C–director is easier); hence β^C maybe greater or less than 45°.

Now, by substituting Eq. (3.18) into Eq. (3.16), and employing the definition $\bar{K_n} = (K_n^{cp} + \sqrt{K_n^{cc} K_n^{pp}})/2$, Chung *et al.* obtain the for the equilibrium radius of the tubule:

$$R_n^{tubule} = 2\frac{\bar{K_n}}{K_n^*} \sin 2\beta^C. \tag{3.19}$$

This result implies that the radius R of the tubule scales inversely proportionally to the chirality parameter, K_n^*. In a nonchiral membrane, $K_n^* \to 0$, and the radius $R \to$

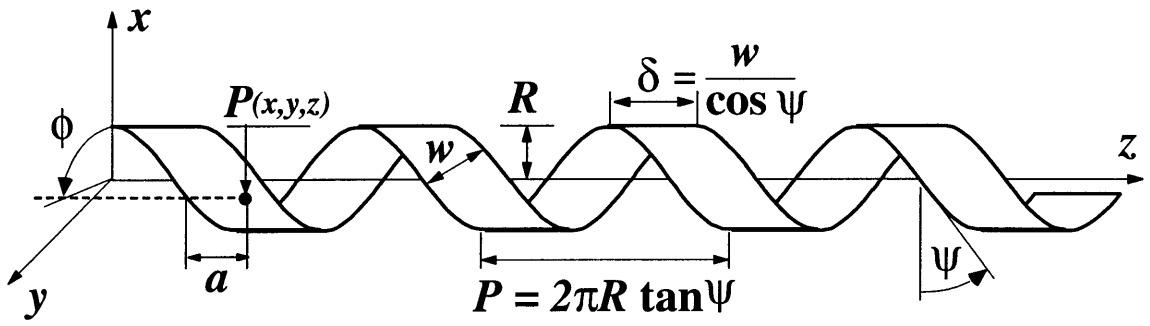

Figure 3.4: Geometry of a helical ribbon. R is the radius, ψ is the pitch angle, P is the pitch length, w is the ribbon width, δ is the width of ribbon along the z-axis, $P(x, y, z)$ is the position of a point P on the surface of a helical ribbon, a is the distance from the edge of the ribbon to the point P along the z-axis, and ϕ is the azimuthal angle at which the point P is located.

∞, i. e. a flat plate is formed. Substituting Eq. (3.18) and Eq. (3.19) into Eq. (3.9), the minimum elastic free energy per unit area of the tubule is

$$\mathbf{a}_{tubule}^{min} = -K^{*2}_{n} / \left(8\bar{K}_{n}\right). \tag{3.20}$$

Next, Chung *et al.* showed that similar derivations can be made to calculate the elastic free energy and the equilibrium geometrical shape of a helical ribbon. Chung *et al.* constructed their ribbon by cutting a parallel strip out of a tubule along a constant helical pitch angle ψ. Figure 3.4) describes the geometrical quantities necessary to describe the surface of a right–handed helical ribbon. A point on this surface can be described as follows:

$$P(x, y, z) = \left(R\cos\phi, R\sin\phi, R\phi\tan\psi + a\right), 0 \leq a \leq \delta = w/\cos\psi \tag{3.21}$$

and, in addition to the assumption that the tilt direction β^C is uniform everywhere on the membrane, another assumption is made that the helical strip is cut parallel to the direction of the molecular tilt, i.e. $\beta^C = \psi$. Since the ribbon edges are exposed to the surrounding aqueous medium at the expense of some free energy, an additional elastic free energy term, $\mathbf{a}^{\mathbf{C}}{}_{\text{edge}}$, must be added to the expression for the free energy to obtain an expression for the total free energy per unit area of a helical ribbon:

$$\mathbf{a}^{\mathbf{C}}{}_{\text{helix}} = \mathbf{a}^{\mathbf{C}}{}_{\text{tubule}} + \mathbf{a}^{\mathbf{C}}{}_{\text{edge}}. \tag{3.22}$$

Like Helfrich,[77] Chung *et al.* employed the results of Bugl and Fujita[86] to obtain

$\mathbf{a}^{\mathbf{C}}{}_{\text{edge}}$ and discovered that the curvature of the ribbon does not contribute to $\mathbf{a}^{\mathbf{C}}{}_{\text{edge}}$.[d] It is, however, completely described by the torsion τ of the two edges of a helical ribbon of width w as follows

$$\mathbf{a}^{\mathbf{C}}{}_{\text{edge}} = \left[\frac{\Lambda_n}{2}\left(\tau - \tau_n^0\right)^2 + \gamma_0\right]\frac{2l}{lw} = \frac{\Lambda_n}{w}\left(\tau - \tau_0\right)^2 + \frac{2\gamma_0}{w}, \tag{3.23}$$

where l is the ribbon contour length, Λ_n is the torsional rigidity integrated over the ribbon thickness, $\tau = \cos\psi \sin\psi / R$ and τ_n^0 are the torsion and the spontaneous torsion of the ribbon edge, and $\gamma_0 = \gamma_{\text{curve}}(\kappa_0, \tau_0)$ is the free energy per unit length of a curved edge with the spontaneous curvature κ_0 and torsion τ_0. Then, $\mathbf{a}^{\mathbf{C}}{}_{\text{helix}}$ in Eq. (3.22) becomes

$$\begin{aligned}\mathbf{a}^{\mathbf{C}}{}_{\text{helix}} &= \frac{K_n^{cc}\cos^4\psi + K_n^{pp}\sin^4\psi + (K_n^{cp}/2)\sin^2 2\psi}{2R^2} - \frac{K_n^*\sin 2\psi}{2R} \\ &+ \frac{\Lambda_n}{w}\left(\frac{\sin 2\psi}{2R} - \tau_n^0\right)^2 + \frac{2\gamma_0}{w},\end{aligned} \tag{3.24}$$

where the condition $\mathbf{a}^{\mathbf{C}}{}_{\text{helix}} = 0$ corresponds to an infinitely wide planar strip.

Proceeding as in the case of a tubule, the condition for the equilibrium geometrical configuration of a helical ribbon is given by

$$\partial \mathbf{a}^{\mathbf{C}}{}_{\text{helix}}/\partial R = \partial \mathbf{a}^{\mathbf{C}}{}_{\text{helix}}/\partial \psi = 0, \tag{3.25}$$

and

$$\begin{aligned}\partial^2 \mathbf{a}^{\mathbf{C}}{}_{\text{helix}}/\partial R^2 &> 0, \\ \partial^2 \mathbf{a}^{\mathbf{C}}{}_{\text{helix}}/\partial \psi^2 &> 0.\end{aligned} \tag{3.26}$$

Performing the differentiation, again assuming that elastic moduli are independent of R and ψ, one obtains

$$\begin{aligned}R\left(K_n^* w + 2\Lambda_n \tau_n^0\right) &= \left(K_n^{cc}\cos^3\psi\csc\psi + K_n^{pp}\sin^3\psi\sec\psi\right. \\ &+ \left. K_n^{cp}\sin 2\psi\right) w + \Lambda_n \sin 2\psi\end{aligned} \tag{3.27}$$

and

$$\begin{aligned}R\left(K_n^* w + 2\Lambda_n \tau_n^0\right) &= \left(-K_n^{cc}\cos^2\psi\tan 2\psi + K_n^{pp}\sin^2\psi\tan 2\psi\right. \\ &+ \left. K_n^{cp}\sin 2\psi\right) w + \Lambda_n \sin 2\psi.\end{aligned} \tag{3.28}$$

[d]The inclusion of the edge curvature term to the elastic free energy density results in a change in helix pitch angle as a function of ribbon width. Since experimentally this dependence of pitch angle on helix width did not occur, Chung *et al.* considered the magnitude of the curvature term negligible in comparison to the torsion term.

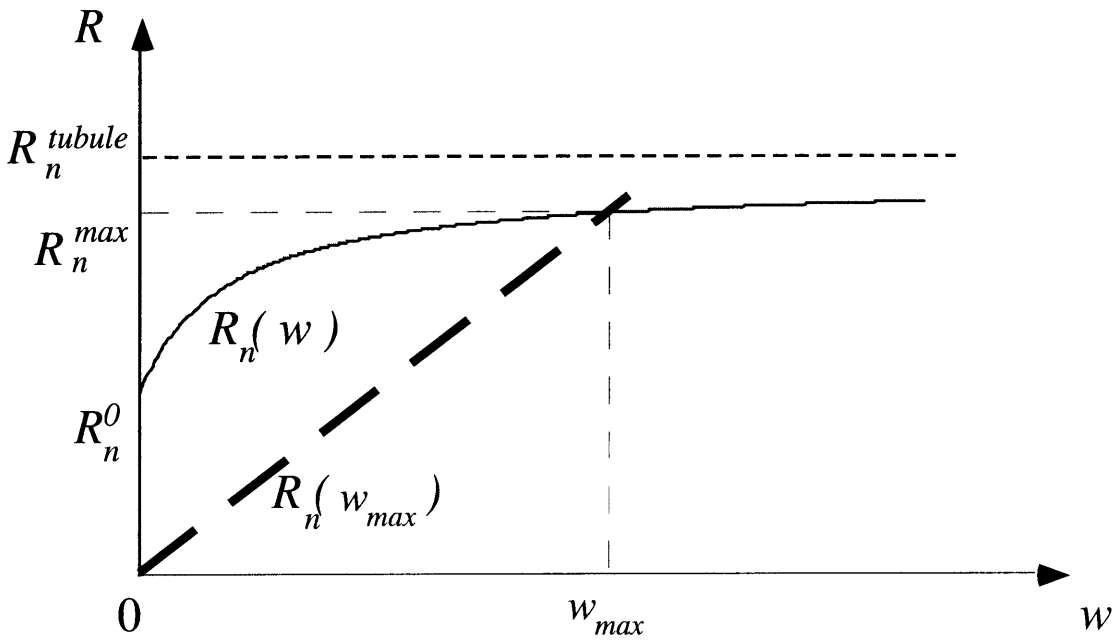

Figure 3.5: Theoretical form of radius versus width relationship for the helical ribbons. $R_n(w_{max})$ is shown as a dashed line and $R_n(w)$, calculated from Eq. (3.30), is shown as a solid line. These two lines intersect at the maximum radius attained by tubules grown from helical ribbons, R_n^{max}.

Combining Eq. (3.27) and Eq. (3.28), one can obtain a result for an equilibrium pitch angle of helical ribbons, this result being similar to that of tubules in Eq. (3.18):

$$\tan^4 \psi_0^C = K_n^{cc}/K_n^{pp} \tag{3.29}$$

The two implications of Eq. (3.29) are the same as those of Eq. (3.18). First, the pitch angle of a helical ribbon is independent of all elastic moduli except for K_n^{cc} and K_n^{pp}. It is also independent of the ribbon width w, torsional rigidity Λ_n, and the spontaneous torsion of the edges τ_n^0. Second, regardless of the edges, the helical pitch angle is equal to the molecular tilt angle $\psi = \beta^C$.

Substituting Eq. (3.29) into Eq. (3.27), it is easy to obtain an expression for the optimal radius $R_n(w)$ of an n-bilayer helical ribbon:

$$R_n(w) = \frac{\sin 2\psi}{2\tau_n^0}\left[1 + \frac{\left[4\tau_n^0\left(\bar{K}_n/K_n^*\right) - 1\right]w}{2\tau_n^0\left(\Lambda_n/K_n^*\right) + w}\right] = R_n^0 + \frac{\left(R_n^{tubule} - R_n^0\right)w}{w + 2\left(\Lambda_n/K_n^*\right)\tau_n^0}, \tag{3.30}$$

where $R_n^0 = \sin\psi\cos\psi/\tau_n^0$ is the radius of an n-bilayer helix in the limit of $w \to 0$, and R_n^{tubule} is given by Eq. (3.19). It is important to note that the maximum ribbon width occurs when two of its edges merge, i. e. when $\delta = \mathrm{P}$ in Figure 3.4. Therefore, for

the plot of $R_n(w)$ versus w, no points should lie below the line $R_n(w_{max}) = R_n(\delta) = R_n(P) = w_{max}/2\pi \sin\psi$ since Chung *et al.* assume that the ribbon width can only grow until the two ribbon edges merge. Figure 3.5 presents a theoretical form for the radius versus width relationship, where $R_n(w_{max})$ is shown as a dashed line and $R_n(w)$ calculated from Eq. (3.30) is shown as a solid line. Chung *et al.* predict that a tubule grown from a helical ribbon by increasing ribbon's width also increases in its radius from R_0^n at $w \to 0$ to the radius R_n^{max} at $w = w_{max}$; this is represented by the intersection between the lines $R_n(w)$ and $R_n(w_{max})$.

By inserting Eq. (3.29) and Eq. (3.30) into Eq. (4.13), one obtains the dependence of the optimal elastic free energy of a helical ribbon on its width:

$$\begin{aligned} \mathbf{a}_{helix}^{min}(w) &= -\frac{K_n^{*2}}{8\bar{K}_n} + \frac{\Lambda_n\left(K_n^* - 4\bar{K}_n\tau_n^0\right)^2}{8\bar{K}_n\left(2\bar{K}_n w + \Lambda_n\right)} + \frac{2\gamma_0}{w} \\ &= \mathbf{a}_{tubule}^{min}\left\{1 + \left[\frac{R_n^{tubule}}{R_n(w)} - 1\right]^2\right\} + \mathbf{a}_{edge}^{C}. \end{aligned} \tag{3.31}$$

From Eq. (3.31), it can be inferred that increasing the width of a helical ribbon to the point where it becomes a tubule must decrease its elastic free energy. It is also clear that $\mathbf{a}_{helix}^{min}$ decreases monotonically as w increases. When w reaches its maximum value w_{max}, $\mathbf{a}_{helix}^{min}$ loses an energy $\mathbf{a}_{edge}^{C}$ due to the edges; however, it is still larger than the minimum value, $\mathbf{a}_{tubule}^{C}$, by the amount $\Delta\mathbf{a} = |\mathbf{a}_{tubule}^{min}|\left(R_n^{tubule}/R_n^{max} - 1\right)^2$, as can be seen from Eq. (3.31). Hence, a tubule that is grown from a helical ribbon by increasing its width, can have a lower free energy if its radius can be expanded to the value of R_n^{tubule}. This implies that a cylindrically grown tubule possesses the lowest elastic free energy, i. e. the tubule is the equilibrium configuration.

It is instructive to conclude this section with a discussion of the deviation of Chung *et al.*'s model from the experimental observations. First, the calculated ratios of the phenomenological elastic moduli K_{cc} and K_{pp} for high and low pitch helical ribbons, respectively, are

$$\begin{aligned} K_n^{cc}/K_n^{pp}\,|_{53.7^\circ} &= 3.4 \\ K_n^{cc}/K_n^{pp}\,|_{11.1^\circ} &= 1.5 \times 10^{-3}. \end{aligned} \tag{3.32}$$

While the first result appears reasonable, the second value is quite surprising. Even the ratio of the elastic modulus of steel to that of the rubber would not yield such a low value. It seems very unreasonable that for the low pitch helices the membrane

is almost 700 times more more stiff to bends in the direction perpendicular to the molecular tilt ($\hat{\mathbf{k}}$) than it is in the direction parallel to the molecular tilt ($\hat{\mathbf{c}}$). Second, Chung *et al.* made the assumption that helically grown tubules are formed by ribbons growing in width until a merging of the edges occurs. However, in the latest experiments we have observed that ribbon edges often grow beyond maximum width w_{max} as one edge of the ribbon is subducted underneath another as described in Chapter 2. The Chung *et al.*'s model does not take into account the experimental observation that the subduction of one edge by another can occur. Therefore, there are points on the plot of $R_n(w)$ versus w that lie below the line $R_n(w_{max})$, which was not permitted by the assumptions upon which Chung *et al.*'s theory is based. Third, the helically grown tubules always have a higher free energy density than cylindrically grown tubules, the latter possessing the equilibrium configuration, i. e. the lowest elastic free energy density. It would be reasonable to expect large yield of these structures in comparison to the helically grown tubules. However, the yield of cylindrically grown tubules observed experimentally was negligible; rather, we observed very large yields of tubules with helical markings, in contrast to the predictions of Chung *et al.* (Due to the very low yield, we did not discuss cylindrically grown tubules in Chapter 2 as metastable intermediates in the process of cholesterol crystallization.) Fourth, the radius versus width relationship predicted by Chung *et al.*'s model, $R_n(w)$, was carefully studied for a large variety of high and low pitch helical ribbons. The processes of helical ribbon growth and dissolution were followed for each structure individually (data not shown). Our results do not support the prediction that the data can be grouped into sequences of curves $R_n(w)$ whose radii R_n^{tubule} increase asymptotically with ribbon thicknesses. Finally, our observation that right- and left-handed helical ribbons of high ($\sim 54°$) and low ($\sim 11°$) pitch angle form in a large variety of quaternary sterol systems, as described in Chapter 2, calls Chung *et al.* theory into question: it is very unlikely that the same two (or more) molecular packings occur for each of the diverse molecular species in the various systems, so that the helical ribbons of the same high and low pitch angles resulting all the systems investigated; it is also unlikely that molecular chirality is the dominant factor in helix formation. Our experimental observations suggest that helical ribbons are crystalline rather than liquid crystal in nature. We will address this issue again when describing Selinger *et al.*'s model.[18]

3.2.3 Theory for the elastic free energy and the shape of tubules and helical ribbons developed by Selinger *et al.*[a]

I would like to thank Dr. Selinger for helpful discussions regarding his theoretical work.

Whereas Chung *et al.* based their model completely on the de Gennes' theory of SmC* liquid crystals and derived results similar to the Helfrich-Prost theory,[78] Selinger *et al.* took a different route.[18] They generalized the Helfrich-Prost free energy to the case of chiral molecules in a membrane. The inclusion of the chiral term into the free energy resulted not only in the membrane twisting into a cylinder, but also in the molecular tilt direction varying along the tubule. With this in mind, Selinger *et al.* predicted that when periodic modulation of the molecular tilt is formed in the tubules, this modulation occurs within helically wound stripes encircling the tubules.[14] Selinger *et al.* argued that the stripes correspond to a helical substructure. This model was further developed to account for the elastic anisotropy. In this new model, Selinger *et al.* expressed the average direction of molecular tilt modulation and the helical windings in terms of elastic moduli and showed that these two directions are different. The authors also argued that the same theory can be applied to helical ribbons, showing that these structures can be stable for a certain range of parameters and are not necessarily intermediates in the formation of tubules.[18] In what follows, we will briefly discuss Selinger *et al.*'s findings and compare them to Chung *et al.*'s results. To make the comparison more tangible, we will introduce analogies between Chung *et al.*'s and Selinger *et al.*'s notations during our derivations; however, we will preserve the names of the elastic moduli introduced in Selinger *et al.*'s model.

In their theory, Selinger *et al.* used 2D differential geometry and Einstein summation notation. For the purposes of this section, we will not use such notation. Here, instead of using the curvature tensor

$$K_{ab} = \begin{pmatrix} -1/R & 0 \\ 0 & 0 \end{pmatrix}, \tag{3.33}$$

we will employ $\vec{\nabla}\hat{\mathbf{k}}$ to describe the membrane curvature. Selinger *et al.* described the orientation of the molecular tilt in the tangent plane by the unit vector $\hat{\mathbf{m}}$; however, we will employ Chung *et al.*'s notation of $\hat{\mathbf{c}}$.

[e]In what follows, we will use the superscript S to denote Selinger *et al.*'s theory.[18]

As mentioned above, Selinger *et al.* argued that a bilayer membrane in the shape of a tubule consists of domains, i. e. stripes, that wind around the tubule. These domains are separated by domain walls, i. e. the lines along which domains merge to each other. In the case of low curvature, $K_{ab} = \vec{\nabla}\hat{\mathbf{k}}$, and smooth variation in $\hat{\mathbf{c}}$, only a single domain is present throughout the whole tubule. In this case, the elastic free energy density for a tubule can be written as

$$\begin{aligned} \mathbf{a}^S_{\text{tubule}} &= \frac{1}{2}\kappa(\text{Tr } \vec{\nabla}\hat{\mathbf{k}})^2 + \frac{1}{2}\kappa'(\hat{\mathbf{c}}\cdot\vec{\nabla}\hat{\mathbf{k}}\cdot\hat{\mathbf{c}})(\text{Tr } \vec{\nabla}\hat{\mathbf{k}}) \\ &+ \frac{1}{2}\kappa''(\hat{\mathbf{c}}\cdot\vec{\nabla}\hat{\mathbf{k}}\cdot\hat{\mathbf{c}})^2 - \kappa^*_{HP}(\hat{\mathbf{c}}\cdot\vec{\nabla}\hat{\mathbf{k}}\cdot\hat{\mathbf{p}}) \\ &- \lambda_{LS}\vec{\nabla}\times\hat{\mathbf{c}} + \gamma(\text{Tr } \vec{\nabla}\hat{\mathbf{k}})\vec{\nabla}\cdot\hat{\mathbf{c}} + \frac{1}{2}c\left[\left(\vec{\nabla}\times\hat{\mathbf{c}}\right)^2 + \left(\vec{\nabla}\cdot\hat{\mathbf{c}}\right)^2\right], \end{aligned} \quad (3.34)$$

where $\hat{\mathbf{p}}$ is defined as in Chung *et al.*'s model as $\hat{\mathbf{p}} = \hat{\mathbf{k}}\times\hat{\mathbf{c}}$ with $\hat{\mathbf{k}}$ being the bilayer normal. The coefficient κ is the isotropic bending rigidity. The coefficient κ' is the difference between the free energy required to bend the membrane parallel to the molecular tilt $\hat{\mathbf{c}}$ and the free energy required to bend it perpendicular to $\hat{\mathbf{c}}$. The third term represents an additional elastic anisotropy considered by Chung *et al.* (in their notation, $A_{11}/2(\hat{\mathbf{c}}\cdot\vec{\nabla}\hat{\mathbf{k}}\cdot\hat{\mathbf{p}})^2$) but was explicitly ignored by Selinger *et al.* For comparison, we leave this term in the Selinger *et al.*'s free energy density. The fourth term was introduced by Helfrich and Prost, and the coefficient κ^*_{HP}, analogous to κ^* in Eq. (3.10) and to K^*_n in Eq. (3.9), is a measure of the energy of interaction between the chiral molecules in the membrane. The fifth term was introduced by Langer and Sethna[87] and is chiral term favoring a bend in the $\hat{\mathbf{c}}$ direction by the amount λ_{LS}. This term is equivalent to the D_1 term in G_{chiral} of the Chung *et al.* model. The sixth term, with coefficient γ, is the coupling between the curvature of the membrane and the splay of $\hat{\mathbf{c}}$. It describes the curvature of the monolayers and breaks the symmetry between the two monolayers in a bilayer inducing a splay in $\hat{\mathbf{c}}$. This coupling term disfavors the flatness of the bilayers. Again, such a term was considered by Chung *et al.* and is equivalent to the energy contribution G_{kc} due to coupling of deformations along $\hat{\mathbf{k}}$ and $\hat{\mathbf{c}}$. Lubensky and MacKintosh also considered this contribution in their theory of Pβ' rippled phases.[88,89] The final pair of terms in Eq. (3.34) represents the 2D Frank elastic free energy for distortions along $\hat{\mathbf{c}}$ within a layer and is described by the Frank constant $c \propto (1/R)$. This pair of terms is equivalent to the anisotropic elastic terms B_1 and B_2 in G_c of the Chung *et al.* model. The first two terms in Eq. (3.34) are equivalent to the first two terms in Chung *et al.*'s Eq. (3.9). Also,

the sum of the first and the fourth terms corresponds exactly to the expression for the elastic free energy density for the isotropic case derived by Helfrich and Prost[78] in Eq. (3.10).

It is already evident that both the Selinger *et al.* and the Chung *et al.* models, though derived differently, obtain similar expressions for the elastic free energy of the bilayer membrane tubule. To expose this similarity further, we simplify the free energy in Eq. (3.34) using 2D cylindrical coordinates (ϕ, z). As before, $\hat{\mathbf{c}}(\beta^S, z)$ is the angle in the local tangent plane between the tilt direction and the equator of the cylinder (Fig. 3.3). Thus, the tilt director field can be written as $\hat{\mathbf{c}}(\phi, z) = (\cos\beta^S, \sin\beta^S)$. Then, the Selinger *et al.*'s free energy becomes

$$\begin{aligned} \mathbf{a}^S_{\text{tubule}} &= \frac{1}{2}\kappa\left(\frac{1}{R}^2\right) + \frac{1}{2}\kappa'(\frac{1}{R})^2\cos^2\beta^S + \frac{1}{2}\kappa''(\frac{1}{R})^2\cos^4\beta^S - \kappa^*_{HP}\left(\frac{1}{R}\right)\sin\beta^S\cos\beta^S \\ &- \lambda_{LS}\vec{\nabla}\times\hat{\mathbf{c}} + \gamma\left(\frac{1}{R}\right)\vec{\nabla}\cdot\hat{\mathbf{c}} + \frac{1}{2}c\left[\left(\vec{\nabla}\times\hat{\mathbf{c}}\right)^2 + \left(\vec{\nabla}\cdot\hat{\mathbf{c}}\right)^2\right], \end{aligned} \tag{3.35}$$

where expressions for $\vec{\nabla}\times\hat{\mathbf{c}}$ and $\vec{\nabla}\cdot\hat{\mathbf{c}}$ are defined in Eqs. 3.6 and 3.7. Eqs. 3.35 is much easier to work with and the terms equivalent to the terms in expression of Chung *et al.* are more obvious.

To continue drawing attention to the similarities between the model of Chung *et al.* and that of Selinger *et al.*, we start by considering tubules with a uniform tilt direction β^S_0. In this case, the entire tubule is a single domain, with no domain walls.[18] In terms of R and β^S_0 the free energy per unit area in Eq. (3.35) is

$$\mathbf{a}^S_{\text{tubule}} = \frac{1}{2}\kappa(\frac{1}{R})^2 + \frac{1}{2}\kappa'(\frac{1}{R})^2\cos^2\beta^S_0 + \frac{1}{2}\kappa''(\frac{1}{R})^2\cos^4\beta^S_0 - \kappa^*_{HP}(\frac{1}{R})\sin\beta^S_0\cos\beta^S_0. \tag{3.36}$$

Minimizing this expression with respect to R and β^S_0 simultaneously, the equilibrium radius of the tubule, R^S_0, and the equilibrium molecular phase angle are

$$R^S_0 = \frac{\kappa^{1/4}(\kappa+\kappa'+\kappa'')^{1/4}}{\kappa^*_{HP}} \frac{\left[2\kappa+\kappa'+2\kappa^{1/2}(\kappa+\kappa'+\kappa'')^{1/2}\right]}{\kappa^{1/2}+(\kappa+\kappa'+\kappa'')^{1/2}} \tag{3.37}$$

$$\tan^4\beta^S_0 = \frac{\kappa+\kappa'+\kappa''}{\kappa} \tag{3.38}$$

This result is, as expected, similar to the one obtained by Chung *et al.* and leads to the same conclusions. For tubules with uniform molecular tilt, β^S_0,

- the tubule radius scales inversely with the Helfrich-Prost chirality parameter κ^*_{HP}, the absence of which leads to $R^S_0 \to \infty$;

- this tilt direction is determined by the ratio of the stiffness to bends parallel to the molecular tilt, $(\kappa+\kappa'+\kappa'')$ (equivalent to K_n^{cc} in Chung *et al.* notation), to the membrane stiffness to bends perpendicular to the tilt direction, κ (equivalent to K_n^{pp} in Chung *et al.* notation).

Since both theories come to very similar conclusions via two different routes, it is quite reasonable to say that the derivations and the assumptions made in both theories are compatible.

Comparison of the Selinger *et al.*'s result in Eq. (3.38) to Chung *et al.*'s result in Eq. (3.29) for high pitch helices with pitch angle $\psi = 53.7°$ and low pitch helices with pitch angle $\psi = 11.1°$ found in quaternary sterol systems reveals an unexpected conclusion. Recall that, Chung *et al.* assumed that the helical ribbons are "cut out" from the tubules along the molecular tilt direction, so that $\beta_0^C = \psi_0^C = 53.7°$ and $\beta_0^C = \psi_0^C = 11.1°$ for each type of helix. Then, using Eq. (3.38), equivalent to Eq. (3.29), the ratio of the elastic moduli for helices of each pitch angle are

$$\begin{aligned} \left.\frac{\kappa+\kappa'+\kappa''}{\kappa}\right|_{53.7°} &= 3.4 \\ \left.\frac{\kappa+\kappa'+\kappa''}{\kappa}\right|_{11.1°} &= 1.5\times10^{-3}. \end{aligned} \tag{3.39}$$

In comparison to Eq. (3.32), the ratios in Eq. (3.39) consist of the sum of elastic moduli in the numerators. However, the implication of these expressions that for the low pitch helices a bend in the membrane perpendicular to the tilt direction costs 700 times more energy than a bend parallel to the molecular tilt direction, still needs to be addressed.

For this reason, Selinger *et al.* went further to explain the very low ratio of the elastic moduli for low pitch helices obtained by Chung *et al.* in Eq. (3.32). Selinger *et al.* reexamined the assumption that the domain walls of tubules and the edges of helices are aligned along the molecular tilt direction. They proposed that if the average tilt direction and the direction of domain walls are different, this would explain the surprising results of Chung *et al.* By allowing the tilt direction to vary with the cylindrical coordinates ϕ and z, the parametric equation for $\hat{\mathbf{c}}$ becomes $\hat{\mathbf{c}}(\phi,z) = [\cos(\beta^S(\phi,z)), \sin(\beta^S(\phi,z))]$. Now, suppose that there are n_s distinct stripes in the tilt direction, in other words, there exist n_s domains each of which is separated by a domain wall. Further suppose that the tilt direction β^S varies smoothly across each stripe, but changes sharply across each domain wall. Using these assumptions,

Selinger *et al.* then obtained the amplitude of the tilt variation $\Delta\beta^S$ from the average tilt direction β_0^S. Since the second and third terms in Eq. (3.35) favor a particular orientation of the tilt, Selinger *et al.* expanded these terms in a power series in $\Delta\beta^S$. Up till now, we have described the contribution to the free energy from the domains only. At this point, the contribution to the free energy density from the domain walls needs to be added. Selinger *et al.* defined the energy due to domain walls per unit length as an additive constant ε_w. The total free energy density of a tubule with domains and domain walls the is

$$\mathbf{a}^S_{\text{total}} = \mathbf{a}^S_{\text{tubule}} + \varepsilon_w \tag{3.40}$$

Putting all these pieces together and further taking n_s to be a continuous variable (a good approximation for $n_s \gg 1$), the elastic free energy per unit area in Eq. (3.35) becomes

$$\begin{aligned}\mathbf{a}^S_{total} &= \frac{\kappa + \kappa' \cos^2\beta_0^S + \kappa'' \cos^4\beta_0^S}{2R^2} - \frac{\kappa^*_{HP}}{R}\sin\beta_0^S\cos\beta_0^S \\ &+\frac{1}{2}\nu(\Delta\beta^S)^2 - \lambda_{LS}\frac{\Delta\beta^S\cos\delta}{L} - \frac{\lambda}{R}\frac{\Delta\beta^S\sin\delta}{L} \\ &+\frac{1}{2}c\left(\frac{\Delta\beta^S}{L}\right)^2 + \frac{\varepsilon_w}{L},\end{aligned} \tag{3.41}$$

where L is the stripe width, δ is the difference between the average tilt direction and the stripe direction, and

$$\nu = \frac{1}{6}\left[\left(\frac{\kappa'}{2R^2}\right)^2 + \left(\frac{\kappa^*_{HP}}{R}\right)^2\right]^{1/2}. \tag{3.42}$$

Minimizing the free energy with respect to the angle δ, Selinger *et al.* obtained the following:

$$\tan\delta = \frac{\gamma}{R\lambda_{LS}}. \tag{3.43}$$

This expression explains the questionable result of Chung *et al.* for the ratio of the elastic moduli for the helical domains of tubules and the pitch angles of helical ribbons both equal to 11.1°. The very small ratio $K_n^{cc}/K_n^{pp} = (\kappa + \kappa' + \kappa'')/\kappa$ in Eq. (3.32) can be explained as follows. If the helical markings indicate the stripe direction, then this ratio could be 1, i.e. $\beta_0^S = 45°$, while the stripe direction is 11.1°. In other words, Selinger *et al.* suggested that though the results in Chung *et al.*'s theory are correct, the interpretation of these results must be different. By measuring helix pitch angles, Chung *et al.* were determining the stripe direction, not the average molecular

tilt direction. We can also argue that the pitch angle of 53.7° corresponds to an unmodulated phase, since the ratio of the elastic moduli for $\beta_0^S = 54°$ is reasonable.

Selinger *et al.* further discovered the existence of a first order phase transition between single domain tubules and tubules with tilt modulation, where the elastic free per unit area of a membrane abruptly jumps from

$$\mathbf{a}_{total}^S = \frac{\kappa + \kappa' \cos^2 \beta_0^S + \kappa'' \cos^4 \beta_0^S}{2R^2} - \frac{\kappa_{HP}^*}{R} \sin \beta_0^S \cos \beta_0^S \tag{3.44}$$

to the value of

$$\mathbf{a}_{total}^S = \frac{\mathbf{a}_{tot}^S}{A} = \frac{1}{2}\kappa(\frac{1}{R})^2 + \frac{1}{2}\kappa'(\frac{1}{R})^2 \cos^2 \beta_0^S - \kappa_{HP}^*(\frac{1}{R}) \sin \beta_0^S \cos \beta_0^S + \frac{\mathbf{a}_{stripe}^S}{A}, \tag{3.45}$$

where $\mathbf{a}_{stripe}^S$ is the sum of the four last terms in Eq. (3.41). It is obvious that Eq. (3.36) is exactly the free energy considered in an unmodulated state of the tubule. Hence, all the equations derived by Chung *et al.* are valid, but only for an unmodulated, single domain state of tubules.

An explicit analogy can be drawn between a single stripe of a modulated tubule and a single ribbon. Selinger *et al.* showed how this analogy works and that all the equations above apply to the case of helical ribbons with the replacement of the free energy density due to domain walls with the free energy density due to the edges of a helical ribbon

$$\frac{\varepsilon_w L_w}{A} = \mathbf{a}_{edge}, \tag{3.46}$$

where $\mathbf{a}_{edge}$ is given in Eq. (3.23), ε_w is a constant, and $L_w = A/L$ is the total length of all the domain walls with A being the total area of the membrane.

3.2.4 Conclusion

In this section, we have presented two models for the elastic free energy of chiral anisotropic tubules and helical ribbons based on two different approaches. Chung *et al.* derived equations for these equilibrium state of tubules and helical ribbons to analyze the microstructures in bile. In contrast, Selinger *et al.*'s theory was originally intended to describe diacetylenic lipid tubules; this theory was later modified to include helical ribbons. Although the two models were intended to describe different experimental systems and the starting points of the derivations are different (Chung *et al.* based their model on a reformulated de Gennes' theory of SmC* layers, while Selinger *et al.* based their model on the Helfrich-Prost theory) both came to very

similar conclusions. First, both models predict that the tubule radius scales inversely with the elastic modulus associated with molecular chirality, as shown in Eqs. 3.27 and 3.37. This implies that for non-chiral membranes ($K^* = 0 = \kappa^*_{\mathrm{HP}}$), the tubule radius is infinitely large, i. e. the tubule curvature approaches zero, since curvature $\propto 1/R$. Second, both models predict that the molecular tilt angle is determined entirely by the ratio of the elastic moduli associated with bends parallel to the molecular tilt to those associated with bends perpendicular to the molecular tilt direction. Third, when reduced to the isotropic case both models are in exact agreement with the Helfrich-Prost model.[78]

In Section 3.2.2, we showed that Chung *et al.* based their model on multiple assumptions. For example, they assumed that helical ribbons and tubules are made of liquid crystalline bilayer membranes and that molecular chirality plays a dominant role in helix and tubule formation by explicitly including chiral term, K^*, in their expression of elastic free energy density (Eqn. 4.13). To model helical ribbons, they assume that a parallel strip can be cut out of a tubule along a constant molecular tilt angle ψ. Chung *et al.* further allow helical ribbons to grow in width but only until the point when edges on successive turns of a helix merge. None of these assumptions are based on experimental evidence. In fact, the experiments of Konikoff *et al.*[20,28] in model bile, one representative of the quaternary sterol systems, the precursors of helical ribbons (filaments) are a polymorph of cholesterol monohydrate and anhydrous cholesterol crystals covered by a lipid layer. Furthermore, helical ribbon successors are stable cholesterol monohydrate crystals, as was discussed in Section 2.3. This suggests that helical ribbons may actually have a crystalline, positionally ordered molecular structure, rather than a liquid crystal structure. Furthermore, for an enantiomerically pure system, Chung *et al.* predict the formation of helices of only one-handedness; however, we showed that helices of both handednesses form in some quaternary sterol systems (Section 2.5) thus questioning the assumption that molecular chirality is the major factor in helix formation. Section 3.2.2 further called Chung *et al.*'s theory in question by addressing the numerous deviations of this theory from the experimental observations.

By modifying their original theory, Selinger *et al.* intended to correct the prediction of Chung *et al.* that for low pitch helical ribbons that the bilayer membrane from which low pitch helices helices and tubules formed from low pitch helices are constructed is 700 times more stiff perpendicular to the molecular tilt than parallel

to the molecular tilt. As a result, in addition to the assumption that helices and tubules are made from a liquid crystal bilayer membrane, Selinger *et al.* made the assumption that the molecular tilt direction varies within the membrane. This resulted in a description of tubules composed of domains and domain walls. The conclusion was made that tubules with high pitch stripes are made from a single domain in which molecular tilt does not vary. In comparison, low pitch helices are made from multiple domains with molecular tilt modulation. This result corrected the unreasonable ratio of 700 ($= 1/1.5 \times 10^{-3}$) between the stiffnesses of low pitch helical ribbons predicted by Chung *et al.* However, there exists no experimental verification that helical ribbons and tubules made from quaternary sterol systems are liquid crystal in nature; neither does there exist experimental evidence that the molecular tilt within the membrane of helical ribbons and tubules varies. It is possible that Selinger *et al.*'s model is applicable to some systems of helical ribbons and tubules other than quaternary sterol systems. Experimentally, there exist results supporting the idea that chiral molecular packing plays an important role in the formation of tubules and helical ribbons in some systems. On one hand, a number of researchers[11,14,18] have observed the helical markings that wind around tubules; on the other hand, recent experiments have found that diacetylenic lipid tubules have a very strong circular dichroism, indicating a local chiral packing of molecules.[90] Unfortunately, there has not been, to date, any direct confirmation of the prediction of tilt modulation.

Several experiments can be performed to probe the models of Chung *et al.* and Selinger *et al.* to discern whether the nature of helical ribbons and tubules made from quaternary sterol and other systems is crystalline or liquid crystal. Electron microscopy experiments could be performed to directly determine molecular orientation. Also, attaching a fluorescent group to the molecules, fluorescence and polarized laser excitation could be used to detect variations in the direction of the molecular tilt by illuminating the tubules with polarized light from a laser source and observing the variation in the intensity of fluorescence with near-field or confocal microscopy. These and similar probes could illuminate the molecular picture and help to further refine theoretical models and their applicability to various experimental systems.

3.3 Proposed Theory of Elasticity – Crystalline Model

3.3.1 Introduction

By 1998, the necessity for the development of a new model explaining the properties of helical ribbons had become more apparent than ever. Chung *et al.*'s 1993 theory, though sound, predicted the unphysical requirement that, for low pitch helices, the stiffness to bends perpendicular to the molecular tilt is nearly 700 ($= 1/[1.5 \times 10^{-3}]$) times greater than that parallel to the molecular tilt.[12] In 1995, Selinger *et al.* tried to solve this problem by allowing the molecular tilt direction to vary across the helical ribbon width.[18] This assumption had no physical or experimental justification, however it led Selinger *et al.* to explain the existence of low pitch helices without the unphysical ratio of energies predicted by Chung *et al.* Three years later, in 1998, Komura *et al.* made another attempt to explain the properties of helical ribbons.[19] They derived Euler-Lagrange equations from the expressions for the elastic free energy and tried to solve these to find the variation of molecular tilt across the helical ribbon width. Although they did not obtain an analytical solution, Komura *et al.* were able to show graphically that the form of the elastic free energy for the low pitch helical ribbons might indeed be derivable if the molecular tilt varies across the ribbon's width.

Our observation (Chapter 2) that the formation of helical ribbons is a general phenomenon of a large number of multicomponent systems composed of a bile salt or non-ionic detergents, a phosphatidylcholine or fatty acids, and a steroid analog of cholesterol in water, calls the previous theories into question. As mentioned in Chapter 2, this evidence suggests that helical ribbons might be crystalline rather than liquid crystal in nature, and that molecular chirality might not be the driving force in helix formation. It is essential at this point to develop a new theory consistent with all experimental data, and to perform new experiments that would be explicitly sensitive to the microscopic helical structure. We first develop such a theory, and in the Chapter 4 we show that our experimental data, both obtained originally by Chung *et al.* and that recently obtained for a variety of quaternary sterol systems, is consistent with this new theory.

3.3.2 Crystalline Model

I would like to thank Aleksey Lomakin for proposing the conceptual model described in this Section and for consulting us in the process of the derivation of the crystalline theory. Special thanks are sent to Brice Smith for his boldness in the initial derivation of the theory and for his intellectual support writing this Section. I would also like to thank Professor Emeritus Eugene Kangas for his insight and aid in the visualization of three-dimensional helical structures.

To present a description of helical ribbons within the formalism of the crystalline model, we will pursue the following outline.

1. We will give a brief presentation of the theory for the bending of thin plates set forth by Landau and Lifshitz.[37]

2. We will find the components of the deformation tensor for locally small deformations in two different ways.

   (a) We will define the deformation tensor by describing a parametrization of a helical ribbon in terms of a new orthogonal coordinate system.

   (b) We will perform a self-consistency check by writing down the actual deformation that occurs when a flat thin plate is bent.

3. We will finally present a formal definition of a small deformation.

4. With the components of the deformation tensor defined, we will write the stress-strain relationship and find a general form of the parametrization coefficients [f] in terms of the non-zero coefficients of the elastic modulus tensor.

5. We will determine the form of the elastic free energy density.

The Landau and Lifshitz' Theory For The Bending Of Thin Plates.
In order to formulate a description of helical ribbons within the formalism of the crystalline model, we begin with the theory for the bending of thin plates set forth by

[f]The parametrization coefficients will be introduced when defining a parametrization of a helical ribbon in terms of a new orthogonal coordinate system, as described in the item 2(a) above.

Landau and Lifshitz in their *Theory of Elasticity*.[37] The general form of the elastic free energy per unit volume of a deformed crystal [g] in this theory is given by (see Appendix 3.A[91])

$$F = \frac{1}{2}\lambda_{ijkl}U_{ij}U_{kl}, \tag{3.47}$$

where the elastic modulus tensor λ_{ijkl} is a three-dimensional tensor of rank four and the deformation tensor U_{ij} is a three-dimensional tensor of rank two that describes the strain in the crystal. Since the strain tensor is symmetrical (see Appendix 3.B[92]), i.e. $U_{ij} = U_{ji}$, and can be diagonalized, the product of the two strain tensors in Eq. (3.47) must remain constant under exchange of suffixes i and j, or k and l, or simultaneously i, j and k, l. In other words,

$$U_{ij}U_{kl} = U_{ji}U_{kl} = U_{ij}U_{lk} = U_{ji}U_{lk} = U_{kl}U_{ij}, \quad \text{etc.} \tag{3.48}$$

This leads to the property that the elastic modulus tensor λ_{ijkl} possesses the same universal symmetries,

$$\lambda_{ijkl} = \lambda_{jikl} = \lambda_{ijlk} = \lambda_{jilk} = \lambda_{klij}, \quad \text{etc.} \tag{3.49}$$

With these symmetries, the number of independent components in the elastic modulus tensor is reduced from 81 to 21 (see Appendix 3.C). If the underlying crystal possesses additional symmetries, the number of independent components in the elastic modulus tensor can be further reduced.

A body is said to be "undeformed" when there are no external forces acting on the body and it is at a constant temperature throughout (to prevent thermal expansion). For a displacement $u_{ij} = 0$, the internal stresses are zero, $\sigma_{ij} = 0$ (see Appendices 3.A and 3.B). At constant temperature, the stress tensor, σ_{ij}, can be calculated from the elastic free energy expression in Eq. (3.47) in terms of the elastic modulus tensor, λ_{ij}, as follows

$$\sigma_{ij} = \partial F/\partial U_{ij} = \lambda_{ijkl}U_{kl}, \tag{3.50}$$

so that the expression for the elastic free energy of a crystal in terms of the deformation tensor, U_{ij}, and stress tensor, σ_{ij}, or in terms of the deformation tensor, U_{ij}, and elastic modulus tensor, λ_{ij}, is given by

$$F = \frac{1}{2}\lambda_{ijkl}U_{ij}U_{kl} = \frac{1}{2}\sigma_{ij}U_{ij}. \tag{3.51}$$

[g] This is a free energy per unit volume of ANY deformed crystal of ANY initial geometrical shape.

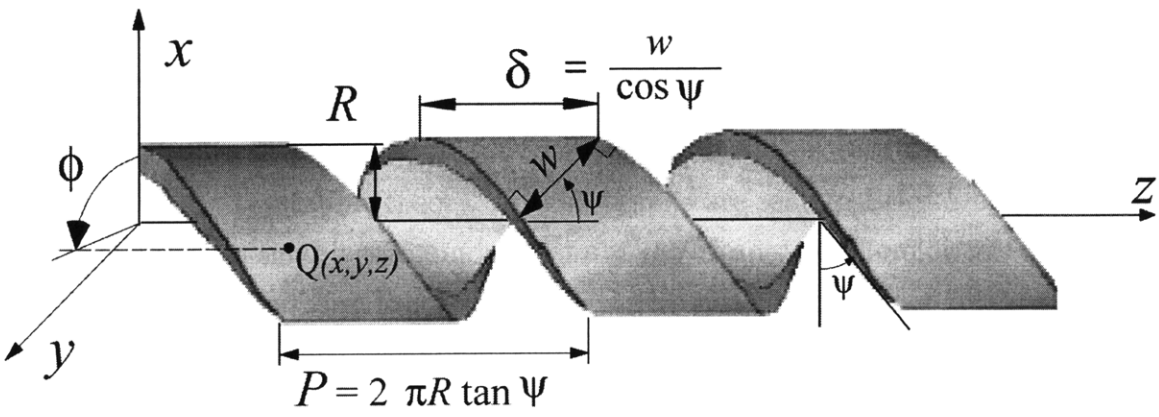

Figure 3.6: The three–dimensional rendition of a thick helical ribbon of radius R, pitch angle ψ, and ribbon width w. The length of the helical ribbon along the axis of symmetry, $\delta = w/\cos\psi$, is shown. An arbitrary point $Q(x,\ y,\ z)$ is also shown.

As with U_{ij}, σ_{ij} is also symmetric under the exchange of indices. The elastic free energy per unit area, $\mathbf{a}$, can be derived from the elastic free energy per unit volume, F, through

$$\mathbf{a} = \int F dh, \tag{3.52}$$

where the integral is taken over the thickness h of the body.

Determination Of The Components Of The Deformation Tensor.

The formalism of Landau and Lifshitz can now be applied to the case of helical ribbons. Here, an originally flat ribbon with the same thickness and width as the final helix, is wrapped around a cylindrical core of the designated radius, R. The flat ribbon is modeled as a thin elastic plate possessing an underlying crystalline structure and having zero elastic free energy. Only when such a ribbon is deformed away from a flat structure does the elastic free energy become non-zero; we will be considering only locally small deformations from a flat structure. In order to explain the appearance of helical ribbons, we add a spontaneous bending term to the expression for the elastic free energy. This term is responsible for creating a ribbon with non-zero equilibrium curvature.[h] The width of the ribbon w wound around a cylindrical core of radius R dictates whether the resultant structure is a helical ribbon of pitch ψ (when the

[h]A curvature is defined as $C = 1/R$, where R is the radius of the cylinder. For a flat ribbon the curvature is zero since the radius is infinite, i. e. $R \to \infty$.

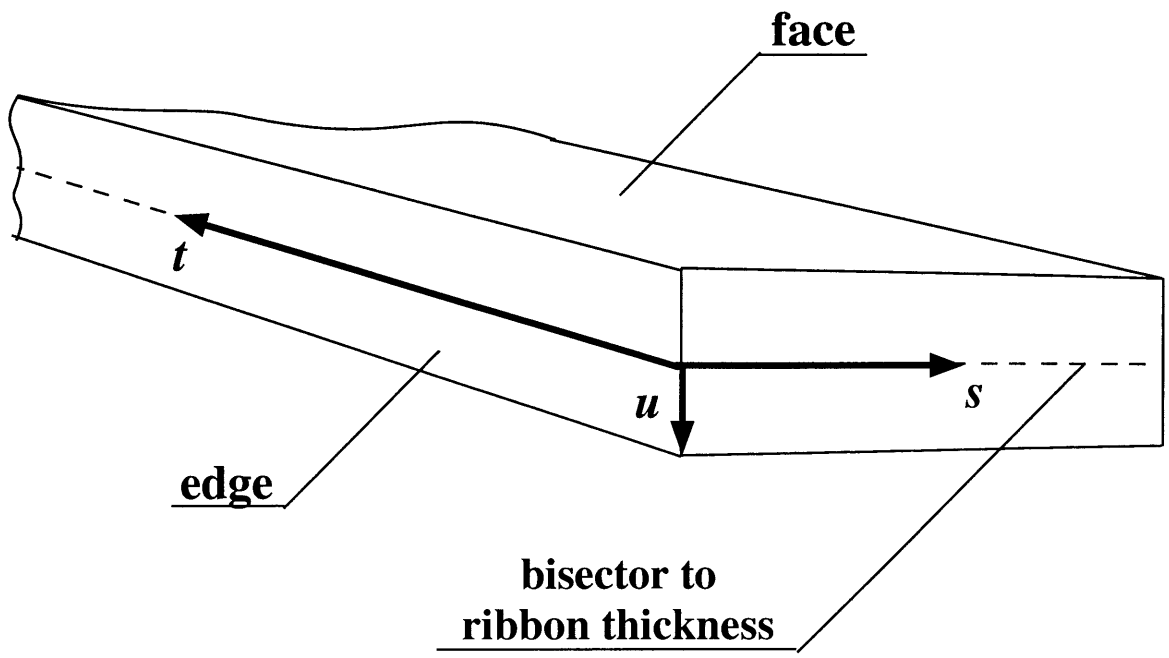

Figure 3.7: The local Frenet coordinate system (t, s, u) defined for a ribbon.

length of the ribbon along the axis of symmetry $\delta = w/\cos\psi$, as shown in Figure 3.6, is smaller than the helix pitch length, $P = 2\pi R\tan\psi$, i. e. $\delta < P$) or a tubule (when the length of the ribbon along the axis of symmetry is larger than the helix pitch length, i. e. $\delta > P$). However, before the form of the elastic free energy density can be deduced, we need to find the stress–strain relationship. Defining the elements of the strain tensor in the Landau-Lifshitz formalism, and imposing the conditions of mechanical equilibrium on the stress tensor, the stress-strain relationship can be uniquely defined. In what follows, we attempt to create the most general model for the elastic free energy of a helical ribbon, independent of the particular microscopic nature of the molecular ordering within helical ribbon walls.

Description Of Parametrization Of A Helical Ribbon In Terms Of A New Orthogonal Coordinate System.

To start, we need to make a transformation between the global Cartesian coordinate system, (x, y, z), and the local Frenet coordinate system,[93] (t, s, u). The Frenet system is a curvilinear system. In this system each point is described by three curvilinear coordinates t, s, and u. (Polar coordinates are an example of curvilinear coordinates

in the plane; latitude and longitude are the curvilinear coordinates of a point on a sphere, a familiar procedure in geography.) For notational simplicity, we will define two local Frenet coordinate systems, one for a flat elastic plate (or a ribbon) and the other one for the same elastic plate (or ribbon) bent into a helical shape by winding it around a cylindrical core.

We will begin by describing the Frenet coordinate system for a flat elastic plate. To define the location of a point in such a ribbon in this new coordinate system, we need to supply the origin and the orientation of the Frenet system. This is done as follows:

- we will define the large surface of a ribbon as a "face" and the small side surface of a ribbon as an "edge", as shown in Figure 3.7;

- the origin of the local Frenet coordinate system (t, s, u) may be chosen at an arbitrary point along the "edge" of a ribbon on the bisector of the ribbon thickness, as shown in Figure 3.7,

- coordinate t describes the location of a point along the contour length of a ribbon; the t coordinate originates and is located on the ribbon edge and runs along the intersection of the ribbon edge and the bisector to the ribbon thickness. For a helical ribbon whose contour length is T, the t coordinate of a point along the ribbon can take any value, such that

$$t \in [0, T] \tag{3.53}$$

- coordinate s describes the location of a point along the ribbon width; the s coordinate originates on the ribbon edge and is located in the plane of the bisector to the ribbon thickness. The s coordinate forms a normal to the ribbon edge and points into the ribbon. If the width of a ribbon is given as w, then the s coordinate of a point in the ribbon can take any value, such that

$$s \in [0, w], \tag{3.54}$$

- from the above two items, it is clear that the s and t coordinates define a surface equidistant from the two faces of a ribbon, i. e. the surface bisecting the ribbon thickness;

- the coordinate u describes the location of a point along the ribbon thickness; the u coordinate originates and is located on the ribbon edge and defines the normal to the surface bisecting the ribbon thickness, i. e. to the st-surface. The direction of the u coordinate is defined by right hand rule after the directions of the s and t coordinates have been specified, such that $\hat{u} = \hat{t} \times \hat{s}$, as shown in Figure 3.7. If the total thickness of the ribbon is h, then the u coordinate of a point in the ribbon can take any value such that

$$u \in [-\frac{h}{2}, \frac{h}{2}]. \tag{3.55}$$

Now we will define a new Frenet coordinate system for an elastic plate (or ribbon) bent into a helical ribbon. Due to the finite thickness of the flat plate, the coordinates of a point within the plate will change upon bending. As the thin plate is bent, one of its sides is compressed while the other one is stretched. Therefore, there exists a neutral surface within the ribbon which experiences neither stretching nor compression but rather undergoes a pure bend. For a *thin* plate, this neutral surface coincides with the surface bisecting the plate thickness.[37] Therefore, the new Frenet coordinate system for an elastic plate bent into a helical shape is defined with respect to this neutral surface. We will call the new Frenet coordinate system "the primed system", in which a point is described in terms of t', s' and u' coordinates as $P' = (t'_P, s'_P, u'_P)$. For the primed coordinate system, the coordinates t', s', and u' are defined in the same manner as the coordinates t, s and u above with the only exception that we will use this system to describe a point in a bent state. As before, the u' coordinate originates on the surface bisecting the thickness (which is also a neutral surface) such that the t' and s' coordinates span this surface. When the ribbon is undeformed (flat), the unprimed Frenet coordinate system (t, s, u) and primed system (t', s', u') coincide with one another. However, when a bent is introduced to a ribbon, the two Frenet coordinate systems diverge, as shown in Figure 3.11.

The transformation between the global Cartesian coordinate system, in which a point is specified by the (x, y, z) coordinates, and the local Frenet coordinate system, in which a point is specified by the (t', s', u') coordinates, is performed by recalling that (see Figure 3.6)

$$\begin{aligned} x &= R\cos\phi, \\ y &= R\sin\phi, \\ z &= \rho\phi + \Delta, \end{aligned} \tag{3.56}$$

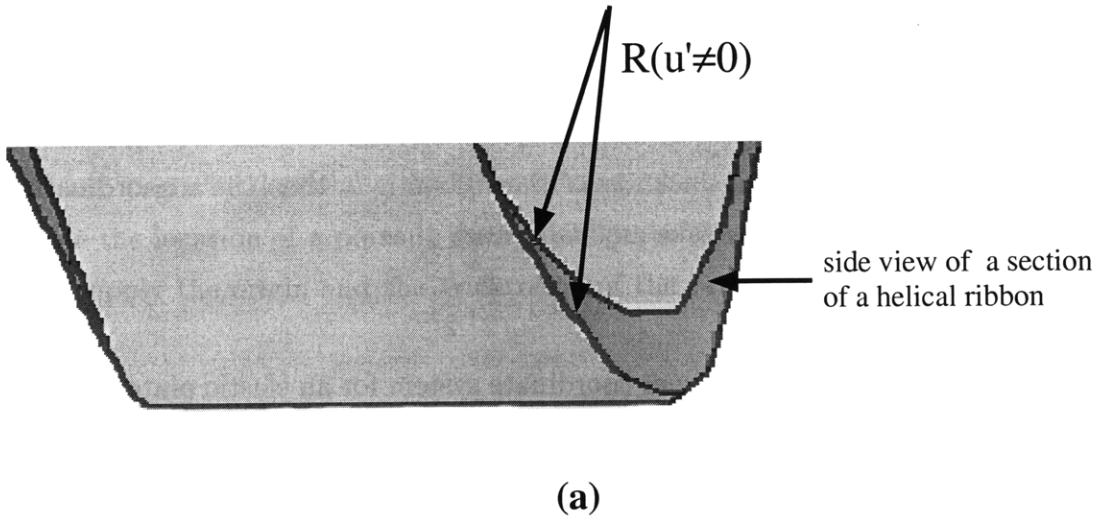

(a)

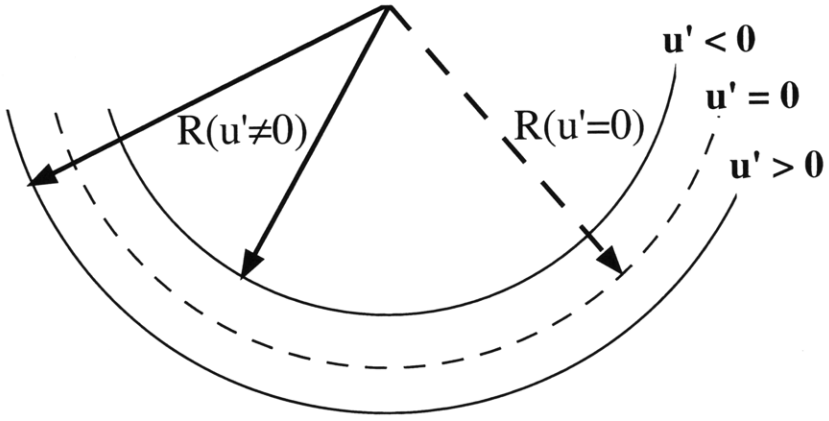

(b)

Figure 3.8: (a) A section of a helical ribbon showing the distances between the center of the curvature and the faces of a helical ribbon $R(u' \neq 0)$; (b) side view of a section of a helical ribbon showing the distances between the faces of the helical ribbon $R(u' \neq 0)$, and the distance between the center of the curvature and the bisector to the helix thickness $R(u' = 0)$.

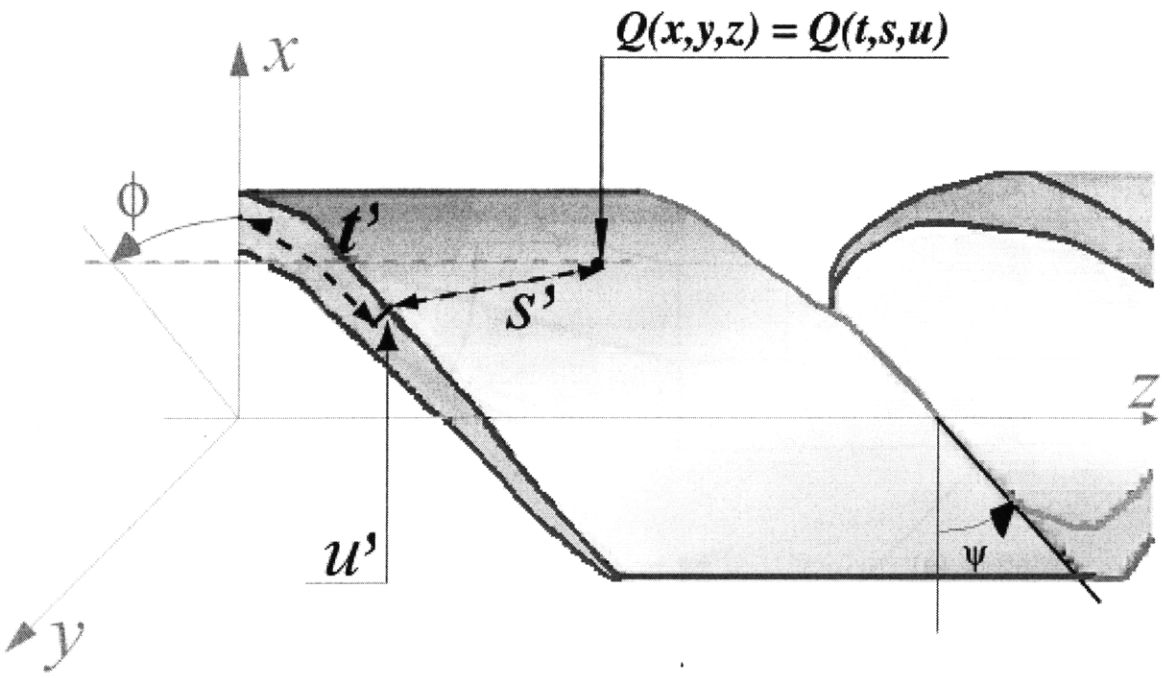

Figure 3.9: Local coordinate system of a helix and its relationship to the Cartesian coordinates. The coordinates of an arbitrary point P are shown. The pitch angle ψ is shown.

as described by Chung *et al.*[12] Here $R = R(u')$ is the distance between the helix axis of symmetry (i. e. the center of helix curvature) and a point in the helical ribbon, as shown in Figure 3.8, ϕ is the azimuthal angle, as shown in Figure 3.6, $\rho = R(u)\tan\psi = P/2\pi$, where P is the pitch length as shown in Figure 3.6, ψ is the helical ribbon pitch angle, and $\Delta \in [0, \delta = w/\cos\psi]$, such that δ is the edge–to–edge distance along the helix axis, as shown in Figure 3.6. Using Figures 3.9 and 3.10, which relate Cartesian coordinate system to the local Frenet coordinate system, we recognize that the Cartesian coordinate z of a point can be described in terms of the helix pitch angle ψ and t' and s' Frenet coordinates as

$$z = t'\sin\psi + s'\cos\psi. \tag{3.57}$$

The parametrization in the above equation implies that the z coordinate of a point is given by the sum of the projections of contour length (the t' coordinate of a point) and ribbon width (the s' coordinate of a point) onto the z axis. However, from the last equation in Eq. (3.56), the z coordinate of a point is also given by

$$z = (R(u'=0)\tan\psi)\phi + \delta = (R(u'=0)\tan\psi)\phi + \frac{s'}{\cos\psi}. \tag{3.58}$$

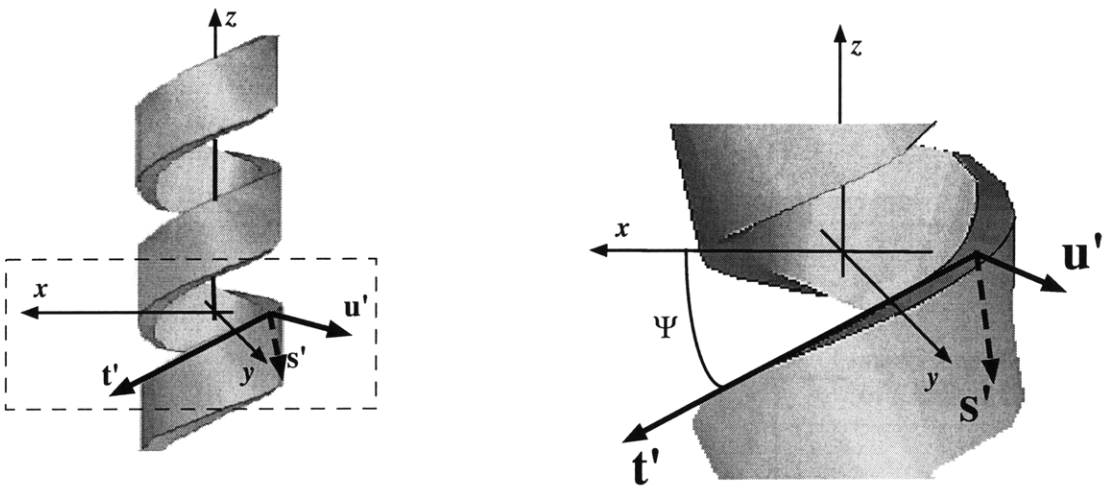

Figure 3.10: (a) Local coordinate system of a helix and its relationship to the Cartesian coordinates; (b) enlarged view of a section of a helical ribbon with the local Frenet coordinate system and the global Cartesian coordinate system shown. The pitch angle ψ is shown.

In order for the right hand sides of the Equations 3.57 and 3.58 to be equal, we recognize that the azimuthal angle ϕ is given by

$$\phi = \frac{t' \cos\psi - s' \sin\psi}{R(u'=0)}. \tag{3.59}$$

(For further reading please address *Lectures on Classical Differential Geometry* by D. J. Struik[93]). Therefore, we can rewrite x, y, and z in terms of the new coordinates as:

$$\begin{aligned} x &= R(u') \cos\left(\frac{t' \cos\psi - s' \sin\psi}{R(u'=0)}\right), \\ y &= R(u') \sin\left(\frac{t' \cos\psi - s' \sin\psi}{R(u'=0)}\right), \\ z &= (R(u'=0)\tan\psi)\phi + \delta = (R(u'=0)\tan\psi)\left(\frac{t' \cos\psi - s' \sin\psi}{R(u'=0)}\right) + \frac{s'}{\cos\psi} \\ &= t' \sin\psi + s' \cos\psi. \end{aligned} \tag{3.60}$$

From the above equations, the mapping between the global Cartesian coordinate system (x, y, z) and the local Frenet coordinate system (t', s', u') becomes clear. In what follows, we will use R and ψ as the parameters of the problem characterizing the helix, and t', s', and u' as the coordinates in terms of which the problem will be discussed.

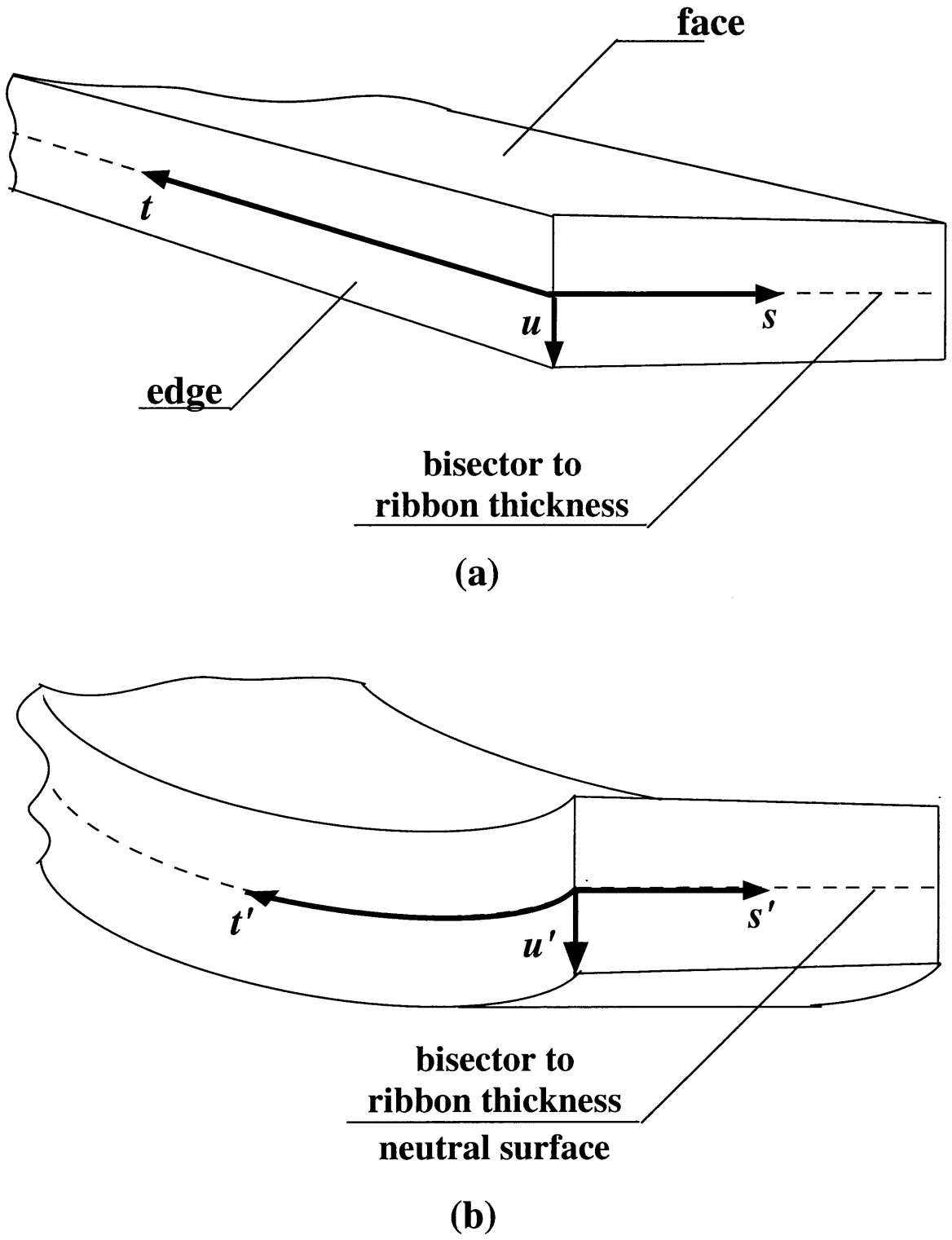

Figure 3.11: (a) A section of a flat elastic plate (or a ribbon) with the local unprimed coordinate system shown; (b) a section of the same flat elastic plate (or a ribbon) in a bent state with the primed Frenet coordinate system, in which the $s't'$ surface coincides with the neutral surface.

When describing the deformation of a flat ribbon into a helical shape, each point $P = (t_P, s_P, u_P)$ in a flat state is described as $P' = (t'_P, s'_P, u'_P)$ in the deformed state. Then, any two points $P = (t_P, s_P, u_P)$ and $Q = (t_Q, s_Q, u_Q) = (t_P+dt, s_P+ds, u_P+du)$ located close to each other within a flat ribbon, are also located close to each other when the flat ribbon is deformed into a helical shape with P becoming P' and Q becoming $Q' = (t'_Q, s'_Q, u'_Q) = (t'_P + dt', s'_P + ds', u'_P + du')$. The displacement $d\vec{l}$ between the points P and Q in the undeformed state of a ribbon becomes $d\vec{l}'$ in the deformed state between the points P' and Q', i. e.

$$d\vec{l} \Rightarrow d\vec{l}' \tag{3.61}$$

or

$$(dt, ds, du) \Rightarrow (dt', ds', du'). \tag{3.62}$$

(For convenience purposes, one can arbitrarily choose one point to be at the origin (see Section 3.B).) The experimental observation that helical ribbons are very thin relative to the other two dimensions, i.e. $u \ll 1$ μm, leads to the conclusion that neither the exact change of coordinates of each of the two points above, nor the exact value of $\sqrt{(dl')^2 - (dl)^2} = \sqrt{(dt' - dt)^2 + (ds' - ds)^2 + (du' - du)^2}$ are required to describe the deformation of a flat ribbon into a helical shape. Rather we can approximate $\sqrt{(dl')^2 - (dl)^2}$ by a truncated expansion in the thickness coordinate u. That is, we can express each coordinate as a Taylor expansion in terms of the thickness u of the ribbon. This mathematical expansion, however, will not define the change in the coordinates of each point resulting from bending deformation of a ribbon. Rather this expansion will represent how stretching and compressing of the ribbon results in changes of the coordinates of each point in the ribbon bulk on moving away from a neutral surface[i] in the deformed state. In other words, we will show how the position of a point $P = (t_P,\ s_P,\ u_P)$ in a flat state described in the $(t,\ s,\ u)$ coordinate system is related to the position of the same point, $P' = (t'_P,\ s'_P,\ u'_P)$, in the $(t',\ s',\ u')$ coordinate system. This relationship is to be provided by means of the Taylor's series.

We will first provide the truncated Taylor's series expansions for each of the coordinates u', s', and t' in terms of u, s, and t, respectively, and then explain the intuition behind these expansions. Keeping terms to the second order in u, the local

[i]The neutral surface is defined as the surface that undergoes no stretching or compression when a plate (ribbon) is deformed.

coordinates of a point within the helical ribbon can be represented as:

$$\begin{aligned} u' &= u + \frac{Au^2}{2R}, \\ s' &= s + \frac{Bu^2}{2R}, \\ t' &= t + \frac{Cu^2}{2R}, \end{aligned} \tag{3.63}$$

where the constants A, B, and C are functions of the ribbon pitch angle and will be determined later by the conditions of mechanical equilibrium at the ribbon's edge and $R = R(u' = 0)$. Intuitively, these expressions are correct for the following reasons. First, in the limit that $u \to 0$, the ribbon thickness becomes infinitely thin and shrinks down to the neutral surface. By definition, a neutral surface does not undergo either extension or compression but rather experiences a pure bend. Mathematically, this implies that in this limit, $s' \to s$ and $t' \to t$, which is precisely the case in Eq. (3.63). Second, in the limit that $R \to \infty$, the ribbon curvature $1/R$ becomes infinitely small and a bent ribbon approaches the flat state. Mathematically, this implies that in this limit the coordinates u', s', and t' must reduce to u, s, and t, respectively. Again, the mathematical expressions in Eq. (3.63) indeed reduce to a correct form. Third, we expect the thickness coordinate of a point in a bent ribbon u' to be linearly dependent on the thickness coordinate of the same point in a flat state, $u' \sim u$. That is if a point was located above (below) a surface bisecting the ribbon thickness prior to the bent, this point must be located above (below) this surface after the ribbon is bent. Combining this requirement with the limits discussed above, the fact that $u' = u + A(u^2/2R)$ becomes intuitively plausible. It is also reasonable that the s' and t' coordinates of a point in the helical ribbon do not depend linearly on where in the bulk the point is located, i. e. they do not depend linearly on the thickness position of the point. Rather, it is reasonable that $s' \sim s + \mathcal{O}(\sqcap^{\epsilon})$ and $t' \sim t + \mathcal{O}(\sqcap^{\epsilon})$, as is the case in Eq. (3.63).

In obtaining the mathematical constructs in Eq. (3.63), we incorporated the following assumptions. First, we only considered locally small deformations. The meaning of a small deformation for a long ribbon is very subtle, since locally small deformations of a long ribbon can lead to very large end to end displacements. We will address this issue in detail in the next subsection. For the purposes of this subsection, we assumed that a *small* deformation (displacement of the coordinates of a point) can be written as a Taylor's series in the thickness coordinate u approximated to the

second order in u. The second order term in u describing various displacements of coordinates of a point in a ribbon must be dimensionally correct, i. e. be measured in units of length. Combining this with our reasoning in the above paragraph, the term to second order in u describing various displacements must be proportional to u^2/R. This second order term is necessary and sufficient if the constant in front of the u^2/R term is non-zero. If, on the other hand, this constant is zero, further expansion may be necessary. (For further intuitive analysis and rigor, the reader is invited to examine *Elementary Theory of Elastic Plates* by L. G. Jaeger.[94]) Second, we recall that a strain tensor is related to the derivatives of the displacements of coordinates of a point. Therefore, the elements of the unitless strain tensor U_{ij} can also be written as a Taylor's series in the thickness coordinate u. However, this Taylor's series will be approximated to first order in u and to preserve the dimensionless nature of the strain tensor, the lowest order terms will have the form of u/R.

To obtain the components of the strain tensor, one usually needs to know the exact displacements of each point in an elastic body occurring when this body is deformed. Since we do not yet know what these displacements are when a flat ribbon is deformed into a helical shape, we can attain the same goal of finding the strain tensor in a different manner. We will compare the square of the distances between two infinitesimally close points in the ribbon before and after the deformation of a flat ribbon into a helical shape. To do so, we will use the following definitions, to find the components of the displacement $\vec{\omega}$ (see Appendix 3.B) in the local Frenet coordinate system:

$$\begin{aligned} \omega_u &= u' - u, \\ \omega_s &= s' - s, \\ \omega_t &= t' - t, \end{aligned} \tag{3.64}$$

where ω_i is the infinitesimal displacement of a coordinate $u_i (= u,\ s,$ or $t)$ of a point when a flat plate is bent. We can now redefine the strain tensor U_{ij} for the local Frenet coordinate system $(t,\ s,\ u)$ in terms of the ω_i's above as

$$U_{ij} = \frac{1}{2}\left(\frac{\partial \omega_i}{\partial u_j} + \frac{\partial \omega_j}{\partial u_i}\right). \tag{3.65}$$

Then, applying Eq. (3.166) from the Appendix 3.B to Eqs. 3.61 and 3.62, we obtain:

$$(dl')^2 = (dl)^2 + 2U_{ij} du_i du_j, \tag{3.66}$$

where u_i is again one of the u, s, or t coordinates of a point in the ribbon, and ω_i is the infinitesimal displacement of the u_i coordinate of a point when a flat ribbon is bent. Using the definition of the strain tensor in the local Frenet system, as shown in Eq. (3.65), we can write the expression in Eq. (3.66) explicitly by performing the summation, we obtain

$$\begin{aligned}(dl')^2 &= (dl)^2 + 2\left[\frac{d\omega_u}{du}dudu + \frac{d\omega_s}{ds}dsds + \frac{d\omega_t}{dt}dtdt\right] \\ &+ \left[\frac{d\omega_u}{ds} + \frac{d\omega_s}{du}\right]duds \\ &+ \left[\frac{d\omega_u}{dt} + \frac{d\omega_t}{du}\right]dudt \\ &+ \left[\frac{d\omega_s}{dt} + \frac{d\omega_t}{ds}\right]dsdt.\end{aligned} \tag{3.67}$$

We choose to leave the right hand side of the above equation in terms of the local Frenet coordinate system, and to rewrite the left hand side of this equation in terms of the global Cartesian coordinate system:

$$\begin{aligned}dx^2 + dy^2 + dz^2 &= (du^2 + ds^2 + dt^2) + 2U_{uu}du^2 + 2U_{ss}ds^2 + 2U_{tt}dt^2 \\ &+ 4U_{us}duds + 4U_{ut}dudt + 4U_{st}dsdt,\end{aligned} \tag{3.68}$$

where we have employed Eq. (3.66) and the symmetry property of the strain tensor in Eq. (3.48).

We will now express dx, dy, and dz in terms of helix radius $R(u)$, helix pitch angle, ψ, the azimuthal angle ϕ, and the Frenet coordinates t, s, and u. We will do so by using Eq. (3.60):

$$\begin{aligned}dx &= d\left[R(u')\cos\phi\right] = \cos\phi d\left[R(u')\right] - R(u')\sin\phi d\phi, \\ dy &= d\left[R(u')\sin\phi\right] = \sin\phi d\left[R(u')\right] + R(u')\cos\phi d\phi, \\ dz &= d\left[t'\sin\psi + s'\cos\psi\right] = \sin\psi d\left[t'\right] + \cos\psi d\left[s'\right],\end{aligned} \tag{3.69}$$

where $d\phi$ can be obtained from Eq. (3.59) to be

$$d\phi = d\left[\frac{t'\cos\psi - s'\sin\psi}{R(u'=0)}\right] = \frac{\cos\psi}{R(u'=0)}d\left[t'\right] - \frac{\sin\psi}{R(u'=0)}d\left[s'\right]. \tag{3.70}$$

Finally, we note that from Eq. (3.63),

$$\begin{aligned}d\left[s'\right] &= ds + \frac{Bu}{R}du, \\ d\left[t'\right] &= dt + \frac{Cu}{R}du,\end{aligned} \tag{3.71}$$

(3.72)

where again $R = R(u' = 0)$. Substituting the expressions in Eqs. 3.70 and 3.71 into 3.69 and squaring the result, we obtain

$$\begin{aligned} dx^2 &= \left\{\left[(\cos\phi)(1+A\frac{u}{R}) + (\sin\phi)f(u)\left((\sin\psi)B\frac{u}{R} - (\cos\psi)C\frac{u}{R}\right)\right]du \right. \\ &\quad +[(\sin\phi)f(u)(\sin\psi)]ds \\ &\quad \left. -[(\sin\phi)f(u)(\cos\psi)]dt\right\}^2, \qquad (3.73) \\ dy^2 &= \left\{\left[(\sin\phi)(1+A\frac{u}{R}) + (\cos\phi)f(u)((\sin\psi)B\frac{u}{R} - (\cos\psi)C\frac{u}{R}\right]du \right. \\ &\quad -[(\cos\phi)f(u)(\sin\psi)]ds \\ &\quad \left. + [(\cos\phi)f(u)(\cos\psi)]dt\right\}^2, \qquad (3.74) \\ dz^2 &= \left\{\left[(\cos\psi)B\frac{u}{R} + (\sin\psi)C\frac{u}{R}\right]du \right. \\ &\quad +[\cos\psi]ds \\ &\quad \left. + [\sin\psi]dt\right\}^2, \qquad (3.75) \end{aligned}$$

where we have combined the terms that go as du, ds, and dt. In the above expression we also used the notation

$$f(u) = 1 + \frac{u}{R} + \frac{Au^2}{2R^2}. \qquad (3.76)$$

After performing the squaring of all components in Eq. (3.73) and combining the result into terms that go as du^2, ds^2, dt^2, $duds$, $dudt$, and $dsdt$, we can find the components of U_{ij} in Eq. (3.68) to be:

$$\begin{aligned} U_{uu} &= \frac{1}{2}\left[\left[\left(R\frac{df}{du}\right)^2 - 1\right] + \left(f^2(u)-1\right)\left[\sin\psi\frac{Bu}{R} - \cos\psi\frac{Cu}{R}\right]^2 + \left(\frac{Bu}{R}\right)^2 + \left(\frac{Cu}{R}\right)^2\right], \\ U_{ss} &= \frac{1}{2}(f^2(u)-1)\sin^2\psi, \\ U_{tt} &= \frac{1}{2}(f^2(u)-1)\cos^2\psi, \qquad (3.77) \\ U_{us} &= \frac{1}{2}\left(\frac{Bu}{R} + (f^2(u)-1)\sin\psi\left(\sin\psi\frac{Bu}{R} - \cos\psi\frac{Cu}{R}\right)\right), \\ U_{ut} &= \frac{1}{2}\left(\frac{Cu}{R} - (f^2(u)-1)\cos\psi\left(\sin\psi\frac{Bu}{R} - \cos\psi\frac{Cu}{R}\right)\right), \\ U_{st} &= \frac{1}{2}(1-f^2(u))\sin\psi\cos\psi, \end{aligned}$$

where $f(u)$ is given in Eq. (3.76). It is worthwhile noting that the terms proportional to $\sin\phi$ and $\cos\phi$ do not contribute to Eq. (3.77) as they cancel each other in the process of squaring and recombination that we performed on going from Eq. (3.73) to Eq. (3.77). Since our original parametrization only included terms to order u^2/R,

and since elastic free energy (Eq. (3.47)) is squared in U_{ij}, to the same level of approximation, we should only keep terms to the order u/R. Thus,

$$\begin{aligned} U_{uu} &= A\frac{u}{R}, \\ U_{ss} &= \sin^2\psi\frac{u}{R}, \\ U_{tt} &= \cos^2\psi\frac{u}{R}, \\ U_{us} &= \frac{1}{2}\frac{Bu}{R}, \\ U_{ut} &= \frac{1}{2}\frac{Cu}{R}, \\ U_{st} &= -\sin\psi\cos\psi\frac{u}{R}, \end{aligned} \tag{3.78}$$

where $R = R(u' = 0)$.

Self-Consistency Check: Consideration Of The Physical Deformation That Occurs When A Flat Thin Plate Is Bent.

The components of the strain tensor in Eq. (3.78) can be derived using a more traditional approach, by writing down the physical deformation occurring when a thin flat plate (or a ribbon) is bent into a helical shape. The deformation that occurs (or the displacement of a point that occurs) upon application of any arbitrary stress (see Appendix 3.B) can be written as in eqneqn:displacements

$$\begin{aligned} \omega_u &= u' - u, \\ \omega_s &= s' - s, \\ \omega_t &= t' - t. \end{aligned} \tag{3.79}$$

Then with the definition of strain tensor,

$$U_{ij} = \frac{1}{2}\left(\frac{\partial\omega_i}{\partial u_j} + \frac{\partial\omega_j}{\partial u_i}\right), \tag{3.80}$$

we find

$$\begin{aligned} U_{ss} &= \frac{1}{2}\left(\frac{\partial\omega_s}{\partial s} + \frac{\partial\omega_s}{\partial s}\right) = \frac{\partial\omega_s}{\partial s}, \\ U_{tt} &= \frac{1}{2}\left(\frac{\partial\omega_t}{\partial t} + \frac{\partial\omega_t}{\partial t}\right) = \frac{\partial\omega_t}{\partial t}, \\ U_{st} &= \frac{1}{2}\left(\frac{\partial\omega_s}{\partial t} + \frac{\partial\omega_t}{\partial s}\right). \end{aligned} \tag{3.81}$$

We will now consider a short segment of the flat plate (or ribbon) and determine the relationship of the unprimed and primed Frenet coordinates of a point when the plate (ribbon) is bent. We will be considering only locally small deformations.[j] The condition of locally small deformations also implies that the following assumption can be made: any normal to the neutral surface in the undeformed (flat) state will remain normal to the neutral surface in the deformed (helical) state.[95,96] By definition, the neutral surface remains unstrained after bending. We will consider a section of the ribbon parallel to the ut surface, as shown in Figure 3.12. After bending, a point P on the neutral surface is deflected into the point P', which remains on the neutral surface but is deflected by a distance w. If we choose a point Q to be initially on the normal to the neutral surface at a distance u from the point P, after bending the flat plate (ribbon) the point Q' must be laying at a distance u' from P' on the normal to the neutral surface in the bent state. Examining the geometrical configuration described in Figure 3.12, we observe that the displacement of the point Q' along the t-axis is

$$\omega_t = t' - t = -u' \sin\alpha \approx -u' \tan\alpha. \tag{3.82}$$

Since the deflection of the plate (ribbon) is small, we can use the approximation that $\alpha \approx \tan\alpha$. From the Figure 3.12, it can be observed that the line OP' is the tangent to the neutral surface. By comparing the two triangles $Q'P'D$ and $OP'P$, it can be observed that the angle at the apex O of the triangle $OP'P$ is the same as that at the apex P' of the triangle $Q'P'D$ and is equal to α. Then, $\tan\alpha = \partial w/\partial t$. That is, we can rewrite Eq. (3.82) as

$$\omega_t = -u' \frac{\partial w}{\partial t}. \tag{3.83}$$

By a similar argument, we can describe the displacement of the point Q' along the s-axis as

$$\omega_s = -u' \frac{\partial w}{\partial s}. \tag{3.84}$$

Recalling that $u' = u + 1/2A(u^2/R)$, we will use $u' \approx u$ since we need the strain tensor components only to the first order in u. Then, Eqs. 3.83 and 3.84 become

$$\begin{aligned} \omega_t &= -u \frac{\partial w}{\partial t} \quad \text{and} \\ \omega_s &= -u \frac{\partial w}{\partial s}. \end{aligned} \tag{3.85}$$

[j]For now, we will define locally small deformations as those, in which the deflection of the neutral surface, i. e. the surface that undergoes no stretching or compression upon plate (ribbon) deformations, are small compared to the thickness h of the plate (ribbon).

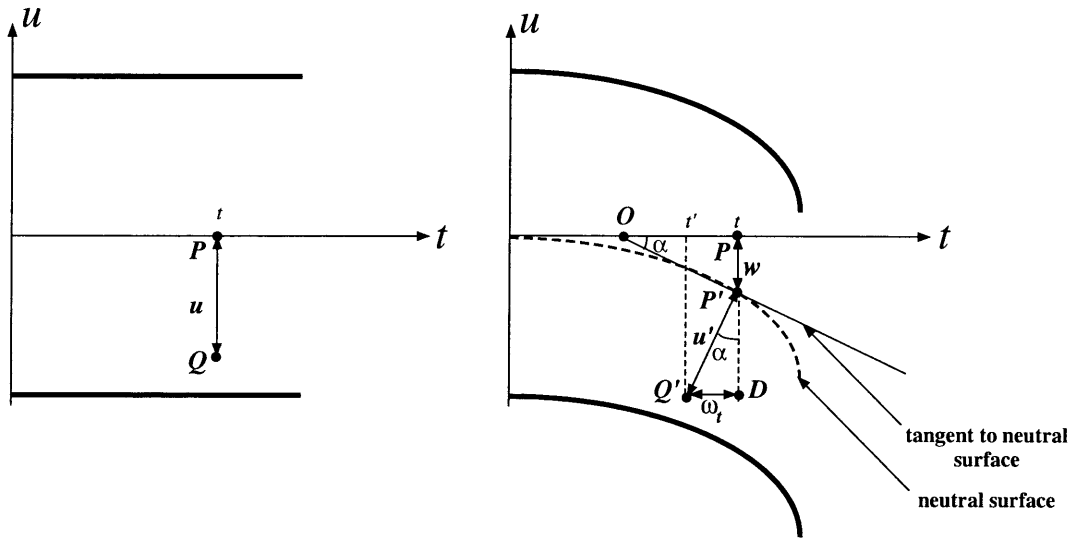

(a) (b)

Figure 3.12: (a) A section of a flat elastic plate (or a ribbon) in the ut-plane. Two points P and Q are shown. The point P is located on a neutral surface. The point Q is located on the normal to the neutral surface a distance u away from the point P. The neutral surface coincides with the t-axis. (b) The same section of an elastic plate (or a ribbon) under a bending deformation. The point P has been deformed into P' and the point Q has been deformed into the point Q'. The latter point is still located on the normal to the neutral surface a distance u' from the point P'. The distance between the points P and P' is characterized by a displacement w along the u-axis (for small deflections of a plate, there is no displacement of the point P' with respect to P along the t-axis The neutral surface is shown as a dashed line.

With these coordinate transformations, we can rewrite the strain tensor components U_{ss}, U_{tt}, and U_{st} in Eq. (3.81) as

$$\begin{aligned} U_{ss} &= -u\frac{\partial^2 w}{\partial s^2}, \\ U_{tt} &= -u\frac{\partial^2 w}{\partial t^2}, \\ U_{st} &= -u\frac{\partial^2 w}{\partial s \partial t}. \end{aligned} \tag{3.86}$$

We now have to describe the deflection of the neutral surface, w, in terms of the radius, $R(u'=0)$ (the distance from the helix axis to the neutral surface), and the azimuthal angle, ϕ. This deflection is depicted in Figure 3.13. A small deformation of the neutral surface, i. e. the deformation in which $w < h$, can be approximated as

$$\begin{aligned} w = x_f - x_i = R(u'=0)\cos\phi - R(u'=0) \\ \approx R(u'=0)\left(1 - \frac{\phi^2}{2} - 1\right) = -\frac{1}{2}R(u'=0)\phi^2. \end{aligned} \tag{3.87}$$

Substituting the expression for the azimuthal angle ϕ in terms of the Frenet coordinates t' and s', as described in Eq. (3.59), we find

$$w \approx -\frac{1}{2}R(u'=0)\left(\frac{t'\cos\psi - s'\sin\psi}{R(u'=0)}\right)^2 = -\frac{1}{2}\frac{(t'\cos\psi - s'\sin\psi)^2}{R(u'=0)}. \tag{3.88}$$

To the first order in the thickness parameter u, the above expression can be approximated as

$$w \approx -\frac{1}{2}\frac{(t\cos\psi - s\sin\psi)^2}{R(u'=0)}, \tag{3.89}$$

since to that order $u' \approx u$, $s' \approx s$, and $t' \approx t$. This expression for the deflection w of the neutral surface allows us to calculate the s and the t components of the deformation tensor in Eq. (3.86). Taking the necessary derivatives (as in Eq. (3.86)) of w in Eq. (3.89), we obtain

$$\begin{aligned} U_{ss} &= \sin^2\psi\frac{u}{R}, \\ U_{tt} &= \cos^2\psi\frac{u}{R}, \\ U_{st} &= -\sin\psi\cos\psi\frac{u}{R}. \end{aligned} \tag{3.90}$$

Comparing our results in Eq. (3.90) to those in Eq. (3.78), we observe that the two different techniques of calculating the components of the deformation tensor are

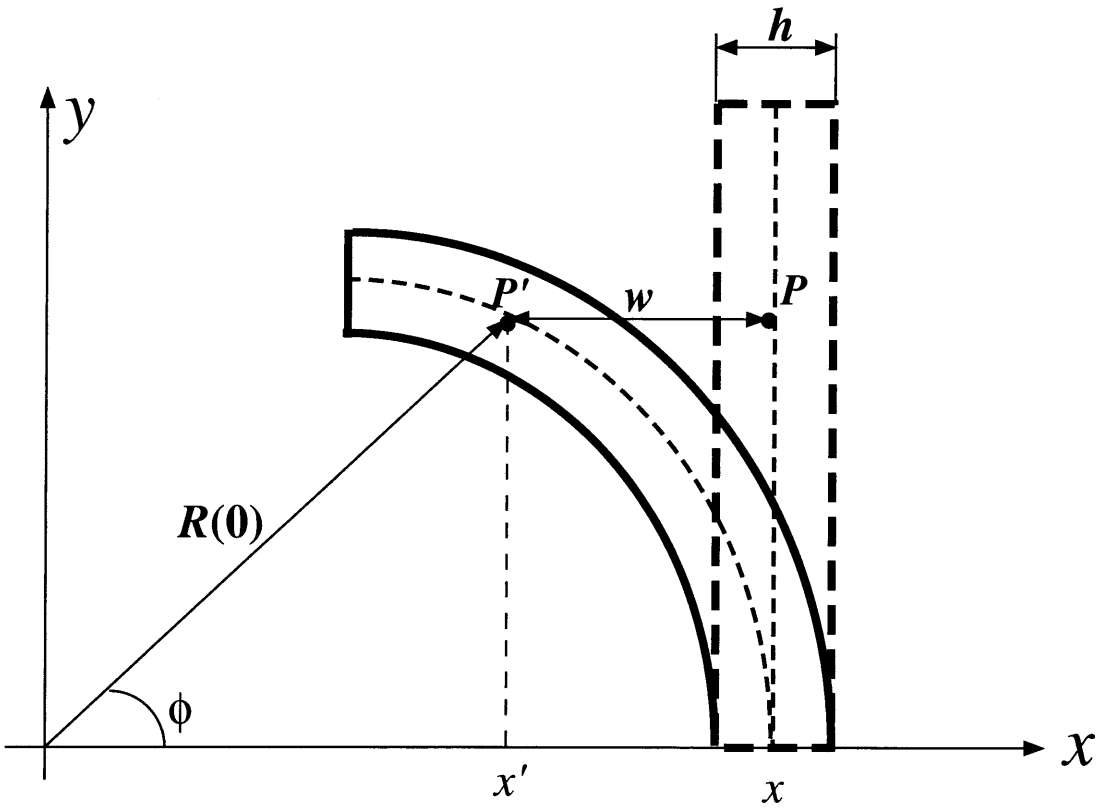

Figure 3.13: (a) A section of a flat elastic plate (or a ribbon) in the xy-plane is shown as a bold dashed line. A deformed section of the same elastic plate (or a ribbon) is shown as a bold solid line. The neutral surface for both undeformed (flat) case and the deformed case is shown as a bold dashed line. The plate is deformed into a helical shape of radius $R(u' = 0)$ (measured from the center of curvature to the neutral surface). The section of ribbon shown spans the azimuthal angle ϕ. The deflection w of a point P on the neutral surface into the point P' that is still located on the neutral surface is shown. The thickness of the plate (ribbon) is h. The Cartesian coordinate system is shown.

internally self–consistent. Unlike the first technique though, the second method has not given us any direct information regarding the U_{ij} components, in which either or both i and j are equal to u. However, we can solve for these components of the strain tensor by applying the boundary condition of zero bending force on the edges of the ribbon, as will be described below. In addition to being able to provide a self–consistency check, the second technique of finding the deformation tensor components is also useful in defining what "a small deformation" is in the case when a flat plate (ribbon) is bent into a helical shape.

Definition of "A Small Deformation".

As described above, the condition that a deformation is small implies that the deformation w of a neutral surface is small in comparison to the ribbon thickness h (see Figure 3.13). It is clear that this definition is not valid for a long plate (ribbon) wound in a helical shape and requires some clarification. The condition for the small deformation then must be that w on Figure 3.13 is small in comparison to h only over the ribbon length comparable to the thickness. This implies that a good model for a small deformation would be a bent plate of thickness h and of length and width on the order of h, $t' = h$ and $s' = h$, respectively, such that the bending moment is along the t' and s' axes, as shown in Figure 3.14. In this case, the deflection of the neutral surface must be small in comparison to h. This condition may be written in the analytical form using Eq. (3.88):

$$\left| -\frac{1}{2} \frac{(h\cos\psi - h\sin\psi)^2}{R(u'=0)} \right| \ll h \tag{3.91}$$

or

$$\frac{h/2}{R(u'=0)} \ll \frac{2}{(\cos\psi - \sin\psi)^2}. \tag{3.92}$$

The parameter $(h/2)/R(u'=0)$ on the left hand side of the above expression is the familiar u/R parameter that we obtain in all of the components of the strain tensor calculated on a surface of a helical ribbon. Therefore, we can rewrite Eq. (3.92) as

$$\frac{u|_{\text{surface}}}{R} \ll \frac{2}{(\cos\psi - \sin\psi)^2}. \tag{3.93}$$

To obtain the result in Eq. (3.93) we have used a relatively arbitrary condition that the deformation occurs over a length and width equal to h. In fact, this condition

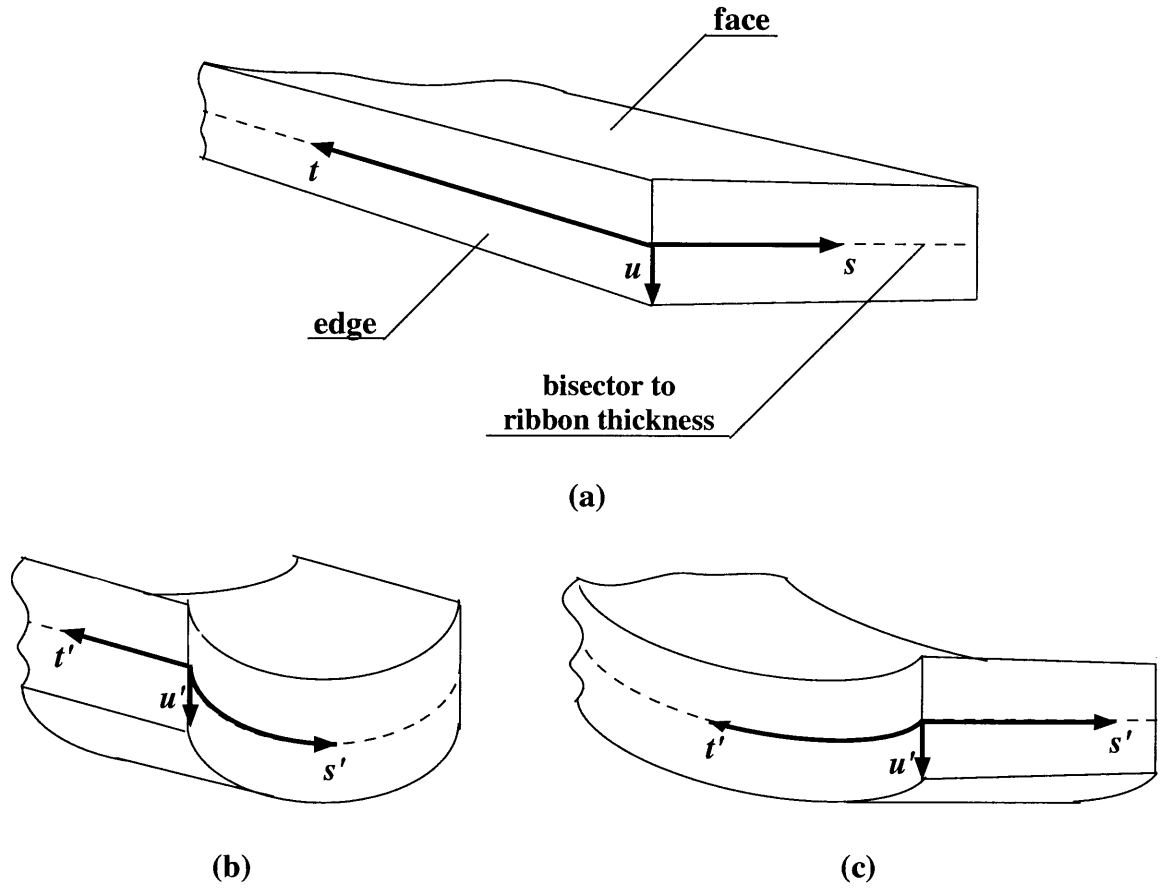

Figure 3.14: (a) A section of a flat ribbon (or an elastic plate) with a local Frenet coordinate system shown. (b) a section of a ribbon (or an elastic plate) with a bending moment along the t' axis and with a local Frenet coordinate system shown; (c) a section of a ribbon (or an elastic plate) with a bending moment along the s' axis and with a local Frenet coordinate system shown.

does not apply to the case of helical ribbon with a pitch angle $\psi = 45°$ since the expressions in Eqs. 3.92 and 3.93 diverge. Therefore, in this case we can choose a different area to avoid divergence.

This condition is consistent with our understanding of what a "small deformation" is for a helical ribbon.

The Stress–Strain Relationship.

To obtain the stress–strain relationship, it is necessary to take into account the condition of mechanical equilibrium for a plate (ribbon) in a deformed state. We will do so by following the example from *Theory of Elasticity* by Landau and Lifshitz.[37] In equilibrium, the external forces that cause the plate to bend must be equal in magnitude but opposite in direction to the internal forces in the plate. If an external force $\vec{\Sigma^{ext}}$ is acting on a unit area dA of the body, then the external force $\Sigma^{ext}dA$ acts on the surface element dA. Then, in equilibrium the internal force $\sigma_{ij}dA_j$ must be acting on this surface element dA. Therefore,

$$\Sigma_i^{ext}dA = \sigma_{ij}dA_j. \tag{3.94}$$

Assuming the notation that $\hat{n}$ is a unit normal vector to the surface of the plate (ribbon), the above condition translates into

$$\Sigma_i^{ext} = \sigma_{ij}n_j. \tag{3.95}$$

Now, since the plate is thin, the external stresses that hold the plate (ribbon) in a deformed state are much smaller than the internal stresses caused by compression and extension of various parts of the plate (ribbon). Therefore, Σ_i^{ext} in the above expression becomes effectively zero, such that

$$\sigma_{ij}n_j = 0, \tag{3.96}$$

where n_j is parallel to the u coordinate, since the latter is normal to the ribbon "face" or surface just as $\hat{n}$ is. Therefore, mathematically the mechanical equilibrium condition for the ribbon is $\sigma_{iu} = 0$, i.e. using the symmetry property of the stress tensor,

$$\sigma_{uu} = \sigma_{su} = \sigma_{us} = \sigma_{tu} = \sigma_{ut} = 0 \tag{3.97}$$

This condition uniquely determines the three independent parameters in the stress tensor:

$$\sigma_{ij} = \begin{pmatrix} 0 & 0 & 0 \\ 0 & \sigma_{ss} & \sigma_{st} \\ 0 & \sigma_{ts} & \sigma_{tt} \end{pmatrix} \tag{3.98}$$

Recalling that $\sigma_{ij} = \lambda_{ijkl} U_{kl}$, as shown in Eq. (3.50), the expressions in Eq. (3.97) can be solved for A, B, and C in terms of the λ_{ijkl}'s. For example, for σ_{uu} term, using Eq. (3.50) we have

$$\begin{aligned} 0 = \sigma_{uu} &= \lambda_{uuuu}U_{uu} + \lambda_{uuss}U_{ss} + \lambda_{uutt}U_{tt} \\ &\quad +2\lambda_{uuus}U_{us} + 2\lambda_{uuut}U_{ut} + 2\lambda_{uust}U_{st} \\ &\approx \lambda_{uuuu}A\frac{u}{R} + \lambda_{uuss}\sin^2\psi\frac{u}{R} + \lambda_{uutt}\cos^2\psi\frac{u}{R} \\ &\quad +2\lambda_{uuus}\frac{1}{2}B\frac{u}{R} + 2\lambda_{uuut}\frac{1}{2}C\frac{u}{R} + 2\lambda_{uust}(-\sin\psi\cos\psi\frac{u}{R}. \end{aligned} \tag{3.99}$$

Rearranging this expression and repeating the same procedure for σ_{us} and σ_{ut}, we obtain

$$\begin{aligned} A\lambda_{uuuu} + B\lambda_{uuus} + C\lambda_{uuut} &= -\lambda_{uuss}\sin^2\psi - \lambda_{uutt}\cos^2\psi + \lambda_{uust}\sin 2\psi, \\ A\lambda_{usuu} + B\lambda_{usus} + C\lambda_{usut} &= -\lambda_{uuss}\sin^2\psi - \lambda_{ustt}\cos^2\psi + \lambda_{ussst}\sin 2\psi \\ A\lambda_{utuu} + B\lambda_{utus} + C\lambda_{utut} &= -\lambda_{utss}\sin^2\psi - \lambda_{uttt}\cos^2\psi + \lambda_{utst}\sin 2\psi. \end{aligned} \tag{3.100}$$

These expressions are very complicated and lead to no physical insight into the system. However, the importance of calculating these expressions lies in the fact that each of the parameters A, B, and C is a linear combination of sin's and cos's:

$$\begin{aligned} A &\sim a_1\sin^2\psi + a_2\sin\psi\cos\psi + a_3\cos^2\psi, \\ B &\sim b_1\sin^2\psi + b_2\sin\psi\cos\psi + b_3\cos^2\psi, \\ C &\sim c_1\sin^2\psi + c_2\sin\psi\cos\psi + c_3\cos^2\psi. \end{aligned} \tag{3.101}$$

where a_i, b_i, and c_i are functions of elastic moduli λ_{ijkl}'s.

Now, we are ready to write down the general form of the elastic free energy per unit volume in Eq. (3.51) in terms of A, B, and C. To begin, let us rewrite Eq. (3.51) as

$$\begin{aligned} F &= \frac{1}{2}\lambda_{uuuu}U_{uu}U_{uu} + \frac{1}{2}\lambda_{ssss}U_{ss}U_{ss} + \frac{1}{2}\lambda_{tttt}U_{tt}U_{tt} \\ &\quad +2\lambda_{uuus}U_{uu}U_{us} + 2\lambda_{uuut}U_{uu}U_{ut} + \lambda_{uuss}U_{uu}U_{ss} \\ &\quad +2\lambda_{uust}U_{uu}U_{st} + \lambda_{uutt}U_{uu}U_{tt} + 2\lambda_{usus}U_{us}U_{us} + \ldots \end{aligned} \tag{3.102}$$

Altogether, there are 21 terms in the above expression for the elastic free energy per unit volume. Now, using Eq. (3.78), the above expression becomes

$$\begin{aligned} F &= \frac{u^2}{R^2}\Big[\frac{1}{2}\lambda_{uuuu}AA + \frac{1}{2}\lambda_{ssss}\sin^4\psi + \frac{1}{2}\lambda_{tttt}\cos^4\psi \\ &\quad +2\lambda_{uuus}AB + 2\lambda_{uuut}AC + \lambda_{uuss}A\sin^2\psi \\ &\quad - 2\lambda_{uust}A\cos\psi\sin\psi + \lambda_{uutt}A\cos^2\psi + \frac{1}{2}\lambda_{usus}B^2 + ...\Big] \end{aligned} \tag{3.103}$$

Taking into account the general form of A, B, and C given in Eq. (3.101), we can rewrite the elastic free energy per unit volume in Eq. (3.103) as

$$\begin{aligned} F &= \frac{u^2}{R^2}\Big[K_1\cos^4\psi + K_2\cos^3\psi\sin\psi + K_3\cos^2\sin^2\psi \\ &\quad +K_4\cos\psi\sin^3\psi + K_5\sin^4\psi\Big] \end{aligned} \tag{3.104}$$

where coefficients K_i's are again some combination of the λ_{ijkl}'s and we have grouped the terms corresponding to each $\cos^4\psi$, $\cos^3\psi\sin\psi$, $\cos^2\sin^2\psi$, $\cos\psi\sin^3\psi$, and $\sin^4\psi$. Since we cannot find the λ_{ijkl}'s theoretically, the coefficients in the Eq. (3.104) may be replaced by phenomenological parameters that can be measured experimentally.

We further need to find the elastic free energy per unit area of the helical ribbons. This is done by integrating the elastic free energy in Eq. (3.104) over the ribbon thickness, u, with an assumption that the K_i's do not depend on the ribbon thickness. This yields to an overall multiplicative factor of $h^3/24$ which can be absorbed by the coefficients K_i's making them explicitly dependent on ribbon thickness. Defining

$$K_i' = K_i\frac{h^3}{24}, \tag{3.105}$$

the form of the elastic free energy per unit area of a helical ribbon is given by:

$$\begin{aligned} \mathbf{a}_{elastic} &= \frac{1}{R^2}[K_1'\cos^4\psi + K_2'\cos^3\psi\sin\psi \\ &\quad +K_3'\cos^2\sin^2\psi + K_4'\cos\psi\sin^3\psi + K_5'\sin^4\psi]. \end{aligned} \tag{3.106}$$

However, this is not the full form of the free energy per unit area of a helical ribbon, since a term describing the spontaneous bending needs to be present in this expression. It is reasonable to have this term, $\mathbf{a}_{bend}$, be proportional to $1/R$ in analogy with a surface tension model, and to some constant K, which in general may depend on the pitch angle, ψ:

$$\mathbf{a}_{bend} = -K(\psi)/R, \tag{3.107}$$

where the negative sign implies that the $\mathbf{a}_{bend}$ term is lowering the total free energy per unit area of a helix, $\mathbf{a}_{\text{helix}}$. However, any dependence of $\mathbf{a}_{bend}$ on pitch angle has the physical consequence of predicting a dependence of the helical radii on the pitch angle. Since this dependence has not been found experimentally, the inclusion of $K = K(\psi)$ is not necessary and $\mathbf{a}_{bend}$ becomes

$$\mathbf{a}_{bend} = -K/R. \tag{3.108}$$

This leads to

$$\begin{aligned} \mathbf{a}_{helix} &= \mathbf{a}_{elastic} + \mathbf{a}_{bend} \\ &= \frac{1}{R^2}[K_1' \cos^4\psi + K_2' \cos^3\psi \sin\psi \\ &\quad + K_3' \cos^2 \sin^2\psi + K_4' \cos\psi \sin^3\psi + K_5' \sin^4\psi] - \frac{K}{R}. \end{aligned} \tag{3.109}$$

The above expression for the free energy per unit area of a helical ribbon represents the simplest and most general model describing helical ribbons as crystalline structures. It does not rely on any knowledge of the detailed underlying structure of a helix, i.e. neither the nature of underlying molecules nor their arrangements within helix walls is assumed. We also have employed the minimum set of requirements and assumptions in order to create this model.

We can further simplify this general form of the elastic free energy density of a helical ribbon by taking into account experimentally observed symmetries. The ribbons grow symmetrically both in width and in length. This growth occurs very anisotropically, i.e. ribbons grow quickly along the t-axis, contour length, and slowly along the s-axis, width. If a ribbon contains a mirror plane, than that mirror plane must lie along one of the above mentioned axes. This means that if the underlying crystal is invariant under reflections about such a mirror plane, then the elastic modulus tensor is also invariant under such reflections. Mathematically, this means that λ_{ijkl} is invariant under reflections that change s to $-s$, i.e. reflections about ut symmetry plane, or under reflections that change t to $-t$, i.e. reflections about us symmetry plane. Let us consider the consider the consequences of the existence of each mirror symmetry plane separately.

For the ut symmetry plane, all the contributions to $\mathbf{a}_{elastic}$ from components of λ_{ijkl} with an odd number of suffixes s vanish. Then A, B, and C in Eq. (3.100) can be calculated in terms of the rest of the λ_{ijkl}'s to be:

$$A = \frac{1}{\lambda_{uuuu} - \frac{\lambda_{uuut}}{\lambda_{utut}}\lambda_{uuut}}[(\frac{\lambda_{uuut}}{\lambda_{utut}}\lambda_{utss} - \lambda_{uuss}) \sin^2\psi + (\frac{\lambda_{uuut}}{\lambda_{utut}}\lambda_{uttt} - \lambda_{uutt}) \cos^2\psi],$$

$$B = \frac{\lambda_{usst}}{\lambda_{usus}} \sin 2\psi, \tag{3.110}$$

$$C = \frac{1}{\lambda_{uuut} - \frac{\lambda_{uuuu}}{\lambda_{uuut}}\lambda_{utut}}[(\frac{\lambda_{uuuu}}{\lambda_{uuut}}\lambda_{utss} - \lambda_{uuss})\sin^2\psi + (\frac{\lambda_{uuuu}}{\lambda_{uuut}}\lambda_{uttt} - \lambda_{uutt})\cos^2\psi].$$

With these A, B, and C we can calculate all the K_i''s in $\mathbf{a}_{helix}$.

We note that with ut symmetry, K_4', i.e. the constant of the cross term $\cos\psi\sin^3\psi$, comes from:

$$\begin{aligned}&\lambda_{uuus}AB - 2\lambda_{uust}A\cos\psi\sin\psi + \lambda_{usut}BC \\ &-2\lambda_{ssst}\cos\psi\sin^3\psi - 2\lambda_{utst}C\cos\psi\sin\psi + \lambda_{ssus}B\sin^2\psi\end{aligned} \tag{3.111}$$

This expression is equal to zero since each λ_{ijkl} contains an odd number of suffixes s. With the same symmetry, K_2', i.e. the constant of the cross term $\cos^3\psi\sin\psi$, comes from:

$$\begin{aligned}&\lambda_{uuus}AB - 2\lambda_{uust}A\cos\psi\sin\psi + \lambda_{usut}BC \\ &-2\lambda_{sttt}\cos^3\psi\sin\psi - 2\lambda_{utst}C\cos\psi\sin\psi + \lambda_{ttus}B\cos^2\psi\end{aligned} \tag{3.112}$$

This expression is also equal to zero since again each λ_{ijkl} contains odd number of suffixes s. Therefore under the assumption of ut symmetry, both cross terms are identically zero.

Now, let us look at the us symmetry plane. In this case, all the contributions to $\mathbf{a}_{elastic}$ from components of λ_{ijkl} with odd number of suffixes t vanish. Then we calculate A, B, and C in Eq. (3.100) in terms of the rest of the λ_{ijkl}'s to be:

$$\begin{aligned}A &= \frac{1}{\lambda_{uuuu} - \frac{\lambda_{uuus}}{\lambda_{usus}}\lambda_{uuus}}[(\frac{\lambda_{uuus}}{\lambda_{usus}}\lambda_{usss} - \lambda_{uuss})\sin^2\psi \\ &\quad +(\frac{\lambda_{uuus}}{\lambda_{usus}}\lambda_{ustt} - \lambda_{uutt})\cos^2\psi] \\ B &= \frac{1}{\lambda_{uuus} - \frac{\lambda_{uuuu}}{\lambda_{uuus}}\lambda_{usus}}[(\frac{\lambda_{uuuu}}{\lambda_{uuus}}\lambda_{usss} - \lambda_{uuss})\sin^2\psi \\ &\quad +(\frac{\lambda_{uuuu}}{\lambda_{uuus}}\lambda_{ustt} - \lambda_{uutt})\cos^2\psi] \\ C &= \frac{\lambda_{utst}}{\lambda_{utut}}\sin 2\psi\end{aligned} \tag{3.113}$$

Calculating all the K_i''s in $\mathbf{a}_{helix}$ with these A, B, and C, we note that with us symmetry, K_4', i.e. the constant of the cross term $\cos\psi\sin^3\psi$, comes from:

$$\begin{aligned}&\lambda_{uuut}AC - 2\lambda_{uust}A\cos\psi\sin\psi + \lambda_{usut}BC \\ &-2\lambda_{ssst}\cos\psi\sin^3\psi - 2\lambda_{usst}B\cos\psi\sin\psi + \lambda_{ssut}C\sin^2\psi\end{aligned} \tag{3.114}$$

Again, this expression is equal to zero since each λ_{ijkl} contains odd number of suffixes t. We repeat the same calculation for K_2', i.e. the constant of the cross term $\cos^3\psi\sin\psi$, and find that it comes from:

$$\begin{aligned}&\lambda_{uuut}AC - 2\lambda_{uust}A\cos\psi\sin\psi + \lambda_{usut}BC\\&-2\lambda_{sttt}\cos^3\psi\sin\psi - 2\lambda_{usst}B\cos\psi\sin\psi + \lambda_{ttut}C\cos^2\psi,\end{aligned} \tag{3.115}$$

which is also equal to zero since again each λ_{ijkl} contains odd number of suffixes t. Thus we find that under the assumption of either ut or us symmetry planes, the coefficients in front of both cubic cross terms are identically zero.

Thus the anisotropic growth of the ribbons in their width and length suggests that the underlying crystal has at least one mirror plane aligned with either the t-axis or the s-axis, respectively. The experimental observation that helical ribbons grow symmetrically both in width and in length further suggests that underlying crystal may possess both symmetry planes. With this assumption, the resulting free energy density for the helical ribbons $\mathbf{a}_{helix}$ is simplified to:

$$\mathbf{a}_{helix} = \frac{1}{R^2}(K_\alpha cos^4\psi + 2K_\beta\cos^2\psi\sin^2\psi + K_\gamma\sin^4\psi) - \frac{K}{R}, \tag{3.116}$$

where K_α, K_β, and K_γ are the remaining phenomenological parameters which are different under either of the two choices of symmetry. However, when both mirror symmetries are assumed, K_α, K_β, and K_γ take on the following simple form in terms of the components of the elastic modulus tensor:

$$\begin{aligned}K_\alpha &\equiv K_1' = \frac{h^3}{24}\left(\lambda_{tttt} - \frac{\lambda_{uutt}^2}{\lambda_{uuuu}}\right)\\K_\beta &\equiv \frac{K_3'}{2} = \frac{h^3}{24}\left(\lambda_{sstt} + 2\lambda_{stst} - \frac{\lambda_{uuss}\lambda_{uutt}}{\lambda_{uuuu}}\right)\\K_\gamma &\equiv K_5' = \frac{h^3}{24}\left(\lambda_{ssss} - \frac{\lambda_{uuss}^2}{\lambda_{uuuu}}\right)\end{aligned} \tag{3.117}$$

The locations of the extrema in the expression of the elastic free energy density (Eq. (3.116)) are found by simultaneously minimizing Eq. (3.116) with respect to radius, R and pitch angle, ψ. The resulting expression for the equilibrium value of radius is:

$$R_0 = \frac{2}{K}\frac{(K_\alpha K_\gamma - K_\beta^2)}{(K_\alpha - 2K_\beta + K_\gamma)} \tag{3.118}$$

As one can see, the equilibrium value of the helix radius is independent of the pitch angle by construction, i.e. $K \neq K(\psi)$. This assumption was made due to our experimental observation of helical pitch angle being independent of helix radius. Minimization of $\mathbf{a}_{helix}$ with respect to pitch angle leads to the following equilibrium pitch value:

$$\psi_0 = \arctan\left[\left(\frac{K_\alpha - K_\beta}{K_\gamma - K_\beta}\right)^{\frac{1}{2}}\right]. \tag{3.119}$$

It is worthwhile noting that crystalline model predicts the equilibrium pitch angle to be a ratio of elastic moduli, analogous to the results in the theories of Chung *et al.* and Selinger *et al.*. However, the crystalline theory predicts a ratio of 1.85 for the high pitch helical ribbons ($\psi = 53.7°$) and a ratio of 0.0385 for the low pitch helical ribbons ($\psi = 11.1°$). We also notice that since the helical pitch angle is a real number, one of the two following conditions on the phenomenological elastic coefficients must hold:

$$\begin{gathered} K_\alpha > K_\beta \quad \text{AND} \quad K_\gamma > K_\beta \\ \text{OR} \\ K_\alpha < K_\beta \quad \text{AND} \quad K_\gamma < K_\beta \end{gathered} \tag{3.120}$$

We can further narrow the condition in Equation Eq. (3.120) by observing that for ψ_0 to be a minimum of $\mathbf{a}_{helix}$, the second derivative of the elastic free energy density with respect to the equilibrium pitch angle

$$\begin{aligned} \frac{\partial^2 \mathbf{a}}{\partial \psi^2} &= \frac{1}{R^2}\left[2\sin^2 2\psi(K_\alpha - 2K_\beta + K_\gamma)\right. \\ &\quad \left. +4\cos 2\psi \cos^2\psi[(K_\beta - K_\alpha) + \tan^2\psi(K_\gamma - K_\beta)]\right] \end{aligned} \tag{3.121}$$

must be positive. This leads to the following inequality:

$$\frac{\partial^2 \mathbf{a}}{\partial \psi^2}\,|_{\psi_0} = \frac{1}{R^2}\frac{\partial^2 f}{\partial \psi^2}\,|_{\psi_0} = 2\left(\frac{\sin 2\psi_0}{R}(K_\alpha - 2K_\beta + K_\gamma)\right) > 0, \tag{3.122}$$

where $f = K_\alpha cos^4\psi + 2K_\beta \cos^2\psi \sin^2\psi + K_\gamma \sin^4\psi$. Combining this result with the condition in Eq. (3.120), we obtain that for the ψ_0 extremum to be a minimum, the allowed values for the elastic coefficients must satisfy:

$$K_\alpha > K_\beta \quad \text{AND} \quad K_\gamma > K_\beta. \tag{3.123}$$

In terms of the coefficients of the elastic modulus tensor this condition translates into:

$$\lambda_{tttt} - 2\lambda_{sstt} + \lambda_{ssss} + 4\lambda_{stst} > \frac{1}{\lambda_{uuuu}}(\lambda_{uutt} + \lambda_{uuss})^2, \tag{3.124}$$

where we have used Equation Eq. (3.117) to express the phenomenological elastic energy coefficients in terms of the components of the elastic modulus tensor with even numbers of the suffixes s and t.

At this point it is important to examine the form of the elastic energy density of a helix, $\mathbf{a}_{helix}$, given the above conditions on the elastic moduli. Upon close observation, we note that minimizing $\mathbf{a}_{helix}$ with respect to ψ leads to the third order polynomial in the cos and sin of the pitch angle. A general third order polynomial has three solutions, i.e. either two minima and one maximum or two maxima and one minimum. In our case, one of the solutions is ψ_0, which is a minimum. The two additional extrema are located at $\psi = 0 \text{and} \psi = \frac{\pi}{2}$:

$$\left.\frac{\partial \mathbf{a}}{\partial \psi}\right|_{\psi=0} = \left.\frac{\partial \mathbf{a}}{\partial \psi}\right|_{\psi=\frac{\pi}{2}} = \frac{1}{R^2} 2 \sin 2\psi [\cos^2(K_\beta - K_\alpha) + \sin^2(K_\gamma - K_\beta)] \mid_{\psi=0, \psi=\frac{\pi}{2}} = 0. \tag{3.125}$$

We can further show that these two extrema are indeed the maxima of $\mathbf{a}_{helix}$ by taking a second derivative of the elastic free energy density with respect to pitch angle:

$$\left.\frac{\partial^2 \mathbf{a}}{\partial \psi^2}\right|_{\psi=0} = \frac{4}{R^2}(K_\beta - K_\alpha), \tag{3.126}$$

which is indeed negative since $K_\alpha > K_\beta$ (Eq. (3.123)). This shows that $\psi = 0$ is a maximum of the elastic free energy density with the above conditions. Now, let's show explicitly that the same holds for $\psi = \frac{\pi}{2}$:

$$\left.\frac{\partial^2 \mathbf{a}}{\partial \psi^2}\right|_{\psi=\pi/2} = \frac{4}{R^2}(K_\gamma - K_\alpha), \tag{3.127}$$

which is also negative when $K_\gamma > K_\beta$ (Eq. (3.123)).

We are now in a position to compare the previous models for elastic free energy density of helices with this crystalline model, and to recognize the elements critical to both sets of theories and those elements that are unnecessary to explain the existing data.

3.3.3 Crystalline Model: Improvements on and Consistencies with Chung *et al.*'s and Selinger *et al.*'s theories

We developed a new theory based on the theory of elasticity of crystals by L. Landau and E. Lifshitz.[37] This theory explains the observed phenomena of anisotropic yet symmetrical in width and length ribbon growth, taps into the phase separation phenomenon, and gives further insight into helical stiffness (the latter topics will be discussed in further detail in later sections). With the aid of this theory, we are now in a position to compare the microscopic structure of high and low pitch helices, which will be performed in a later section.

The new crystalline model also provides more physical insight into the helical ribbon system. It includes a minimum set of requirements that are consistent with experimental observations: $\mathbf{a}_{elastic} = 0$ for a flat structure; spontaneous bending that is proportional to $1/R$; no dependence on pitch angle in the term for spontaneous bending; existence of mirror planes that, as we will show later, allows for the separation of a helical ribbon into helical and flat parts.

The crystalline theory, like the previous theories, predicts that the pitch angle is the ratio of elastic moduli. The ratios of 1.85 and 0.0385 for high and low pitch helices, respectively, are much more physical than those of 3.4 and 0.0015 predicted by Chung *et al.* Since these ratios are much closer to unity in the crystalline theory, they do not require such tremendous differences between the two helical pitch types: there is less than a factor of 50 between the ratios in the crystalline theory, but nearly a factor of 23000 between the ratios in Chung *et al.*'s theory. Additionally, in the crystalline theory, the pitch angle is defined by the ratio of differences between the elastic moduli, not by the ratio of the absolute values of the elastic moduli, as in Chung *et al.* This eradicates the claim that the ratio of 0.0385 is unphysical, since all this number says is that the energy required to bend a ribbon in one direction is much closer to the cross-term, then that required to bend it in the perpendicular direction.

We have shown and will further show in later sections that the crystalline theory is in agreement with a large amount of experimental data. However, we still cannot eliminate any of the previous theories describing helical ribbons.

3.A Elastic Strain Free Energy

The work done by a force $\vec{f}$ on an object upon displacing it from point x_1 to point x_2 is defined as

$$W = \int_{x_1}^{x_2} \vec{f} \cdot d\vec{x}. \tag{3.128}$$

In the above expression, for a solid deformable body, a force is defined as stress multiplied by the area it is acting on, and a displacement resulting from the force acting on the body is defined as a deformation. As such an elastic body is deformed from its equilibrium by externally applied forces, stresses are developed in its interior. The forces associated with these stresses, perform the internal work during the deformations. This internal work is stored in a body as an internal elastic energy of deformation or the so-called elastic strain free energy. For an elastic body without hysteresis, work done by the internal forces is completely recoverable as the body returns to its equilibrium upon removing the stresses causing the deformations.

To begin, we will define the notion of strain. We will take a simple example of a one-dimensional object, i. e. a bar placed along the x_1-axis under axial loading along the x_1-axis, as shown in Figure 3.15. A simple measure of the amount by which the bar has been stretched by a force $\vec{f}$ is given by the change in the length of the bar $L' - L = \Delta$, where L' and L are the deformed and undeformed lengths of the bar, respectively. The average extensional strain in this case is then given by[91]

$$U_{\text{av},11} = \frac{\Delta}{L}, \tag{3.129}$$

where the subscript '11' in the strain $U_{\text{av},11}$ implies that both the deformation in the bar and the measurement of this deformation have been performed along the x_1-axis.

To obtain the extensional strain at a point in the bar, consider two points $P = (x_1^P, 0, 0)$ and $Q = (x_1^Q, 0, 0) = (x_1^P + \Delta x_1, 0, 0)$ located close to each other within the bar a distance $PQ = \Delta x_1$ apart, as shown in Figure 3.16. As a result of stretching of this bar due to an axial loading by a force $\vec{f}$, the points P and Q are deformed into the points $P' = (x_1^P + u_1(P), 0, 0)$ and $Q' = (x_1^Q + u_1(Q), 0, 0) = (x_1^P + \Delta x_1 + u_1(Q), 0, 0)$, respectively. Therefore, as a result of the extensional deformation by the axial loading of the bar, the points P' and Q' are now located a distance $P'Q' = \Delta x_1 + u(Q) - u(P)$ apart. We can define the extensional strain at the point P by[91]

$$\begin{aligned} U_{11}(P) &= \lim_{\Delta x_1 \to 0} \frac{P'Q' - PQ}{PQ} = \lim_{\Delta x_1 \to 0} \frac{u_1(Q) - u_1(P)}{\Delta x_1} \\ &= \lim_{\Delta x_1 \to 0} \frac{\Delta u_1}{\Delta x_1} = \frac{du_1}{dx_1}(P). \end{aligned} \tag{3.130}$$

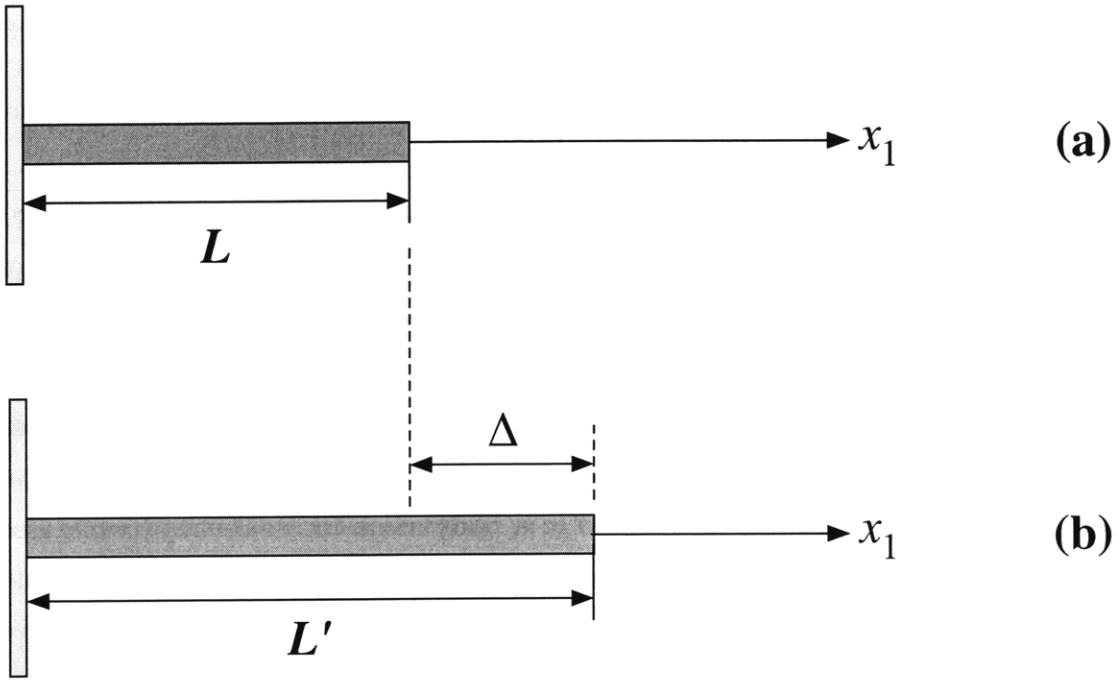

Figure 3.15: A one–dimensional object, a solid elastic bar in an undeformed state (a) and in a deformed state under axial force $\vec{f}$ acting in the x_1 direction (b).[91]

The above expression is referred to as the strain–displacement relation.[91] (For a more general expression of the strain–displacement relation, refer to Appendix 3.B.)

Now, consider a three–dimensional object with an infinitesimal volume element $dV = dx_1 dx_2 dx_3$, around a point $P = (x_1^P, x_2^P, x_3^P)$, subject to a normal stress σ_{11} (Figure 3.17), for example a thick bar under axial loading. During the deformation, point P is displaced in the x_1 direction by the amount $\omega_1(P) = \omega_1$. Then the point $Q = (x_1^Q, x_2^Q, x_3^Q) = (x_1^P + dx_1, x_2^P + dx_2, x_3^P + dx_3)$ located on the right face of the volume element is displaced in the x_1 direction by the amount $\omega_1(Q) = \omega_1(P) + d\omega_1 = \omega_1 + d\omega_1$. Therefore, due to the force, $\vec{f}$, acting along the x_1-axis on the surface of the infinitesimal volume element dV, the volume element elongates by $d\omega_1$, as shown in Figure 3.17. We can rewrite this elongation of the volume element in terms of the strain U_{11} on the bar under axial loading. In this particular case, the strain is purely extensional since the only deformation the bar undergoes is the extension of its length. Using the strain–displacement relation in Eq. (3.130) we obtain

$$\begin{aligned} U_{11}(P) &= \frac{d\omega_1}{dx_1}(P), \qquad (3.131) \\ U_{11}(Q) &= \frac{d\omega_1}{dx_1}(Q) = \frac{d(\omega_1(P) + d\omega_1)}{dx_1} = U_{11}(P) + \frac{d(d\omega_1)}{dx_1} = U_{11}(P) + dU_{11}, \end{aligned}$$

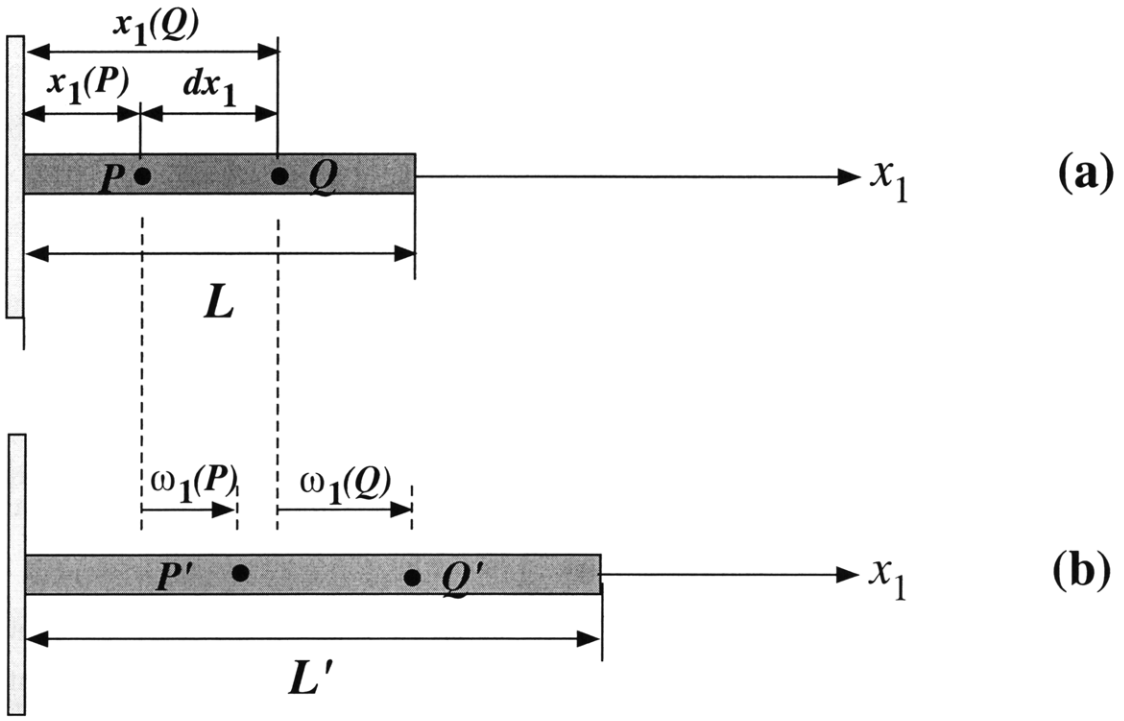

Figure 3.16: (a) A one–dimensional object, a solid elastic bar in an undeformed state with points P and Q shown; (b) the same bar in a deformed state under axial force $\vec{f}$ acting in the x_1 direction with points P' and Q' shown.[91]

where dU_{11} is the infinitesimal change in strain on moving from the point P' to the point Q'. Using the first expression in Eq. (3.131), we can express the displacement of the point P upon the stretching deformation in terms of the strain $U_{11}(P)$ as

$$\omega_1(P) = U_{11}(P)dx_1. \tag{3.132}$$

Analogously, using the second expression in Eq. (3.131), the displacement of the point Q upon the stretching deformation can be expressed in terms of the strain $U_{11}(P)$ and the infinitesimal change in strain dU_{11} as

$$\omega_1(Q) = U_{11}(Q)dx_1 = U_{11}(P)dx_1 + dU_{11}dx_1. \tag{3.133}$$

Combining Eqs. 3.132 and 3.133, the volume element dV elongates by by

$$d\omega_1 = dU_{11}dx_1. \tag{3.134}$$

The force acting on the left face of this volume element is $-(\sigma_{11}dx_2dx_3)$, where σ_{11} is the stress normal to the x_2x_3-plane applied in the positive x_1 direction. Therefore the work done on this face is

$$dW_{left} = -(\sigma_{11}dx_2dx_3)(\omega_1). \tag{3.135}$$

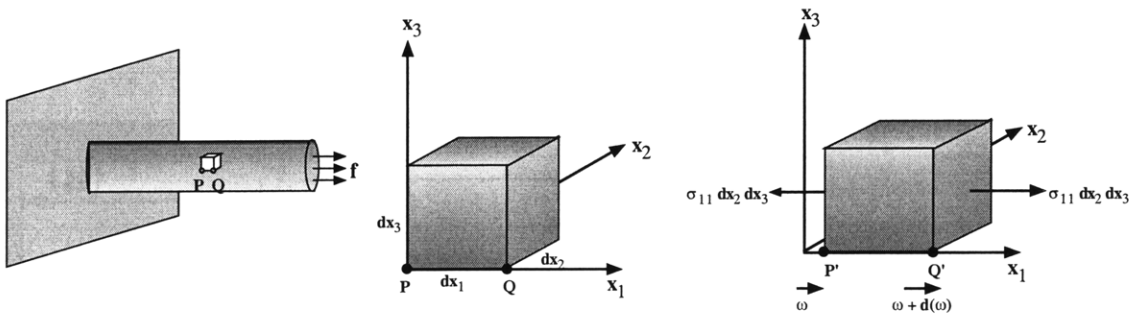

a) **b)** **c)**

Figure 3.17: (a) A solid elastic bar under axial force $\vec{f}$ acting in the x_1 direction; (b) infinitesimal volume element around a point P before force is applied; (c) infinitesimal volume element under axial force.

For axial deformation shown in Figure 3.17, the stress is assumed to be constant independent of x_1. Then, the force acting on the right face of this volume element is $(\sigma_{11}dx_2dx_3)$, and therefore the work done on this face of the infinitesimal volume element is

$$dW_{right} = (\sigma_{11}dx_2dx_3)(\omega_1 + d\omega_1). \tag{3.136}$$

Then the total work done on the infinitesimal volume element by the stress σ_{11} during this deformation is

$$dW^{(11)} = dW_{right} + dW_{left} = (\sigma_{11}dx_2dx_3)(d\omega_1) = (\sigma_{11}dx_2dx_3)dU_{11}dx_1, \tag{3.137}$$

where we used the expression Eq. (3.134). The total work done on the bar then becomes

$$W^{(11)} = \int_0^f dW^{(11)} = \int_0^f \int_V (\sigma_{11}dx_2dx_3)d(U_{11})dx_1 = \int_0^f \int_V \sigma_{11}d(U_{11})dV, \tag{3.138}$$

where 0 and f refer to the initial (undeformed, zero strain) and final (deformed, non-zero strain, U_{11}) states of the body, respectively, as depicted in Figure 3.17, and $\int_V$ is the integral over the volume of a bar. Alternatively, we can find the total work on a body from the expression

$$W = \int_V \int_0^f dF dV, \tag{3.139}$$

where dF is the total work on the body per unit volume. Then, in our particular case the work done on the bar per unit volume becomes

$$\int_0^f dF^{11} = \int_0^f \sigma_{11}dU_{11}. \tag{3.140}$$

The assertion that the elastic body under consideration deforms without hysteresis, i.e. the work done on the body is independent of the path taken, implies that we can define the strain elastic free energy per unit volume, F, as

$$F^{(11)} = \int_0^f dF^{(11)} = \int_0^f \sigma_{11} dU_{11} = \int_0^f \frac{\partial F^{(11)}}{\partial U_{11}} dU_{11}, \tag{3.141}$$

such that

$$\sigma_{11} = \frac{\partial F^{(11)}}{\partial U_{11}}. \tag{3.142}$$

Then we can rewrite the strain energy density in Eq. (3.149) in terms of stress-strain relationship in Eq. (3.142) as

$$F^{(11)} = \int_0^f \sigma_{11}(U_{11}) d(U_{11}). \tag{3.143}$$

In general, the strain energy density F can be found graphically by determining the area under the stress-strain curve, as shown in Figure 3.18. In the case that a body is made of a linearly elastic material as in our example, the stress is proportional to the strain. That is, the initially undeformed stress-free infinitesimal volume element will be under linearly increasing stress until it attains its final value with the increasing deformations. Then, using the graphical method for determining the strain energy density, we find in Eq. (3.143) that

$$F^{(11)} = \frac{1}{2}\sigma_{11}U_{11} \tag{3.144}$$

or alternatively, we can recognize that, as in Section 3.3.2

$$\sigma_{11} = \lambda_{11kl}U_{kl}, \tag{3.145}$$

which means that in our particular case,

$$F^{(11)} = \int_0^f \lambda_{11kl}U_{kl} d(U_{11}) = \frac{1}{2}\lambda_{11kl}U_{kl}U_{11} = \frac{1}{2}\sigma_{11}U_{11}. \tag{3.146}$$

We can repeat similar calculations for the stresses σ_{22} and σ_{33}. The resultant strain energy densities are respectively,

$$F^{(33)} = \frac{1}{2}\lambda_{22kl}U_{kl}U_{22} = \frac{1}{2}\sigma_{22}U_{22} \tag{3.147}$$

and

$$F^{(22)} = \frac{1}{2}\lambda_{33kl}U_{kl}U_{33} = \frac{1}{2}\sigma_{33}U_{33}. \tag{3.148}$$

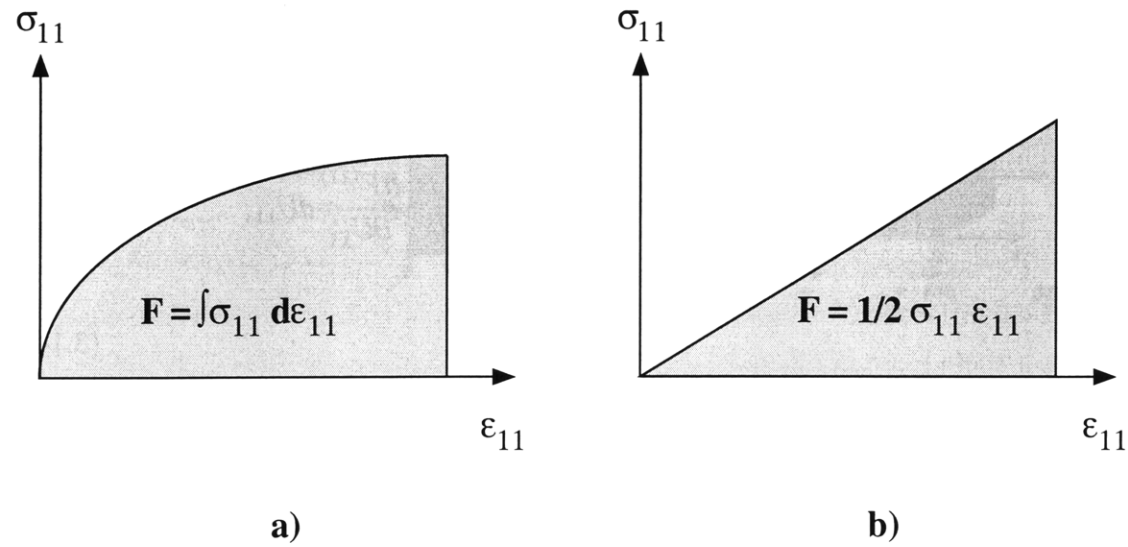

Figure 3.18: (a) General stress-strain curve for an elastic body; (b) stress-strain curve for a linearly elastic body.

Next we perform equivalent calculations to find the strain energy density for a state of pure shear, i.e. F_{ij} when $i \neq j$ (see Figure 3.19). Continuing with the assertion that the elastic body deforms without hysteresis, the strain energy density in a state of pure shear is

$$F^{(ij)} = \frac{W^{(ij)}}{V} = \int_0^f dF^{(ij)} = \int_0^f \sigma_{11} d(U_{11}), \tag{3.149}$$

which again can be determined from the area under the stress–strain curve, as shown in Figure 3.18. For an elastic isotropic body, the stress is directly proportional to strain, which implies that the area under the curve in Figure 3.18 is

$$F^{(ij)} = \frac{1}{2}\sigma_{ij}U_{ij}. \tag{3.150}$$

Utilizing the fact that in general $\sigma_{ij} = \lambda_{ijkl}U_{kl}$, we find the strain energy density for a state of pure shear to be

$$F^{(ij)} = \frac{1}{2}\lambda_{ijkl}U_{kl}U_{ij} = \frac{1}{2}\sigma_{ij}U_{ij}. \tag{3.151}$$

Therefore, for a general stress σ_{ij} applied to an elastic deformable body, the strain energy per unit volume is given by

$$F^{(ij)} = \frac{1}{2}\lambda_{ijkl}U_{kl}U_{ij} = \frac{1}{2}\sigma_{ij}U_{ij}. \tag{3.152}$$

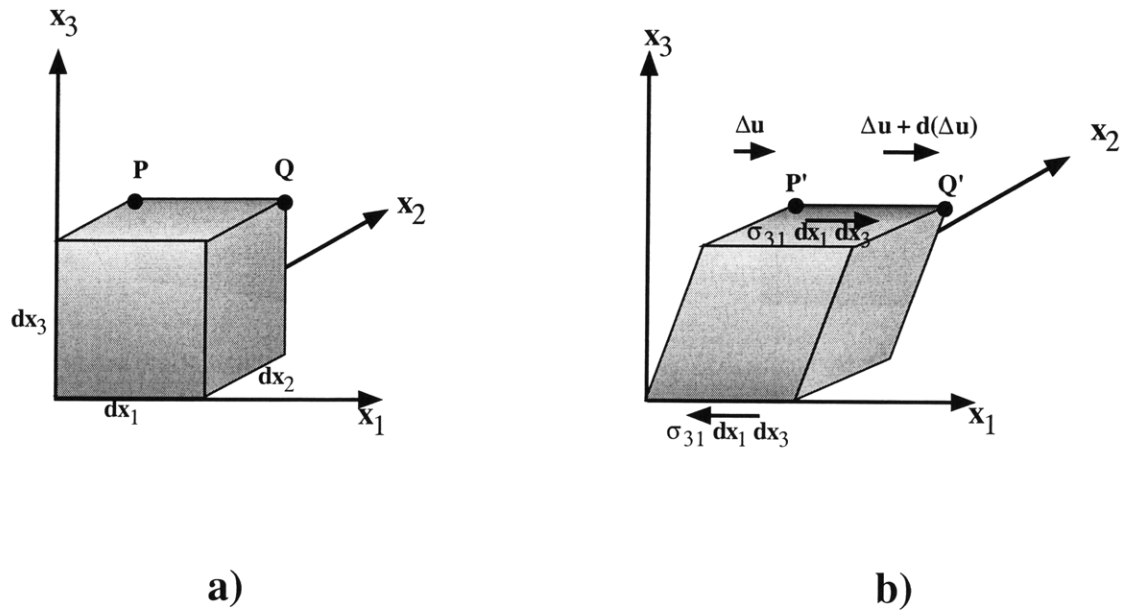

Figure 3.19: Infinitesimal volume element at a point P before shearing force (a); infinitesimal volume element under shearing force σ_{31} (b).

3.B Strain Tensor

In this Appendix, we will derive a general expression for the strain tensor and will show that the strain tensor is symmetrical.

Let's consider a general deformation of an elastic body. Any point in such a body can be described in terms of the coordinates in the undeformed and deformed states. Defining (x_1, x_2, x_3) as the coordinate system, we select two points within the body located close to each other (see Figure 3.20). Let

$$P = (x_1^P, x_2^P, x_3^P) \tag{3.153}$$

and

$$Q = (x_1^Q, x_1^Q, x_1^Q) = (x_1^P + dx_1, x_2^P + dx_2, x_3^P + dx_3) \tag{3.154}$$

be such two points in the undeformed state, and

$$P' = (x_1'^P, x_2'^P, x_3'^P) \tag{3.155}$$

and

$$Q' = (x_1'^Q, x_2'^Q, x_3'^Q) = (x_1'^P + dx_1', x_2'^P + dx_2', x_3'^P + dx_3') \tag{3.156}$$

be the same points in the deformed state of the elastic body. Points P and Q are separated by the differential distance

$$(dl)^2 = (dx_1)^2 + (dx_2)^2 + (dx_3)^2 = dx_i dx_i, \tag{3.157}$$

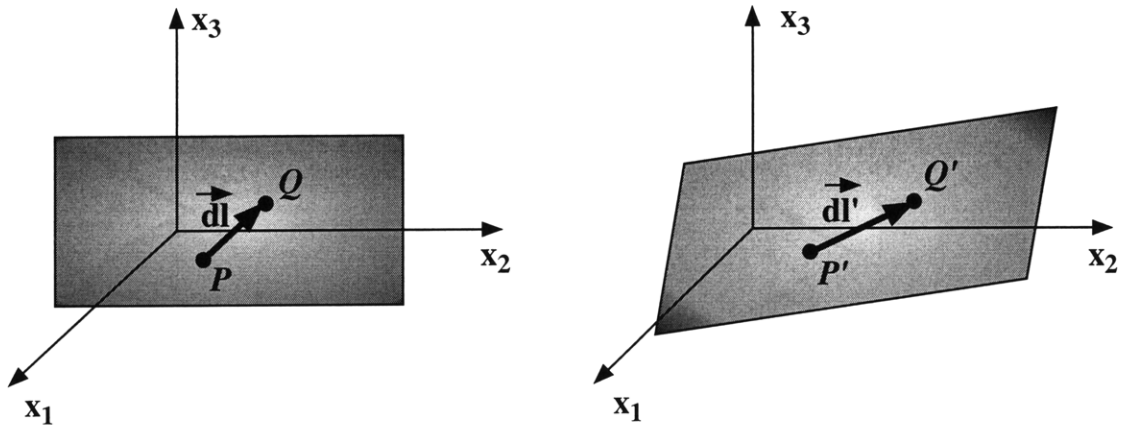

(a) **(b)**

Figure 3.20: An elastic body in the (x_1, x_2, x_3) coordinate system: (a) the undeformed state of the body; (b) the deformed state of the body.

and points P' and Q' are separated by the differential distance

$$(dl')^2 = (dx_1')^2 + (dx_2')^2 + (dx_3')^2 = dx_i' dx_i', \tag{3.158}$$

where we have used the Einstein summation notation, i.e. summation summation is performed over all repeated indices. Figure 3.21 is a vector diagram of the displacement $\vec{\omega}$ of point P to P' and the displacement $\vec{\omega} + d(\vec{\omega})$ of point Q to Q'. From the figure, we observe that

$$d\vec{l} + \vec{\omega} + d(\vec{\omega}) = \vec{\omega} + d\vec{l'} \tag{3.159}$$

or simply

$$d(\vec{\omega}) = d\vec{l'} - d\vec{l}. \tag{3.160}$$

We can further rewrite Eq. (3.160) as

$$d(\omega_i) = dx_i' - dx_i, \quad \text{or} \tag{3.161}$$

$$\omega_i = x_i' - x_i. \tag{3.162}$$

Using the approximation $dl \cdot dl' \approx dl^2$, and Eqs. 3.157 and 3.158, the above expression in Eq. (3.160) becomes

$$(d(\omega))^2 = (dl')^2 + (dl)^2 - 2dl'dl = dx_i' dx_i' - dx_i dx_i. \tag{3.163}$$

At this point we choose to represent the coordinates of the points in the deformed state as a function of the coordinates of the same points in the undeformed state.

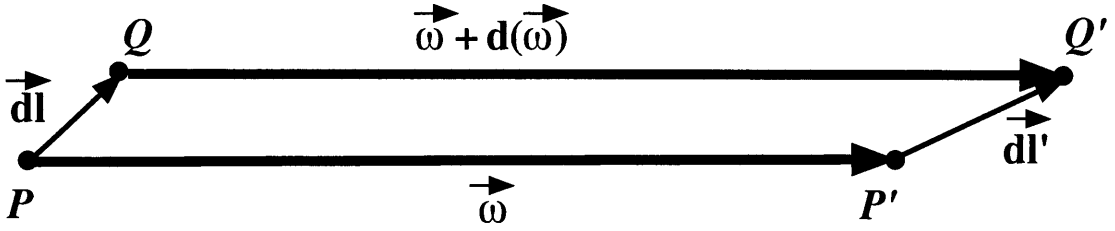

Figure 3.21: The vector diagram.

(Alternatively, we can choose to represent the coordinates of the points in the undeformed state as functions of the coordinates of the same points in the deformed state.) That is, in what is to follow we will have for each coordinate x_i

$$x_i' = x_i'(x_1, x_2, x_3). \tag{3.164}$$

In the differential form, the above statement is the displacement gradient whose form is

$$dx_i' = d[x_i'(x_1, x_2, x_3)] = \frac{\partial x_i'}{\partial x_1}dx_1 + \frac{\partial x_i'}{\partial x_2}dx_2 + \frac{\partial x_i'}{\partial x_3}dx_3 = \partial_{x_j}x_i'dx_j, \tag{3.165}$$

where we have again used the Einstein notation, that is $\Sigma_{i,j=1}^{3}\partial_{x_j}x_i'dx_j = \partial_{x_j}x_i'dx_j$. Then combining Eq. (3.157), Eq. (3.158), Eq. (3.165), and Eq. (3.163), we obtain

$$\begin{aligned}
(dl')^2 - (dl)^2 &= dx_i'dx_i' - dx_idx_i = (\partial_{x_j}x_i'dx_j)(\partial_{x_k}x_i'dx_k) - dx_idx_i \\
&= [(\partial_{x_j}x_i')(\partial_{x_k}x_i') - \delta_{jk}]dx_jdx_k \\
&= [(\partial_{x_j}(x_i + \omega_i))(\partial_{x_k}(x_i + \omega_i)) - \delta_{jk}]dx_jdx_k \\
&= [(\delta_{ij} + \partial_{x_j}\omega_i)(\delta_{ik} + \partial_{x_k}\omega_i) - \delta_{jk}]dx_jdx_k \\
&= [\delta_{jk} + \partial_{x_j}\omega_k + \partial_{x_k}\omega_j + \partial_{x_j}\omega_i\partial_{x_k}\omega_i - \delta_{jk}]dx_jdx_k \\
&= [\partial_{x_j}\omega_k + \partial_{x_k}\omega_j + \partial_{x_j}\omega_i\partial_{x_k}\omega_i]dx_jdx_k \\
&= [\partial_{x_j}\omega_i + \partial_{x_i}\omega_j + \partial_{x_i}\omega_k\partial_{x_j}\omega_k]dx_idx_j \\
&= 2U_{ij}dx_idx_j,
\end{aligned} \tag{3.166}$$

where in the second to last line we have made an exchange of dummy subscripts in comparison to the previous line and in the last line we have used the definition:

$$U_{ij} = \frac{1}{2}[\partial_{x_j}\omega_i + \partial_{x_i}\omega_j + \partial_{x_i}\omega_k\partial_{x_j}\omega_k]. \tag{3.167}$$

U_{ij} in the above equation is the *definition* the strain tensor. We note at this point that the components of the differential gradient in Eq. (3.165) are small, implying that the

product $\partial_{x_i}\omega_k\partial_{x_j}\omega_k$ is of second order in smallness and thus negligible. Therefore, we can approximate the strain tensor by

$$U_{ij} = \frac{1}{2}[\partial_{x_j}\omega_i + \partial_{x_i}\omega_j] = \frac{1}{2}\left[\frac{\partial\omega_i}{\partial x_j} + \frac{\partial\omega_j}{\partial x_i}\right]. \tag{3.168}$$

Finally, this derivation clearly shows that strain tensor is indeed symmetrical, i.e.

$$U_{ij} = U_{ji}. \tag{3.169}$$

Expressions 3.168 and 3.169 are what we set out to determine, the definition of the strain tensor and the symmetry of the strain tensor.

3.C Coefficient Number in the Elastic Modulus Tensor

The elastic modulus tensor λ_{ijkl} is a three-dimensional tensor of rank four. Therefore, it has $3^4 = 81$ seemingly independent elements. We have shown in Section ??, that this tensor possesses three inherent symmetries which reduce the number of independent elements to 21, which we shall show below. These symmetry operations are

$$\lambda_{ijkl} = \lambda_{jikl} = \lambda_{ijlk} = \lambda_{jilk} = \lambda_{klij}, \tag{3.170}$$

The first symmetry operation we shall consider is

$$\lambda_{ijkl} = \lambda_{ijlk}. \tag{3.171}$$

This means that for any pair of indices ij, of which there are $3^2 = 9$, the elements with indices kl are equal to those with indices lk. This is analogous to a 3×3 symmetric matrix, in which there are only six independent elements, instead of nine. This symmetry operation reduces the total number of the elements in the elastic modulus tensor to $3^2 \times 6 = 54$.

The second symmetry operation,

$$\lambda_{ijkl} = \lambda_{jikl}, \tag{3.172}$$

is analogous to the first symmetry operation. In this case, for any given kl the elements of the elastic modulus tensor with indices ij are equal to those with indices ji. By the previous analogy, this reduces the number of independent elements for

fixed kl from $3^2 = 9$ to six. As a result, the total number of elements in the elastic modulus tensor becomes $6 \times 6 = 36$.

The first two symmetries were concerned with interchangeability of the indices within the first or second pair of indices. The last inherent symmetry operation,

$$\lambda_{ijkl} = \lambda_{jikl}, \tag{3.173}$$

is concerned with the interchangeability of the pairs of indices, i.e. ij pair with kl pair. We have shown that each pair of indices can take on six possible values. This constraint on the pairs of indices is analogous to a 6×6 symmetric matrix, which has $(6^2 - 6)/2 + 6 = 21$ independent elements. Therefore, the elastic modulus tensor under these three symmetry operations has 21 independent elements.

Chapter 4

Measurement of Helix Spring Constant

4.1 Introduction

Recent developments of various phenomenological theories describing helical ribbons in quaternary sterol systems leave open the question of their validity with respect to experiments sensitive to the actual microscopic helical structures. Measurements of the energies associated with various deformations of a helix are an obvious choice of experiments to test these theories. The results of such measurements can then be compared to the theoretically predicted values and to the values measured in other biological systems, cell membranes, micelles, vesicles, monolayers bilayers.

In the following we will describe experimental and theoretical work related to the axial extension and compression of low pitch helices formed in CDLC. We will illustrate the bulk behavior of a helix under an applied uniaxial force in terms of a spring constant, K_{helix}.[a] Relating this spring constant to the microscopic elastic moduli of a system, will provide a simple and direct measurement of what values these moduli can attain.

We will start this Chapter by introducing the Materials and Methods necessary to perform described experimental work: nanofabricated Si-Ni cantilevers as force transducers in measurements of helix spring constant, epoxy adhesives as means of helix attachment to various structures (including force– measuring devices), and finally the

[a]In what follows, K_{helix} will be used to describe "helix spring constant," a quantity that is described by units of $[Force/Length]$. The term "elastic modulus" will be used to describe a quantity associated with the helix free energy or liquid crystalline bilayer free energy. This latter quantity has units of $[Force \times Length]$ and will be denoted as K_i and K_{bilayer} for helices and bilayers, respectively.

equipment necessary for visualization of the experimental procedure. Next, we will describe how experimental application of a uniaxial force to a helix is manifested in all three existing theoretical models (Chung *et al.*[12], Selinger *et al.*[18], and crystalline model). Finally, we will illustrate the experimental procedure for measurements of the helix spring constant and the results we obtained when a force is applied to a helix. We will conclude by comparing the measured values of helix spring constant with spring constants of other biological materials, cell membranes, thick filaments, etc.

4.2 Materials and Methods

4.2.1 Nanofabricated Si-Ni Cantilevers as Force Probes.

Introduction

I would like to thank Prof. G. Pollack (University of Washington) for his generosity in sharing Si-Ni cantilevers that were produced in his laboratory. I would also like to thank Mr. M. Fauver for his enthusiasm and patience in explaining the implementation techniques of Si-Ni cantilevers.

Recent interest in studying the forces and energies active at the molecular and subcellular levels has lead to the growth of a new field, biological nanotechnology.[97,98] As of this writing, biological nanotechnology is one of the fastest growing areas of research in the scientific community, combining fields as diverse as molecular biology and silicon-based micromachining. Various methods and apparati have been developed for nanoscale force measurements. These methods usually involve the accurate measurement of the deflection of a flexible cantilever acting as a force transducer. Such measurements are usually difficult and often imprecise. The development of Atomic Force Microscopes (AFM), Scanning Probe Microscopes (SPM), and Molecular Force Probe (MPB) have made such measurements easier and more accurate.[99–105] However, AFM, SPM and MPB are very expensive and, at times, cumbersome. Less expensive, yet highly accurate methods that involve micromanipulation techniques have recently been developed. These methods include optical traps or tweezers,[106–111] pulling on or twisting ferromagnetic particles attached to molecular or cellular surfaces by the technique of magnetometry,[112,113] probing cell surfaces,[114] micropipette suction,[115–117] and application of forces by microneedles.[118–124]

The particular choice of a force measurement technique depends on the force–energy range to be measured, and on the spatial resolution of the apparatus. For example, even though Silicon cantilevers for AFM and SPM techniques only have elastic constants as low as 10 pN/nm, the fact that these techniques resolve angström scale deflections of the cantilever tips, renders these technique very sensitive. In other words, AFM and SPM today can resolve forces on the subpiconewton scale.[125,126] Recently, with the new *state–of–the–art* micromachining the most effective stiffnesses of AFM have been lowered to the order of 1 pN/nm, which has been used in detection of single hydrogen bonds.[100] However, if the spatial resolution of an apparatus is on the order of microns (e.g., light microscopy), then the forces resolvable via deflection of the most flexible AFM tip are only on the order of 10 nN, which is usually too large for measurements of inter- or intramolecular forces.[103–105] On other hand, optical traps possess very low elastic constants, as low as 0.007 pN/nm, which makes these devices very useful in application of forces on the order of 1 pN.[127] However, optical traps are useful only for a 1 - 100 pN range of forces since the high laser power, necessary to measure forces in excess of 100 pN, may damage the biological material studied.[128] In comparison, glass microneedles can be made to have elastic constants as low as 0.004 pN/nm.[122] However, production and use of glass needles are very difficult due to very high irreproducibility, their sensitivity to slight fluctuations, and the requirement of meticulous individual calibration.

In our experimental measurements of helix spring constants, we used nanofabricated cantilevers as force transducers. These cantilevers possess both low elastic constants (as low as 0.05 pN/nm) and high dimensional and elastic reproducibility; these cantilevers also do not require individual calibration because the fabrication process allows one to calibrate large groups of identical cantilevers all at once.[129,130] In what follows we will provide a short description of the cantilever nanofabrication methodology and the application of these cantilevers. It is not the intent of this report to give a detailed account of these force transducers. Such account, however, can be found in work by Fauver *et al.*[129]

Fabrication of the Cantilevers

The principle underlying the design of cantilevers as force transducers relies on a proportionality between the force applied to a cantilever and the resulting cantilever displacement. The displacement of a cantilever from its equilibrium position is moni-

tored optically. The cantilevers are made in pairs attached to one another at their base so as to allow for differential measurements. The displacement of a cantilever from its equilibrium position is then measured as the displacement between two cantilevers. (However, in our experiments we used single cantilevers rather than cantilever pairs due to geometrical constrictions, as will be further discussed in Section 4.2.1.) To increase optical contrast, the cantilevers are coated with gold, which is especially important for the thinnest cantilevers. The force on the cantilever is deduced from the measurement of the cantilever displacement and the value of the cantilever stiffness. In what follows, we will describe the nanofabrication and calibration methodologies for these cantilevers.

The cantilevers were produced at the Cornell Nanofabrication Facility (Ithaca, NY) using the methods of multistage lithography and etching. The process of cantilever nanofabrication can be outlined in the following manner:

1. A thin film of Si-Ni is coated onto single crystal Si wafer.

2. The wafer is etched in a form of 186 windows, leaving free-standing films of Si-Ni coating each window.

3. Chemical etching is used to manufacture cantilevers from the free-standing films of Si-Ni in each window of wafer.

This process is further illustrated in Figures 4.1 and 4.2 and is detailed as follows. The cantilevers are fabricated from Si-Ni films of various thicknesses (310 ± 10, 650 ± 10, and 830 ± 20 nm). These films are deposited on the surface of a wafer using low pressure chemical vapor deposition (panel (b) of Figure 4.1). Subsequently one of the wafer surfaces is coated with a photoresist[a] (bottom surface on panel (c) of Figure 4.1). Exposing the photoresist to light through a contact mask (bottom surface on panel (d) of Figure 4.1), i.e., optical lithography results in the development of rectangular areas (bottom surface on panel (e) of Figure 4.1), which reveal Si-Ni film on the bottom surface of the wafer. The Si-Ni film is further removed from these rectangular areas by plasma etching (bottom surface on panel (f) of Figure 4.1). Finally, the wet etching of the exposed rectangular areas on the bottom surface of the wafer produced 186

[a] A light-sensitive polymer that is spread as a uniform thin film on the wafer. After solidifying the polymer, a photomask is used to expose a specific pattern on a wafer. The portions of polymer not exposed to light shield the underlying regions of the wafer from subsequent etching or implanting operations.

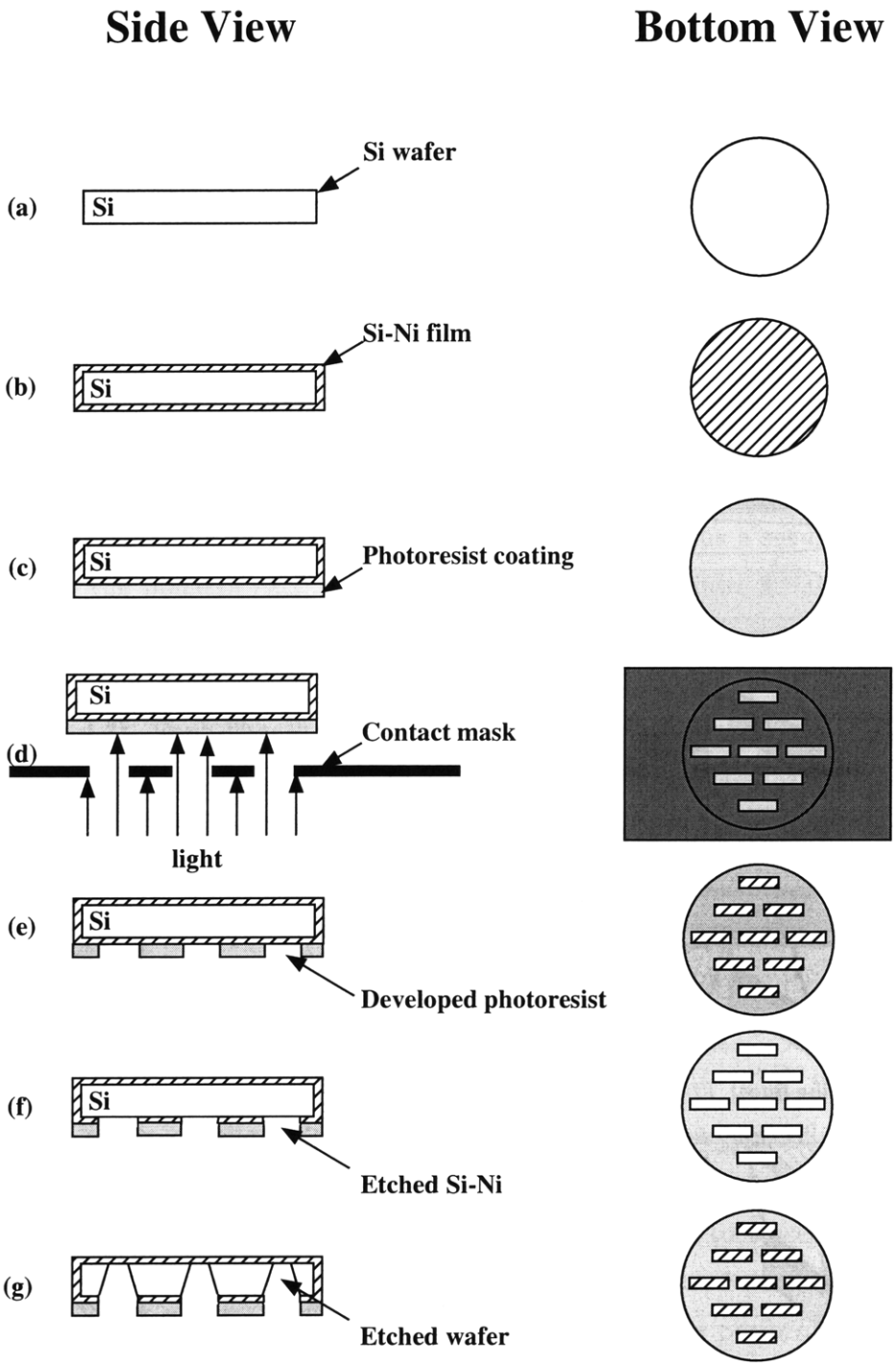

Figure 4.1: The schematic representation of cantilever nanofabrication (views from a side and bottom of the wafer). A single circular crystal Si wafer (a) is coated by a thin film (of variable thickness) of Si-Ni (b). The bottom surface of the wafer is then coated by photoresist (c), which is exposed to light through a contact mask (d). The development of the photoresist results in a rectangular area of exposed Si-Ni film on the bottom surface of the wafer (e). Plasma etching is then used to remove Si-Ni film from the bottom of the wafer (f). Finally, the rectangular areas can be incised from the single crystal Si wafer by wet etching (g). This results in "windows" that are covered by a membrane of Si-Ni on the top surface of the wafer.

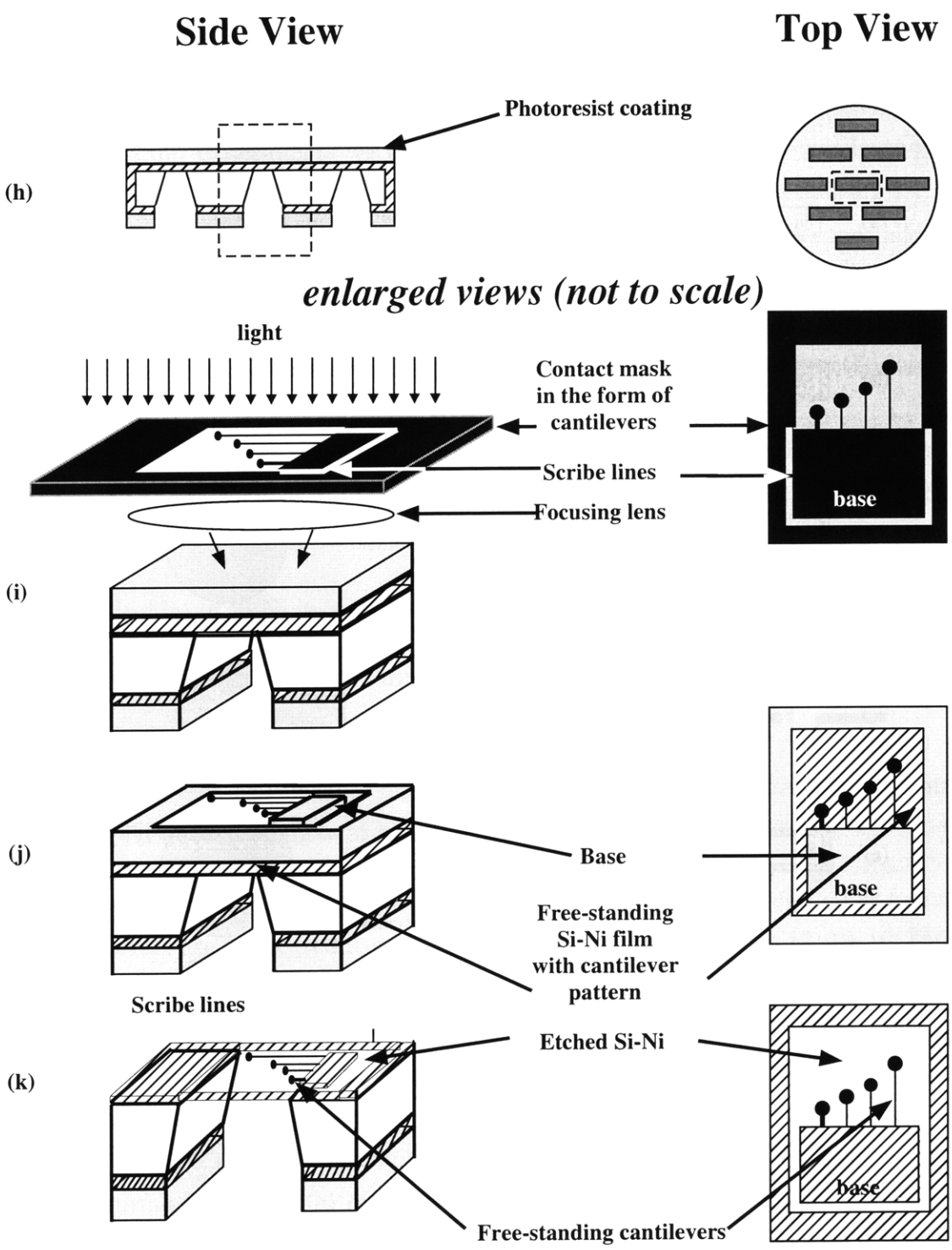

Figure 4.2: The schematic representation of cantilever nanofabrication (continued). Views from the side and the top of the wafer are presented. For convenience, one cantilever represents each pair of cantilevers on this schematic diagram. To produce cantilevers from the Si-Ni membrane that coats the "windows" on the wafer, the same methodology is applied: the surface of Si-Ni film is coated with photoresist (h); the photoresist is then exposed to light through a contact mask; the contact mask has a shape of cantilevers and allows for scribe lines, along which wafer segments with cantilevers (or bases) can be broken off from the wafer (i); the development of the photoresist results in areas of exposed Si-Ni film on the top surface of the wafer (j); finally, the plasma etching of Si-Ni film uncovers the cantilevers (attached to a wafer "base") (k). Each base with cantilevers can then be separated from the wafer by gently applying pressure along scribe lines and pressing the "base" out of the wafer (this process is not shown). A "base" with cantilevers is shown in Figure 4.3.

separate free–standing Ni-Si membranes, each 440 × 1240μm in size (bottom surface on panel (g) of Figure 4.1). These windows, however, were still covered by a The Si-Ni membrane remained on surfaces unexposed to photoresist (the top surface of the wafer on panel (g) of Figure 4.1). From these free–standing Si-Ni membranes the cantilevers were etched in the following steps.

Photoresist was then applied to the surface of the silicon-nitride membrane (top surface of the wafer on panel (h) of Figure 4.2). This time a new contact mask was created with the purpose of exposing the cantilever pattern onto each free–standing Si-Ni membrane. The product of exposing the photoresist to light through the contact mask (top surface of the wafer on panel (i) of Figure 4.2), developing the photoresist (top surface of the wafer on panel (j) of Figure 4.2), and etching the exposed surfaces (top surface of the wafer on panel (k) of Figure 4.2), was a set of free–standing cantilevers in the place of each free–standing membrane. Figure 4.3 displays a wafer segment, i.e. a "base", with 4 pairs of free–standing cantilevers, each of different length, while their widths, and of course their thicknesses, were kept constant (panel (b) of Figure 4.3). Each "base" also has two shorter and wider calibration cantilevers, as shown in Figure 4.3. As mentioned before, for the final stage of cantilever fabrication, the tips of all of cantilevers were coated with a thin layer of gold to increase their resolution when viewed using light microscopy. Depending on their geometrical dimensions, the cantilevers possessed different elastic constants that could be used for the measurement of elasticities of various biological samples.

Once manufactured, the cantilever elastic constants, $k_{\text{cantilever}}$[b], were calibrated in groups of 372 while cantilevers are still attached to the wafer base. Since by design the force applied to cantilevers is proportional to the displacement of cantilever tips, the cantilever elastic constant serves the role of the coefficient of proportionality. It is also important to note that this elastic constant applies to forces acting on the cantilevers in the plane plane parallel to the wafer "base" and perpendicular to the cantilever axes, as shown in Figure 4.3. This calibration was performed by methods of Peterson *et al.*[131] and Kiesewetter *et al.*,[132] who described the cantilever elastic constant, $k_{\text{cantilever}}$, as a function of the modulus of elasticity of the silicon–nitride

[b]The term "elastic constant" will be used to describe cantilever stiffness $k_{\text{cantilever}}$, a quantity that is measured in units of $[Force/Length]$. We will also use the term "modulus of elasticity" E to describe the elastic properties of the Si-Ni film from which cantilevers are manufactured. The cantilever modulus of elasticity is measured in units $[Force \times Length]$.

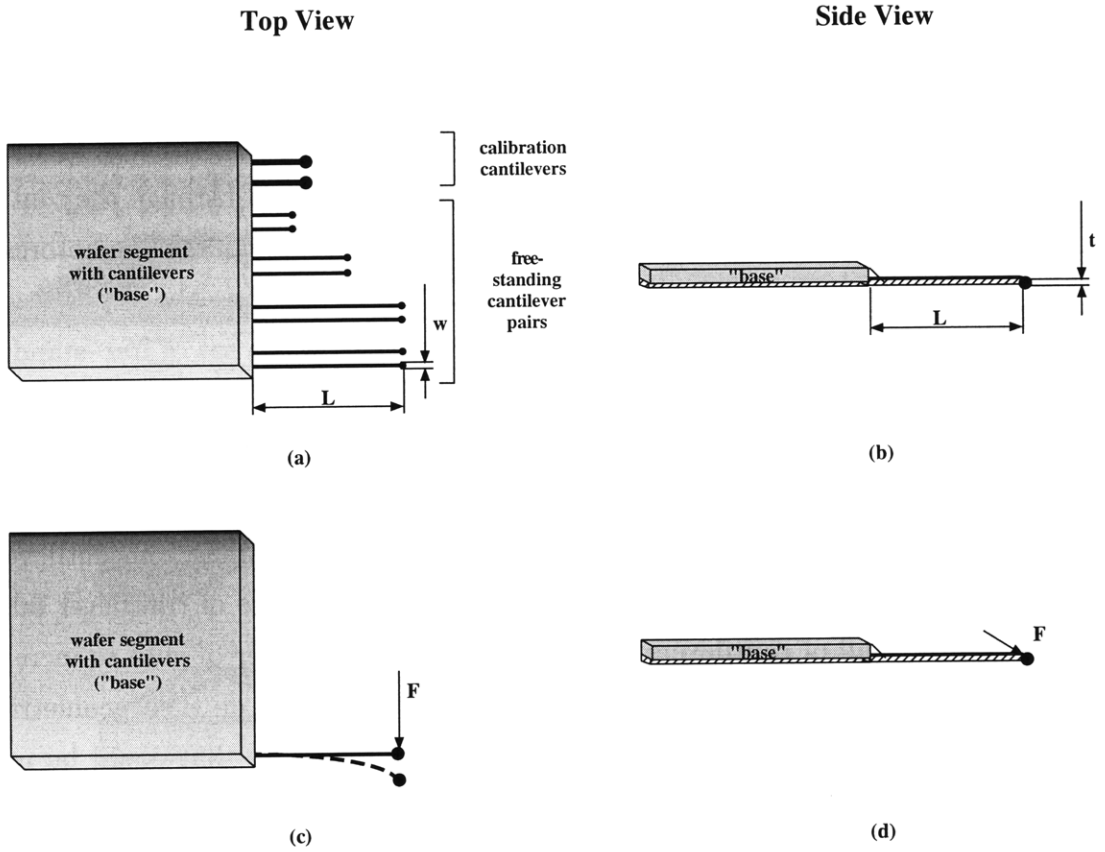

Figure 4.3: A schematic representation of a wafer segment, a "base", with 4 pairs of free–standing cantilevers and one pair of calibration cantilevers. Cantilevers were manufactured in pairs to simplify the measurements of their displacement under an applied force in cantilever plane perpendicular to their axes. However, in our experiments we used single cantilevers rather than pairs due to geometrical constraints. (a) Top view of a "base" with cantilevers. The cantilever length L and width w are indicated. (b) A side view of a "base" with cantilevers. The cantilever length L and thickness t are indicated. (c) The nature of intended forces ($\mathbf{F}$) and cantilever deformations (shown by a dashed line): parallel to the plane of the wafer segment and perpendicular to the cantilever length. (For convenience, only one cantilever is shown.) (d) Side view of a "base" with cantilevers and the nature of applied force $\mathbf{F}$.

film, E, and the geometrical dimensions of a cantilever through

$$k_{\text{cantilever}} = E\frac{tw^3}{4L^3}, \tag{4.1}$$

where t is the cantilever thickness, i.e. the film thickness, w the is cantilever width, and L is the cantilever length, as shown in Figure 4.3. The fabrication process permitted precise control of the geometrical dimensions of the cantilevers, the length L and the width w, which were measured using electron micrographs (Environmental Scanning Electron Microscope, ElectroScan 2020, ElectroScan Corporation, Wilmington, MA). The film thicknesses, which determine the cantilever thicknesses t were measured using the Leitz Thickness Measurement System (MV-SP Spectrophotometer). The only unknown in Eq. (4.1) is then the modulus of elasticity of Si-Ni film, E. The calibration strategy then rested principally on the determination of E.[129–132] The modulus of elasticity of films on various wafers were calculated from measurements of the cantilever resonant frequency.[129,130] From the modulus of elasticity and cantilever dimensions, cantilever elastic constants could be calculated using Eq. (4.1).

For the purpose of measuring the spring constants of the helical ribbons, we used the cantilevers with elastic constant $k_{\text{cantilever}} = 0.050 \pm 0.008$ pN/nm. The geometrical dimensions of these cantilevers were the following: length $L = 568 \pm 0.4\mu$m and width $w = 1 \pm 0.04\mu$m. The thickness of these cantilevers was $t = 830 \pm 20$ nm, which was the same as the thickness of Si-Ni film from which the cantilevers were made. The elastic constants of the cantilevers used were found by cross-calibration with stiffer cantilevers of $k_{\text{cantilever}} = 0.237 \pm 0.038$ pN/nm.

Implementation of Cantilevers

In this section we shall describe how nanofabricated Si-Ni cantilevers were employed in our experimental measurements of the helix elastic bulk constant. We present the experimental procedures for cantilever and helix preparation, including isolation of the cantilevers from the wafer and their attachment to a micromanipulator, preparation of a sample with helical structures and selection of a single helix for attachment to a rigid support, and achievement of contact and bonding between cantilever and helix. We conclude this section by describing how cantilever deflections and helix displacements are achieved. The discussion of how these results provide a measure of the helix spring constant is left for Section 4.6.

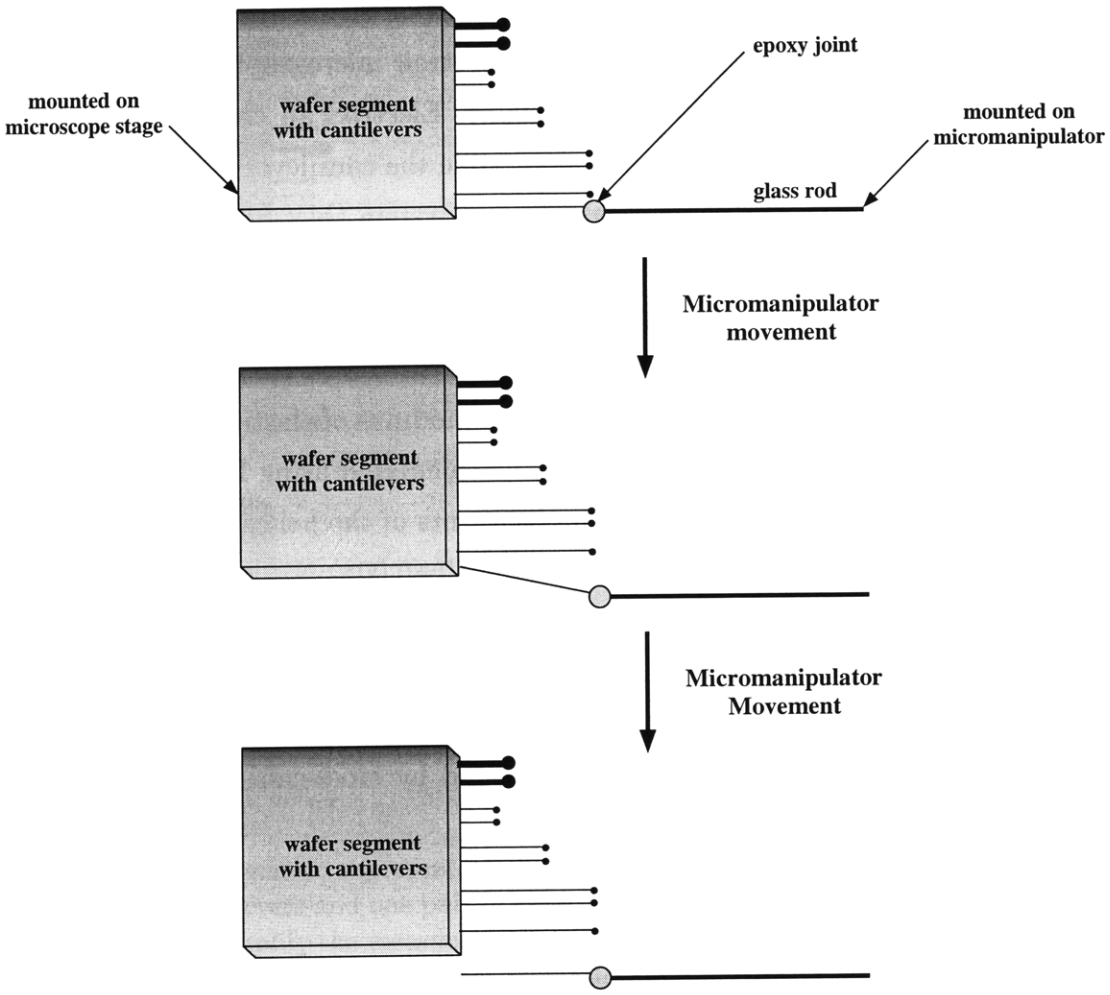

Figure 4.4: Preparation of a glass rod–cantilever system. A glass rod on a micromanipulator with a small amount of epoxy on its tip is brought into contact with cantilever. By gently moving micromanipulator, a cantilever is broken off at its base.

Preparation of a cantilever

Manufactured by a multi-stage lithographic and etching process, the nanofabricated Si-Ni cantilevers are created in pairs, attached to a wafer segment (a "base"). To employ cantilevers, it was necessary to determine the best method of establishing a contact between cantilever and helix. In our preliminary experiments, we found that the use of a cantilever pair for measuring the relative deflection of one lever with respect to the other is impossible in our experimental setup. Therefore, we established the method of extracting a single cantilever from the wafer. To begin with, a wafer segment containing all four pairs of cantilevers and two calibration cantilevers (Figure 4.3) was broken off from the wafer along the scribed lines, as shown in Figure 4.2. This wafer segment with cantilevers was then cleaned with gently blown pressurized air and stabilized horizontally on a microscope stage. A glass rod, which was intended to support a cantilever, was then mounted on a micromanipulator and positioned opposite to the wafer segment. The tip of this glass rod was dipped in a small amount of Devcon 5-Minute Epoxy® and placed in close proximity to the chosen cantilever on the wafer segment. With the aid of optical microscopy, the cantilever was brought into contact with the epoxy which cured in this position. By gently moving the micromanipulator's glass rod away from the wafer, the cantilever was broken off from its original base while remaining glued to the glass rod as shown in Figure 4.4.

Preparation of a helix

Cells for samples with helices were prepared by gluing silicon rubber walls onto a transparent plastic slide. By changing the size and placement of these rubber walls, we were able to control the amount of sample in each cell. This was necessary since each helix investigated had to be situated in the bulk of the sample for the duration of the experiment. Prior to filling each cell with a sample containing a large number of helices, we glued a rigid glass rod to the bottom of the slide. This rigid glass rod was then used as a helix support and a "reference beam" for measurements of helix displacement from equilibrium when uniaxial tension is applied.

The helices employed in our experiments were grown from Chemically Defined Lipid Concentrate (CDLC) system. Specifically, we used the low pitch helical ribbons grown from this system. After placing CDLC into the sample cell, and allowing helical ribbons to sediment half-way to the bottom (usually 15 - 30 minutes, depending on the size of the sample), we placed a small amount of Devcon 5-Minute Epoxy® on

the "reference beam." A helical ribbon was then selected from the bulk of the sample and carefully placed via micromanipulation in contact with the epoxy on the reference beam. Once this contact was made, the epoxy was allowed to completely cure. Precise schedules were followed for this procedure because there was a limited window of time before the epoxy cured.

Once the helical ribbon was firmly attached to the reference beam, a Si-Ni cantilever attached to a micromanipulator was placed into the sample (see *Preparation of a Cantilever* above). At the same time, a small amount of Devcon 5-Minute Epoxy® was placed inside the sample cell. After carefully "dipping" into the epoxy, the tip of a cantilever was allowed to be "hooked" and glued onto one of the last turns of the helix on the reference beam. The epoxy holding this cantilever–helix system was then allowed to cure. In an aqueous solution, this process usually took 15-30 minutes.

The deflection of the cantilever and the displacement of the helix were achieved by one of the two methods: either the cantilever was moved horizontally via the micromanipulator while the microscope stage was held fixed, or the microscope stage was moved horizontally while holding the cantilever was held fixed. The geometrical configuration of this process is given in Figure 4.5. The displacement of the helix and the deflection of the cantilever were then measured, analyzed, and related to the value of the helix spring constant. The description of this procedure is presented below in Section 4.6.

4.2.2 Visualization Instrumentation

The experimental procedures were visualized using an inverted microscope (Diaphot-TMD, Nikon) with phase contrast optics. Images were projected onto a CCD camera (Sony, DXC-970MD) which was used for both visual monitoring and quantitative data acquisition. The images were recorded with a SVHS video recorder (Panasonic AG-1960) and further digitized with a built-in frame grabber on a Power Macintosh computer. For image enhancement and measurements, we used the public domain NIH-Image software package.[47] The microscope was placed on a vibration isolation tabletop (Newport Corporation, Irvine, CA). A piezoelectric micromanipulator (Burleigh, PCS-5000) was used to execute the delicate procedure of moving the cantilevers. With a 60 nm resolution and a drift of less than one micron per hour (which was insignificant on the time scale of the experimental measurement), we found this system to be adequate for our experimental work.

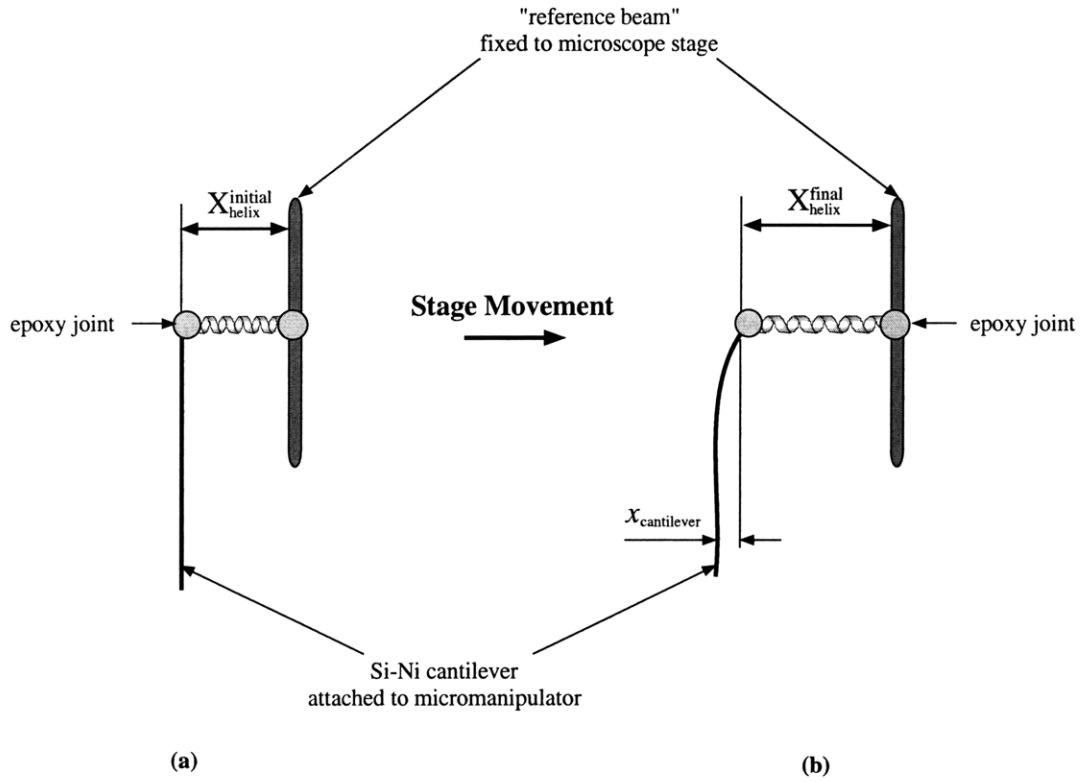

Figure 4.5: The experimental arrangement for the measurement of the helix spring constant: (a) Initial position of the helix–cantilever system prior to the application of an axial force to the helix. (b) The arrangement of the helix–cantilever system when a small axial force is applied to the helix via Si-Ni cantilever. This arrangement is achieved by moving the microscope stage, and therefore the reference beam, to the right. As a result helix elongates by $X^{final}_{helix} - X^{initial}_{helix}$ and therefore $X_{helix} = X^{final}_{helix} - X^{initial}_{helix}$ is the helix displacement or helix elongation. While the helix elongates, the cantilever undergoes a deflection $x_{cantilever}$ in the direction of helix displacement.

4.2.3 Tethering Methodology: Historical Background and Experimental Observations

There exist a multitude of methods by which microscopic forces can be applied to a helical ribbon.[106–124] In order to produce a physical deformation (stretching, compression, twisting, bending, buckling, etc.), many of these methods require the helical structures to be fixed or "tethered" to "deformation-producing" device. When choosing an adhesive for this purpose, one needs to pay attention to several very important issues. First, it is necessary to know whether the biological material is secured to the surface strongly enough that the application of a force will not tear the glued object off of the supporting surface. Second, it is necessary that the the structural integrity of the biological material be preserved when adhesive is applied to its exterior, that is:

- the glue curing conditions (temperature, wavelength of light, electric field, etc.) must not be damaging to the biological functions and geometrical properties of a material, and
- the glue must not be toxic to the biological system.

Third, the chosen glue must preserve its adhesive qualities in the ambient environment of the biological material studied. For example, helical ribbons reside in an aqueous solution at room temperature; therefore, the chosen glue must maintain its physical and chemical properties in an aqueous solution at room temperature. Finally, the curing time of the chosen adhesive must be short relative to the life times of biological materials.

Varied applications in cell biology and many new applications arising in the field of bioengineering require the development of new techniques and new materials for tissue adhesion. The standard adhesives used for tissue fixation are poly-L-Lysine, aminoalkylsilane, egg albumin, 3-aminopropyltriethoxysilane, Elmer's glue, chrome alum, silane, etc.[133–135] However, most of these materials are designed to be applied to the surfaces of glass to either minimize the effects of the electrostatic charges on the glass surfaces or to supply extra charge to the glass surfaces that would target a specific biological tissue.[133–135] Silicone-based adhesives have also been used to bond myofibrils to glass surfaces[129] and to attach rat heart cells to polysilicon surfaces.[136] To target a specific protein, the antigen–antibody "gluing" technique has been widely used,[137] as well as biotin–streptavidin bonding.[138] In recent years, the use of "natural

adhesives" for both *in vivo* and *in vitro* experiments has become wide spread. For example, fibronectin and vitronectin are two major adhesive proteins in plasma and serum that have been used as a thin coating on tissue culture surfaces to promote cell attachment, spreading, and proliferation;[139–141] laminin is a major component of basement membranes, one of whose activities is to promote cell adhesion.[141] Finally, Cell-Tak^{TM} Cell and Tissue Adhesive has become one of the major adhesives in biological applications. Derived from the marine mussel, *Mytilus edulis*, this adhesive employs the protein "glue" secreted by the mussel to anchor itself to solid substrates in its marine environment.[141–145]

Listed above are just a few of the options for the fixation of biological materials available today. In experiments where the biological material to be fixed has a known structure, some of these fixation methods can be very useful. Unfortunately, in the case of helical ribbons we are faced with the fact that their chemical composition is unknown. As discussed in Chapter 2, a few attempts have been made to study helix composition, both indirectly and directly. The indirect study of helix composition was made by studying the helix structure via X-ray crystallography of the filamentous predecessors of helical ribbons, and of cholesterol crystals, the successors of helical ribbons. The filamentous predecessors of helices were also studied via density gradient centrifugation techniques.[20,25,28] The direct study of helix composition using the fluorescence techniques is described in Section 2.4.2. However, all of these experiments failed to unambiguously describe the helix structure as it relates to helix composition, both surface and internal. Without knowledge of which chemical groups to target for adhesion purposes, we had to find a suitable class of adhesives by performing a multitude of "trial-and-error" experiments, eliminating adhesives and groups of bonding agents one-by-one. By doing so, we were also indirectly probing the helix surface structure. As mentioned above, several things had to be kept in mind:

1. helical ribbons reside in an aqueous solution; dehydration results in helices collapsing on themselves,

2. the curing of the "glue" must occur at room temperature,

3. the curing time of the "glue" must not exceed the life time of helices and must be much shorter than cell dehydration times, i. e. the curing time must be on the order of an hour or less.

Each glue was investigated using at least two different quaternary sterol systems, CDLC and one of the bile salt/cholesterol/phosphatidylcholine systems. A drop of glue was placed on a thin glass rod and placed into a sample cell with high and low pitch helical ribbons. The glue was placed in contact with a helix by gently pushing a glass rod against the helix surface. If the contact between helix and epoxy was lost prior to curing of epoxy, the experimental trial to attach helix to epoxy was considered to be unsuccessful. We also assumed that the experimental trial was unsuccessful if upon curing of epoxy, the attachment point was lost while very small forces are applied to a helix, i.e. prior to helix elongation. We assumed that 10 to 20 such trials on a variety of helical structures was enough to establish the applicability of a glue to our experimental needs. Both high and low pitch helices were tested in this manner.

Altogether, we have tried more than 50 different adhesives, glues, and epoxies in our attempts to attach helical ribbons to flat and rod-like glass surfaces. In our qualitative preliminary observation of helix behavior in glass sample cells, we detected that upon sedimentation, helical ribbons tend to adhere to the glass bottom of these experimental cells. Since glass surfaces are moderately hydrophilic, we concluded that helices are probably coated by a layer of phospholipids with hydrophilic headgroups, and we were witnessing the attractive interactions of two hydrophilic surfaces, one (or both) of which might be electrostatically charged. This was not unexpected since, in their experiments, Konikoff *et al.* observed that both precursors and successors of helical ribbons are coated with phospholipid molecules.[20,25,28] Therefore, we started the search for a "helix glue" with hydrophilic adhesives that are employed in biological tissue culture fixation (poly-L-lysine, silane, 3-aminopropyltriethoxysilane). We found that although helical ribbons tend to attach to surfaces coated with these materials more strongly than to uncoated surfaces, the bond was still not strong enough to hold a helix during the force studies. This was qualitatively determined by shaking the experimental cells in both the horizontal and the vertical directions once a helix had been attached to a surface coated with one of the above adhesives. We also had very little control over the geometrical positioning of a helix on a coated surface, i. e. the location and orientation of a helix–surface joint. This property of the adhesion of helices to coated surfaces is inconvenient for performing force–displacement experiments.

Next, we tried Cell-Tak^{TM} as an adhesive. A big advantage of this material is that it is capable of being both applied and cured under water, unlike the previous group of materials which had to be coated and dried on the glass surface prior to placing them in contact with helices in water. Using the same techniques described above to test the strength of helix–surface joint, we found that Cell-Tak^{TM}, though seeming very promising, did not attach helical ribbons strongly enough to withstand even small disturbances. It is possible that with the use of additives, Cell-Tak$^{\text{TM}}$ may achieve useful bond strengths for our experiments. In prior experiments, it has been observed that some cross-linking agents (oxygen, polyvalent metal ions, aldehydes, and other bi/polyfunctional cross-linkers[145]), copolymers,[146] and anionic polymers/macromolecules (collagen, casein, keratin, etc.[145,147]) can be used to increase the bonding strength of Cell-Tak^{TM}. However, we have did not explore this avenue of investigation.

From the experimental work described above, it is clear that without knowledge of the helix surface structure, it is difficult to predict how biological adhesives, even those present in cell membranes or extra cellular matrices, will interact with helical ribbons. Thus, we proceeded to test synthetic adhesives, some of which have previously been used for biological materials. We examined a wide variety of these synthetic adhesives, from those used for bonding metals to those used for attaching wood and leather. We started with cyanoacrylates for two reasons. First, these adhesives are commercially available and are rich in their variety. Examples of adhesives based on cyanoacrylates are Superglue (Elmer's Products, Inc., FPC Corp.), Instant Bonder (Loctite Corp.), Krazy Glues (Elmer's Products, Inc.), Quick Bond (Aron Alpha), Tissue Adhesive (Permabond), Nail Enamel (L'Oreal), etc. Second, these adhesives have already been used in medicine as an affective alternative for wound stitches for patching skin lacerations and surgical incisions.[148] Therefore we had reason to expect that this type of adhesive might be suitable for our applications. Unfortunately, most cyanoacrylates can withstand moisture only in small concentrations while curing, and when placed in an aqueous solution prior to being completely cured, they tend to dissipate. The time scale of this dissipation varied from just a few seconds to an hour, which made most of the cyanoacrylate–based adhesives infeasible to use. Helix attachment to the few cyanoacrylates that did not rapidly dissipate was practically impossible to achieve: the helices did not have a strong affinity for the glue surfaces, i. e. it took 20 or more trials to get a single helix to form a weak bond to them (Tissue Adhesive and Quick

Bond).

Finally we tried epoxies as adhesives, although they have not been widely used in the biological sciences. Epoxies were appealing to us, since we had the opportunity to mix and match various epoxy resins with a variety of hardeners, change the mixing proportions of the two, and add extra accelerators to the various hardeners. Epoxies from Loctite Corp., Devcon Consumer Products, Armstrong Products Company, Progressive Epoxy Polymers, and CVC Inc. were studied. The procedure for bonding the helices to the various epoxies is described in Section 4.2.1. Each mixture of an epoxy resin and a hardener was evaluated separately. We also evaluated the ratio of the components in each mixture to obtain the best adhesion for each trial. In formulating the mixtures of epoxy resins with various hardeners, we paid special attention to the chemical composition of each component. Unfortunately, the precise composition of many epoxy resins and hardeners was proprietary knowledge, and therefore was unknown to us. However, by the method of elimination and by comparing the effects of each epoxy resin mixed with a variety of hardeners and vice versa, we were able to find the best combinations and ratios of these components for our purposes. Our results for *some* combinations of Loctite and Devcon products are briefly summarized in Tables 4.1 and 4.2.3. These tables describe only a small subset of our experiments and are representative of our findings.

The first column of both Tables 4.1 and 4.2.3 presents the names of the epoxies used. Table 4.1 addresses the behavior of epoxies when they are placed in small quantities into an aqueous solution, i. e. when epoxies in an aqueous solution form small spheres with diameters of $\sim 5-10\mu$m (second column).[c] Table 4.1 also describes the effectiveness of these epoxies in forming a strong bond with high pitch (third column) and low pitch (fourth column) helical ribbons in CDLC. As can be seen in Table 4.1, the epoxy mixtures studied display a wide variety of behaviors when placed in an aqueous medium in contact with helical ribbons in CDLC.

The following notation is used in the Table 4.1:

- "N/A": observations were not possible for fast–drying and fast–dissipating epoxies since the time for epoxy dissipation or curing was much shorter than the time necessary for selecting a helix and bringing it into a contact with the epoxy,

[c]When "dissipating" epoxies (see Table 4.1) were placed in an aqueous solution in large quantities, they formed large spheres with diameters of $15 - 20\mu$m. The surfaces of these spheres were found to solidify while their interior continued to be tacky for > 2 hours.

Table 4.1: The list of epoxies from Loctite Corporation and Devcon Consumer Products used in attempts to bond helical structures in CDLC to a rigid glass surface. The table contains the names of each epoxy adhesive, the behavior of each adhesive in an aqueous solution, and their effectiveness in bonding high and low pitch helical ribbons in CDLC. For an explanation of the notation, see the text.

Name of Epoxy	Behavior in an Aqueous Solution	Effectiveness on High Pitch Helices	Effectiveness on on Low Pitch Helices
Loctite Epoxies			
Toughened (fast-setting)	dries in $\sim$ 15 min	insignificant	significant
Toughened (slow-setting)	dissipates immediately	N/A	N/A
Metal Bonder	dissipates immediately	N/A	N/A
Glass Bonder	dissipates immediately	N/A	N/A
Ultra Strength	dissipates in $\sim$ 5 min	N/A	N/A
High Strength	dissipates in $\sim$ 5 min	N/A	N/A
Electrical (Non-Corrosive)	hardens in $\sim$ 30 min	none	none
Fast Setting	dries in $<$ 1 min	N/A	N/A
Devcon Epoxies			
5-Minute Epoxy®	dries in $\sim$ 15 min	insignificant	significant
2 Ton Epoxy	hardens in $\sim$ 30 min	none	none

Table 4.2: The list of epoxies from Loctite Corp. and Devcon Consumer Products used in attempts to bond helical structures in CDLC to a rigid glass surface: the chemical composition of each epoxy resin and hardener. The ratio of epoxy resin to hardener is also given. The proprietary chemical components are shown in "Italic" script.

Name of Epoxy	Chemical Composition of Epoxy Resin	Chemical Composition of Hardener	Mix Ratio by volume (Resin:Hardener)
Loctite Epoxies			
Toughened (fast-setting)	*3 Resin Types*	*Mercaptan-Terminated Polymer Tertiary Amine, Amine Compound*	1:1
Toughened (slow-setting)	*1 Resin*, Clay	*Amine*, Clay, Silica Substituted Aminophenol Phenolic Acid, Glycerine	1:1
Metal Bonder	*1 Resin*, Modified SiO_2 Quartz, Silica Nontoxic Ingredients	*Amine*, Quartz, *Epoxy Resin* Nonylphenol, $Si0_2$, Silica, Diethylenetriamene	2:1
Glass Bonder	*1 Resin*	*2 Substituted Polyamines*	2:1
Ultra Strength	*2 Resin Types*, *Additive*, Modified SiO_2	*Amine resin*, *2 Aliphatic Amines*	2:1
High Strength	*1 Resin*, *Additives*	*2 Polyamines*, SiO_2 Diethyleneglycol Monoethyl Ether Glycerine, 1 Aminophenol	2:1
Electrical (Non-Corrosive)	*2 Resin Types*, *Organic Resin*	*1 Amine Compound*, Nonylphenol, *Substituted Alcohol*	1:1
Fast Setting	*1 Resin*	*Mercaptan-Terminated Polymer*, *Tertiary Amine, Amine Compound*	1:1
Devcon Epoxies			
5-Minute Epoxy®	DGEBPA[a]	Mercaptan Amine Blend, DMP[b]	1:1
2 Ton Epoxy	DGEBPA	APE[c], Nonylphenol	1:1

[a]Bisphenol A Diglycidyl Ester Resin

[b]DMP = 2,4,6-Tri(dimethylaminomethyl)phenol

[c]Aminoethylpiperazine

- "none": no attachment of a helix to the epoxy was observed after 30 trials,
- "insignificant": some attachment could be observed after roughly 20 trials,
- "significant": strong attachment was observed in 3-5 trials.

Table 4.2.3 further describes the general composition of each epoxy resin (second column) and hardener (third column) used for the mixtures in Table 4.1. The fourth column in Table 4.2.3 contains the ratio of resin to hardener used in each mixture. As can be observed from Table 4.2.3, the composition of most of epoxies is proprietary (denoted by "Italic" script). Therefore, it is impossible to state the exact nature of the chemical reactions that take place in both the process of epoxy curing and the process of helix adhesion to an epoxy. We can only qualitatively speculate on the nature of helix–epoxy bonding and the factors that serve a stabilizing role in the formation of this bond. The experimental results described in Tables 4.1 and 4.2.3 can be qualitatively summarized in the following manner for the helical structures in CDLC:

1. ONLY mercaptan–containing epoxies do not dissipate in an aqueous medium (Toughened (fast-setting) and Fast Setting epoxies by *Loctite Corp.*, and 5-Minute Epoxy® by *Devcon Consumer Products*); non-mercaptan containing epoxies do not dissipate ONLY if they contain accelerators, such as nonylphenol (Electrical (Non-Corrosive) epoxy by *Loctite Corp.* and 2 Ton Epoxy® by *Devcon Consumer Products*),

2. ONLY mercaptan–containing epoxies attract either pitch helical ribbons (Toughened (fast-setting) epoxy by *Loctite Corp.* and 5-Minute Epoxy® by *Devcon Consumer Products*; note that *Loctite*'s Fast Setting epoxy cures quicker than we are able to perform the experiment),

3. low pitch helical ribbons adhere easily and strongly to mercaptan–containing epoxies (Toughened (fast-setting) epoxy by *Loctite Corp.* and 5-Minute Epoxy® by *Devcon Consumer Products*),

4. high pitch helical ribbons exhibit a very insignificant attraction, if any, to mercaptan–containing epoxies (Toughened (fast-setting) epoxy by *Loctite Corp.* and 5-Minute Epoxy® by *Devcon Consumer Products*).

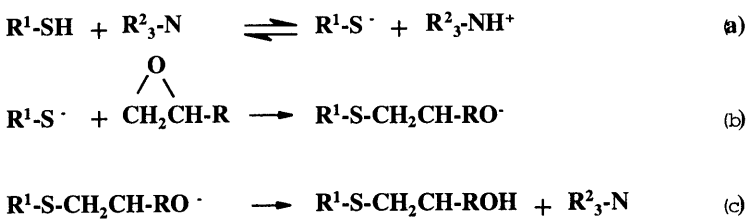

Figure 4.6: Catalysis of the epoxide-mercaptan reaction: (a) the mercaptan reacts with an amine to give the mercaptide ion; (b) mercaptide ion reacts with an epoxide; (c) a reactive intermediate from the previous reaction interacts with amine cation.

First, from these observations, it is clear that mercaptan–containing (-SH containing) hardeners have a dual role in helix adhesion, as can be seen in items 1 and 2 above. First, mercaptan groups seem to have a stabilizing effect on the curing of epoxies in an aqueous medium, i.e. mercaptan–containing epoxies do not dissipate in an aqueous medium. Without mercaptan groups (-SH), the hardeners must contain at least a single accelerator (nonylphenol, 2,4,6-Tri(dimethylaminomethyl)phenol, tetramines, such as triethylenetetramine, and others[149–151]). This is necessary to keep the epoxy from dissolving in an aqueous medium prior to the initiation of the curing reaction between the amines in the hardeners and the epoxides in the epoxy resins ($\widehat{OCH_2C}H-$). Second, the mercaptan groups seem to be facilitating helix adhesion to the epoxies. In the absence of mercaptan groups, even non-dissipating epoxies do not show any affinity for the helical ribbons, as can be seen in items 3 and 4 above. It is interesting to note that although the *Loctite*'s "Fast Setting" epoxy contains mercaptan groups, it is impractical for our purposes since its curing time in CDLC is less than a minute. It is known[150] that one possible catalysis of the epoxide–mercaptan reaction in the presence of amines occurs first by the mercaptan reacting with an amine to give a mercaptide ion. The latter then reacts with an epoxide (Figure 4.6). Alternatively, nucleophilic catalysis can occur. In this case, the amine first reacts with epoxide to produce a reactive intermediate, which then reacts with the mercaptan in a nucleophilic displacement (Figure 4.7).[150] The products in both of these reactions are a tertiary amine, which can participate further in mercaptan–amine catalysis, and an alcohol (Figures 4.6 and 4.7).

Based on these observations, we believe that it is the hydroxyl group of the alcohol (the product of epoxy–hardener reaction) that is responsible for the adhesion of helices. Since we observed that helix surfaces are hydrophilic, it is reasonable that

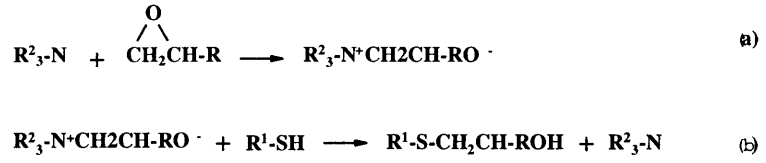

Figure 4.7: Nucleophilic catalysis: (a) amine reacts with epoxide to produce a reactive intermediate; (b) a reactive intermediated reacts with mercaptan in a nucleophilic displacement.

the hydroxyl groups of the cured epoxy act as adhesion points (or hydrogen bond donors) for helix surfaces. Another speculation on the nature of the helix attraction to various epoxies is that cholesterol is stacked inside the helical ribbons in such a way that its hydroxyl group is positioned at the helix surface. If this is true, then it is also feasible that hydrogen bonding could occur between the hydroxyl group of a curing epoxy and the hydroxyl group of cholesterol. Though reasonable, this hypothesis needs to be further investigated, the mechanism of helix adhesion needs to be understood, and the exact nature of the helix–epoxy interaction has to be exactly delineated.

There exist other implications of our observations in Tables 4.1 and 4.2.3. It appears that the high pitch and low pitch helical ribbons produced in the same material, CDLC, have very different affinities for one and the same epoxy. We therefore conjuncture that high and low pitch helical ribbons have different surface structures. This is an important observation in the context of our experimental observations in Chapter 2, where we have noted different fluorescent signatures for high and low pitch helices coated with one and the same type of phospholipid molecule. The nature of the structural differences between high and low pitch helices needs to be further investigated. In this context, it is important to point out that we performed a series of similar experiments with other quaternary sterol systems, in which the affinity of high and low pitch helices for various epoxies was observed. In these experiments, we were unable to obtain significant adhesion of any of the helical ribbons to any of the above mentioned adhesives. This result suggests that although the general geometrical parameters of helical ribbons are not affected by the chemical composition of the helix environment, the helix surface chemistry is highly sensitive to this composition. Clearly, further investigation of the exact internal and external chemistry of the helical ribbons needs to be performed. This investigation has to be done across a variety of quaternary sterol systems, such that the role of each chemical component in each

system is clearly identified.

4.3 The Force Term in the Theoretical Models

4.3.1 The Theoretical Form of the Axial Force Term

In order to experimentally probe the elastic properties of helical ribbons, they must be placed under external stresses. In our experiments, the external stresses were provided by the force directed uniaxially along the primary axis of the helix. This was the easiest force to apply with our experimental setup. It also allowed us to define an effective spring constant for the helices.

A theoretical understanding of the behavior of helical structures under such force can be obtained by carefully evaluating the theoretical models currently used to explain the geometrical characteristics of helical ribbons. The goal of this evaluation is to extract a term reflecting the applied force from the framework of current theoretical models.

The three current models describing the geometrical characteristics of helical ribbons, Chung *et al.*'s,[12] Selinger *et al.*'s,[18] and crystalline, present three different forms of phenomenological Helmholtz free energy for helical structures. The Helmholtz is a reasonable choice of ensemble since these models consider helical ribbons free from external forces. However, even in the presence of external forces, the description of helical structures in terms of a Helmholtz free energy is valid. This is true since experimentally we control the axial length of the helix and allow the applied force to take whatever values are necessary to maintain the prescribed axial length.

To begin our analysis, we make an analogy with a gas–liquid system. In this analogy, the following parameters from the helix system are taken to be equivalent to the parameters from the gas–liquid system: the applied force J and the negative pressure $-P$; the helix axial length L and the gas volume V; the helix contour length l and the number of particles N; the chemical potentials of helical and straight phases of a helix for its two phases (experimental evidence is discussed in Section 2.6.3) μ_h and μ_s, and the chemical potentials of liquid and gas phases μ_l and μ_g, respectively. All experiments were performed at constant temperature; thus, we will not be explicitly including temperature in our equations. This set of analogies identifies all the parameters necessary to continue our discussion. In this analogy, it becomes clear that the description of helical ribbons in terms of Helmholtz free energy is valid since

experimentally we control helix "volume" (i. e. axial length) and allow the "negative pressure" (i. e. the tension) on helix to take the values necessary to preserve the prescribed axial helix length.

We continue by examining the thermodynamic definition of the Helmholtz free energy and its various partial derivatives. First, we recall that the Helmholtz free energy is defined as

$$A = E - TS, \tag{4.2}$$

where E is the internal energy of the system, T is the temperature, and S is the entropy. By the first law of thermodynamics,

$$E = Q + W, \tag{4.3}$$

where Q is the heat transferred to the system and W is the work done on the system. For a process involving only infinitesimal changes in the thermodynamic parameters, i. e. an infinitesimal process, the first law becomes[152]

$$dE = đ Q + đ W, \tag{4.4}$$

where $đ$ implies that the amount of heat transferred and the amount of work done on the system is an inexact differential, i. e. it is not the differential of of an actual function of thermodynamic parameters.[152] If the infinitesimal process is quasi-static, then dE and $đ W$ can be expressed in terms of thermodynamic parameters P, V, T, S, etc. In such process the amount of heat transferred to the system can also be defined from the second law of thermodynamics as

$$dS = \frac{đ Q}{T}, \tag{4.5}$$

where T is the absolute temperature of the system. Then, the infinitesimal change in the Helmholtz free energy is given by

$$\begin{aligned} dA &= dE - d(TS) = đ Q + đ W - SdT - TdS \\ &= TdS + đ W - SdT - TdS = -SdT + đ W, \end{aligned} \tag{4.6}$$

where we have employed Eqs. 4.2, 4.3, 4.4, and 4.5. The two ways in which work may be done on a helix in the framework of the Helmholtz free energy $A(T, V, N)$ are

1. increasing the helix axial length L ("volume V") while holding the contour length l ("number of particles N") fixed, and

2. increasing the helix contour length l ("number of particles N") while holding the axial length L ("volume V") fixed.

Then infinitesimal work done on the system (helix) by the first method is

$$đW_1 = JdL(= -PdV), \tag{4.7}$$

where we defined the positive work done on the system as a positive change in helix axial length and J as the external force applied to helix. The infinitesimal work done on the system (helix) by the second method is

$$đW_2 = \mu_h dl(= \mu dN), \tag{4.8}$$

where we defined the positive work on the system as the work done on a helix to increase its contour length. The "force" applied to the system to increase its contour length l is the chemical potential μ_h for helix not separated into helical and straight phases. Now, the infinitesimal change in the Helmholtz free energy in Eq. (4.6) becomes

$$dA = -SdT + JdL + \mu dl. \tag{4.9}$$

This equation can be simplified even further if we note that in our experiments the contour length was kept fixed and temperature was kept constant. As a result, we can obtain an expression for the force applied to the helix in terms of partial derivatives as

$$J = \left.\frac{\partial A}{\partial L}\right|_{l,T}. \tag{4.10}$$

This expression can be evaluated directly from expressions of the elastic free energy in the framework of each of the current theories.

An alternative method for finding the force J applied to a helix is through the Gibbs ensemble, where the force J is explicit. In the Gibbs free energy J is a variable, that is $G = G(T, J, l)$, which is analogous to $G = G(T, P, N)$ for the gas–liquid system. From this definition, the Gibbs free energy can be obtained from the Helmholtz free energy by

$$G = A - JL, \tag{4.11}$$

where J is the force applied to the helix and L is the helix axial length. In what follows, we will use the first approach to find the applied force J.

4.3.2 Relevance to Theoretical Models

I would like to thank Mr. Brice Smith for his great contribution to the theoretical part of this work.

Given the form of theoretical expressions for the force J evaluated in the framework of each of the current theories, one can deduce expressions for the helix spring constant K_{helix} when the uniaxial force J stretches or compresses a helix by an amount ΔL:

$$K_{helix} = \frac{J}{\Delta L}. \tag{4.12}$$

In this section, we will present the derivations of the expressions for J from the Helmholtz ensembles within the context of Chung *et al.*'s,[12], Selinger *et al.*'s,[18] and the crystalline theories. We will then deduce the expressions for the helix spring constants K_{helix} using each theoretical model and examine the helix spring constants' dependences on the microscopic elastic moduli and helix geometrical dimensions.

We then perform order of magnitude estimates for the value of the helix spring constants based on the measured values of the helix geometrical parameters and the experimental values of elastic moduli for liquid crystalline bilayers made of cholesterol and phospholipids. These estimates are performed only within the context of Chung *et al.*'s theory.[12] In Section 4.5.2, we compare these estimates to the measured values of the helix spring constant.

The theoretical predictions for the helix spring constant K_{helix} obtained in this section are further used in Section 4.5, where we infer whether and how the internal helix structure may affect its spring constant, K_{helix}. To do so, we first normalize out the contribution of external geometrical parameters from the measured values of K_{helix}. Such dimensional parametrization is performed within context of Chung *et al.*'s,[12], Selinger *et al.*'s,[18] and the crystalline theories.

Relevance to Chung *et al.*'s Theory[12]

We begin by extracting the expressions for the force term J and the helix spring constant K^C_{helix} from the model of Chung *et al.*.[12] To do so, we first recall the full expression for the Helmholtz free energy per unit area of a helix as described by Chung *et al.*[12] and reviewed in Eq. (4.13):

$$\mathbf{a}^C_{\text{helix}} = \frac{K_n^{cc}\cos^4\psi + K_n^{pp}\sin^4\psi + (K_n^{cp}/2)\sin^2 2\psi}{2R^2} - \frac{K_n^*\sin 2\psi}{2R}$$

$$+ \quad \frac{\Lambda_n}{w}\left(\frac{\sin 2\psi}{2R} - \tau_n^0\right)^2 + \frac{2g_0}{w}, \tag{4.13}$$

where the superscript C stands for Chung *et al.*'s model and the elastic moduli $K_n^{cc}, K_n^{pp}, K_n^{cp}, K_n^*, \Lambda_n,$ andτ_n^0 are integrated over the ribbon thickness, i. e. they are functions of the number of bilayers making up the helical ribbon. In the case that $J = 0$ by minimizing this free energy density with respect to helix radius R and helix pitch angle ψ^C, the equilibrium values of helix radius and pitch angle are as shown in Eq. (3.27) and Eq. (3.29), respectively

$$R_0^C = \frac{\left(K_n^{cc}\frac{1}{\tan^2\psi} + K_n^{pp}\tan^2\psi + 2K_n^{cp} + 2\frac{\Lambda_n}{w}\right)\sin 2\psi}{K_n^* + 2\frac{\Lambda_n}{w}\tau_n^0} \tag{4.14}$$

and

$$\psi_0^C = \arctan\left[\left(\frac{K_n^{cc}}{K_n^{pp}}\right)^{\frac{1}{4}}\right], \tag{4.15}$$

where the superscript C again signifies that the above expression is derived from Chung *et al.*'s model.[12]

This theory may be applied to a case of a helical ribbon under axial tension. To do so, we first note that the Helmholtz free energy density in Eq. (4.13) is related to the Helmholtz free energy by

$$\mathbf{A}_{\text{helix}} = \mathbf{a}_{\text{helix}}(lw), \tag{4.16}$$

where l is the helix contour length and w is the helical ribbon width. We then employ the above result to the expression in Eq. (4.10) where J is explicit:

$$J^C = \left.\frac{\partial \mathbf{A}_{\text{helix}}^C}{\partial L}\right|_{l,T} = \left.\frac{\partial \mathbf{A}_{\text{helix}}^C}{l\partial(\frac{L}{l})}\right|_{l,T} = \left.\frac{\partial \mathbf{A}_{\text{helix}}^C}{l\partial(\sin\psi)}\right|_{l,T}, \tag{4.17}$$

where the ratio of helix axial length to its contour length, $\frac{L}{l}$, is replaced by a trigonometric function, as can be inferred from Figure 3.4:

$$\frac{L}{l} = \sin\psi. \tag{4.18}$$

Using Eq. (4.14) in Eq. (4.17), we find the following expression

$$\begin{aligned} 0 \;=\; & K_n^{cc} - K_n^{pp}\tan^4\psi^C + \frac{J^C}{w}\frac{1}{(K_n^* + 2\frac{\Lambda_n}{w}\tau_n^0)^2}\sin^3\psi^C\left(K_n^{cc}\frac{1}{\tan^2\psi^C}\right. \\ & + \left. K_n^{pp}\tan^2\psi^C + 2K_n^{cp} + 2\frac{\Lambda_n}{w}\right)^2. \end{aligned} \tag{4.19}$$

This equation cannot be solved analytically for the change in the helix axial length ΔL^C as a function of elastic moduli, $K_n^{cc}, K_n^{pp}, K_n^{cp}, K_n^*$, and Λ_n, and thus we cannot obtain an expression for the helix spring constant K_{helix}^C directly from Eq. (4.19). Therefore, to obtain an expression for the helix spring constant, we linearized this equation around the unstressed pitch angle ψ_0^C. This approach is applicable only for small forces, whose contribution to the elastic free energy density in Eq. (4.19) is much smaller than the value of the equilibrium elastic free energy density given by Eq. (4.13). The linearization is constructed by letting

$$\psi^C = \psi_0^C + \Delta\psi^C, \tag{4.20}$$

where ψ_0^C is the equilibrium pitch angle in the absence of the external force and $\Delta\psi^C$ is the change in pitch angle when the force is applied. $\Delta\psi^C$ can be found in terms of ψ_0^C, the equilibrium helix radius R_0, the ribbon width w, the applied force J, and the elastic modulus K_n^{pp}

$$\Delta\psi^C = \frac{(R_0^C)^2}{4wK_n^{pp}} \frac{1}{\tan^2\psi_0^C(1+\tan^2\psi_0^C)^{\frac{1}{2}}} J^C. \tag{4.21}$$

For any theoretical model, the fractional change of a helix axial length when an external force is applied can be found in terms of the equilibrium pitch angle of the unstressed spring ψ_0 and the change in helix pitch angle $\Delta\psi$ as

$$\frac{\Delta L}{L_0} = \frac{\sin\psi}{\sin\psi_0} \sim \frac{\Delta\psi}{\tan\psi_0}. \tag{4.22}$$

Using this expression and the expression for the change in the pitch angle as an axial force is applied to the helix (Eq. (4.21)), we can find the fractional change in helix axial length, i. e. fractional elongation

$$\frac{\Delta L^C}{L_0^C} = \frac{(R_0^C)^2}{4wK_n^{pp}} \frac{1}{\tan^3\psi_0^C(1+\tan^2\psi_0^C)^{\frac{1}{2}}} J^C. \tag{4.23}$$

The fractional change in helix radius can be also found for any theoretical model in terms of the equilibrium pitch angle ψ_0 and the change in helix pitch angle, $\Delta\psi$, which occurs when an external force is applied to a helix. This fractional change of helix radius is

$$\frac{\Delta R}{R_0} = \frac{R - R_0}{R_0} \sim \Delta\psi \frac{1-\tan^2\psi_0}{\tan\psi_0}. \tag{4.24}$$

Then, re-expressing the fractional change in helix radius in terms of the applied force, we obtain

$$\frac{\Delta R^C}{R_0^C} = \frac{(R_0^C)^2}{4wK_n^{pp}} \frac{1-\tan^2\psi_0^C}{\tan^3\psi_0^C(1+\tan^2\psi_0^C)^{\frac{1}{2}}} J^C. \tag{4.25}$$

The expression $\Delta R^C/R_0^C$ in Eq. (4.25) makes physical sense only when $\Delta R^C < 0$ for $J^C > 0$ and when $\Delta R^C > 0$ for $J^C < 0$, if the helical ribbon is to behave like an ordinary spring. That is, when a helix is stretched, we expect the radius to decrease, and conversely, when a helix is compressed, we expect its radius to increase.[d] It is therefore interesting to observe that in the above expression for $\Delta R^C/R_0^C$ this condition is true only for $\tan\psi_0^C > 1$, i. e., $\psi_0^C > 45°$. This result is attractive since Chung *et al.*'s model[12] is in question for low pitch helices ($\psi^C = 11°$) since this model predicts that the energy cost for bending a helical ribbon perpendicular to the tilt of molecules underlying a helical structure is approximately 1000 times greater than the energy cost of bending the helical ribbon parallel to the molecular tilt. The phase transition phenomenon described qualitatively in Chapter 2 further demonstrates that low pitch structures can behave quite differently than ordinary "Hookean" springs during large deformations.

Using the expression for the helix elongation (Eqn. 4.23), we find the following expression for the helix spring constant within the Chung *et al.* formalism to be

$$K^C_{\text{helix}} = \frac{J^C}{\Delta L^C} = \frac{4wK_n^{pp}}{L_0(R_0^C)^2}\tan^3\psi_0^C(1+\tan^2\psi_0^C)^{\frac{1}{2}}. \tag{4.26}$$

The above expression for the helix spring constant is proportional to the ribbon width and inversely proportional to the equilibrium axial length and square of the equilibrium radius. These dependences of the helix spring constant on its geometrical dimensions are not surprising since they can be simply derived for ordinary springs from physical arguments.[153] It is clear that helix geometrical parameters and the value of the elastic modulus K_n^{pp} govern the value of the helix spring constant K_{helix}. Therefore, knowledge of the helix geometrical parameters and the measured value of the helix spring constant can be used to predict the phenomenological elastic modulus K_n^{pp}.

---

[d]Mathematically, this is easily proved using the conservation of helix contour length. For one turn of helix, the contour length is $2\pi R_0\sin\psi_0 = 2\pi R\sin\psi$, where R_0 and ψ_0 are radius and pitch angle of an unstressed helix, respectively, and R and ψ are radius and pitch angle of a stressed helix. Then for small changes in pitch angle $\Delta\psi = \psi - \psi_0$, one finds that $\sin\psi \sim \sin\psi_0(1 + \Delta\psi/\tan\psi_0)$, which combined with the conservation of helix contour length results in the following expression for the change in helix radius:

$$\Delta R = -\frac{R_0\cos\psi_0\Delta\psi}{\sin\psi_0+\cos\psi_0\Delta\psi}.$$

It is clear that the change in helix radius ΔR always has an opposite sign to the change in helix pitch angle $\Delta\psi$ and therefore to the direction of an external axial force (Eqn. 4.21).

Now we can perform an estimate for the values of the helix spring constant based on the measured values of the helix geometrical parameters and the measured values of K_n^{pp} for cholesterol–phospholipid bilayers, which is a curvature (bending) elastic modulus measured in units of energy ($[N \times m]$). If we believe that helices are formed of liquid crystal bilayers, than we can use the data for the measured elastic moduli for phospholipid bilayers as a benchmark value for the elastic moduli of the cholesterol–phospholipid bilayers since the presence of cholesterol in the bilayer typically changes the value of K_n^{pp} by no more than a factor of 3.[154,155] The value of the elastic moduli of fluid phospholipid bilayers, K_n^{pp}, has been measured in a variety of systems. In all cases, the values have been found to be on the order of 10^{-19} N m or smaller.[156–161] This implies that for a high pitch helix with a pitch angle of $\psi^C = 54°$ and with typical geometrical parameters (ribbon width $w \sim 10 \times 10^{-6}$ m, helix radius $R \sim 5 \times 10^{-6}$ m, and helix axial length $L \sim 100 \times 10^{-6}$ m), the maximum spring constant can be estimated from Eq. (4.26) to be on the order of

$$K^C_{\text{helix}} \sim 2 \times 10^{-8}\text{N/m} = 2 \times 10^{-5}\text{pN/nm}. \tag{4.27}$$

To compare this result with values of spring constants found in other biological systems, we look at the stretching of the DNA molecule with laser tweezers and AFM technology. Stretching the DNA molecule with these techniques yields the values for the spring constant that are three orders of magnitude greater than the value estimated above ($\sim (8.9 \pm 1.1) \times 10^{-5}$ pN/nm).[103,138] We have to note at this point that such an estimation for the low pitch helices would yield even smaller spring constants, since the pitch angle $\psi_0^C = 11°$ results in a much smaller tangent. In fact, using the above derivation, we estimate that a typical low pitch helical ribbon of width $w \sim 5 \times 10^{-6}$ m, radius $R \sim 10 \times 10^{-6}$ m, and axial length $L \sim 50 \times 10^{-6}$ m, made of cholesterol–phospholipid bilayers would have a spring constant in excess of

$$K^C_{\text{helix}} \sim 9 \times 10^{-11}\text{N/m} = 9 \times 10^{-8}\text{pN/nm}, \tag{4.28}$$

where we have employed the maximum value of the curvature elastic modulus for the phospholipid bilayers $K_n^{pp} = 1 \times 10^{-19}$ N m. This value is six orders of magnitude smaller than that measured for a DNA molecule.[103] However, it is difficult to say whether this estimation is valid as the nature of our estimate for the elastic modulus of cholesterol–phospholipid bilayer, K_n^{pp}, is not definite.

Relevance to Selinger *et al.*'s Theory[18]

Now we perform similar type of calculations using Selinger *et al.*'s theory,[18] i. e. we extract the expressions for the force term J and the helix spring constant K^S_{helix} from the model of Selinger *et al.*.[18] To do so, we first recall the full expression for the Helmholtz free energy per unit area of a helix as described by Selinger *et al.*[18]:

$$\mathbf{a}^S_{\text{helix}} = \frac{1}{2R^2}(\kappa + \kappa' \cos^2\psi + \kappa'' \cos^4\psi) - \frac{1}{2R}\kappa^*_{HP}\sin(2\psi), \tag{4.29}$$

where the superscript S denotes Selinger *et al.*'s model, and $\frac{1}{2R^2}\kappa'' \cos^4\psi$ is an additional elastic anisotropy term. This term has also been considered by Chung *et al.*, in whose work κ'' was labeled as K^{cp}.[12] Selinger *et al.* explicitly ignored this term since it does not play an important role in the zero minimization of the free energy density.[18] For the purpose of comparison of the Chung *et al.*'s and Selinger *et al.*'s theories, we retain this elastic anisotropy term in our calculations. The equilibrium pitch angle can then be calculated as follows

$$\psi^S_0 = \arctan\left[\left(\frac{\kappa + \kappa' + \kappa''}{\kappa}\right)^{\frac{1}{4}}\right]. \tag{4.30}$$

Using this result, we can also calculate the equilibrium helix radius from

$$R^S_0 = \frac{2}{\kappa^*_{HP}} \frac{\kappa + \kappa' \cos^2\psi^S_0 + \kappa'' \cos^4\psi^S_0}{\sin(2\psi^S_0)}. \tag{4.31}$$

As in the case of Chung *et al.*'s theory above, we can rewrite the Helmholtz free energy density in Eqn.4.29 as Helmholtz free energy and then employ Eq. (4.10) to find

$$J^S = \left.\frac{\partial \mathbf{A}^S_{\text{helix}}}{\partial L}\right|_{l,T} = \left.\frac{\partial \mathbf{a}^S_{\text{helix}}(lw)}{l\partial(\frac{L}{l})}\right|_{l,T} = \left.\frac{\partial \mathbf{A}^S_{\text{helix}}}{\partial(\sin\psi)}\right|_{l,T}, \tag{4.32}$$

where the ratio L/l is replaced by $\sin\psi$, as shown in Eq. (4.18). Using Eq. (4.31) in Eq. (4.32) results in the following relation:

$$\begin{aligned} 0 = \kappa' + 2\kappa'' \cos^2\psi^S \quad &+ \frac{4(\kappa + \kappa' \cos^2\psi^S + \kappa'' \cos^4\psi^S)}{\tan(2\psi^S)\sin(2\psi^S)} \\ &+ \frac{4J^S}{w(\kappa^*_{HP})^2} \frac{f^2(\psi^S)}{(\sin\psi^S \sin^2(2\psi^S))}, \end{aligned} \tag{4.33}$$

where $f(\psi^S) = (\kappa + \kappa' \cos^2\psi^S + \kappa'' \cos^4\psi^S)$. As in Chung *et al.*'s theory,[12] this equation cannot be solved analytically for ΔL^S, a change in helix axial length as a result of an external force. Therefore, helix spring constant K^S_{helix} cannot be found

directly from Eq. (4.33). As a result, we find an approximate solution to this equation by linearizing it with around the unstressed pitch angle ψ_0^S, which is valid for small forces. We again construct the approximation by letting

$$\psi^S = \psi_0^S + \Delta\psi^S, \tag{4.34}$$

where ψ_0^S is the equilibrium pitch angle given in Eq. (4.30), and $\Delta\psi^S$ is the change in the pitch angle due to the applied force. Substituting Eq. (4.34) into Eq. (4.33) we obtain $\Delta\psi^S$, the change in helix pitch angle, in terms of the equilibrium pitch angle ψ_0^S, the equilibrium helix radius R_0^S, the ribbon width w, the applied force J^S, and the elastic moduli κ, κ', and κ''

$$\Delta\psi^S = \frac{(R_0^S)^2}{w}\frac{1}{\sin\psi_0^S\alpha(\psi_0^S)}J^S, \tag{4.35}$$

where

$$\begin{aligned}\alpha(\psi_0^S) &= 2\kappa''\sin(2\psi_0^S) \\ &+ \frac{4}{\tan(2\psi_0^S)}\left[\frac{2(2+\tan^2(2\psi_0^S))}{\sin(2\psi_0^S)\tan(2\psi_0^S)}(\kappa+\kappa'\cos^2\psi_0^S+\kappa''\cos^4\psi_0^S)\right. \\ &+ \left.(\kappa'+2\kappa''\cos^2(2\psi_0^S))\right].\end{aligned} \tag{4.36}$$

It is clear that the expression for the change in the helix pitch angle $\Delta\psi^S$ in Eq. (4.35) derived from Selinger *et al.*'s model is much more complicated than the respective expression for $\Delta\psi^S$ in Eq. (4.21) derived from Chung *et al.*'s model. It is also worthwhile noting that $\Delta\psi^S$ depends on all three elastic moduli, unlike $\Delta\psi^C$ which depends only on one elastic modulus K_n^{pp}.

Using the expression for the change in the pitch angle we just derived and Eq. (4.22), we find the fractional change in helix axial length to be

$$\frac{\Delta L^S}{L_0^S} = \frac{(R_0^S)^2}{w}\frac{\cos\psi_0^S}{\sin^2\psi_0^S\alpha(\psi_0^S)}J^S. \tag{4.37}$$

Similarly, we can find the fractional change in helix radius as an axial force is applied to a helical spring to be

$$\frac{\Delta R^S}{R_0^S} = \frac{(R_0^S)^2}{w}\frac{\cos\psi_0^S}{\sin^2\psi_0^S}\frac{1-\tan^2\psi_0^S}{\alpha(\psi_0^S)}J^S. \tag{4.38}$$

Unlike the expression for the fractional change in helix radius derived from Chung *et al.*'s theory, we cannot easily assess the physical meaning of the fractional change in

helix radius in Eq. (4.38): as can be observed, Eq. (4.38) is a very complicated function of all three elastic moduli, one of which, κ', can be negative, and of trigonometric functions of the equilibrium pitch angle ψ_0^S; therefore we will not further comment on this expression as we did for Eq. (4.25).

We are finally ready to derive the expression for the helix spring constant, which with the use of Eq. (4.12) becomes

$$K^S_{\text{helix}} = \frac{J^S}{\Delta L^S} = \frac{w}{L_0(R_0^S)^2} \frac{\sin^2 \psi_0^S}{\cos \psi_0^S} \alpha(\psi_0^S). \tag{4.39}$$

Again this is a far more complicated expression than that obtained in Chung *et al.*'s theory. However, the dependence of the spring constant K^S_{helix} on the geometrical parameters of a helical ribbon is the same as in Eq. (4.26) for K^C_{helix} in Chung *et al.*'s theory: $K^S_{\text{helix}} \sim w/(L_0(R_0^S)^2)$. As K^S_{helix} is a very complicated function of all three elastic moduli, we cannot proceed with its order of magnitude estimate as we have done with Chung *et al.*'s model. Therefore, we will stop with any further development of Selinger *et al.*'s model and press forward with the same type of calculations using the crystalline model.

Relevance to the Crystalline Model

The necessity for introducing the crystalline model was discussed in Chapter 3. First, our observation that the formation of helical ribbons of three distinct pitch angles is a general phenomenon found in a large variety of quaternary sterol systems led us to believe that the helical structures are fundamentally similar, unlike the theoretical predictions of Chung *et al.* and Selinger *et al.* Second, Chung *et al.* and Selinger *et al.* have made numerous, often unjustified assumptions in their theories to explain experimental observations of high and low pitch helical ribbons. Third, as is shown later in this chapter, upon deducing an expression for the helix spring constant from Chung *et al.*'s model and substituting experimental values of the elastic moduli for a different cholesterol–phospholipid system into this expression, we obtained estimates of the helix spring constant that were much higher than those obtained experimentally. All of the above reasons indicate that the nature of helical ribbons may be different than presumed; for instance, helical ribbons may be crystalline rather than liquid crystal in nature. To extend our line of reasoning to the crystalline model, we proceed by first recalling the form of the Helmholtz elastic free energy density within the

formalism of crystalline model (Eqn. 3.116)

$$\mathbf{a}_{helix} = \frac{1}{R^2}(K_\alpha cos^4\psi + 2K_\beta \cos^2\psi \sin^2\psi + K_\gamma \sin^4\psi) - \frac{K}{R}, \tag{4.40}$$

where K_α, K_β, and K_γ are phenomenological elastic parameters with dimensions of energy per unit area. These elastic parameters explicitly depend on the helical ribbon thickness and can be expressed in terms of the components of the elastic modulus tensor. K is the anisotropic spontaneous bending modulus with dimensions of energy per unit length and may depend on the ribbon thickness. As has been shown in Chapter 3, the expressions for the helix equilibrium radius and pitch angle are

$$R_0 = \frac{2}{K}\frac{(K_\alpha K_\gamma - K_\beta^2)}{(K_\alpha - 2K_\beta + K_\gamma)} \tag{4.41}$$

and

$$\psi_0 = \arctan\left[\left(\frac{K_\alpha - K_\beta}{K_\gamma - K_\beta}\right)^{\frac{1}{2}}\right], \tag{4.42}$$

respectively. It is worthwhile noticing that for the case of $K_\alpha = K_\gamma$ we are dealing with an isotropic case, in which the energy cost of bending a helical ribbon perpendicular and along ribbon length are K_α and K_γ, respectively. As expected, the helix equilibrium pitch angle in this case is $\psi_0 = 45°$. The expression for helix radius also reduces to a very simple form:

$$R_0 = \frac{K_\alpha + K_\beta}{K}, \tag{4.43}$$

which is independent of K_γ. In the case of cylinder, for which the pitch angle is $\psi_0 = 0$, the energy cost of bending helical ribbon perpendicular to the ribbon length is the same as the energy cost attributed to the cross-term, $K_\alpha = K_\beta$, which reduces the expression for helix radius to

$$R_0 = -\frac{2K_\alpha}{K}, \tag{4.44}$$

which depends only on spontaneous bending term and energy cost of bending a ribbon perpendicular to its length. We can obtain similar results for a flat ribbon, for which $\psi_0 = 90°$, in which case $K_\gamma = K_\beta$, and

$$R_0 = \frac{2K_\gamma}{K}, \tag{4.45}$$

which depends only on the spontaneous bending term and on energy cost associated with bending a ribbon parallel to its length.

Rewriting Eq. (4.40) for the full Helmholtz free energy and utilizing Eq. (4.10) in

$$J = \left.\frac{\partial \mathbf{A}_{\text{helix}}}{\partial L}\right|_{l,T} = \left.\frac{\partial \mathbf{a}_{\text{helix}}(lw)}{l\partial(\frac{L}{l})}\right|_{l,T} = \left.\frac{\partial \mathbf{A}_{\text{helix}}}{\partial(\sin\psi)}\right|_{l,T}, \tag{4.46}$$

we can find the following relationship:

$$\begin{aligned} 0 &= -(K_\beta - K_\alpha)\tan\psi + (K_\gamma - K_\beta)\tan^3\psi \\ &- \frac{J\cos^5\psi}{2K^2}[K_\alpha + 2K_\beta\tan^2\psi + K_\gamma\tan^4\psi]^2, \end{aligned} \tag{4.47}$$

where we used Eq. (4.41). As before, we find an approximate solution to the expression above by linearizing it around the unstressed pitch angle ψ_0. For small forces, we linearize Eq. (4.47) by letting

$$\psi = \psi_0 + \Delta\psi, \tag{4.48}$$

where ψ_0 is the equilibrium pitch angle given in Eq. (4.42), and $\Delta\psi$ is the change in the pitch angle due to the application of the external force. Proceeding as in the previous sections, we obtain the following results for the linearized crystalline model

$$\Delta\psi = \frac{R_0^2}{8w(K_\gamma - K_\beta)}\frac{(1+\tan^2\psi_0)^{\frac{1}{2}}}{\tan^2\psi_0}J, \tag{4.49}$$

$$\frac{\Delta L}{L_0} = \frac{R_0^2}{8w(K_\gamma - K_\beta)}\frac{(1+\tan^2\psi_0)^{\frac{1}{2}}}{\tan^3\psi_0}J, \tag{4.50}$$

where we used Eq. (4.22). However, upon calculation of $\Delta R/R$ for crystalline theory, we come to a very interesting discovery that

$$\frac{\Delta R}{R_0} = 0. \tag{4.51}$$

This expression is different from those described by Eqs. 4.25 and 4.38, where there is an explicit dependence of the fractional change of the helix radius on the change in the helix pitch angle. Expression 4.51 states that the fractional change in helix radius is independent of the change in the helix pitch angle due to an external force, and is zero for small changes in the pitch angle. This is reasonable because crystalline theory assumes that the helix pitch angle is independent of the radius, i.e., the last term in Eq. (4.40) does not carry pitch angle dependence. For comparison, in both Chung *et al.*'s and Selinger *et al.*'s theories, the respective terms do include a dependence on pitch angle (Eqs. 4.13 and 4.29). This is precisely the reason that the fractional change of helix radius on pitch angle is explicit in Eqs. 4.25 and 4.38. Experimentally,

we have confirmed our result of no dependence (Eq. (4.51)) by measuring fractional change of low pitch helix radius as a function of helix pitch angle when an axial force is applied to a helical ribbon (data are not shown). We have observed no change of helix radius when a low pitch helix was stretched from approximately 11° to approximately 30°. This confirms our original assumption in the crystalline model that the helix radius and the pitch angle are independent.

From the expression for $\Delta L/L_0$ above, we find the analytical form of the helix spring constant to be

$$K_{\text{helix}} = \frac{J}{\Delta L} = \frac{8w(K_\gamma - K_\beta)}{L_0 R_0^2} \frac{\tan^3 \psi_0}{(1 + \tan^2 \psi_0)^{\frac{1}{2}}}. \tag{4.52}$$

Again, it is quite clear from the form of the helix spring constant that K_{helix} depends on the helix dimensions through $w/(LR_0^2)$. This factor in the spring constant is identical to those found in the linearization of Chung *et al.*'s and Selinger *et al.*'s models. It is also important to keep in mind that K_{helix} is a linear function of the phenomenological elastic energy coefficients that are explicitly dependent on the helical ribbon thickness, while ψ_0 is more complex function of the elastic moduli, as shown in Eq. (4.42). We also notice that the expression for the helix spring constant derived from the crystalline model is quite simple and very similar to the expression found by linearizing Chung *et al.*'s model. However, unlike in Chung *et al.*'s model, K_{helix} here depends on the difference of two phenomenological elastic parameters, K_γ and K_β, rather than on one modulus K_n^{pp}. Therefore, we cannot perform an order of magnitude estimate for K_{helix} at this time, since we cannot estimate the correct scale for the value of $(K_\gamma - K_\beta)$. However, it is possible to calculate this value from experimental measurements of K_{helix}. This is precisely the issue we will address in the next section.

Conclusions

So far, we have developed a theoretical framework for understanding the experimental determinations of the helix spring constant measured through small axial deformations. We have extended all three theoretical models to accommodate the effects of the applied axial forces and then linearized each model around the equilibrium pitch angle. Although the expressions for helix spring constant K_{helix} obtained in

this manner are valid only for small axial forces,[e] we can now compare these three models to the experimental results. In the next section, we describe the experimental measurements of the helix spring constant via helix relaxation in aqueous solution.

At this point, we know that all three theories can be extended to demonstrate the same simple dependence of the spring constant K_{helix} on the helix geometrical parameters (ribbon width, helix axial length, and diameter), $K_{\text{helix}} \sim w/(L_0 R_0^2)$. However, the details of the other multiplicative factor (a combination of trigonometric functions of the helix equilibrium pitch angle and the phenomenological elastic moduli) in the three expressions of K_{helix} are also very important.For example, in Chung *et al.*'s theory K_{helix} is proportional to only one phenomenological elastic modulus, whereas in Selinger *et al.*'s model, it is dependent on all three moduli, and in crystalline model, K_{helix} depends on a difference of two phenomenological elastic moduli. The form of K_{helix} derived from Chung *et al.*'s model has the simplest form, whereas the one derived from Selinger *et al.*'s model is the most complex. However, both Chung *et al.* and Selinger *et al.* made numerous assumptions in creating their models, whereas we are able to extract the same amount of information from the crystalline model based on a greatly reduced number of assumptions, as discussed in a great detail in Chapter 3.

4.4 Thermal Fluctuations

One of the simplest experiments to probe the helix spring constant applies a uniaxial force extending or compressing the helix. As described in previous sections, one may implement such an experiment by pulling (or compressing) a helical spring with a flexible rod of known elastic constant. For this technique to yield accurate results, the elastic rod must have an elastic modulus not significantly larger than that of the helix, since observations are performed with a light microscope, whose limit of resolution is on the order of 1 μm. The only existing theoretical estimate of the helix spring constant comes from the work of Helfrich in 1986.[77] In his manuscript, Helfrich estimates the elastic modulus of stretching for an isotropic helical ribbon made of liquid crystalline bilayer to be $E_H = J/(\Delta L/L) = 3 \times 10^{-12}$ N, where J is

[e]The experimental observations detailed in Section 4.6 indicate that low pitch helical ribbons obey Hooke's law for axial extensions of up to 200%, that is for $\Delta\psi$ of up to 28°. This suggests that the linearization of the elastic models should be applicable to the extension of low pitch helices ($\psi_0 = 11°$) up to 28°.

the axial force applied to the helix and $\Delta L/L$ is the fractional extension/compression of the helix. This value is related to the helix spring constant by

$$K_{\text{helix}} = \frac{E_H}{L}, \tag{4.53}$$

where L is the axial length of a helix. The typical axial length of a helix is on the order of 100 μm, therefore the corresponding spring constant for a helix should be on the order of

$$K^{\text{H}}_{\text{helix}} \sim \frac{3 \times 10^{-12}}{100 \times 10^{-6}} \sim 3 \times 10^{-8}\text{N/m} = 3 \times 10^{-5}\text{pN/nm}. \tag{4.54}$$

Interestingly, the above estimate falls very close to our previous estimate obtained in Section 4.3.2 for low pitch helices ($K^{C}_{\text{helix}} \sim 2 \times 10^{-8}$N/m $= 2 \times 10^{-5}$pN/nm). This latter estimate was obtained by using the expression of the helix spring constant deduced from Chung *et al.*'s model in conjunction with experimental measurements of the elastic modulus of cholesterol–phospholipid liquid crystal bilayers.

The calculation in Eq. (4.54) suggests that the elastic constant of "an ideal measuring elastic rod" must be of $\sim 1 \times 10^{-8}$ pN/nm order of magnitude. However, even an elastic rod whose constant exceeds the above value by one order of magnitude will suffice. All of our attempts to produce such rods by heating glass needles and pulling them with large velocities failed. The glass rods produced in this manner had elastic moduli two orders of magnitude too large. This implies that in order to resolve a rod deflection of 1 μm, the smallest magnitude resolvable by a light microscope, we would need to extend a helical ribbon by 100 μm, i. e. to double the typical length of a helix. This obviously poses a problem, since, the light microscopy technique makes it impossible to make simultaneous observations at the 1 μm and 100 μm scales. (We found experimentally that the act of changing the objective lens perturbs the system making a simultaneous measurement at the above scales impossible.)

To generate the first experimental estimates of the value of K_{helix} and to provide a comparison of the measured helix spring constant with the values inferred from Helfrich's[77] theory and those estimated in Section 4.3.2, we set out to perform measurements of the thermally excited fluctuations of a helix. If the spring constant of the helical structures is slightly smaller than the current estimates, it would be possible to observe thermally induced oscillations for sufficiently large temperatures. Conversely, if the helix spring constant is much larger than those inferred from Helfrich's[77] theory and in Section 4.3.2, we would see no indication of thermal fluctuations. Therefore, if

fluctuations are not observed, this technique provides an estimate of the lower bound of the helix spring constant.

This experiment was carried out by placing helical ribbons in a temperature controlled cell and slowly raising the temperature from the ambient value. At a temperature of 80°C, the structures started to melt, which placed an upper limit on the thermal energy delivered to the helices without destroying their structure. At this temperature, we observed that the most flexible helical springs (i. e. the ribbons with the smallest resolvable widths and thicknesses), began vibrating slightly. Unfortunately, we were not able to resolve these vibrations as the spring fluctuations were less than 1 μm in extent. Using the simple assumption that the energy of these fluctuations was on the order of the thermal energy, i. e.

$$\frac{1}{2}K_{\text{helix}}^{\text{thermal}}(\Delta x)^2 = \frac{1}{2}k_B T, \tag{4.55}$$

we were able to estimate a lower bound on helix spring constant: the spring constant of even the most flexible helical ribbons must be such that

$$K_{\text{helix}}^{\text{thermal}} > 5 \times 10^{-9}\text{N/m} = 5 \times 10^{-6}\text{pN/nm}. \tag{4.56}$$

This means that for $K_{\text{helix}} > K_{\text{helix}}^{\text{thermal}}$, we cannot observe thermal fluctuations (Δx), which is precisely the reason that we observed fluctuation of only the most flexible helical ribbons – helical wires.

The outcome of 4.56 is consistent with the current estimates of helix spring constant in that both results deduced from Helfrich's theory[77] and our estimates in Section 4.3.2 are in excess of the $K_{\text{helix}}^{\text{thermal}}$ in 4.56. We now need a new technique for measuring helix spring constants, whose values are too large to be determined through thermal fluctuations measurements and too small for measurements using glass cantilevers.

The techniques that are sensitive to measurement of the helix spring constants are

1. calculation of the helix spring constant by measuring the time constant for relaxation of a stressed helix back to its equilibrium position when the force is suddenly removed, and

2. and measurement of the helix spring constant by using flexible cantilevers whose elastic constants are smaller than those of glass rods but larger than the lower bound value obtained from the thermal estimates, i. e. 5×10^{-6}pN/nm.

In what follows, we first describe the measurements of helix elastic constants using the relaxation method, and then we describe the measurements made using Silicon-Nitride cantilevers.

4.5 Relaxation

4.5.1 Theory

Theoretical Calculation of the Helix Spring Constant from Helix Relaxation

In their *Introduction to the Mechanical Properties of Solid Polymers*,[162] Ward and Healey identified a few important mechanical properties of an ideal elastic body:

- deformations are independent of the history or rate of load application
- all applied stresses and strains are reversible if they do not exceed the elastic limit[91]
- the linear relationship between stresses and strains, i.e. Hooke's Law, with Young's modulus as the constant of proportionality is applicable until the elastic limit is reached[91]
- the definitions of stress and strain are valid until the elastic limit is reached, which can occur at large values, depending on a material
- the inherent symmetries of a solid simplify the application of Hooke's Law tremendously.

A perfectly elastic material stores all of the energy imparted to it by the deformation forces; on removal of the forces, it returns to its original geometry in the presence of the internal or external dissipative forces. However, the viscosity of the medium in which this process takes place may affect the rate at which the elastic body returns to its original shape. This section describes loading of helical ribbons formed in CDLC and the subsequent observation of their relaxation upon the removal of the load. For the purpose of this study, we assume that helical ribbons in CDLC are perfectly elastic, i. e. they obey Hooke's law.

There are several theoretical approaches to examining the stress–strain relaxation of an elastic body. One model considers a massless structure moving through a

viscous liquid, such that it experiences viscous drag (i.e. a velocity dependent shear stress). In the case of helical ribbons moving in a viscous medium, this process can be described by the first order differential equation

$$b\dot{x} + K_{\text{helix}}x = 0, \tag{4.57}$$

where b is a drag coefficient due to the viscosity of the medium in which the helical ribbon is traveling, K_{helix} is the helix spring constant, and x is helix displacement from equilibrium. This approximation is possible since, for a helical ribbon in aqueous solution, the inertial term is effectively zero in comparison to the drag term due to the very small Reynolds number (a detailed explanation of this is given in the Section 4.5.1). Eqn. 4.58 has the very simple solution:

$$x = x_0 \exp\left[-\frac{K_{\text{helix}}}{b}t\right] = x_0 \exp\left[-\frac{t}{\tau}\right], \tag{4.58}$$

with the following simple result for the helix spring constant:

$$K_{\text{helix}} = \frac{b}{\tau}, \tag{4.59}$$

where x_0 is the original extension of a helical ribbon and $\tau = \frac{b}{K}$ is the relaxation time constant. An alternative way of obtaining the expression for the spring elastic constant K_{helix} in Eq. (4.59) is by applying the Kelvin-Voight model. A brief description of this model and its prediction are given in Appendix 4.A.

Approximating the Drag Coefficient

I would like to thank Mr. J. Teichman for his assistance in finding an approach for estimating a form of the drag coefficient.

To estimate the drag coefficient of a helix moving axially in a fluid, we first have to obtain an order of magnitude estimate of the Reynolds number. To start, we assume that the fluid in which the helix is moving is Newtonian; that is, the viscosity is independent of helix velocity (for example, pure water is a Newtonian fluid). By the definition of shear viscosity (or simply, viscosity) this means that the fluid produces a shear stress on the walls of the helix in the following manner[163]

$$\sigma = \frac{F}{A} = \eta\frac{\partial v}{\partial r}, \tag{4.60}$$

where η is the viscosity of a fluid, v is its speed, and r is the distance perpendicular the fluid flow.

Now, the Reynold's number is the dimensionless number, Re, that relates the inertial forces acting on a structure in a flowing fluid to the viscous forces acting on this structure

$$\mathrm{Re} = \frac{\text{inertial forces}}{\text{viscous forces}} \tag{4.61}$$

The Reynold's number can be easily obtained from one of the equations that govern the flow of Newtonian fluids, namely the Navier–Stokes equation for an incompressible fluid

$$\rho[\frac{\partial \vec{V}}{\partial t} + (\vec{V} \cdot \nabla)\vec{V}] = \eta \nabla^2 \vec{V} - \nabla p, \tag{4.62}$$

where ρ is the fluid density, V is the fluid velocity, η is the fluid viscosity, and p is the fluid pressure which results in internal fluid stresses. The inertial terms can be found on the left hand side of the Navier–Stokes equation (Eq. (4.62)); they are the terms related to the kinetic energy of a flowing fluid and the kinetic drag stress, i.e. ρV^2. The viscous terms, on the other hand, can be found on the right hand side of the Navier–Stokes equation (Eq. (4.62)); they represent the shear stresses acting on the walls of the structure in the flowing fluid, $\eta(v/d)$, i.e. the expression given in Eq. (4.60). Before proceeding, we make the approximations of steady flow, $\frac{\partial \vec{V}}{\partial t} = 0$, and of very small pressure gradients over the geometrical dimensions we work with. For unidirectional flow, the inertial term then can then be approximated as

$$\rho \mid (\vec{V} \cdot \nabla)\vec{V} \mid \sim \rho \frac{v^2}{d}, \tag{4.63}$$

and the viscous term can be approximated as

$$\eta \mid \nabla^2 \vec{V} \mid \sim \eta \frac{v}{d^2}, \tag{4.64}$$

where v is the characteristic speed of the fluid flow and d is the characteristic geometrical dimension associated with flow (in our case, d is the helix diameter). Then Reynold's number is

$$\mathrm{Re} = \frac{\frac{\rho v^2}{d}}{\frac{\eta v}{d^2}} = \frac{\rho v^2}{\frac{\eta v}{d}} = \frac{\rho v d}{\eta}. \tag{4.65}$$

Even before continuing with our estimations, it is clear that we expect the experimental value of the Reynold's number to be very small since there is hardly any inertia in the length scale associated with helical ribbons. That is, viscous forces predominate and a moving structure will will come to a stop unless pushed by an external force. One of the features of flow at low Reynold's numbers is that it is laminar: the viscosity quickly damps out any turbulent effects. This means that in our

experimental work, the fluid moves as distinct lamina with very little interlamellar mixing, unlike in turbulent flow where very complex interlamellar mixing can occur.

With this in mind, we can perform a scale analysis to obtain an order of magnitude estimate for the Reynold's number and for the shear forces inside and outside of a helix moving in a fluid. These quantities will be then used to obtain a model describing the drag on a helix moving axially in a viscous medium. This is a difficult problem that has not been approached in literature because it has no analytical solution. Therefore, we consider two limiting cases: first, a helix whose width is on the order of its pitch length ($w \approx P$); second, a helical wire, whose width is much smaller than helix pitch length ($w << P$).

In the first case, to obtain an upper bound on the Reynold's number, we can use the maximum measured speed of a helix, $v \approx 400\mu$m/s, and the maximum measured helix diameter, $d \approx 70\mu m$. Then from Eq. (4.65) the maximum value the Reynold's number can be for an axially moving helix in a fluid is

$$\mathrm{Re}_{max} \approx \frac{(1 \times 10^3 kg/m^3)(400 \times 10^{-6} m/s)(70 \times 10^{-6} m)}{1 \times 10^{-3} kg/(m \times s)} \approx 0.3. \tag{4.66}$$

This value of Reynold's number is much too small for any turbulent effects to play a role for an axially flowing helix, since the turbulent flow does not have an effect till the values of Reynold's number becomes greater than 2100 (for 2100 $\leq$Re$\leq$ 4000, the flow seems to pulsate between laminar and turbulent, and the effects of fully developed turbulent flow commence at Re = 4000). Therefore, the inertial forces play a very insignificant role in an axial flow of a helix even for the maximum value of the Reynold's number. The estimated average value of the Reynold's number (calculated from the average values of helix speed, $v \approx 100\mu$m/s, and helix diameter $d \approx 10\mu$m) is even smaller:

$$\mathrm{Re}_{av} = 0.001. \tag{4.67}$$

This latter number is a better description, making inertial effects in helix flow negligible in comparison to viscous effects. With such a low Reynold's number, we can safely ignore turbulent effects altogether and consider the axial movement of a helix to produce completely laminar flows. We also can ignore inertial forces altogether and consider the drag outside of the helix to be a consequence of the viscous forces alone.

At this point, we are ready to perform a scaling analysis of the drag force on the outer walls of a helix. This problem has not been addressed in literature to

any detail since a case of a solid cylinder placed in an axially flowing fluid cannot be solved analytically. Therefore, we will use the following approximation: characteristic distance over which velocity of the fluid (with respect to the helix) decays from v at the helix walls to 0 far from the helix is approximately equal to the characteristic size, i. e. the helix diameter d. Using this approximation and the definition of viscosity as a ratio of the shear stress to shear rate in Eq. (4.60), we can find the shear stress on the outer walls of the helix as follows

$$\sigma = \frac{F_{\text{outside}}}{A} = \eta\frac{v}{d}, \tag{4.68}$$

where σ is the shear stress on the helix walls, A is the helix surface area, v is flow speed (in our case, speed of helix being dragged through the viscous medium), d is a characteristic geometrical length scale (in our case, helix diameter), and η is viscosity of the medium. To obtain the drag force on the outer walls of a helix, we need to multiply the shear stress by the surface area of a helix

$$F_{\text{outside}} = \left(\eta\frac{v}{d}\right) A = \left(\eta\frac{v}{d}\right) (\pi dL) = \pi\eta v L, \tag{4.69}$$

where L is helix axial length. The length scale used here to calculate the shear stress and shear force is based on the size of the disturbance in the ambient quiescent fluid, which in this case is the helix diameter d.

Up till now we have not needed any knowledge of the detailed geometry of a helix other than its diameter. Therefore, the above approximation is valid for a rod, cylinder, or a helical ribbon, whose width is approximately the same as its pitch length, flowing axially in a fluid. What is happening inside of this structure? The flow of a fluid at low Reynold's number inside a channel or a cylinder is called Poiseuille flow. The velocity of a fluid inside of this cylinder can be calculated from the Navier–Stokes equation (Eq. (4.62)). With assumptions of steady flow ($(\partial\vec{V}/\partial t) = 0$), and of the fluid velocity having only an axial component along the z-axis, i. e.

$$\vec{V}(\vec{r}, t) = V_z\hat{z} = V_z(r)\hat{z} = v(r)\hat{z}, \tag{4.70}$$

the Navier–Stokes equation in cylindrical coordinates reduces to[163]

$$\begin{aligned} 0 &= -\frac{\partial p}{\partial r}, \\ 0 &= -\frac{1}{r}\frac{\partial p}{\partial r}, \\ 0 &= -\frac{\partial p}{\partial z} + \eta\frac{1}{r}\frac{\partial}{\partial r}\left(r\frac{\partial V_z}{\partial r}\right), \end{aligned} \tag{4.71}$$

for the radial, azimuthal, and axial components, respectively. Since all flow lines are parallel to the cylinder walls (Eq. (4.70)), the partial derivatives in the last equations can be rewritten as d/dr and d/dz. It is also clear that the pressure p is independent of the radial and azimuthal coordinates, such that

$$p = p(z). \tag{4.72}$$

Therefore only the axial component is left in the Navier–Stokes equation; this can be rewritten as

$$\frac{1}{r}\frac{d}{dr}r\frac{dV_z}{dr} = \frac{1}{\eta}\frac{dp}{dz}. \tag{4.73}$$

Solving this equation and using a no-slip boundary condition at the cylinder walls, we obtain

$$V_z(r) = v(r) = \frac{1}{4\eta}\left(\frac{\Delta p}{L}\right)\left(\left(\frac{d}{2}\right)^2 - r^2\right), \tag{4.74}$$

where Δp is the pressure drop along the length of the cylinder, L is the axial length of the cylinder, and d is the cylinder's diameter. Noticing from Bernouli's equation that the pressure drop is just the kinetic energy of a flowing fluid per unit volume, i. e.

$$\Delta p = \frac{1}{2}\rho v^2, \tag{4.75}$$

the velocity of the fluid flowing in a cylinder can be described as having a parabolic distribution of the form

$$V_z(r) = v(r) = \frac{1}{8\eta}\left(\frac{\rho v^2}{L}\right)\left(\left(\frac{d}{2}\right)^2 - r^2\right). \tag{4.76}$$

We are finally in a position to calculate the shear stress on the internal walls of the cylinder. We do so by directly utilizing the definition of viscosity in Eq. (4.60),[163] and Eq. (4.76) above to obtain

$$\sigma = \eta\left.\frac{\partial v}{\partial r}\right|_{r=\frac{d}{2}} = \eta\frac{\rho v^2 d}{8\eta L} = \frac{\rho V^2 d}{8L}. \tag{4.77}$$

The drag force, being just a product of the cylinder surface area and shear stress, is

$$F_{\text{inside}} = \left(\frac{\rho v^2 d}{8L}\right)(\pi d L) = \frac{1}{8}(\pi\rho v^2 d^2). \tag{4.78}$$

Now, with these expressions for the internal and external shear (drag) forces on the walls of a cylinder, Eqs. 4.78 and 4.69, respectively, we can perform a scaling

analysis and compare these forces. Noticing that

$$\frac{F_{\text{inside}}}{F_{\text{outside}}} = \frac{\frac{1}{8}(\pi\rho v^2 d^2)}{\pi\eta v L} = \frac{\rho v d^2}{8\eta L} = \frac{1}{8}\frac{d}{L}\text{Re}, \tag{4.79}$$

we can use the Reynold's number as approximated in Eq. (4.67) and an estimated average aspect ratio of $d/L \approx 0.15$ to find

$$\frac{F_{\text{inside}}}{F_{\text{outside}}} \approx 2 \times 10^{-5}. \tag{4.80}$$

This means that the internal drag forces on the walls of a cylinder are negligible compared to the external drag forces; they are five orders of magnitude smaller, as can be seen in Eq. (4.80). Therefore, for all intents and purposes we can ignore the internal drag force; there is effectively no flow inside the cylinder with the geometrical dimensions above.

Now we shall address the question of whether it is important that our structure is a helix rather than cylinder. Based on the above derivation, it does not in fact matter whether the structure is a helix or a cylinder, as long as the ribbon width is on the order of the helix pitch length ($w \approx P$). The only important factor is that there is no flow inside the structure: all of the forces on it result from shear stresses on its outer walls, i.e. $F_{\text{outside}} = \eta(v/d)A = \pi\eta v L$ in Eq. (4.69). From this we can define the drag coefficient in Eq. (4.58) to be

$$b_{w\to P} = \frac{F_{\text{outside}}}{v} = \pi\eta L. \tag{4.81}$$

This result is independent of helix width since in the limit of width being of the same order as the helix pitch length, we are considering helical ribbons whose edges on successive turns almost touch each other. In this limit, the only geometrical dimension that is important to calculate the drag coefficient is helix axial length L.

Now, consider the second case, when the width of helical ribbon is much smaller then the spacing between the successive turns (the helix pitch length). In the terminology of Chapter 2, in this case, we consider a helical wire being dragged through a viscous fluid. We again use the approximation that the velocity of the flowing fluid (with respect to the helical wire) decays over the characteristic length scale that is approximately equal to the size of a moving object, the helical wire. For a helical wire that is being dragged axially through a fluid, the characteristic length scale is either the width or the thickness of the helical wire, whichever is larger. In what follows, we will assume that the wire width is larger than wire thickness, and use w as the

characteristic length scale of the structure. We then use Eq. (4.68) to calculate the drag stress on the walls of the helical wire:

$$\sigma = \frac{F^{\text{wire}}_{\text{outside}}}{A} = \eta\frac{v}{w}, \tag{4.82}$$

where σ is the shear stress on the helix walls, A is the helix surface area, v is flow speed (in our case, speed of helix being dragged through the viscous medium), w is the width of a helical wire, and η is viscosity of the medium. To obtain the drag force on the outer walls of this helical wire, we need to multiply the shear stress by the surface area of a helix

$$F^{\text{wire}}_{\text{outside}} = \left(\eta\frac{v}{d}\right) A = \left(\eta\frac{v}{d}\right)(2wl) = 2\eta v l, \tag{4.83}$$

where l is helix contour length and the characteristic length scale d is the width of helical wire w. Then the drag coefficient on the helical wire can be found as in Eq. (4.81) to be

$$b_{w\to 0} = \frac{F^{\text{wire}}_{\text{outside}}}{v} = 2\eta l. \tag{4.84}$$

This result is again independent of helix width since in the limit of width being much smaller than the helix pitch length ($w << P$), we are considering helical wires with $w \to 0$. In this limit, the only geometrical dimension that is important to calculate the drag coefficient is helix axial length l.

It is worthwhile noting that the drag coefficients in the two limiting cases we considered in Eqs. 4.81 and 4.84 are of the same order of magnitude. In fact, $b_{w\to P}$ in Eq. (4.81) is only a factor of 1.5 greater than $b_{w\to 0}$ in Eq. (4.84). To test our above assumptions in estimating the drag coefficient, we shall perform an estimate for the drag coefficient b in Section 4.6.3, where we shall use the measured value of K_{helix} in conjunction with various measured relaxation times.

This introduction of the theoretical drag coefficient, Eq. (4.81) and Eq. (4.84), into the equations for helix spring constant, Eq. (4.59) or Eq. (4.102), allows us to to experimentally estimate the spring constant by measuring helix relaxation time constants.

4.5.2 Experimental Results

General Results

This set of experiments was performed by attaching one end of a helical ribbon to a stationary glass rod using Devcon 5-Minute Epoxy®, while attaching the other end

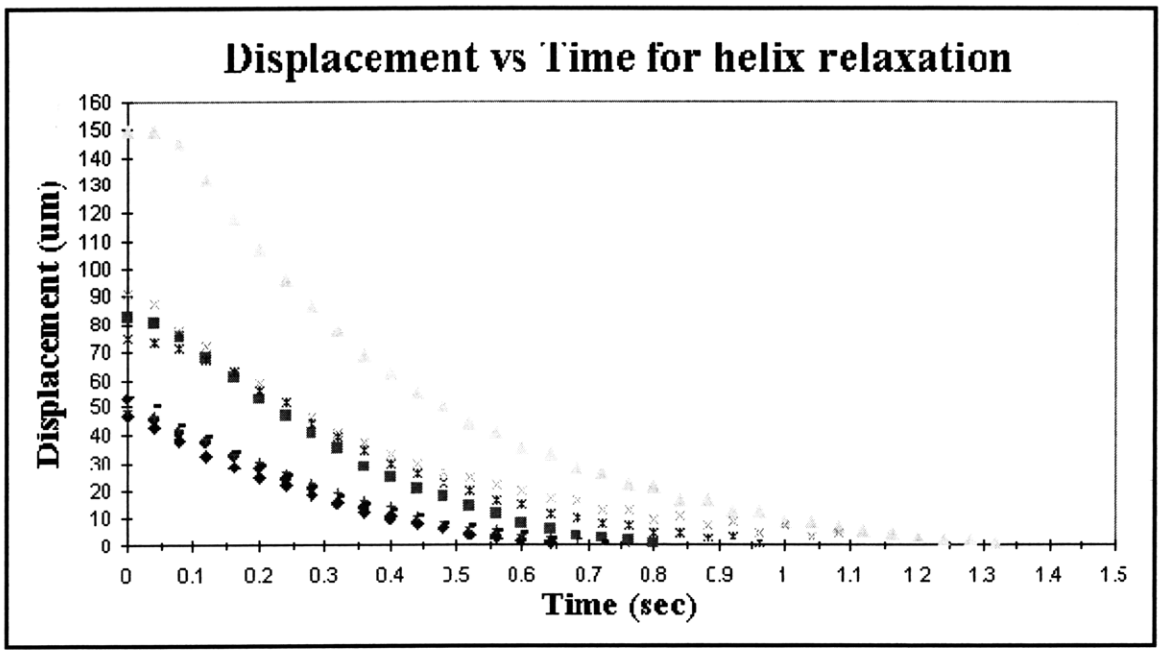

Figure 4.8: Typical curves showing relaxation of a helix from different extensions. These curves display an exponential decay. Time constants were calculated for each curve and were found to be within the experimental error of each other.

to a mobile glass rod connected to a micromanipulator. By pulling on the helical ribbon until one of the glue joints fails, we were able to follow a process of helix relaxation using light microscopy. This was done by following a characteristic point on the helix as it returned to equilibrium. The relaxation of each helix was observed several times for various extensions, and the time constants were found for each of these trials. For each helix these time constants were within experimental error of each other. Figure 4.8 displays a typical set of relaxation curves on a displacement versus time graph for one of these helices. Since the time constants found for each helix are independent of helix extension, the helices indeed follow Hooke's law over the entire range studied. Measuring the relaxation time constants and geometrical dimension of each helix and using the drag coefficient from Eqs. 4.81, we were able to find helix spring constants for six different helical ribbons. For all these helices, we used an approximation of $w \approx P$. In the particular case of the helix in Figure 4.8, the spring constant can be estimated using Eq. (4.81) from the measured time constant of 0.384 ± 0.031 seconds to be

$$\begin{aligned} K_{\text{helix}} = \pi\eta L/\tau &= (9.59 \pm 0.77) \times 10^{-7}\text{N/m} \\ &= (9.59 \pm 0.77) \times 10^{-4}\text{pN/nm}, \end{aligned} \tag{4.85}$$

where $L = 117 \pm 3\mu$m is the helix axial length and $\eta = 1 \times 10^{-3}$ kg/(m s). It is worthwhile noting that the estimated value of helix spring constant in Eq. (4.85) is one to four orders of magnitude larger than several theoretical estimates made in previous sections. First, the theoretical result deduced from Helfrich's theory[77] in Eq. (4.54) ($K^{\mathrm{H}}_{\mathrm{helix}} \sim 3 \times 10^{-8}$N/m $= 3 \times 10^{-5}$pN/nm) was obtained for phospholipid liquid crystalline bilayers. Therefore, it is reasonable that for the cholesterol–phospholipid liquid crystalline bilayer the helix spring constant must be larger. This finding, however, does not invalidate the idea that helices may be crystal in nature, rather than liquid crystalline. Second, our experimental estimate in Eq. (4.85) is approximately 200 times larger than the estimate for the helix spring constant made in Section 4.4 from the thermal measurements. This is reasonable as we expect $K^{\mathrm{thermal}}_{\mathrm{helix}}$ to be greater than 5×10^{-9}N/m $= 5 \times 10^{-6}$pN/nm. Finally, the above result in Eq. (4.85) is in excess of our estimates deduced from Chung *et al.*'s theory in Section 4.3.2, where we obtained that for high pitch helices, $K^{C}_{\mathrm{helix}} \sim 2 \times 10^{-8}$N/m $= 2 \times 10^{-5}$pN/nm, and for low pitch helices, $K^{C}_{\mathrm{helix}} \sim 9 \times 10^{-11}$N/m $= 2 \times 10^{-8}$pN/nm. The latter two estimates were made for cholesterol–phospholipid liquid crystalline bilayers. We note, that the estimate deduced from Chung *et al.*'s theory for low pitch helices is two orders of magnitude smaller than the result of thermal measurements for minimum spring constant and four orders of magnitude smaller than the experimental estimate in Eq. (4.85). The large value of helix spring constant obtained from the relaxation experiments indicates that helical ribbons in CDLC are much stiffer (have larger spring constant) than expected for helical structures made of either phospholipid or cholesterol–phospholipid liquid crystalline bilayers. Therefore, it seems reasonable that the nature of helical ribbons in CDLC may indeed be crystal rather than liquid crystalline.

The data for all six helices is shown in Table 4.3. As can be observed in Table 4.3, all experimental errors in helix spring constant, K_{helix}, are less than about 15%. Therefore, the large spread of spring constants covering approximately 1 order of magnitude is not due to any systematic error, but rather it must be the result of the drastically different geometrical dimensions of helices studied. To see whether this is the case, it is necessary to normalize out the geometrical parameters from the measured values of K_{helix}, the helix spring constant. Such dimensional parametrization is performed within the context of each of Chung *et al.*'s,[12] Selinger *et al.*'s,[18] and the crystalline theories, as described in Section 4.3.2, where we examine the dependence

Table 4.3: Six helices with different geometrical dimensions, their relaxation constants, and calculated spring constants.

Helix Label	Radius, R, μm	Width, w, μm	Axial Length, L, μm	Time Constant, τ, s	Spring Constant, K_{helix}, N/m
One	50 ± 2	4.6 ± 0.5	117 ± 2	0.384 ± 0.031	$(9.6 \pm 0.8) \times 10^{-7}$
Two	21 ± 2	2.9 ± 0.5	89 ± 2	0.174 ± 0.026	$(1.6 \pm 0.2) \times 10^{-6}$
Three	24 ± 1	4.4 ± 0.5	150 ± 2	0.204 ± 0.030	$(2.3 \pm 0.3) \times 10^{-6}$
Four	9 ± 1	2.1 ± 0.5	52 ± 1	0.067 ± 0.007	$(2.5 \pm 0.3) \times 10^{-6}$
Five	21 ± 2	5.2 ± 0.5	77 ± 1	0.143 ± 0.016	$(1.7 \pm 0.2) \times 10^{-6}$
Six	18 ± 1	8.2 ± 0.5	93 ± 2	0.034 ± 0.005	$(8.5 \pm 1.3) \times 10^{-6}$

Table 4.4: Measured values of the spring constant, as presented in Table 4.3, and their normalized values for the six helices investigated.

Helix Label	Radius, R, μm	Width, w, μm	Axial Length, L, μm	Spring Constant, K_{helix}, N/m	$\tilde{K} = K_{\text{helix}}(L\ R^2/w)$, N m
One	50 ± 2	4.6 ± 0.5	117 ± 2	$(9.6 \pm 0.8) \times 10^{-7}$	$(6.1 \pm 1.0) \times 10^{-14}$
Two	21 ± 2	2.9 ± 0.5	89 ± 2	$(1.6 \pm 0.2) \times 10^{-6}$	$(2.1 \pm 0.5) \times 10^{-14}$
Three	24 ± 1	4.4 ± 0.5	150 ± 2	$(2.3 \pm 0.3) \times 10^{-6}$	$(4.4 \pm 1.0) \times 10^{-14}$
Four	9 ± 1	2.1 ± 0.5	52 ± 1	$(2.5 \pm 0.3) \times 10^{-6}$	$(4.7 \pm 1.3) \times 10^{-15}$
Five	21 ± 2	5.2 ± 0.5	77 ± 1	$(1.7 \pm 0.2) \times 10^{-6}$	$(1.1 \pm 0.2) \times 10^{-14}$
Six	18 ± 1	8.2 ± 0.5	93 ± 2	$(8.5 \pm 1.3) \times 10^{-6}$	$(2.9 \pm 0.6) \times 10^{-14}$

of the helix spring constant K_{helix} on the phenomenological elastic moduli and on the helix geometrical dimensions. As discussed in Section 4.3.2, a linear dependence of the helix spring constant on the geometrical factor $w/(LR^2)$ can be deduced from all theories. In the following, we perform a rescaling of the measured helix spring constants by eliminating the explicit geometrical size effects, i. e. by multiplying each of the values of K_{helix} by the factor $(LR^2)/w$.

Rescaling of the Elastic Spring Constant

To understand the underlying physics of the helical structures, it is instructive to remove the explicit geometrical size effects from the measured values of the elastic spring constants, as described in the previous section. To normalize out the geometrical dependencies of the spring constant and to see whether the geometrical effects account fully for the range of K_{helix}, we need to multiply the measured values of helix spring constants in Table 4.3 by the factor $(LR^2)/w$, so $\tilde{K} = K(LR^2/w)$. The results

of this rescaling are summarized in the Table 4.4.

As can be observed from Table 4.4, the scaled helix spring constants still cover a wide range of values. Therefore, normalizing the helix spring constants by eliminating geometrical effects does not eradicate the puzzle of large range of K_{helix}. A clue to solution to this puzzle comes from the expressions for the spring constants obtained in Section 4.3.2, Eqs. 4.26, 4.39, and 4.52 derived from each of Chung *et al.*'s, Selinger *et al.*'s, and the crystalline theories, respectively. Normalizing these expressions for the spring constant, we find

$$\begin{aligned} \tilde{K^C} &= K^C_{\text{helix}} \frac{LR^2}{w} = 4K_n^{pp} \tan^3 \psi_0^C (1 + \tan^2 \psi_0^C)^{\frac{1}{2}}, \\ \tilde{K^S} &= K^S_{\text{helix}} \frac{LR^2}{w} = \frac{\sin^2 \psi_0^S}{\cos \psi_0^S} \alpha(\psi_0^S), \\ \tilde{K} &= K_{\text{helix}} \frac{LR^2}{w} = 8(K_\gamma - K_\beta) \frac{\tan^3 \psi_0}{(1 + \tan^2 \psi_0)^{\frac{1}{2}}}. \end{aligned} \tag{4.86}$$

It is clear from studying these normalized expressions for the spring constants that each $\tilde{K}$ is a linear function of the microscopic elastic moduli and some function of the unstressed equilibrium pitch angle ψ_0. Since all of the helices studied were low pitch, i. e. their pitch angle was approximately 11°, the wide range of $\tilde{K}$ seems to imply that the elastic moduli are different in the six structures studied. This conclusion is reasonable since the elastic moduli in all three theories are known to be functions of the helical ribbon thickness. If the variation in $\tilde{K}$ indeed occurs due to variations in the ribbon thickness the ratios between the various $\tilde{K}$'s should be rational numbers, indicating quantization. It is also interesting to examine the ratios of the scaled spring constants, since any overall numerical corrections due to the approximation of the drag coefficient cancel out, eliminating the numerical uncertainty introduced by the drag forces. We choose to examine the ratios of the scaled spring constants by dividing them by the value for helix "One," since it has the smallest uncertainty. The results are shown below in Table 4.5.

It is clear that the uncertainties in the measurements of the above values are too large and the number of helices studied too small to be able to make definite conclusions. However, it appears that helices fall into families grouped by their thicknesses depending on a number of bilayers, if we speak in the terminology of Chung *et al.* and Selinger *et al.*, or a small number of "crystalline layers" in the terminology of the crystalline model. This conclusion is reasonable since the ratios of $\tilde{K}_i$'s are rational numbers, as can be seen in Table 4.5. This conclusion is also consistent with the

Table 4.5: Ratios of normalized spring constants to the value of the helix "one".

Helix Label	$\tilde{K} = K_{\text{helix}}(L\ R^2/w)$, N m	$\tilde{K}_i/\tilde{K}_1$	Approximate $\tilde{K}_i/\tilde{K}_1$
One	$(6.1 \pm 1.0) \times 10^{-14}$	$1/(1.0 \pm 0.0)$	1:1
Two	$(2.1 \pm 0.5) \times 10^{-14}$	$1/(2.8 \pm 0.8)$	1:3
Three	$(4.4 \pm 1.0) \times 10^{-14}$	$1/(1.4 \pm 0.4)$	1:1
Four	$(4.7 \pm 1.3) \times 10^{-15}$	$1/(12.8 \pm 4.0)$	1:13
Five	$(1.1 \pm 0.2) \times 10^{-14}$	$1/(5.3 \pm 1.3)$	1:5
Six	$(2.9 \pm 0.6) \times 10^{-14}$	$1/(2.1 \pm 0.5)$	1:2

qualitative observation of Chung *et al.*,[12] in which radius versus width data appear to be grouped into sequences of curves that represent families of varying number of bilayers. However, in our abundant measurements (not shown here) of helix radius versus width, we found no such relationship between the helix radius and width to support Chung *et al.*'s observations.

At this point we can continue the comparison of our experimental measurements of the helix spring constants with the values deduced from the theoretical models. In Section 4.3.2, we estimated the value of the helix spring constant, which was done in the framework of Chung *et al.*'s model. This estimation was possible because the derived expression for the spring constant, K^C_{helix}, in this model is very simple: it depends linearly on the elastic modulus, K^{pp}_n, which has been measured experimentally for a variety of phospholipid bilayers and one type of phospholipid–cholesterol bilayer,[154,155] and on a combination of trigonometric functions of the equilibrium pitch angle (Eq. (4.26)). Our estimation for a low pitch helix resulted in the value of $K^C_{\text{helix}} \sim 3 \times 10^{-11}$ N/m $= 3 \times 10^{-8}$ pN/nm (Eq. (4.28)) when we used the maximum measured value of $K^{pp}_n < 10^{-19}$ N m.[156–161] However, it is clear that this deduced value is more than 30,000 times smaller than the smallest measured value of K_{helix} in our relaxation measurements. Earlier in this section we made further comparison of the theoretically deduced values of spring constant to the smallest experimentally estimated value of K_{helix} (Eqn. 4.85). At that time, we indicated that the large experimental estimate of helix spring constant may be due to the crystal nature of helical ribbons.

Alternatively, we can estimate the expected value of the elastic modulus K^{pp}_n from

our measured spring constants. For the most flexible low pitch helix (with the smallest spring constant), we find

$$K_n^{pp} \sim 2.02 \times 10^{-12}\text{N m}. \tag{4.87}$$

This value is *seven* orders magnitude larger than the largest measured value of K_n^{pp} for phospholipid fluid bilayers,[156–161] which is far too big a difference to be accounted for by the stiffening role of cholesterol in a phospholipid bilayer (experimentally it was determined that the modulus of elasticity of cholesterol–phospholipid bilayers is only three times larger than that for cholesterol free phospholipid bilayers.[154]) Chung *et al.*'s entire theory is based upon the premise that each helical ribbon is made out of a number of weakly interacting bilayers. If we assume that the large value of the elastic modulus K_n^{pp} reflects the number of bilayers, we should be able to calculate what this number is; i. e., we should be able to calculate the ribbon thickness. The typical thickness of a phospholipid bilayer is on the order of 4 nm.[164–172] When cholesterol is added to a phospholipid bilayer, its thickness changes depending on cholesterol concentration and ambient conditions. However, to the first order, the bilayer thickness stays unchanged at 4 nm.[173] This implies that to account for the factor of 10^7 in the elastic modulus K_n^{pp}, the ribbon thickness must be greater than $10^7 \times 4 \times 10^{-3} = 4000\mu$m. This number is clearly absurd since the thickness of a helix wall cannot exceed 1μm, as we cannot resolve it with a light microscope.

The above estimates imply that the helical ribbons in our experiment are far more rigid than the fluid bilayers studied previously.[156–161] This further supports the argument that helical ribbons are crystalline rather than liquid crystal in nature. Therefore, it is reasonable to question whether Chung *et al.*'s[12] and Selinger *et al.*'s[18] theories would be able to fully explain the behavior of the helices we are working with. However, at this time we can only state that the crystalline model presents a better alternative, as we cannot directly measure the individual elastic moduli required to estimate helix spring constant within the framework of this model.

4.6 Cantilevers in Helix Spring Constant Measurements

4.6.1 Introduction

In the last few years, investigations of the elastic properties of biological materials on the microscopic scale have become possible due to technological innovations. Di-

rect measurements of single macromolecule elasticity have been obtained by using flexible tapered glass needles,[122,123] atomic force microscopy (AFM),[174,175] optical traps,[137,176–179] nanofabricated silicon-nitride cantilevers,[129,130] and by other techniques. Most of the work to date has been conducted on biological polymers such as DNA,[103,138,180,181] RNA Polymerase,[182] titin,[137,174,179,183] actin,[122,124,128,129,137,176–178,184] myofibril,[129] kinesin,[185–188] isolated thick filaments,[130] spermatozoa,[110,189] and others. To our knowledge, this is the first time that the measurement of the spring constants have been performed on the self-assembly of helical ribbons formed in quaternary sterol systems.

In our measurements, we employed nanofabricated silicon-nitride cantilevers as force transducers. The fabrication and calibration of these cantilevers has been described in the Materials and Methods Section 4.2.1. Prior to our work, these cantilevers had been successfully employed in measuring the elastic properties of thick filaments, *Mytilus edulis* and *Limulus polyphemus*,[130] and also of single fibers of myosin and actin filaments.[129] The limitation of these cantilevers is that the displacements should be no greater than $\sim$ 10% of their length to insure a linear response. This implies that to perform an accurate measurement of forces applied to helical ribbons, a 568-μm cantilever can be displaced for up to 56.8 μm. Therefore, for cantilevers of the above length whose elastic constant is $k_{\text{cantilever}} = 0.05$ pN/nm, application of forces up to 2.84 nN was feasible. When subjected to forces on the order of hundreds of piconewtons to $\sim$ 1 nN, low pitch helical ribbons in Chemically Defined Lipid Concentrate (CDLC) underwent linear extension. Beyond about 1.2 nN, helical ribbons usually experienced phase separation into a helical part with pitch angle of $\sim 17°$ and a straight part with a "pitch angle" of $\sim 90°$, as described in Section 2.6.3. The Si-Ni cantilevers allowed us to perform measurements of the helix elastic constants in the region prior to phase separation.

Due to excessive difficulties associated with performing this experiment, such as tethering a helix to a tethering post and a cantilever in a geometrical configuration appropriate for spring constant measurements and prevention of vibrations, we have been able to measure the spring constant of only one low pitch helical ribbon. However, the data obtained has proven to be an important first step in the measurement of the elastic properties of helical ribbons in quaternary sterol systems. In what follows, we will briefly discuss the methodology of measurement of the helix spring constant, theoretical interpretation and results of these measurements.

4.6.2 Materials and Methods

The helix spring constant was measured for the low pitch helical ribbon formed in Chemically Defined Lipid Concentrate (CDLC). This choice of structures for the measurements of helix spring constants was obviated by our experiments on the tethering of helical ribbons to rigid surfaces as described in Section 4.2.3. These experiments showed that only low pitch helices in CDLC can be easily attached to cantilevers with Devcon 5-Minute Epoxy®.

The elastic constant of the silicon-nitride cantilevers used for the measurement of helix spring constants was measured to be 0.05 pN/nm (courtesy of M. Fauver *et al.*).[129] The cantilevers of this particular flexibility were chosen as a result of our previous work in thermal and relaxation experiments. The cantilevers were prepared and implemented as described in Materials and Methods Section 4.2.1. The visualization instrumentation used in the experiment is described in Materials and Methods Section 4.2.2.

4.6.3 Experimental Results and Discussion

The experimental setup is illustrated in Figure 4.5. Panel (*a*) in the figure depicts the initial position of the helix–cantilever system, prior to the application of an axial force to the helix. Panel (*b*) depicts an arrangement of the helix-cantilever system at some later time when a small axial force is applied to the helix via the Si-Ni cantilever. This is the typical arrangement of the system prior to helix phase separation into helical and straight portions. As described in Materials and Methods Section 4.2.1, the axial displacement of the helix and the deflection of the Si-Ni cantilever was achieved by either moving the cantilever via the micromanipulator or by displacing the microscope stage. Panel (*b*) of Figure 4.5 illustrates the latter case, when the microscope stage (and therefore the reference beam) was moved rightward. At this point we note that this experimental procedure was performed quasi-statically: at each displacement of the microscope stage (or micromanipulator), the helix–cantilever system was allowed to equilibrate for $\sim$ 1-1.5 hours prior to the final measurements of helix displacement and cantilever deflection. This was necessary since the helix–cantilever system was found to be in a dynamic state immediately after each displacement of the microscope stage (or the micromanipulator). In our initial work (data not shown), we found that $\sim$ 1-1.5 hours was sufficient for the system to completely equilibrate. The final data set was obtained by measuring the displacements of the helix and cantilever in the

equilibrated system via digital video images. Performed in this way, our experiments resulted in a systematic error of roughly 1-2 μm.

A graph of the cantilever deflection versus helix displacement is shown in Figure 4.9. We were able to measure forces as small as $\sim$ 240 pN and as large as $\sim$ 1.5 nN. The value of $\sim$ 1.5 nN was much smaller than the maximum allowed force of $\sim$ 2.84 nN, at which a cantilever starts displaying non-linear behavior. Therefore, we did not have to worry about reaching the maximum allowed displacements of the cantilevers. The graph in Figure 4.9 corresponds to forces in the range between $\sim$ 240 pN and $\sim$ 1.06 nN. At $\sim$ 1.1 nN the helix, whose displacement due to axial force are given in Figure 4.9, phase separated into helical and a straight parts, at which point further measurements of helix and cantilever displacements were discontinued. As can be seen in Figure 4.9 there is a linear correspondence between cantilever deflection and helix displacement. This behavior is completely reversible and displays no hysteresis.

When a force is applied to the helix–cantilever system (via microscope stage displacement in this case), by Newton's Third Law, the magnitude of the force applied to the cantilever is equal to the magnitude of the force applied to the helix, i. e.

$$F_{helix} = F_{cantilever}. \tag{4.88}$$

This implies that in a region where Hooke's law is applicable, we obtain

$$-K_{\text{helix}} X_{\text{helix}} = -k_{\text{cantilever}} x_{\text{cantilever}}, \tag{4.89}$$

where X_{helix} is the helix displacement or elongation and $x_{\text{cantilever}}$ is the cantilever deflection. The slope of the linear fit in the graph in Figure 4.9, represents $K_{helix}/k_{cantilever}$ and can be measured to be 0.0961 ± 0.0014. Therefore, with the knowledge of the cantilever flexibility, $k_{\text{cantilever}} = 0.050 \pm 0.008$ pN/nm, we can obtain the value of the helix spring constant in this particular case to be

$$K_{\text{helix}} = (4.80 \pm 0.77) \times 10^{-3} \text{pN/nm} = (4.80 \pm 0.77) \times 10^{-6} \text{N/m}. \tag{4.90}$$

The experimental error in this case constitutes about 16%.

To obtain a rescaled value of the helix spring constant, $\tilde{K}$, we follow the procedure of Section 4.5.2. The geometrical dimensions of the undeformed helix above are: width $w = 12.3 \pm 0.5 \mu$m, axial length $L_0 = 103.0 \pm 2 \mu$m, and radius $R_0 = 19.2 \pm 1 \mu$m. When rescaled, the above value of K_{helix} becomes

$$\tilde{K_{\text{helix}}} = K_{\text{helix}}(LR^2/w) = (1.48 \pm 0.10) \times 10^{-14} \text{N m}, \tag{4.91}$$

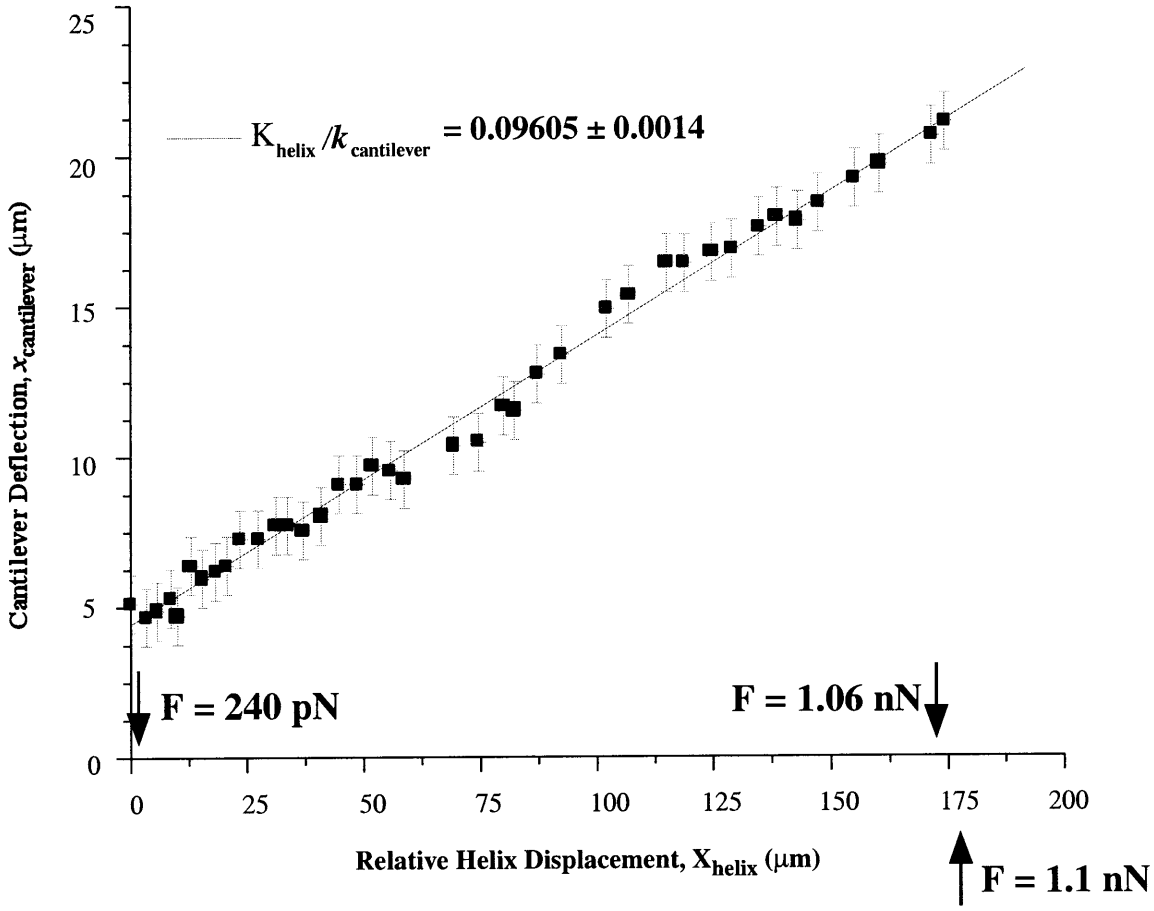

Figure 4.9: A typical graph of cantilever deflection versus helix displacement. The slope of the linear plot gives the ratio of cantilever deflection, $x_{cantilever}$, to helix displacement, X_{helix}. By Newton's Third Law and Hooke's Law this ratio is equal to the ratio of the helix spring constant, K_{helix}, to the cantilever flexibility, $k_{cantilever}$. Therefore, from the slope of the plot we can find the ratio $K_{helix}/k_{cantilever}$, which with knowledge of the cantilever flexibility gives the value of K_{helix}. The arrows show the force corresponding to the relative displacements of the helix.

where L is helix axial length, R is helix radius, and w is helical ribbon width.

As can be seen in Eq. (4.90), and Eq. (4.91), the value of the helix spring constant measured with Si-Ni cantilever is of the same order of magnitude as the values of the helix spring constants measured in the relaxation experiments (Table 4.4). This shows that the two measurements are self-consistent. Although we have not yet been able to measure K_{helix} for one and the same helix with both techniques, our experimental results using the two procedures are in good agreement with each other. Obviously, there is a great need for further experiments, yet these results serve as a first step toward the systematic measurement of the elastic properties of helical ribbons formed in the quaternary sterol systems.

We are now also in a position to re-evaluate our assumptions regarding the drag coefficient presented in Eqs. 4.81 and 4.84. We shall compare the estimates that can be deduced from Eqs. 4.81 and 4.84 to those made from the measurement of K_{helix} above. First, for the helical ribbon in the experiment with the cantilever, we expect the drag coefficient from Eqs. 4.81 and 4.84 to be

$$b_{w\to P} = \pi(1\times 10^{-3})(103\pm 2)\times 10^{-6} = (0.32\pm 0.01)\times 10^{-6}\ \frac{\text{kg}}{\text{s}}, \quad (4.92)$$

$$b_{w\to 0} = 2(1\times 10^{-3})\frac{(103\pm 2)\times 10^{-6}}{\sin(11^\circ\pm 0.5^\circ)} = (1.08\pm 0.05)\times 10^{-6}\ \frac{\text{kg}}{\text{s}}, \quad (4.93)$$

respectively, where we have used Eq. (4.18) in the second equation above. The assumption in the first equation above is that the helical ribbon is approximately a tubule, i.e. $w \to P$ even though $w = 12.3\pm 0.5\mu$m and $P = 23.4\pm 2.9\mu$m. In the second equation above the assumption is made that $w \to 0$.

Second, we recall that, as shown in Eq. (4.59),

$$b = K_{\text{helix}}\tau_{\text{helix}}. \quad (4.94)$$

To estimate the drag coefficient in the above expression for the helix spring constant in Eq. (4.90), we need to choose a value of relaxation time, τ, that is representative of the helix in Eqs. 4.90 and 4.91. This can be achieved by comparing the rescaled value of the helix spring constant in 4.91 to the ones in Table 4.3. By doing so, we find that the $\tilde{K}$'s of helices "Two" and "Five" are close to $\tilde{K_{\text{helix}}}$ in Eq. (4.91), but are not within its experimental error. Therefore, we shall perform linear interpolation to obtain an estimate of the relaxation time for the helix in Eq. (4.90). This is an acceptable technique as the the values of K_{helix} for helices "Two" and "Five" are close

to each other. We use the following interpolation:

$$\tau_{\rm helix} = \frac{1}{K_{\rm helix}^{\tilde{\text{``Five''}}} - K_{\rm helix}^{\tilde{\text{``Two''}}}} \left[\tau_{\rm helix}^{\text{``Two''}} (K_{\rm helix}^{\tilde{\text{``Five''}}} - \tilde{K_{\rm helix}}) + \tau_{\rm helix}^{\text{``Five''}} (\tilde{K_{\rm helix}} - K_{\rm helix}^{\tilde{\text{``Two''}}}) \right], \tag{4.95}$$

which results in

$$\tau_{\rm helix} = (1.55 \pm 0.81) \times 10^{-1} \text{ s}. \tag{4.96}$$

With this interpolated value of the relaxation time for the helix in our experiment with Si-Ni cantilever, we can use Eq. (4.94) to estimate the expected value for the drag coefficient b to be

$$b = (0.74 \pm 0.41) \times 10^{-6} \quad \frac{\text{kg}}{\text{s}}. \tag{4.97}$$

Comparing the results in Eqs. 4.92 and 4.97, we observe that our estimate of the drag coefficient in Eqs. 4.81 and 4.84 were reasonable as our results are within the range of expected values for b for both expressions. Therefore, Eqs. 4.81 and 4.84 are sufficient for the calculations of the helix spring constant in the relaxation experiments. We can choose an appropriate approximation for the drag coefficient for any given helix based upon whether $w \to P$ or $w \to 0$.

4.7 Conclusions

To examine the validity of several recent theoretical models of helical ribbons, we developed a variety of new experimental techniques sensitive to the microscopic helical elastic properties. We estimated the helix spring constant by examining thermal fluctuations and helix relaxation in an aqueous medium, and by direct measurement using Si-Ni cantilevers. A comparison of these results with values deduced from the theoretical models is presented in Tables 4.6 and 4.7 below.

The thermal experiments established that the helix spring constants must be at least $K_{\rm helix}^{\rm thermal} > 5 \times 10^{-9}$N/m pN/nm (line (a), Table 4.6). This constraint on the helix spring constant was very important in determining the type of flexible cantilevers that could be used in measurements of the helix spring constant. This constraint was consistent with the spring constant deduced from Helfrich's theory[77] for helices composed of cholesterol–phospholipid bilayer membranes (line (i), Table 4.6). This "consistency" provided a valuable confirmation of our experimental constraint.

Table 4.6: Summary of the helix spring constants obtained through various experimental methods (lines (a) - (h)) and theoretical estimates (lines (i) and (j)). Line (a) describes experimental constraint on K_{helix} made from thermal measurements. Lines (b) - (g) describe helix spring constant in relaxation experiments. Line (h) represents measurement of K_{helix} made with Si-Ni cantilever. Estimate of the helix spring constant deduced from Helfrich's model[77] in conjunction with experimental elastic modulus for cholesterol–phospholipid bilayer is described in line (i) and that for low pitch helices in Chung *et al.*'s theory[12] is shown in line (j).

	Estimation Technique	Spring Constant, K_{helix}, N/m	Thesis Section	Thesis Equation
		Experimental Measurements		
		Thermal		
(a)	$K_{\text{helix}}^{\text{thermal}}$	$> 5 \times 10^{-9}$	4.4	4.56
		Relaxation		
(b)	$K_{\text{helix}}^{\text{relaxation,"One"}}$	$(9.6 \pm 0.8) \times 10^{-7}$	4.5.2	4.85
(c)	$K_{\text{helix}}^{\text{relaxation,"Two"}}$	$(1.6 \pm 0.2) \times 10^{-6}$	4.5.2	4.85
(d)	$K_{\text{helix}}^{\text{relaxation,"Three"}}$	$(2.3 \pm 0.3) \times 10^{-6}$	4.5.2	4.85
(e)	$K_{\text{helix}}^{\text{relaxation,"Four"}}$	$(2.5 \pm 0.3) \times 10^{-6}$	4.5.2	4.85
(f)	$K_{\text{helix}}^{\text{relaxation,"Five"}}$	$(1.7 \pm 0.2) \times 10^{-6}$	4.5.2	4.85
(g)	$K_{\text{helix}}^{\text{relaxation,"Six"}}$	$(8.5 \pm 1.3) \times 10^{-6}$	4.5.2	4.85
		Si-Ni Cantilever		
(h)	K_{helix}	$(4.8 \pm 0.8) \times 10^{-6}$	4.6.3	4.90
		Theoretical Estimates		
(i)	$K_{\text{helix}}^{\text{Helfrich}}(\psi = 45°)$	$\sim 3 \times 10^{-8}$	4.4	4.54
(j)	$K_{\text{helix}}^{\text{Chung}}(\psi \sim 11°)$	$\sim 9 \times 10^{-11}$	4.3.2	4.28

Table 4.7: Summary of the modulus of elasticity obtained from previous experimental measurements[156–161] and from theoretical estimates based on the relaxation data.

	Estimation Technique	Elastic Modulus, K_n^{pp}, N m	Thesis Section	Thesis Equation
(a)	Cholesterol–Phospholipid Bilayers[154,155]	$< 3 \times 10^{-19}$	4.3.2	
(b)	From $K_{\text{helix}}^{\text{relaxation,"One"}}$	$\sim 2.02 \times 10^{-12}$	4.5.2	4.87

Our determination of the helix spring constant via measurements of helix relaxation times provided us with more definite findings. The results for six different low pitch helices are shown in lines (b) - (g) of Table 4.6. As can be observed, the values of $K_{\text{helix}}^{\text{relaxation}}$ differ quite significantly from one helix to the next. This can be explained by variations in helix dimensions, radius, width, axial length, and thickness. When helix spring constants are rescaled with the three geometrical parameters (radius, width, and axial length), as shown in Table 4.4, we found that these rescaled values are still quite different. Therefore, the variations of helix spring constants can be attributed mostly to thicknesses of helical ribbons. The results for six different low pitch helices (lines (b) - (g) of Table 4.6) were compared to estimates deduced from Chung *et al.*'s theory parametrized with elastic moduli for cholesterol–phospholipid bilayers (line (j), Table 4.6). Our smallest measured spring constant, $K_{\text{helix}}^{\text{relaxation,"One"}} = (9.6 \pm 0.8) \times 10^{-7}$ N/m (line (b), Table 4.6), was four orders of magnitude larger than the estimate of $K_{\text{helix}}^{C}(\psi \sim 11°) \sim 9 \times 10^{-11}$ N/m. In addition, this estimate falls below the range allowed by the thermal constraint (line (a), Table 4.6).

As a further comparison between the experimental and theoretical results, we examined the elastic moduli computed from the measurements of helix spring constants and measured elastic moduli for cholesterol–phospholipid bilayers.[117] We estimated the elastic modulus of the material from which low pitch helices are made by parametrizing Chung *et al.*'s theory[12] with our experimentally measured helix spring constant (line (b), Table 4.7) and compared it to the elastic modulus of cholesterol–phospholipid liquid crystal bilayers (line (a), Table 4.7). The estimate obtained is *seven* orders of magnitude larger than the experimentally known value of K_n^{pp} for cholesterol–phospholipid liquid crystal bilayers ($< 3 \times 10^{-19}$),[156–161]. This suggests that, due to their high rigidity, helical ribbons in quaternary sterol systems, and specifically in CDLC, may not be composed of liquid crystal bilayers, but are more

likely crystalline in nature. We were not able to compare our experimental measurements with the inferences made from Selinger *et al.*'s[18] or the crystalline models due to their complex dependence on a variety of elastic moduli.

After rescaling the helix spring constants by their geometrical dimensions, we found an interesting dependence of these constants on ribbon thickness. It appears that the helix spring constants may fall into "quantized" families depending on their thickness. This is in direct agreement with the previous qualitative inferences made from Chung *et al.*'s theory.

Our measurement of the helix spring constant via flexible cantilevers has yielded additional results consistent with our previous measurements of helix spring constants through helix relaxation (Table 4.6). Though difficult, this experiment provides the most direct and precise measure of the helix elastic properties available to date. Together with further study of helix behavior under applied forces (phase separation, for example), this technique may prove very useful in the future for investigating the microscopic structure of the helices.

The crystalline theory predicts that the fractional change in helix radius $\Delta R/R_0$ due to small axial forces vanishes. In comparison, previous theories predict that the fractional change of helix radius is dependent on force applied. This new and interesting discovery implies an experiment in which this relationship can be verified. This experiment can potentially become the first experimental instrument for deducing the correct form of the terms in the expression of the free energy which results in $\Delta R/R_0 = 0$.

Finally, it is very interesting to compare the measured values of the helix spring constants with those found in other biological systems. The spring constant of low pitch helical ribbons in CDLC appears to be approximately one order of magnitude smaller than the value of the spring constant of a lambda phage double stranded DNA molecule,[103,138]. The stiffnesses of the low pitch helical ribbons in CDLC also appear to be one order of magnitude smaller than those of single titin molecules, as shown by the experiments of Kellermayer *et al.*[137] Comparing the stiffness of low pitch helical ribbons in CDLC to that of a 10 μm long actin filament with cross-sectional area of 18 nm^2,[184] or to those of thick filaments of *Lumilus polyphemus* or myosin,[130] we find that the former are three orders of magnitude smaller than the two latter biological structures. And finally, we can also make a comparison of the elasticity of our helical ribbons to that of a single polymer chain of poly(methacrylic acid) finding

that helical ribbons are five orders of magnitude less stiff than the aforementioned polymer chains.[175]

The above comparisons of the elastic constants of helical ribbons in CDLC to those for other self-assembled structures indicate that helical ribbons may prove to be useful micromechanical devices. Such devices could be used for the measurement of the forces and energies associated with interacting biological macromolecules such as molecular motors and bioreceptors. Conceivably, these structures may also prove to be useful for the quantitative characterization of the elastic properties of biological structures such as one-dimensional chains and two-dimensional membranes. To corroborate the latter statement, it may suffice to compare the low pitch helical ribbon stiffnesses to those of mechanical devices currently used by scientists. For a single–beam optical trap, or optical tweezers, the trapping force is usually of the order of 1 - 100 pN, depending upon the size and refractive index of the particle to be trapped and the power and wavelength of the laser beam. Currently the stiffnesses of optical traps can be as low as 0.007 pN/nm, which is of the same order of magnitude as the stiffness of the low pitch helical ribbons in CDLC. A new technique for measurements of forces of molecular adhesion ranging from 0.01 pN to 1000 pN has been developed by Evans *et al.*[116,155] The force transducer employed in this technique is a "cell–size membrane capsule pressurized by micropipette suction where displacement normal to the membrane under tension is proportional to the applied force." The stiffness of this transducer was found to be in the range between 0.001 pN/nm and 1 pN/nm. The lower range of the stiffnesses for this device is again on the same order of magnitude as the stiffnesses of the low pitch helical ribbons in CDLC. In summary, the above work serves as the beginning of a large investigation into the elastic properties of helical ribbons in quaternary sterol systems, which may be invaluable in measurements of elastic properties of a variety of other systems.

4.A Kelvin-Voight Model

An alternative way of obtaining the expression for the spring elastic constant K_{helix} in Eq. (4.59) is by applying the Kelvin-Voight model, which describes the behavior of elastic materials in a viscous medium.[190] This model is described by a system of two elements connected in parallel: a massless Hookean spring and a dashpot filled with a Newtonian fluid, where the rate of the piston movement is directly proportional to the

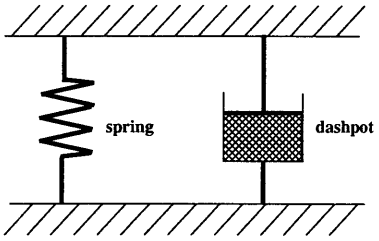

Figure 4.10: Schematic depiction of a Kelvin-Voight model system. This two-element system consists of an elastic spring connected in parallel with a dashpot, i.e. a piston moving in a viscous medium. The Kelvin-Voight model is an alternative way of obtaining the equations of motion for a helical ribbon relaxing in a viscous medium.

viscosity of the fluid and the applied stress. This system is depicted in Figure 4.10. To see how the Voight-Kelvin model can be applied to the case of helical ribbons, we first observe that a helical spring can indeed be considered massless (see Section 4.5.1). We also observe that the stress on a piston in a dashpot must be proportional to the drag coefficient, and we will later correlate this stress with the drag coefficient on a helical ribbon.

In the Kelvin-Voight model system, the strains on the spring and the dashpot, u_{spring} and u_{dashpot}, respectively, are the same, but the total stress is the sum of the stresses, σ's, on each component of the system, i.e.

$$u = u_{spring} = u_{dashpot} \tag{4.98}$$

and

$$\sigma = \sigma_{spring} + \sigma_{dashpot} = Eu + b'\dot{u}, \tag{4.99}$$

respectively, where E is the spring Young's modulus, and b' is the drag coefficient per unit length.Rewriting the stress in Eq. (4.99) in terms of the force on the helical ribbon, and expressing this force in terms of the helix spring constant K_{helix}, and the drag coefficient b, we obtain

$$F = \sigma \times A = F_{spring} + F_{dashpot} = Kx + b\dot{x}. \tag{4.100}$$

where A is the helix cross-sectional area subjected to the drag force. In recovery, when the force on a helix is zero, a solution to this first order differential equation is

$$x = x_0 \exp[-\frac{K_{\text{helix}}}{b}t] = x_0 \exp[-\frac{t}{\tau}], \tag{4.101}$$

where x_0 is the original extension of a helical ribbon and $\tau = b/K$ is the relaxation time constant. Therefore, in recovery, the Kelvin-Voight model predicts exactly the

same relation for the helix spring constant as we found in Eq. (4.59):

$$K_{\text{helix}} = \frac{b}{\tau}. \tag{4.102}$$

Chapter 5

General Conclusions

This thesis embodies the true nature of interdisciplinary research requiring knowledge of such diverse fields as molecular biology, the physical sciences, and materials engineering. Combined, this knowledge leads to an understanding of the molecular, kinetic, and thermodynamic factors that govern biomolecular self-assembly. One example of self-assembly is the formation of helical ribbons and tubules. Though found in a variety of systems, these structures are of particular interest in quaternary sterol systems (QSS), a term specifically coined for systems composed of micelle–forming surfactant(s), bilayer–forming surfactant(s), a sterol, and water. The strong interest in helical ribbons and tubules formed in QSS originates from the uniqueness of their geometry. Three types of helical ribbons are formed in QSS: high pitch with a pitch angle of $54 \pm 2°$, low pitch with a pitch angle of $11 \pm 2°$, and intermediate pitch with a pitch angle in the range between 30° and 47°. Most of the tubules found in these systems are grown from high and low pitch helical ribbons and therefore possess high and low pitch markings. To our knowledge, QSS are the only systems found to date that yield helical ribbons and tubules with these particular pitch angles; QSS are also the only systems producing such a large variety of self-assembling structures.

Built on the original work of Chung *et al.*, this thesis contributes to the understanding of the molecular, thermal, and solution factors that govern the kinetic evolution and geometrical dimensions of helical ribbons and tubules formed from quaternary sterol systems. We have described for the first time the complete pathways of helix and tubule formation and evolution. The study of helix and tubule composition presented in this thesis addressed such important issues as retaining the native geometrical state of the self-assembled structures by placing them in amphiphile–free aqueous solution, as well as controlling helix and tubule growth and dissolution.

This work addresses, for the first time, the question of the manipulation and tethering of the individual structures formed in QSS. We isolated individual structures from the environment in which they form, tethered them to rigid surfaces, and deformed them in a controlled manner. The experimental groundwork required for understanding the adhesion of self–assembled structures formed in QSS to glass surfaces has been provided. The knowledge and development of experimental expertise in helix tethering, and application of forces to individual structures, has led to the observation of helical ribbons' behavior under extensions. We have observed for the first time the tension–induced full elongation of high and low pitch helical ribbons whereby a straight filament is produced. We have also observed that helical ribbons of both pitch angles relax back to their original geometrical shape even after they have been fully elongated. A novel behavior of low pitch helices has also been reported, namely a tension–induced phase separation into straight and helical segments. In order to produce such phase separation, it has been observed that low pitch helical ribbons must have five or more full turns.

We have also for the first time determined experimentally the values of the elastic moduli of helical ribbons associated with their extension. This was achieved by first securely attaching helices to rigid surfaces and then applying well–defined stresses to them. From a variety of devices for measuring microscopic stresses in the pico-newton range that are currently available, we chose to work with the newly fabricated silicon cantilevers that are capable of measuring forces in the upper pico-newton—lower nano-newton range. An alternative method for applying a known stress to a helix used in our experiments was performed by allowing stressed helices to relax in an aqueous solution. This method is identical to the placement of the individually tethered structure in a fluid flowing within a known velocity field. The hydrodynamic force applied in this case was estimated and the values of the helix spring constants were determined. The estimate for the drag coefficient on an axially moving helical ribbon was proposed, and it was shown experimentally that this estimate is reasonable.

A new model for the existence of helical ribbons in QSS has been developed. This model is based on the elastic theory of crystals, whereby helical ribbons are modeled as having a crystalline positionally ordered molecular structure. This theory was originally proposed to correct for the large ratio of the anisotropic elastic moduli predicted by Chung *et al.* for low pitch helical ribbons. The free energy function predicted in the crystalline model is based on the minimum set of assumptions necessary

to describe geometrical features of helical structures, and the symmetries experimentally observed during helix evolution. This theory predicts that the fractional change due to small axial stresses is $\Delta R/R = 0$. This is in comparison to predictions of other theories, in which $\Delta R/R$ is a force dependent quantity. By performing careful experiments sensitive to the fractional changes of helix radius as small axial forces are applied, it must be possible to determine the structure of the elastic moduli in the free energy function. When performed, these experiments will serve as a first experimental comparison of various theoretical models. Using experimentally measured values of helix spring constants and further studying of the phase transitions of low pitch structures, we expect to obtain a full set of elastic moduli describing behavior of low pitch structures. As the behavior of high pitch helices under tension is quite different, a different approach has to be developed to obtain all elastic moduli for these structures.

As a whole, the work described in this thesis is a useful advance in understanding of the molecular factors which govern the kinetic evolution and the geometrical structure of self-assembled microstructures constituted of chiral amphiphiles. The groundwork for the experimental manipulation of individual helical ribbons and tubules presented herein has led to the first observations of novel tension–induced helix behavior, as well as the first measurements of helix spring constants. It is believed that the work presented in this thesis shall provide a basis for further research in this area. For example, it is the hope of the author that these new findings will facilitate further investigations into the elastic properties of helices and tubules. When the elastic properties of these structures are well–understood and predicted, these structures may prove to be useful micro-mechanical devices which could be used for the measurement of the forces and energies associated with interacting biological macromolecules such as molecular motors and bioreceptors. Conceivably, these structures may also prove useful for the quantitative characterization of the elastic properties of biological structures such as one-dimensional chains and two-dimensional membranes.

Bibliography

1. J. G. Tirrell, M. J. Fournier, T. L. Mason, , and D. A. Tirrell. Biomolecular materials. *Chemical and Engineering News* **72**: 40–51 (1994).

2. N. Unwin and R. Henderson. The structure of proteins in biological-materials. *Scientific American* **250**: 78 (1984).

3. L. H. Dubois and R. G. Nuzzo. Synthesis, structure, and properties of model organic surfaces. *Ann. Rev. Phys. Chem* **60**: 437–463 (1992).

4. A. Ulman. *An Introduction to Ultrathin Organic Films: From Langmuir–Blodgett to Self–Assembly.* Academic Press, Boston (1991).

5. K. L. Prime and G. M. Whitesides. Adsorption of proteins onto surfaces containing end–attached oligo(ethylene oxide) — a model system using self–assembled monolayers. *J. Am. Chem. Soc.* **115**: 10714–10721 (1993).

6. T. G. Vargo, P. M. Thompson, L. J. Gerenser, R. F. Valentini, P. Aebischer, D. J. Hook, and J. A. Gardella. Monolayer chemical lithography and characterization of fluoropolymer films. *Langmuir* **8**: 130–134 (1992).

7. A. Kumar, N. L. Abbott, E. Kim, H. A. Biebuyck, and G. M. Whitesides. Patterned self-assembled monolayers and mesoscale phenomena. *Accounts Chem. Res.* **28**: 219–226 (1995).

8. National Research Council. *Hierarchical Structures in Biology As a Guide for New Materials Technology.* National Academy Press, Washington, D. C. (1994).

9. D. D. Lasic. *Liposomes: From Physics to Applications.* Elsevier, Amsterdam (1993).

10. W. Baumeister and G. Lembcke. Structural features of archaebacterial cell envelopes. *J. Bioenerg. Biomembr.* **24**: 567–575 (1992).

11. J. M. Schnur. Lipid tubules: A paradigm for molecularly engineered structures. *Science* **262**: 1669–1675 (1993).

12. D. S. Chung, G. B. Benedek, F. M. Konikoff, and J. M. Donovan. Elastic free energy of anisotropic helical ribbons as metastable intermediates in the crystallization of cholesterol. *Proc. Natl. Acad. Sci. USA* **90**: 11341–11345 (1993).

13. P. Yager and P. E. Schoen. Formation of tubules by a polymerizable surfactant. *Mol. Cryst. Liq. Cryst.* **106**: 371–381 (1984).

14. J. V. Selinger and J. M. Schnur. Theory of chiral lipid tubules. *Phys. Rev. Lett.* **71**: 4091–4094 (1993).

15. Y. M. Lvov, R. R. Price, J. V. Selinger, A. Singh, M. S. Spector, and J. M. Schnur. Imaging nanoscale patterns on biologically derived microstructures. *Langmuir* **15**: 5932–5935 (2000).

16. J. M. Schnur, R. Price, and A. Rudolph. Biologically engineered microstructures — controlled–release applications. *J. Controlled Release* **28**: 3–13 (1994).

17. S. L. Browning, J. Lodge, R. R. Price, J. Schelleng, P. E. Schoen, and D. Zabetakis. Fabrication and radio frequency characterization of high dielectric loss tubule–based composites near percolation. *J. Appl. Phys.* **84**: 6109–6113 (1998).

18. J. V. Selinger, F. C. MacKintosh, and J. M. Schnur. Theory of cylindrical tubules and helical ribbons of chiral lipid membrane. *Phys. Rev. E* **53**: 3804–3818 (1996).

19. S. Komura and O. Y. Zhong-can. High- and low-pitch helical structures of tilted chiral lipid bilayers. *Phys. Rev. Lett.* **81**: 473–476 (1998).

20. F. M. Konikoff, D. S. Chung, J. M. Donovan, D. M. Small, and M. C. Carey. Filamentous, helical and tubular microstructures during cholesterol crystallization from bile: evidence that biliary cholesterol does not nucleate classic monohydrate plate. *J. Clin. Invest.* **90**: 1155–1160 (1992).

21. A. Kaplun, Y. Talmon, F. M. Konikoff, M. Rubin, A. Eitan, M. Tadmor, and D. Lichtenberg. Direct visualization of lipid aggregates in native human bile by light- and cryo-transmition electron-microscopy. *FEBS Letters* **340**: 78–82 (1994).

22. H. Ochi, S. Tazuma, and G. Kajiyama. Lecithin hydrophobicity modulates the process of cholesterol crystal nucleation and growth in supersaturated model bile systems. *Biochem.* **318**: 139–144 (1996).

23. S. Tao, S. Tazuma, and G. Kajiyama. Fatty acid composition of lecithin is a key factor in bile metastablility in supersaturated model bile systems. *Biochim. Biophys. Acta* **1167**: 142–146 (1993).

24. S. Tazuma, H. Ochi, K. Teramen, Y. Yamashita, K. Horikawa, H. Miura, N. Hirano, M. Sasaki, N. Aihara, S. Hatsushika, S. Tao, T. Ohya, and Kajiyama. Degree of fatty acyl chain unsaturation in biliary lecithin dictates cholesterol nucleation and crystal growth. *Biochim. Biophys. Acta* **1215**: 74–78 (1994).

25. F. M. Konikoff, D. E. Cohen, and M. C. Carey. Phospholipid molecular species influence crystal habits and transition sequences of metastable intermediates during cholesterol crystallization from bile salt-rich model bile. *J. Lipid Res.* **35**: 60–70 (1994).

26. D. Q-H. Wang and M. C. Carey. Complete mapping of crystallization pathways during cholesterol precipitation from model bile: influence of physical-chemical variables of pathophysiologic relevance and identification of a stable liquid crystalline state in cold, dilute and hydrophilic bile salt-containing systems. *J. Lipid Res.* **37**: 606–630 (1996).

27. Y. Ringel, G. J. Somjen, F. M. Konikoff, R. Rosenberg, and T. Gilat. Increased saturation of the fatty acids in the sn-2 position of phospholipids reduces cholesterol crystallization in model biles. *Biochim. Biophys. Acta* **1390**: 293–300 (1998).

28. F. M. Konikoff, D. E. Cohen, and M. C. Carey. Filamentous crystallization of cholesterol and its dependence on lecithin species in bile. *Mol. Cryst. Liq. Cryst. - A* **248**: 291–296 (1994).

29. D. Q-H. Wang and M. C. Carey. Characterization of crystallization pathways during cholesterol precipitation from human gallbladder biles: Identical pathways to corresponding model biles with three predominating sequences. *J. Lipid Res.* **37**: 2539–2549 (1996).

30. D. J. Cabral and D. M. Small. *Handbook of Physiology. A critical, comprehensive presentation of physiological knowledge and concepts*, volume Section 6. American Physiological Society, Bethesda, Maryland (1989).

31. N. Nakashima, S. Asakuma, and T. Kunitake. Optical microscopic study of helical superstructures of chiral bilayer membranes. *J. Am. Chem. Soc.* **107**: 509–510 (1985).

32. J. H. Georger, A. Singh, R. R. Price, J. M. Schnur, P. Yager, and P. E. Schoen. Helical and tubular microstructures formed by polymerizable phosphatidylcholines. *J. Am. Chem. Soc.* **109**: 6169–6175 (1987).

33. J.-H. Fuhrhop, P. Schnieder, E. Boekema, and . Helfrich W. Lipid bilayer fibers from diastereomeric and enantiomeric n-octylaldonamides. *J. Am. Chem. Soc.* pages 2861–2867 (1988).

34. B. N. Thomas, R. C. Corcoran, C. L. Cotant, C. M. Lindemann, J. E. Kirsch, and P. J. Persichini. Phosphonate tubules. 1. *J. Am. Chem. Soc.* **120**: 12178–12186 (1998).

35. B. N. Thomas, C. M. Lindemann, and N. M. Clark. Left- and right-handed helical tubule intermediates from a pure chiral phospholipid. *Phys. Rev. E* **59**: 3040–3047 (1999).

36. R. M. Servuss. Helical ribbons of lecithin. *Chem. Phys. Lipids* **46**: 37–41 (1988).

37. L. D. Landau and E. M. Lifshitz. *Theory of elasticity*, volume Volume 7. Pergamon Press, New York, third edition (1986).

38. H. Y. Saad and W. I. Higuchi. Water solubility of cholesterol. *J. Pharm. Sci.* **54**: 1205–1206 (1965).

39. M. C. Carey and M. J. Cahalane. Enterohepatic circulation. In I. M. Arias, W. B. Jakoby, H. Popper, D. Schachter, and D. A. Shafritz, editors, *The Liver: Biology and Pathobiology*, pages 573–616. Raven Press, Ltd., New York (1988).

40. J. M. Donovan and M. C. Carey. Physical-chemical basis of gallstone formation. *Gastroenterology Clinics of North America* **20**: 47–66 (1991).

41. Y. V. Zastavker, N. Asherie, A. Lomakin, J. Pande, J. M. Donovan, J. M. Schnur, and G. B. Benedek. Self-assembly of helical ribbons. *Proc. Natl. Acad. Sci. U.S.A.* **96**: 7883–7887 (1999).

42. F. M. Konikoff and M. C. Carey. Monitoring billiary cholesterol crystallization, transformation, and growth: Density gradient evidence that initial crystals are unhydrous and hydrate slowly. *Hepatology* **16**: 124A (1992).

43. J. M. Donovan, N. Timofeyeva, and M. C. Carey. Influence of total lipid concentration, bile salt:lecithin ratio, and cholesterol content on inter-mixed micellar/vesicular (non-lecithin-associated) bile salt concentrations in model bile. *J. Lipid Res.* **32**: 1501–1512 (1991).

44. S. Lee, H. Park, H. Madani, and E. Kaler. Partial characterization of a nonmicellar system of cholesterol solubilization in bile. *Am. J. Physiol.* **252**: 374–383 (1987).

45. M. C. Carey and D. M. Small. The physical chemistry of cholesterol solubility in bile. relationship to gallstone formation and dissolution in man. *J. Clin. Invest.* **61**: 998–1026 (1978).

46. J. L. Pope. Crystallization of sodium taurocholate. *J. Lipid Res.* **8**: 146–147 (1967).

47. Research Services Branch (RSB) of the National Institute of Mentail Health (NIMH), Bethesda, MD. *NIH Image V1.61*, (1997).

48. C. J. Easton. *Modified Cyclodextrins: Scaffolds and Templates of Supramolecular Chemistry.* Imperial College Press, River Edge, N. J. (1999).

49. J. Szejtli. *Cyclodextrin Technology.* Kluwer Academic Publishers, Boston (1988).

50. G. F. Gibbons, K. A. Mitropoulos, and N. B. Myant. *Biochemistry of cholesterol.* Elsevier Biomedical Press (1982).

51. Claudy et al. *J. Thermal Analysis* (1991).

52. A. E. Christian, M. P. Haynes, M. C. Phillips, and G. H. Rothblat. Use of cyclodextrins for manipulating cellular cholesterol content. *J. Lipid Res.* **38**: 2264–2272 (1997).

53. Inc. Avanti Polar Lipids. Catalog vi. *Company Catalog* **VI**: 49–50 (1999).

54. F. Gunstone. *Fatty Acid and Lipid Chemistry*, volume Chapter 3. Blackie Academic and Professional, Glasgow (1996).

55. D. Marsh. *CRC Handbook of Lipid Bilayers.* CRC Press, Boca Raton, first edition (1990).

56. H. S. Shieh, L. G. Hoard, and C. E. Nordman. Crystal structure of anhydrous cholesterol. *Nature* **267**: 287–289 (1977).

57. M. C. Carey. *Lipid solubilization in bile.* Northfield, T.C., Jazrawi, R.P., Zentler-Munro, P.L. editors. Kluwer, Dordrecht (1988).

58. J. J. Collins and M. C. Phillips. The stability and strucutre of cholesterol-rich codispersions of cholesterol and phosphatidylcholine. *J. Lipid Res.* **23**: 291–298 (1982).

59. D. Jungst, T. Lang, P. Huber, V. Lange, and G. Paumgartner. Effect of phospholipids and bile acids on cholesterol nucleation time and vesicular/micellar cholesterol in gallbladder bile of patients with cholesterol stones. *J. Lipid Res.* **34**: 1457–1464 (1993).

60. N. Nandi and B. Bagchi. Molecular origin of the intrinsic bending force for helical morphology in chiral amphiphilic assemblies: concentration and size dependence. *J. Am. Chem. Soc.* **118**: 11208–11216 (1996).

61. N. Nandi and B. Bagchi. Prediction of the senses of helical amphiphilic assemblies from the effective intermolecular pair potential: studies on chiral monolayers and bilayers. *J. Phys. Chem. A.* **101**: 1343–1351 (1997).

62. A. A. Spector, S. N. Mathur, and T. L. Kaduce. *Progress in Lip. Res.* **19**: 155 (1981).

63. G. Rothblat and D. Kritchevsky. *Lipid Metabolism in Tissue Culture Cells.* The Wistar Institute Press, Philadeliphia (1967).

64. T. E. Mittler and R. H. Dadd. *Metabolic Aspects of Lipid Nutrition in Insects.* Westwood Press Incorporated (1983).

65. R. H. Goodwin. *Cell Biology.* Elsevier Scientific Publ. Ltd. (1985).

66. L. L. Stoll and A. A. Spector. Lipid transfer between endothelial and smooth-muscle cells in coculture. *J. Cell. Physiol.* **133**: 103–110 (1987).

67. C. P. Burns and A. A. Spector. Membrane fatty-acid modification in tumor-cells — a potential therapeutic adjunct. *Lipids* **22**: 178–184 (1987).

68. R. F. Addison, R. G. Ackman, and J. Higley. *J. Fish. Res. Bd. Canada* **25**: 2083–2090 (1968).

69. L. J., Goad, and T. Akishia. *Analysis of Sterols.* Blackie Academic and Professional, first edition (1997).

70. H.-S. Shieh, L. G. Hoard, and C. E. Nordman. The structure of cholesterol. *Acta Cryst.* **B37**: 1538–1543 (1981).

71. P.-G. de Gennes. *The Physics of Liquid Crystals.* Oxford University Press, London (1975).

72. P. G. de Gennes. Electrostatic buckling of chiral lipid bilayers. *C. R. Adad. Sci. II Paris* **304**: 259–263 (1987).

73. J. S. Chappell and P. Yager. Electrolyte effects on bilayer tubule formation by a diacetylenic phospholipid. *Biophys. J.* **60**: 952–965 (1991).

74. J. S. Chappell and P. Yager. Electrostatic interactions within helical structures of chiral lipids. *Chem. Phys.* **150**: 73–79 (1991).

75. M. A. Markowitz, J. M. Schnur, and A. Singh. The influence of the polar headgroups of acidic diacetylenic phospholipids on tubule formation, microstructure morphology and langmuir film behavior. *Chem. Phys. Lipids* **62**: 193–204 (1992).

76. T. C. Lubensky and J. Prost. Orientational order and vesicle shape. *J. Phys. (France) II* **2**: 371–382 (1992).

77. W. Helfrich. Helical bilayer structures due to spontaneous torsion of the edges. *J. Chem. Phys.* **85**: 1085–1087 (1986).

78. W. Helfrich and J. Prost. Intrinsic bending force in anisotropic membranes made of chiral molecules. *Phys. Rev. A* **38**: 3065–3068 (1988).

79. Z. c. Ou-Yang and J. X. Liu. Helical structures of tilted chiral lipid bilayers viewed as cholesteric liquid crystals. *Phys. Rev. Lett.* **65**: 1679–1682 (1990).

80. J. S. Chappell and P. Yager. A model for crystalline order within helical and tubular structures of chiral bilayers. *Chem. Phys. Lipids* **58**: 253–258 (1991).

81. P. Nelson and T. Powers. Rigid chiral membranes. *Phys. Rev. Lett.* **69**: 3409–3412 (1992).

82. N. Nakashima, S. Asakuma, J. M. Kim, and T. Kunitake. Helical superstructures are formed from chiral ammonium bilayers. *Chem. Lett.* **10**: 1709–1712 (1984).

83. K. Yamada, H. Ihara, T. Ide, T. Fukumoto, and C. Hirayama. Formation of helical superstructures from single–walled bilayers by amphiphiles with oligo-l-glutamic acid–head group. *Chem. Lett.* **10**: 1713–1716 (1984).

84. P. Yager, P. E. Schoen, C. Davies, R. Price, and A. Singh. Structure of lipid tubules formed from a polymerizable lecithin. *Biophys. J.* **48**: 899–906 (1985).

85. I. Dahl and S. T. Lagerwall. Elastic and flexoelectric properties of chiral smectic-c phase and symmetry considerations on ferroelectric liquid-crystal cells. *Ferroelectics* **58**: 215–243 (1984).

86. P. Bugl and S. Fujita. *J. Chem. Phys.* **50**: 3137 (1969).

87. S. A. Langer and J. P. Sethna. Textures in a chiral smectic liquid-crystal film. *Phys. Rev. A* **34**: 5035–5046 (1986).

88. T. S. Lubensky and F. C. MacKintosh. Theory of ripple phases of lipid bilayers. *Phys. Rev. Lett.* **71**: 1565–1568 (1993).

89. C.-M. Chen, T. C. Lubensky, and F. C. MacKintosh. Phase transitions and modulated phases in lipid bilayers. *Phys. Rev. E* **51**: 504–513 (1995).

90. J. M. Schnur, B. R. Ratna, J. V. Selinger, A. Singh, G. Jyothi, and K. R. K. Easwaran. Diacetylenic lipid tubules — experimental-evidence for a chiral molecular architecture. *Science* **264**: 945–947 (1994).

91. W. B. Bickford. *Mechanics of Solids: Concepts and Applications.* Irwin, Burr Ridge, IL, first edition (1993).

92. P. L. Gould. *Introduction to Linear Elasticity.* Springer-Verlag, New York, first edition (1983).

93. D. J. Struik. *Lectures on Classical Differential Geometry.* Dover Publications Inc. , New York, second edition (1988).

94. L. G. Jaeger. *Elementary Theory of Elastic Plates.* Pergamon Press Ltd., New York (1964).

95. C.-T. Wang. *Applied Elasticity.* McGraw-Hill Book Company, Inc., New York (1953).

96. M. Filonenko-Borodich. *Theory of Elasticity.* P. Noordhoff N. V. Scientific Publishers, Groningen, the Netherlands (1965).

97. K. E. Drexler, C. Peterson, and G. Pergamet. *Unbounding the Future: The Nanotechnology Revolution.* Quill Press, William Morrow and Company, New York, first edition (1991).

98. C. Lampton. *Nanotechnology Playhouse: Building Machines from Atoms.* The Waite Group Press, Corte Madera, CA, first edition (1993).

99. G. Binnig, C. F. Quate, and C. Gerber. Atomic force microscope. *Phys. Rev. Lett.* **56**: 930–933 (1986).

100. J. H. Hoh, J. P. Cleveland, C. B. Prater, J.-P. Revel, and P. K. Hansma. Quantized adhesion detected by atomic force microscope. *J. Am. Chem. Soc.* **114**: 4917–4918 (1992).

101. E.-L. Florin, V. T. Moy, and H. E. Gaub. Adhesion forces between individual ligand-receptor pairs. *Science* **264**: 415–417 (1994).

102. U. Dammer, O. Popescu, P. Wagner, D. Anselmetti, H.-J. Guntherodt, and G. N. Misevic. Binding strength between cell adhesion proteoglycans measured atomic force microscopy. *Science* **267**: 1173–1175 (1995).

103. S. B. Smith, Y. Cui, and C. Bustamante. Overstretching B-DNA: The elastic response of individual double-stranded and single-stranded DNA molecules. *Science* **271**: 759–761 (1996).

104. H. Clausen-Schaumann, M. Rief, C. Tolsdorf, and H. E. Gaub. Mechanical stability of single DNA molecules. *Biophys. J.* **78**: 1997–2007 (2000).

105. M. Rief, H. Clausen-Schaumann, and H. E. Gaub. Sequence–dependent mechanics of single DNA molecules. *Nat. Struct. Biol.* **6**: 346–349 (1999).

106. M. W. Berns, W. H. Wright, B. J. Tramberg, G. A. Profeta, J. J. Andrews, and R. J. Walters. Use of a laser-induced force trap to study chromosome movement on the mitotic spindle. *Proc. Natl. Acad. Sci. U.S.A.* **86**: 4539–4543 (1989).

107. S. M. Block, D. F. Blair, and H. C. Berg. Compliance of baterial flagella measured using optical tweezers. *Nature* **338**: 514–518 (1989).

108. M. Mammen, K. Helmerson, R. Kishore, S. Choi, W. D. Phillips, and G. M. Whitesides. Optically controlled collisions of biological objects to evaluate potent polyvalent inhibitors of virus-cell adhesion. *Chemistry and Biology* **3**: 757–763 (1996).

109. K. Svoboda and S. M. Block. Biological applications of optical forces. *Ann. Review of Biophys. and Biomol. Structure* **23**: 247–285 (1994).

110. Y. Tadir, W. H. Wright, O. Vafa, T. Ord, R. H. Asch, and M. W. Berns. Force generation by human sperm correlated to velocity and determined using a laser generated optical trap. *Fertility and Sterility* **53**: 944–947 (1989).

111. D. Choquet, D. P. Felsenfeld, and M. P. Sheetz. Extracellular matrix rigidity causes strengthening of integrin–cytoskeletal linkages. *Cell* **88**: 39–48 (1997).

112. P. A. Valberg and D. F. Albertini. Cytoplasmic motions, rheology, and structure probed by a novel magnetic particle method. *J. Cell Biol.* **101**: 130–140 (1985).

113. N. Wang, J. P. Butler, and D. E. Ingber. Mechanotransduction across the cell surface and through the cytoskeleton. *Science* **260**: 1124–1127 (1993).

114. N. O. Petersen, W. B. Mcconnaughey, and E. L. Elson. Dependence of locally measured cellular deformability on position of the cell, temperature, and cytochalasin b. *Proc. Natl. Acad. Sci. U.S.A.* **79**: 5327–5331 (1982).

115. J.-Y. Shao and R. M. Hochmuth. Micropipette suction for measuring piconewton forces of adhesion and tether formation from neutrophil membranes. *Biophys. J.* **71**: 2892–2901 (1996).

116. E. Evans, K. Ritchie, and R. Merkel. Sensitive force technique to probe molecular adhesion and structural linkages at biological interfaces. *Biophys. J.* **68**: 2580–2587 (1995).

117. E. Evans, D. Berk, and A. Leung. Detachment of agglutinin-bonded red blood cells: I. forces to rupture molecular-point attachment. *Biophys. J.* **59**: 838–848 (1991).

118. J. Kolega. Effects of mechanical tension on protrusive activity and microfilament and intermediate filament organization in an epidermal epithelium moving in culture. *J. Cell Biol.* **102**: 1400–1411 (1989).

119. T. Dennerll, P. Lamoreux, R. E. Buxbaum, and S. R. Heidemann. The cytomechanics of axonal elongation and retraction. *J. Cell Biol.* **109**: 3073–3083 (1989).

120. S. Felder and E. L. Elson. Mechanics of fibroplast locomotion: Quantitative analysis of forces and motions at the leading lamellas of fibroplasts. *J. Cell Biol.* **111**: 2513–2526 (1990).

121. S. Kamimura and K. Takahashi. Direct measurement of the force of microtubule sliding in flagella. *Nature (London)* **293**: 566–568 (1981).

122. A. Kishino and T. Yanagida. Force measurements by micromanipulation of a single actin filament by glass needles. *Nature (London)* **334**: 74–76 (1988).

123. A. Ishijima, T. Doi, K. Sakurada, and T. Yanagida. Sub-piconewton force fluctuations of actomyosin *in vitro*. *Nature (London)* **352**: 301–306 (1991).

124. H. Kojima, A. Ishijima, and T. Yanagida. Direct measurement of stiffness of single actin filaments with and without tropomyosin by *in vitro* nanomanipulation. *Proc. Natl. Acad. Sci. U.S.A.* **91**: 12962–12966 (1994).

125. M. Tokunaga, T. Aoki, M. Hiroshima, K. Kitamura, and T. Yanagida. Subpiconewton intermolecular force microscopy. *Biochem. and Biophys. Res. Commun.* **231**: 565–569 (1997).

126. T. Aoki, M. Hiroshima, K. Kitamura, M. Tokunaga, and T. Yanagida. Noncontact scanning probe microscopy with sub-piconewton force sensitivity. *Ultramicroscopy* **70**: 45–55 (1997).

127. R. M. Simmons, J. T. Finer, S. Chu, and J. A. Spudich. Quantitative measurements of force and displacement using an optical trap. *Biophysical J.* **70**: 1813–1822 (1996).

128. H. M. Warrick, R. M. Simmons, J. T. Finer, T. Q. Uyeda, S. Chu, , and J. A. Spudich. *In Vitro* methods for measuring force and velocity of the actin-myosin interaction using purified proteins. *Meth. Cell Biol.* **39**: 1–21 (1993).

129. M. E. Fauver, D. L. Dunaway, D. H. Lilienfeld, H. G. Craighead, and G. H. Pollack. Microfabricated cantilevers for measurement of subcellular and molecular forces. *IEEE Trans. Biomed. Eng.* **45**: 891–898 (1998).

130. T. Neumann, M. E. Fauver, and G. H. Pollack. Elastic properties of isolated thick filaments measured by nanofabricated cantilevers. *Biophys. J.* **75**: 938–947 (1998).

131. K. E. Petersen. Young's modulus measurements of thin films using micromechanics. *J. Appl. Phys.* **50**: 6761–6766 (1979).

132. L. Kiesewetter, J. M. Zang, D. Houdeau, and A. Steckenboom. Determination of young's moduli of micromechanical thin films using the resonance method. *Sensors Actuators A* **35**: 153–159 (1992).

133. Newcomer Supply, Middleton, Wisconsin. *Product Catalog*, (1999).

134. Electron Microscopy Sciences, Fort Washington, PA. *Product Catalog*, (1999).

135. ProSciTech, Australia. *Product Catalog*, (1999).

136. G. Lin, K. S. J. Pister, and K. P. Roos. Micro-scale force transducer system to quantify isolated heart cell contractile characteristics. *Sensor and Actuat. A-Phys.* **46**: 233–236 (1995).

137. M. S. Z. Kellermayer and H. L. Granzier. Elastic properties of single titin molecules made visible through fluorescent f-actin binding. *Biochemical and Biophysical Research Communications* **221**: 491–497 (1996).

138. G. V. Shivashankar and A. Libchaber. Single molecule grafting and manipulation using a combined atomic force microscope and an optical tweezer. *Appl. Phys. Lett.* **71**: 3727–3729 (1997).

139. N. Wang and D. E. Ingber. Control of cytoskeletal mechanics by extracellular matrix, cell shape, and mechanical tension. *Biophys. J.* **66**: 2181–2189 (1994).

140. D. E. Ingber. Fibronectin controls capillary endothelial cell growth by modulating cell shape. *Proc. Natl. Acad. Sci. U.S.A.* **87**: 3579–3583 (1990).

141. Becton, Dickinson and Company, Franklin Lakes, NJ. *Product Catalog*, (2000).

142. C. Q. Davis and D. M. Freeman. Using a light microscope to measure motions with nanometer accuracy. *Opt. Engineering* **37**: 1299–1304 (1998).

143. H. Sackin and L. G. Palmer. Basolateral potassium channels in renal proximal tubule. *Am. J. Physiology* **253**: 476–487 (1987).

144. U. F. Greber and L. Gereace. Nuclear-protein import is inhibited by an antibody to a lumenal epitope of a nuclear-pore complex glycoprotein. *J. Cell Biol.* **116**: 15–30 (1992).

145. Sigma, St. Louis, MO. *Product Catalog*, (2000).

146. P. J. Scheur. *Bioorganic Marine Chemistry* **4**: 120–148 (1991).

147. M. P. Olivieri, R. E. Loomis, A. E. Meyer, and R. E. Baier. Surface characterization of mussel adhesive protein films. *J. Adhesion Sci. Technol.* **4**: 197–204 (1990).

148. J. Quinn et al. *Journal of the American Medical Association* (1997).

149. T. F. Mika and R. S. Bauer. Curing agents and modifiers. In C. A. May, editor, *Epoxy Resins: Chemistry and Technology*, chapter 4. Marcel Dekker, Inc., New York, second edition (1988).

150. Y. Tanaka and R. S. Bauer. Curing reactions. In C. A. May, editor, *Epoxy Resins: Chemistry and Technology*, chapter 3. Marcel Dekker, Inc., New York, second edition (1988).

151. H. Lee and K. Neville. *Epoxy Resins: Their Applications and Technology.* McGraw-Hill Book Company, Inc., New York (1957).

152. M. W. Zemansky and R. H. Dittman. *Heat and Thermodynamics.* Mc-Graw-Hill, Inc., New York, sixth edition (1981).

153. Y. M. M. Bishop, S. E. Fienberg, and P. W. Holland. *Discrete Multivariate Analysis.* MIT Press, Cambridge, Massachusetts (1975).

154. J. Song and R. E. Waugh. Bending rigidity of sopc membranes containing cholesterol. *Biophys. J.* **64**: 1967–1970 (1993).

155. E. Evans and W. Rawicz. Entropy-driven tension and bending elasticity in condensed-fluid membranes. *Phys. Rev. Lett.* **64**: 2094–2097 (1990).

156. G. Beblik, R. M. Servuss, and W. Helfrich. *J. Physique* **46**: 1773–1778 (1985).

157. R. M. Servuss, W. Harbich, and W. Helfrich. *Biochim. Biophys. Acta* **436**: 900 (1976).

158. I. Sakurai and Y. Kawamura. *Biochim. Biophys. Acta* **735**: 189 (1983).

159. M. B. Schneider, J. T. Jenkins, and W. W. Webb. *Biophys. J* **45**: 891 (1984).

160. M. B. Schneider, J. T. Jenkins, and W. W. Webb. *J. Phys.* **45**: 1457 (1984).

161. H. Engelhardt, H. P. Duwe, and E. Sackmann. *J. Phys. Lett.* **46**: L–395 (1985).

162. I. M. Ward and D. W. Healey. *An Introduction to the Mechanical Properties of Solid Polymers.* Jon Wiley and Sons, Ltd., Chichester (1993).

163. M. M. Denn. *Process Fluid Mechanics.* Prentice Hall PTR, Englewood Cliffs, NJ, first edition (1980).

164. H. Hauser et al. *Biochim. Biophys. Acta* **650**: 21 (1981).

165. L. J. Lis, M. McAlister, N. Fuller, and R. P. Rand. *Biophys. J.* **37**: 657 (1982).

166. M. J. Janiak, D. M. Small, and G. G. Shipley. *Biochemistry* **15**: 4575 (1976).

167. M. J. Janiak, D. M. Small, and G. G. Shipley. *J. Biol. Chem.* **254**: 6068 (1979).

168. A. Tardieu, V. Luzzati, and F. C. Reman. *J. Mol. Biol.* **75**: 711 (1973).

169. E. N. Serrallach, R. Dijkman, G. H. de Haas, and G. G. Shipley. *J. Mol. Biol.* **170**: 155 (1983).

170. S. W. Hui, J. T. Mason, and C.-H. Huang. *Biochemistry* **23**: 5570 (1984).

171. R. P. Rand, N. Fuller, V. A. Parsegian, and D. C. Rau. *Biochemistry* **27**: 7711 (1988).

172. R. P. Rand and V. A. Parsegian. *Biochim. Biophys. Acta* **988**: 351 (1989).

173. A. Smondyrev and M. L. Berkowitz. Structure of dppc/cholesterol bilayer at low and high cholesterol concentrations: Molecular dynamics simulations. *Biophys. J.* **77**: 2075–2089 (1999).

174. M. Rief, M Gautel, F. Oesterheld, J. M. Fernandez, and H. E. Gaub. Reversible unfolding of individual titin immunoglobulin domains by afm. *Science (Washington, D.C.)* **276**: 1090–1092 (1997).

175. C. Ortiz and G. Hadziioannou. Entropic elasticity of single polymer chains of poly(methacrylic acid) measured by atomic force microscopy. *Macromolecules* **32**: 780–787 (1999).

176. K. Saito, A. Takaaki, T. Aoki, and T. Yanagida. Movement of single myosin filaments and myosin step size on an actin filament suspended in solution by a laser trap. *Biophys. J.* **66**: 769–777 (1994).

177. J. T. Finer, A. D. Mehta, and J. A. Spudich. Characterization of single actin-myosin interactions. *Biophys. J.* **68**: 291s–297s (1995).

178. D. E. Depuis, W. H. Guilford, J. Wu, and D. M. Warshaw. Actin filament mechanics in the laser trap. *J. Muscle Res. Cell Motil.* **18**: 17–30 (1997).

179. L. Tskhovrebova, J. Trinik, J. A. Sleep, and R. M. Simmons. Elasticity and unforlding of the single molecules of the giant muscle protein titin. *Nature* **387**: 308–312 (1997).

180. A. Noy, D. V. Vezenov, J. F. Kayyem, T. J. Meade, and C. M. Liebner. Stretching and breaking duplex DNA by chemical force microscopy. *Chem. Biol.* **4**: 519–527 (1997).

181. M. D. Wang, H. Yin, R. Landick, J. Gelles, and S. M. Block. Stretching DNA wiht optical tweezers. *Biophys. J.* **72**: 1335–1346 (1997).

182. M. D. Wang, M. J. Schnitzer, H. Yin, R. Landick, J. Gelles, and S. M. Block. Force and velocity measured for single molecules of rna polymerase. *Science* **282**: 902–907 (1998).

183. H. P. Erickson. Protein biophysics — stretching single protein molecules: Titin is a weird spring. *Science* **276**: 1090–1092 (1997).

184. F. Gittes, B. Mickey, J. Nettleton, and J. Howard. Flexural rigidity of microtubules abd actin filaments measured from thermal fluctuations in shape. *J. Cell Biol.* **120**: 923–934 (1993).

185. K. Svoboda, C. F. Schmidt, B. J. Schnapp, and S. M. Block. Direct observation of kinesin stepping by optical trapping interferometry. *Nature* **365**: 721–727 (1993).

186. K. Svoboda and S. M. Block. Force and velocity measured for single kinesin molecules. *Cell* **77**: 773–784 (1994).

187. S. C. Kuo and M. P. Sheetz. *Science* **260**: 232–234 (1993).

188. S. C. Kuo, K. Ramanathan, and B. Sorg. *Biophys. J.* **68**: 74 (1995).

189. K. König, L. Svaasand, L. Yagang, G. Sonek, P. Patrizio, Y. Tadir, M. W. Berns, and B. J. Tromberg. Determination of motility forces of human spermatozoa using an 800 nm trap. *J. Cell Mol. Biol.* **42**: 501–509 (1996).

190. J. D. Ferry. *Viscoelastic Properties of Polymers.* Jon Wiley and Sons, Ltd., New York (1970).